Journal of the CERAMIC SOCIETY of Japan, International Edition 第98集 第1138号 平成2年6月25日発行 (毎月1回25日発行) ISSN 0912-9200

Journal of the CERAMIC SOCIETY of Japan, International Edition

Vol.98 June 1990

- 17 Papers from Nippon Seramikkusu Kyokai Gakujutsu Ronbunshi, Vol.98 No.6 1990

NIPPON SERAMIKKUSU KYOKAI GAKUJUTSU RONBUNSHI Vol.98 1990

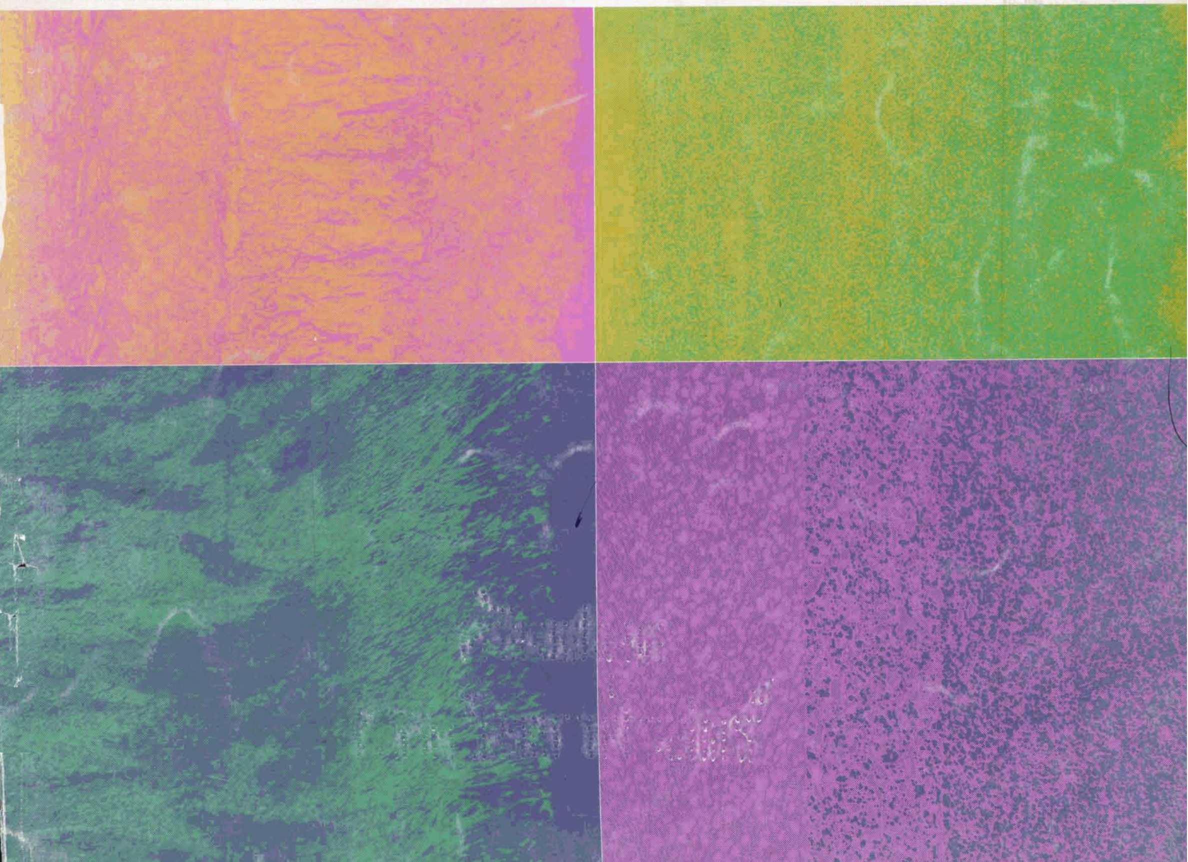

Journal of Ceramic Society of Japan, *International Edition*

Vol.98 No.6
Jun. 1990

Editorial Board
Dr. Teruo Sakaino
Prof. Emeritus, Tokyo Institute of Technology
Dr. Nobuyasu Mizutani
Prof., Tokyo Institute of Technology
Dr. Yusuke Moriyoshi
Director, Nat. Inst. for Res. in Inorganic Materials
Dr. Kitao Takahara
Prof., Nagoya University
Yukio Endo
Chairman
Koyo-sha Co., Ltd.
Dr. Takashi Hanazawa
Executive Director,
The Ceramic Society of Japan
Seiji Iwata
Executive Director,
Japan Fine Ceramics Association
Keiji Hayashi
Managing Editor

Editors

Managing Editor	Keiji Hayashi
Associate Editors	Akiko Ogawa Nigel Madge
Art Director	Prof.Yuji Isa
Assistant Artists	Toshimitsu Irie
Assistant	Kiyoe Kojima
Circulation	Youko Matsumoto
Publisher	Keiji Hayashi

Published Monthly by
FUJI TECHNOLOGY PRESS LTD.
7F Daini Bunsei Bldg.
11-7, Toranomon 1-chome
Minato-ku, Tokyo 105, Japan
Tel:(03)-508-0051
Fax:81-3-592-0648

One year subscription
Air Mail ¥200,000

Copyright - 1990 by The Ceramic Society of Japan and Fuji Technology Press Ltd. All rights reserved.

No part of this publication may be reproduced, stored in a retrieval system, or transmitted, in any form or by any means, electronic, mechanical, photo copying, recording, or otherwise, without the prior written permission of the publishers. The papers, excluding those on information and communications, reviews, etc., were originally received by Nippon Seramikkusu Kyokai Gakujutsu Ronbunshi, and translated for this journal. The responsibility for the translation lies with the Publisher.

Contents

Papers:

Technical reports:

Notes:

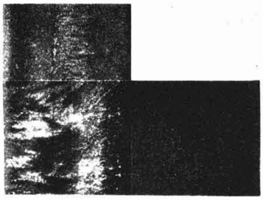

Cover

A concept has been proposed by Japanese scientists to solve the problems of using ceramics as structural materials.

Ceramics are highly heat resistant but have low fracture toughness, while metals have high fracture toughness but less heat resistance. If a new material with the combined advantages of metals and ceramics could be created, it would solve the problems, and thus the concept has been proposed that ceramics and metals should be laminated in layers of atomic order thickness ranging from 100% metal to 100% ceramic. A material with this kind of functional gradient may have the fracture strength of metal combined with the high-temperature resistance of ceramics.

(clockwise from upper left)

1) Cross-sectional surface of SiC-C FGM by SEM
2) Cross-sectional surface of SiC-C FGM by EPMA. (1 & 2: Courtesy of Dr. Hirai and Dr. Sasaki, Institute for Materials Research, Tohoku University)
3) Example of microscopic observation of ZrO2-Ni FGM made by the thin-film lamination method. This sample is a sintered lamination from 100% ceramic to 50% ceramic (Courtesy of Dr. Tamura, NKK)
4) Cross-section photo of C-SiC FGM coated on C/C composite. The composition continuously changes from C to SiC. (Courtesy of Dr. Igarashi and Mr. Kawai, Sumitomo Electric Industries, Ltd.)

Photos taken for "Research on Basic Technologies for Developing Functionally Gradient Materials for Reducing Thermal Stress" supported by the Science & Technology Agency's 1988 Special Coordination Funds for Promoting Science and Technology

Information & Communications

Papers, Letters and Notes

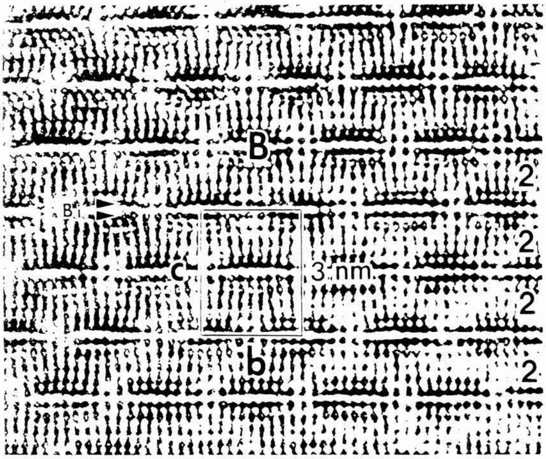

High resolution electron microscope photograph of the modulation doped structure of $Bi_2Sr_2CaCu_2O_y$ ($T_c = 80K$) in the [100] direction. Figures at right side indicate number of copper layers, symbol B indicates bismuth rich region.

Dynamic and Static Fatigue Strength and Crack Propagation of Engineering Ceramics

Tatsuki Ohji, Yukihiko Yamauchi, Wataru Kanematsu and Shoji Ito

Government Industrial Research Institute, Nagoya
Hirate-cho 1-1, Kita-ku, Nagoya 462 Japan

High temperature static (constant stress loading) and dynamic (constant stress rate loading) fatigue tests were conducted on hot-pressed silicon nitride and sintered silicon carbide in vacuum, and the results were treated by two types of crack growth expression, power-law and exponential relations. The log-log representation based on the power-law relation for data on the silicon nitride produced a change in slope, suggesting effects of accelerated crack extension by rapid cavity spreading, and the semi-log representation based on the exponential relation resulted in excellent fit with one straight line. On the other hand, data for the silicon carbide were shown to be better described by both relations. Hence, the superiority of exponential crack growth expression was suggested for life prediction as a consequence.

[Received November 14, 1989; Accepted February 13, 1990]

Key-Words: Silicon nitride, Silicon carbide, Delayed fracture, Dynamic fatigue test, Static fatigue test, Crack growth relation

1. Introduction

Ceramic materials mostly show subcritical crack growth preceding their brittle fractures, which leads to time-dependent fracture. This characteristic of subcritical crack growth, namely the relationship between crack propagation rate and stress intensity factor, can be directly obtained in fracture mechanics tests like double torsion technique, etc.[1] These methods are very expedient in respect to accurate and detailed observation of fracture behavior. However, the initial size of the cracks observed in these tests is much larger than that included in structural parts, and does not sufficiently represent the crack propagation behavior in the ceramic components in use. The fractures of ceramics are usually initiated from cracks of several tens of micrometers, while cracks used in fracture mechanics tests are artificially introduced, and are of the order of millimeters. This discrepancy has some possibility of resulting in a large difference in crack propagation behavior. On the other hand, crack growth data can be inferred from results of strength measurements by applying stress in a static or dynamic manner. Although this method provides only two parameters, time-to-failure and strength, and lacks information about the process until failure, the cracks to be observed in these measurements are pre-existing natural cracks and are the same as those in structural parts.

The relationship between stress intensity factor and crack propagation rate is commonly described in the form of a power-law function of stress intensity factor. This form was first proposed by Charles[2,3] to express water vapor corrosion in glass, and has been widely used for describing crack growth and delayed fracture in engineering ceramics as well as glass, partly due to its ease of mathematical manipulation. However, it has no theoretical background. Besides a power-law relation, several types of expressions for crack propagation rate have been proposed,[4-7] and most of them take exponential forms of stress or stress intensity factor. Trantina proposed three types of exponential crack growth relations and showed their superiority to a power-law relation for high temperature life prediction of hot-pressed silicon nitride.[4] Quinn reported that the expression for time-to-failure taking exponential form of stress successfully described long duration static fatigue lives of hot-pressed silicon nitride at high temperatures.[5] Wiederhorn revealed that a thermally activated crack-growth process expressed by exponential function of stress intensity factor well explained crack growth of glass in vacuum.[6] Furthermore, Charles expressed "diffusion controlled stress rupture at high temperatures" in an exponential form of stress.[7]

Fracture strength of ceramics after long term exposure is substantially affected by the atmosphere. An oxidation atmosphere, particularly, sometimes brings strength improvements due to crack healing by oxidized layer formation or grain boundary strengthening by change of chemical composition,[8,9] and sometimes causes strength degradation due to formation of oxidation pits, etc.[10,11] Most delayed fracture strength measurements have been conducted in air atmosphere, and hence included these effects more or less, resulting in somewhat ambiguous consequences.

In this study the delayed fracture strength under static (constant stress) and dynamic (constant stressing rate) uniaxial tension mode was measured at high temperatures up to 300 hours by use of two types of non-oxide ceramics, hot-pressed silicon nitride and sintered silicon carbide. For the above reason a vacuum atmosphere was employed. The results were analyzed using both of the above models to evaluate each fitness. They were also discussed in association with their microstructure, particularly with grain boundary characteristics.

2. Experimental Procedures

This study used commercially available hot-pressed silicon nitride doped with 5 wt% yttria and 3 wt% alumina and pressureless sintered silicon carbide with 4 wt% alumina. A lot of efforts have been made to clarify the microstructure of both materials.[12-15] The densities were determined to be 3.21 and 3.08 Mg/m^3, respectively, by water immersion. The tensile test specimen, which has plate-like shape as shown in **Fig. 1**, was fabricated from purchased billets in a profile grinding machine. For hot-pressed material the longitudinal direction of the specimen was made perpendicular to the hot-pressing direction. The gauge length area of the specimen was hand polished along its length with 2000 grid diamond paste to eliminate surface flaws introduced in the machining process, though the effects of machining flaws on high temperature strength are expected to be reduced from the fact that strength recovery by this hand-polishing process seen at room temperature is not obtained at high temperatures in sintered silicon nitride.[16)]

The tensile testing apparatus has been described elsewhere in detail.[17,18)] The test specimen was retained by four silicon carbide pins. For the low displacement rate tests and static fatigue tests, the silicon carbide pins to hold holding the specimen were made so that they exactly conformed to the specimen's shoulder to prevent local deformation at the support portion. The specimen holders were connected to pulling rods by universal joints. Axial alignment was ensured for each test by the use of four strain gauges attached to the central parts of the gauge length area. Up to a loading of 500N the bending stress on the surface was suppressed to be within 4% of the tensile stress before raising temperature, and during heating, a load of 5N was constantly applied so as not to disturb the axial alignment by heat expansion. Tests were conducted in a vacuum atmosphere of 10^{-4}torr. The furnace reached test temperatures in about 30 min, and the specimen was held for 30 min at these temperatures to achieve thermal equilibrium before tests were started. Uniformity of temperature along the gauge length area of specimens was verified to be within 3°C using a PtRh6-30 thermocouple. In the testing apparatus used, the displacement rate could be lowered down to 0.00005mm/min, but dynamic fatigue strength data with significant plastic deformations were eliminated from the test results. In static fatigue tests, a load was initially applied at a crosshead speed of 0.1mm/min, and it took several minutes. Thus, when time to fracture is so short, effect of this initial load application is not negligible. Hence, in this study the strength of specimens fractured in less than 10 times as long as the time of the initial load application was also excluded. Static fatigue tests were interrupted at 300 hours in cases of no fracture.

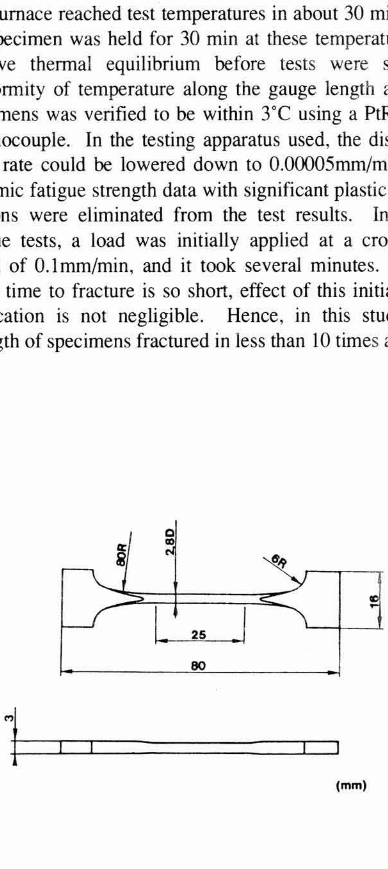

Fig. 1. Geometry and dimensions of tensile test specimen.

3. Experimental Results

3-1. Power-Law Crack Propagation Rate Model

The behavior of subcritical crack growth is usually expressed by the relationship between the stress intensity factor, K_I, and crack propagation rate, v:

$$da/dt = v(K_I) \quad \ldots\ldots (1)$$

where a is the crack length. In this study, this relationship was inferred from the results of both static fatigue (constant stress) and dynamic fatigue (constant stress rate) tests. The $K_{I\text{-}v}$ relationship obtained in the dynamic fatigue test represents characteristics of the high crack propagation rate region, whereas that in the static fatigue test reflects those of the low rate region, as is shown later.

For most structural ceramics, crack propagation rate is commonly expressed by a power-law relation:

$$v = A(K_I/K_{IC})^n \quad \ldots\ldots (2)$$

where K_{IC} is the critical stress intensity factor and A and n are constants which depend on temperature and environment and are determined by obtained strength data. The applied stress, σ, can be related with K_I and a by

$$K_I = \sigma Y \sqrt{a} \quad \ldots\ldots (3)$$

where Y is a constant dependent on the crack geometry. On the assumption that the time to failure is time for a pre-existing flaw to subcritically grow up to the critical size, differentiating equation (3) and substituting into equation (2) yield the time to failure for constant stress, t_f:

$$t_f = 2K_{IC}^2\,(\sigma_{IC} / \sigma_f)^n \,/\, (\sigma_{IC}^2 Y^2 A(n-2) \quad \ldots\ldots (4)$$

where σ_{IC} is the critical strength, and σ_f is the applied constant stress. For constant stress rate loading, the time to failure, t_f', is related to that for constant stress, t_f, by

$$t_f' = (n+1)t_f. \quad \ldots\ldots (5)$$

when σ_f in equation (4) is regarded as the fracture strength in a constant stress rate test.

When log σ_f and log t_f are made vertical and horizontal axes, respectively, the relationship expressed by equation (4) results in a straight line with slope of -1/n. The results of high temperature static and dynamic fatigue tests on hot-pressed silicon nitride and sintered silicon carbide were shown in this manner in **Figs. 2** and **3**, respectively. For constant stress rate, σ_f is the fracture strength (the maximum stress during test), and t_f is the time transformed by equation (5). The σ_{IC} is defined as the inert strength where catastrophic failure occurs without subcritical crack growth. From the results at high displacement rates in constant stress rate tests, σ_{IC} was presumed to be 600 and 540MPa at 1200 and 1240°C, respectively, for silicon nitride, and 320MPa at 1400°C for silicon carbide. In the figures and the following

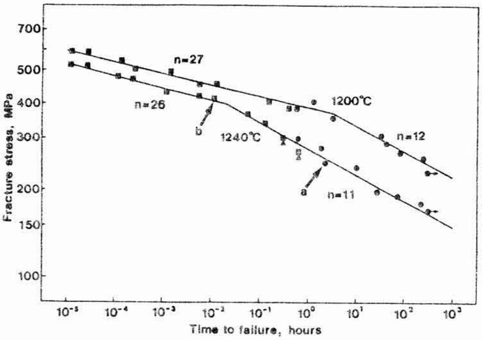

Fig. 2. Log-log representation of the data obtained in static and dynamic fatigue tests of silicon nitride, based on power-law crack growth relation. Circle and square symbols indicate constant stress and constant stress rate data, respectively. Triangle shows plastic failure. Arrows indicate specimens whose fracture surfaces are to be shown in Fig. 6.

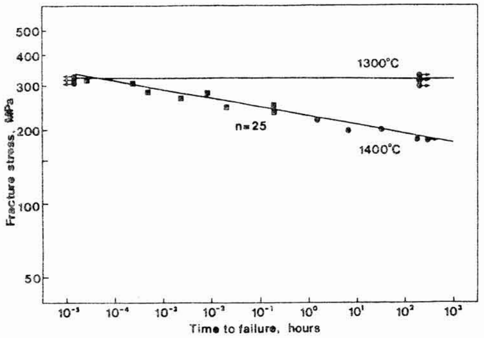

Fig. 3. Log-log representation of the data obtained in static and dynamic fatigue test s of silicon carbide, based on power-law crack growth relation. Circle and square symbols indicate constant stress and constant stress rate data, respectively.

ones, specimen which was not fractured after 300hr. is indicated by an arrow to the right and one that failed in initial load application is shown by an arrow to the left. This study assumed constant displacement rate to be constant stress rate, and linearity between stress and displacement is needed for this assumption. In fact, however, the tests of silicon nitride at displacement rates lower than 0.0005mm/min showed a little non-linearity, and therefore the results are somewhat less reliable. Delayed fracture behavior was observed in all conditions except for that at 1300°C in silicon carbide, where no fracture was obtained unless a specimen failed at initial load application in constant stress tests, and/or the lower rate brought the higher strength in some cases of constant stress rate tests. This is consistent with the results obtained in similar tests in air atmosphere on the same materials.[19]

Fractographic study revealed that almost half the specimens in the high stress-short time area of the constant stress rate tests were fractured from internal defects, though there was no substantial difference in the strength from surface fractured specimens for both materials. In the constant stress tests and low-stress-long time tests of silicon nitride, fractures were mostly initiated from enhanced subcritical crack growth area (rough area) as will be shown later.

The plots on silicon nitride in Fig. 2 clearly indicate the decrease in slope at both temperatures; it occurred around 4 hours and 0.02 hour for 1240°C and 1200°C, respectively. A similar tendency was reported on the tensile fatigue strength of magnesia-doped silicon nitride at high temperatures.[20] Because a representation with one straight line seemed unreasonable in this case, two lines are applied by dividing into two regions as indicated in Fig. 2, and a value of n was obtained by the least square method in each region. In case of the region where both dynamic and static fatigue test data exist, using the n value calculated only from dynamic test data, the time-to-failures in dynamic tests were first transformed by equation (5), and the value of n was then obtained from both test data. Using the new n value, the time-to-failures of dynamic tests were again transformed to calculate newer n values from both test data. This operation was repeated several times to obtain a reproducible n value. On the other hand, the results of delayed fracture at 1400°C on silicon carbide was treated with one straight line in log-log representation. The n value was computed in the same manner as stated above.

3-2. Exponential Crack Propagation Rate Model

As an exponential crack growth relation, the following form was employed in this study.

$$v = A \exp(nK_I/K_{IC}) \quad \ldots\ldots\ldots\ldots\ldots (6)$$

In the same manner as the power-law crack growth model, integrating equation (6) yields the time to failure for constant stress, t_f[4]:

$$t_f = 2K_{IC}^2 \exp(-n\sigma_{IC} / \sigma_f)\,(\sigma_f / \sigma_{IC} + 1/n) / (\sigma_f^2 Y^2 An) \quad \ldots\ldots\ldots\ldots (7)$$

When σ_f/σ_{IC} is sufficiently large relating to $1/n$,

$$t_f = 2K_{IC}^2 \exp(-n\sigma_{IC} / \sigma_f) / (\sigma_{IC}^2 Y^2 A) / (n\sigma_f / \sigma_{IC}) \quad (8)$$

This relation is applicable because the given σ_f/σ_{IC} and n values are all above 1/4 and 24, respectively. The slope of σ_f–ln t_f diagram, n′, is related to n by

$$n' = -d(\ln t_f) / d(\sigma_f / \sigma_{IC}) = n + \sigma_{IC} / \sigma_f \quad \ldots (9)$$

For constant stress rate, Trantina developed the approximate expression for time to failure, t_f', by an incremental computational technique[4]:

$$t_f' = 2K_{IC}^2 \exp(-n\sigma_{IC} / \sigma_f) / (\sigma_{IC}^2 Y^2 A) \quad \ldots (10)$$

where σ_f is the fracture strength of constant stress rate test. The slope of σ_f–ln t_f' diagram, n", is equal to n:

$$n'' = -d(\ln t_f) / d(\sigma_f / \sigma_{IC}) = n \quad \ldots\ldots (11)$$

The time to failure for constant stress rate, t_f', is related Et that for constant stress, t_f, by

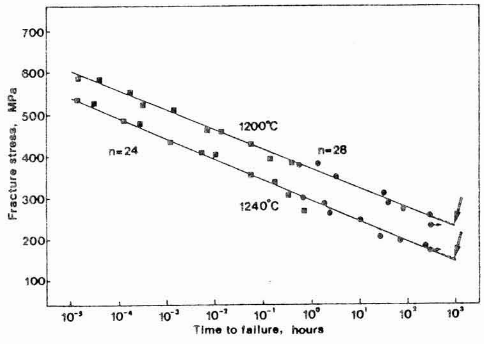

Fig. 4. Semi-log representation of the data obtained in static and dynamic fatigue tests of silicon nitride , based on exponential crack growth relation. Circle and square symbols indicate constant stress and constant stress rate data, respectively. Dotted lines indicated by downward arrows express life prediction curves determined by equation (7).

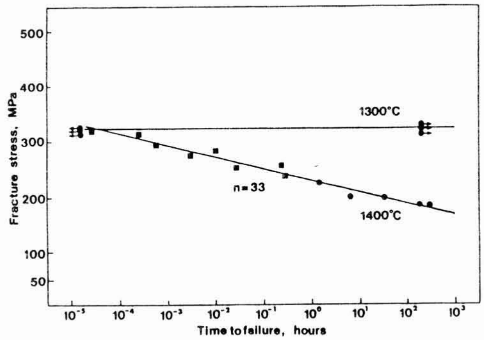

Fig. 5. Semi-log representation of the data obtained in static and dynamic fatigue tests of silicon carbide, based on exponential crack growth relation. Circle and square symbols indicate constant stress and constant stress rate data, respectively. Dotted line to express life prediction curve determined by equation (7) is almost completely duplicated even in low stress area.

$$t_f' = n\sigma_f / \sigma_{IC}\cdot t_f \quad \ldots\ldots\ldots\ldots\ldots\ldots \quad (12)$$

The results of the fatigue tests on hot-pressed silicon nitride and sintered silicon carbide were shown in **Figs. 4** and **5**, respectively, where o_f and log t_f were made vertical and horizontal axes, respectively. For constant stress rate tests, t_f is the time transformed by using equation (11). In these figures a solid line indicates a straight line with the slope of n′, and a dot line is the life prediction curve determined by equation (7). A very slight difference between the curves is observed only in the low stress area, and particularly in the case of silicon carbide with a high n value, they duplicate each other too closely to discriminate them. Hence, it is known that the relationship expressed by equation (7) is almost completely represented by one straight line in the semi-log representation. The n value for $\sigma_f/\sigma_{IC} = 0.7$ was estimated by the least square method. A similar method to that described in the previous section was employed. That is, the time-to-failures in dynamic tests were first transformed by equation (12) using a value of n which was calculated only from dynamic test data by equation (11), and the n value was then obtained for $\sigma_f/\sigma_{IC} = 0.7$ from both test data by equation (9). This n value was again substituted into equation (12) to make a newer n value. Several repetitions of this operation brought a reproducible value of n.

For silicon nitride, in contrast to the log-log representation of Fig. 2, all of the data fell on almost one straight line at both temperatures in Fig. 4, exhibiting the superiority of equation (6) for representing overall fatigue strength data. For silicon carbide, the relationship of a straight line was obtained also in this representation as shown in Fig. 5.

4. Discussion

It is known that, in most cases of yttria and alumina doped silicon nitride, silicon nitride crystalline grains are more or less surrounded by glassy phase.[13)] Although some successful crystallization of glassy phase to melilite is known to improve its high temperature mechanical properties,[12)] powder X-ray analyses of the used material revealed little reflection from Si_3N_4/Y_2O_3 phase. The grain boundary glassy phase may enhance the cavity nucleation and propagation and may accelerate subcritical crack growth by spreading of cavitation zone due to the softening at high temperatures.[21-23)] In high temperature mechanical strength test, though cavity formation is supposed to occur mainly at grain boundary triple junctions in the beginning of load application, cavitation zone spreading is accelerated due to inhomogeneous stress distribution when the initial cavity grows to some extent. This process accompanies grain boundary sliding, which allows some elongation of the specimen. Also, a macrocrack leading to final fracture is formed by connecting microcracks which are generated as a result of coalescence of spread cavities. In consequence, non-linear or visco-elastic behavior is observed in stress-displacement diagrams of mechanical strength measurements, and/or a rough area recognized as enhanced subcritical crack growth wake is seen in fractographic study.[18,20,24-26)]

The stress-displacement diagrams at lower rates than 0.0005mm/min (triangular symbols in Fig. 2) in dynamic fatigue tests for silicon nitride at 1240°C showed a significant deviation from linearity and expressed a symptom of approaching a peak or a plateau. Hence, crack propagations in these fractures most probably received the expanded cavitation zone effects as above described. As will be discussed in detail later, it can be considered that the failures in the right region (small n value) in Fig. 2 are dominated by the macrocrack formation resulting from connection of spread cavities and microcracks, while those in the left region (large n value) do not receive such effects since cavities and microcracks are not so fully distributed. In addition, a fractographic study showed that fracture surface including static fatigue specimens in the former region was partly covered by a rough area recognized as the wake of

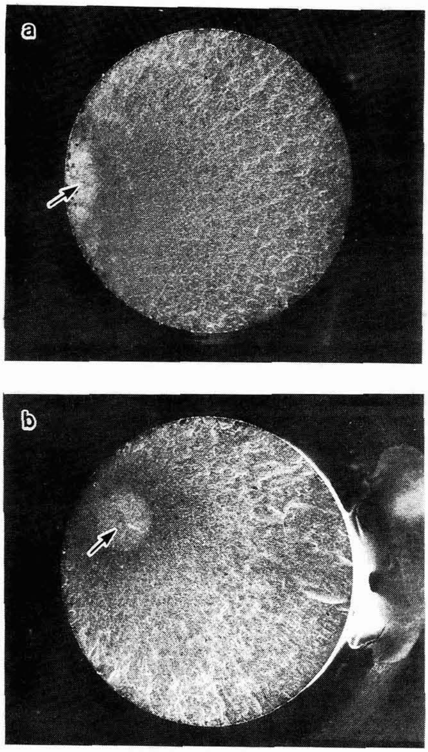

Fig. 6. SEM images of fracture surfaces of specimens failed in static test (a) and in dynamic test (b) at 1240°C, respectively.

subcritical crack growth, but none of those in the latter region showed such an area.

Figure 6(a) and **(b)** show SEM images of fracture surfaces of the silicon nitride specimens which failed in static test with applied stress of 270MPa ((a) in Fig. 2) and in dynamic test with fracture stress of 403MPa ((b) in Fig. 2) at 1240°C, respectively. A typical rough area appears in the fracture initiation range in Fig. 6(a), whereas in Fig. 6(b) a circular area which is whitish but not rough is seen around the fracture origin. The magnified SEM images of the sites indicated by arrows in Figs. 6 (a) and (b) are show in **Figs. 7(a)** and **(b)**, respectively. Substantial difference is present between them at a microstructural level; Fig. 7 (a) includes clear profiles of a lot of protruding fibrous grains, which are not seen in (b), suggesting that a crack propagates at grain boundaries with being promoted by the spread cavities and microcracks at the boundaries. On the other hand, the rather even microstructure seen in Fig. 7(b) implies that the crack extension occurs more independently when receiving less of the above-mentioned promotion. It is supposed that the appearance of a rough area is attributed to a macrocrack connecting randomly located microcracks.[25] During macrocrack formation, the fibrous silicon nitride grains which play a role of bridging crack interfaces are pulled out, resulting in protruding grains in the rough area. Therefore, macrocrack formation is a predominant factor in determining time-to-failure in the region where a rough area appears on fracture surfaces. However, from the fact that only microcracks of about 10μm length were observed in a polished hot-pressed silicon nitride specimen which was fractured at 1380°C with fracture surface fully covered by a rough area,[18,27] it can be estimated that macrocrack formation occurs at the final stage of fatigue life and, therefore, the time taken for it is very short as compared with total time-to-failure. In other words, the time for cavities and microcracks to be fully spread to facilitate macrocrack formation is more important for fatigue life determination. On the contrary, in the region where the rough area does not appear, like Fig.6(b), crack growth enhancement by cavities is presumed to be relatively small, because cavities are not sufficiently grown and not widely spread in a systematic manner as in the above case, though they have some effect on crack propagation behavior and fatigue life as well.

It should be noted that crack propagation behavior and fatigue life property of silicon nitride containing grain boundary glassy phase is largely dependent on the amount

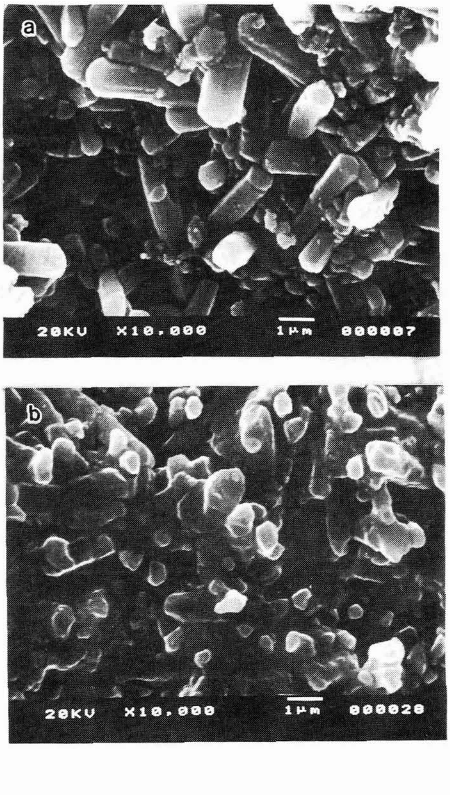

Fig. 7. Magnified SEM images of sites indicated by arrows in Fig. 6(a) and (b).

and characteristics of the glassy phase. For instance, in the case of hot-pressed silicon nitride with a slight amount of glassy phase due to crystallization into melilite phase, static fatigue strength at 300hr. was well estimated by dynamic fatigue strength in bending test at 1200°C.

Charles proposed an expression with exponential form of stress in order to model high temperature stress rupture process of polycrystalline materials, and showed that it closely described a number of metals and high temperature alloys.[7] This model is based on grain boundary parting enhanced by cavities at the tip of the crack within the boundary. The fact that semi-log representation based on the exponential model showed the overall fitness of data suggests a possibility that this model can well describe crack growth characteristics associated with cavities or microcracks as shown above, though it should be discussed and clarified by use of a greater amount of fatigue life data.

As to sintered silicon carbide used in this study, it has been revealed that alumina as a secondary crystal phase was concentrated only at grain boundary triple junctions, and grain morphology was not needle-like but plate-like.[14,15] In addition, the grain boundary glassy phase was not found in our TEM study on this material. **Figure 8** shows a TEM micrograph of the silicon carbide used which shows that alumina particles are present at the triple junction of silicon carbide grains. The strength degradation at 1400°C reported so far on this material[19,20] can be attributed to a lowering in strength of the alumina particles. However as these alumina particles exist independently with each other and there is almost no glassy phase, coalescence of cavities are presumably restrained by rigid bonding of silicon carbide grains, though they may be independently nucleated and expanded. Furthermore, as compared with the needle-like morphology of silicon nitride, the plate-like type is likely to suppress grain boundary sliding, making it more difficult for a cavitation zone to widely spread. Even in a constant stress rate test at 0.0001mm/min at 1500°C for this material, the linear relationship of the stress-displacement diagram was maintained until final fracture, and none of fracture surfaces showed such a rough area as seen in silicon nitride. Hence, though there may be a possibility that crack propagation is accelerated by cavities also in this silicon carbide, they hardly occur simultaneously or systematically for the above reason, and therefore their effects on delayed fracture data are not so clear as in the case of silicon nitride. As results, the data on this material were apparently well treated by both power-law and exponential crack growth relationships.

Differentiating ln t_f of both equations (4) and (8) for ln σ_f/σ_{IC} results in $-n$ and $-n(\sigma_f/\sigma_{IC})$, respectively. This means that both of the slopes are almost identical when σ_f is close to σ_{IC}, while there is a substantial difference when σ_f is much lower than σ_{IC},[7] In other words, if the real crack propagation characteristic is more close to either equation (2) or (6) and the other equation is employed for analysis, a large difference will be caused in the estimation of low stress-long term delayed fracture strength, which is the most important for the application technology of ceramics components. One of the reasons why power-law crack growth expression is commonly used is that it is advantageous in mathematical handling. As a matter of fact, most of crack propagation behaviors of structural ceramics are said to be well described by power-law relation. However, it should be noted that there are some cases where the life predicted by power-law relation from short or middle duration data is much longer than the real one as shown in this study.

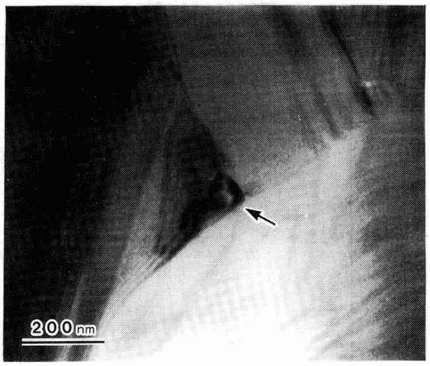

Fig. 8. TEM micrograph of the silicon carbide used. Alumina particle at triple junction of silicon carbide grains is indicated by arrow.

In order to correctly estimate fatigue life of ceramic components being used under actual conditions of gas turbines and other heat engines, factors including oxidation, stress application mode, stress distribution etc. should be taken account of as well as temperature and stress considered in this study. Again, the fatigue life is largely dependent on microstructures of the material used as shown in this paper, and therefore, sufficient understanding of them is indispensable for reliable use of ceramic components.

5. Conclusions

High temperature static (constant stress loading) and dynamic (constant stress rate loading) fatigue tests were conducted on hot-pressed silicon nitride and sintered silicon carbide in vacuum atmosphere. Each result was analyzed by two types of crack growth models, power-law and exponential relations. The log-log representation based on the former model for the obtained stress and time-to-failure data fo silicon nitride produced the difference in slope between short-term and long-term results. Suggested were the effects of accelerated crack extension by rapid or simultaneous cavitation zone spreading due to grain boundary glassy phase. The semi-log representation based on the latter model resulted in an excellent fit with one straight line, implying the capability to cope with such a cavity behavior. On the other hand, the data for silicon carbide were shown to be successfully treated by both relations, supposedly because the cavity formation and propagation were suppressed by its microstructure. As a consequence the superiority of life prediction by exponential crack growth expression was suggested for a design methodology.

Acknowledgments

The authors wish to thank S. Sakai for the specimen preparation. The assistance of M. Awano with TEM observations is also appreciated. This study was conducted as a part of Ceramic Gas Turbine Project, R&D on Energy Conservation Technology, sponsored by AIST, MITI.

References:

1) (For example) A.G. Evans and S.M. Wiederhorn, J. Mater. Sci., 9, 270-78 (1974).
2) R.J. Charles, J. Appl. Phys., 29, 1549-60 (1958).
3) R.J. Charles, J. Appl. Phys., 29, 1657-62 (1958).
4) G.G. Trantina, J. Am. Ceram. Soc., 62, 377-80 (1979).
5) G.D. Quinn and J.B. Quinn, "Fracture Mechanics of Ceramics, Vol. 6", Plenum Press, NY (1983) pp. 603-36.
6) S.M. Wiederhorn, H. Johnson, A.M. Diness and A.H. Heuer, J. Am. Ceram. Soc. 57, 336-41 (1974).
7) R.J. Charles, Metall. Trans. A, 7, 1081-89 (1976).
8) F.F. Lange, B.I. Davis and M.G. Metcalf, J. Mater. Sci., 18 (1983) 1497-505.
9) F. Wakai, S. Sakaguchi, Y. Matsuno and H. Okuda, "Proceedings of the First International Symposium on Ceramic Components for Engines" KTK/Reidal (1984) pp. 279-85.
10) P.F. Becher, J. Am. Ceram. Soc., 66, C120-21 (1983).
11) Y. Yamauchi, S. Sakai, M. Ito, T. Ohji, W. Kanematsu and S. Ito, Nippon Seramikkusu Kyokai Gakujutsu Ronbunshi 98 (1990) to appear in March issue.
12) A. Tsuge and K. Nishida, Am. Ceram. Soc. Bull., 47 (1978) 424-31.
13) C.C. Ahn and G. Thomas, J. Am. Ceram. Soc., 6 (1983) 14-17.
14) K. Suzuki, Rep. Res. Lab. Asahi Glass Co., Ltd., 36 (1986) 25-36.
15) K. Suzuki, "Silicon Carbide Ceramics", Uchida Rokakuho (1988) pp345-60.
16) T. Ohji, unpublished work on sintered silicon nitride.
17) T. Ohji, "Mechanical Testing of Engineering Ceramics at High Temperatures", Elsevier Applied Science (1989) pp.119-33.
18) T. Ohji, S. Sakai, M. Ito, Y. Yamauchi, W. Kanematsu and S. Ito, High Temperature Technology, 5 (1987) pp.139-44.
19) H. Fujita, M. Kawai, H. Takahashi, H. Abe and J. Nakayama, "Fracture Mechanics of Ceramics, Vol. 8", Plenum Press, NY (1986) pp.379-90.
20) M. Kawai, H. Fujita, Y. Kanki, H. Abe and J. Nakayama, "Proceedings of the First International Symposium on Ceramic Components for Engines" KTK/Reidal (1984) pp.269-78.
21) A.G. Evans and A. Rana, Acta Met. 28 (1980) 129-41.
22) C.H. Hsueh and A.G. Evans, Acta Met. 29 (1981) 1907-17.
23) A.G. Evans and W. Blumenthal, in "Fracture Mechanics of Ceramics, Vol. 6", Plenum Press, NY (1983) pp.423-48.
24) R. Kossowsky, D.G. Miller and E.S. Diaz, J. Mater. Sci., 10 (1975) 983-97.
25) T. Ohji, Y. Yamauchi, W. Kanematsu and S. Ito, J. Mater. Sci. (in press).
26) M. Masuda and M. Matsui, Nippon Seramikkusu Kyokai Gakujutsu Ronbunshi 98 (1990) 83-92.
27) T. Ohji, The 8th "Kouon-Zairyou-Kiso-Touronkai" Abstract Book, The Ceramic Society of Japan (1988) pp.66-70.

This article appeared in English in Nippon Seramikkusu Kyokai Gakujutsu Ronbunshi (Japanese version), Vol.98, No.6, 1990.

Effective Oxygen Partial Pressure during HIP

Akio Watanabe, Hajime Haneda, Shun-ichi Hishita, Yusuke Moriyoshi, Shin-ichi Shirasaki and Hiroshi Yamamura*

National Institute for Research in Inorganic Materials, 1 Group
1-1, Namiki, Tsukuba-shi, Ibaraki 305, Japan
*TOSOH Co., Advanced Material Research Laboratories
2747-1, Hayakawa, Ayase-shi, Kanagawa 252, Japan

$SrTiO_3$ ceramics were reduced both by HIP and by Ar-O_2 mixed gas at 1300°C. The degree of reduction of the specimens was characterized by optical transmittance and electric conductivity. The degree of reduction of the HIPed specimens were depended on the HIP pressure. The degree of reduction was low at high pressure, but high at low pressure.

The degree of reduction of the specimens HIPed under 100MPa was equivalent to the specimen reduced under the atmospheric pressure in which oxygen partial pressure was 10^2Pa. This result was explained by the concentration of oxygen included in Ar used as a pressure medium.

[Received November 4, 1989; Accepted February 13, 1990]

Key-words: HIP, $SrTiO_3$, Optical transmittance, Electric conductivity, Oxygen partial pressure

1. Introduction

HIP is well known to be an effective method to densify ceramic materials.[1] In particular, the post-HIP process for highly densified (relative density of 93 to 94% or more) sinters without open pores has been frequently used recently, because it can form highly densified, well-controlled microstructures without the encapsulation and capsule removal steps. It is known, however, that many oxides, such as ZrO_2, turn black by reduction when their surfaces directly contact some HIP media, such as Ar gas.[2] It is essential to accurately measure the oxygen partial pressure in the furnace system and control it to the required level, in order to avoid reduction damage. The high pressure in the furnace, however, prevents direct measurement of oxygen partial pressure, so it has to be measured by an indirect method.

The indirect method to measure oxygen partial pressure used in this study, involved reduction of $SrTiO_3$, which is known to occur relatively easily and varies with the reduction conditions depending on the oxygen partial pressure.[3]

2. Experimental Procedure

The sample was HIP-treated at 1300°C for 2h in an Ar gas atmosphere, with a heating rate of 400°C/h and a cooling rate of 600°C/h

It was also reduced under 1atm in a mixed Ar/O_2 atmosphere at 1300°C for 2h, where the oxygen content of the medium gas was varied. The heating and cooling rates were set at 400°C/h and 600C°/h, to achieve the same reducing conditions as those for the HIP treatment. Two methods, using light transmittance and electrical conductivity, were used to assess the extent of the reduction.

The sample for the light transmittance method was a transparent body of $SiTiO_3$ (10mm in diameter, 1mm thick) HIP-sintered under the conditions of 1300°C and 120MPa for 2h, which was reoxidized for repeated use.[4] The light transmittance was measured after HIP-treatment at various pressures in a range from 5 to 200MPa and after treatment under 1atm with Ar/O_2 gas mixtures with various oxygen partial pressures.

Two types of samples were prepared for the electrical conductivity method; one was of $SrTiO_3$ HIP-sintered under 1300°C, 120MPa and 2h, and the other was $SrTiO_3$ containing 0.5mol% of Nb_2O_5 (to make the sample more reducible[5]) sintered under 1300°C and 2h in a flow of oxygen gas. They were cut into 2.5× 2.5× 10mm blocks. The electrical conductivity was measured at room temperature by the DC, 4-terminal method, after HIP treatment under various pressures from 5 to 200MPa and after reduction at 1atm with Ar/O_2 gas mixtures with various oxygen partial pressures.

The HIP apparatus used in this study was a hot isostatic press (Kobe Steel), provided with Pt-Rh wire heat source and insulated with alumina-based refractory. The Ar gas was super argon (Suzuki Shokan), the composition of which is given in **Table 1**. The light transmittance was determined by a double beam spectrometer (Model 228, Hitachi Ltd.) and the electrical conductivity by the DC, 4-terminal method at room temperature.

3. Results and Discussion

3-1. Light Transmittance

Figure 1 shows representative light transmittance measurements, where the solid line represents results for the untreated sample and the broken line the HIP-treated sample.

Table 1. Impurities in Ar.

Ar	O_2	N_2	H_2	CH_4	CO_2	
99.999%	<2ppm	<6ppm	<1ppm	<3ppm	<3ppm	dew point -65°C

The HIP treatment decreased light transmittance at all wavelengths. The light transmittance reduced by the HIP treatment was easily recovered to the original level after annealing. It was thought that repeated HIP treatment would reduce the residual pores in the sample and increase light transmittance, but no change was observed in the light transmittance of the sample reoxidized repeatedly under the conditions adopted in this study, suggesting that the effects of the HIP and reoxidation cycle on light transmittance were negligible.

Figure 2 shows the effects of HIP pressure on the light transmittance of the treated sample at 800nm, indicating that transmittance increased with HIP pressure. The broken line represents the transmittance of the annealed sample (35%).

Figure 3 shows the effects of oxygen partial pressure in the reducing atmosphere on the light transmittance at 800nm. It was observed that the sample was easily reduced at $P_{o2}=10^2$Pa, a fairly high oxygen partial pressure for a reducing gas, decreasing the transmittance. The transmittance depended on the oxygen partial pressure in the reducing atmosphere; it increased as the oxygen partial pressure increased, as the oxygen partial pressure increased with HIP pressure.

The results shown in Figs.2 and 3 are combined in **Fig.4**, indicating that reduction during the HIP treatment corresponded to that at P_{O_2}=10Pa under normal pressure.

3-2. Electrical Conductivity

Figure 5 shows the effects of HIP pressure on the electrical conductivity of the samples. The electrical conductivity of $SrTiO_3$ treated at 20MPa or less could be measured, but

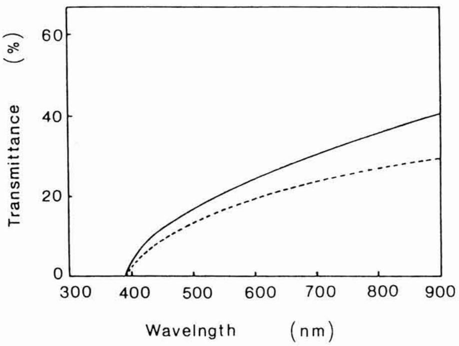

Fig. 1. Typical transmittance of the specimen before and after HIP(1300°C, 120MPa) as a function of wavelength.

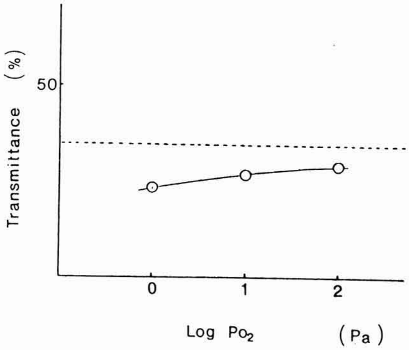

Fig. 3. Change of transmittance at 800nm in $SrTiO_3$ ceramics reduced by mixed gas with Ar and O_2 as function of oxygen partial pressure. Dashed line shows the transmittance of the specimen before reduction.

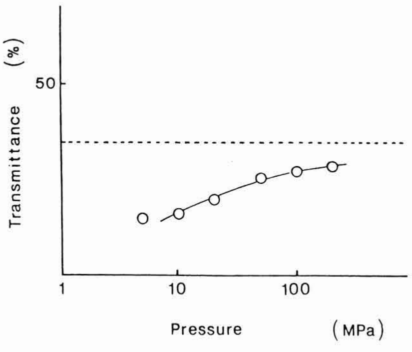

Fig. 2. Change of transmittance at 800nm in $SrTiO_3$ ceramics reduced by HIP as a function of HIP pressure. Dashed line shows the transmittance of the specimen before HIP.

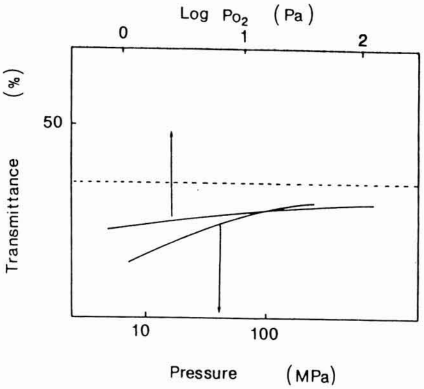

Fig. 4. Comparison of the change of transmittance in $SrTiO_3$ ceramics reduced by HIP and by mixed gas with Ar and O_2.

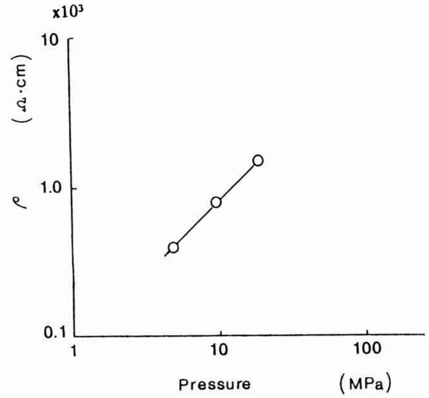

Fig. 5. Change of electronic conductivity of $SrTiO_3$ reduced by

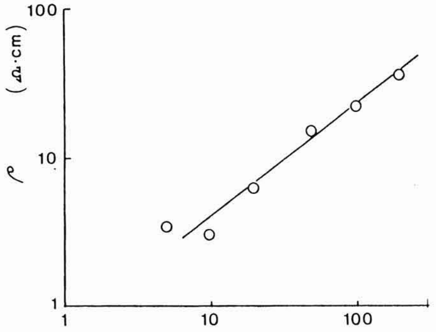

Fig. 6. Change of electronic conductivity of 0.5mol%Nb_2O_5-$SrTiO_3$ reduced by HIP as a function of HIP pressure.

that of the samples treated at 50MPa or more was too low to be measured. Decreasing the HIP pressure increased the conductivity or accelerated the reduction of the sample. The conductivity of those samples reduced by the Ar/O_2 gas mixture was too low to be measured.

Figure 6 shows the effects of HIP pressure on the conductivity of the samples containing 0.5mol% of Nb_2O_5. The additive promoted the reduction of $SrTiO_3$, increasing the conductivity by two orders over the additive-free sample.

Figure 7 shows the effects of oxygen partial pressure on electrical conductivity. The sample was readily reduced at $P_{o2}=10^2$Pa, increasing the conductivity. These results are in good agreement with the results of light transmittance. The

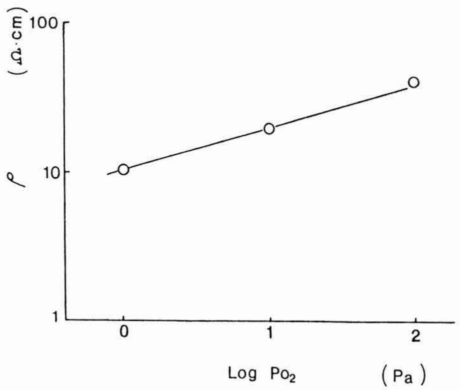

Fig. 7. Change of electronic conductivity of 0.5mol%Nb_2O_5-$SrTiO_3$ by mixed gas with Ar and O_2.

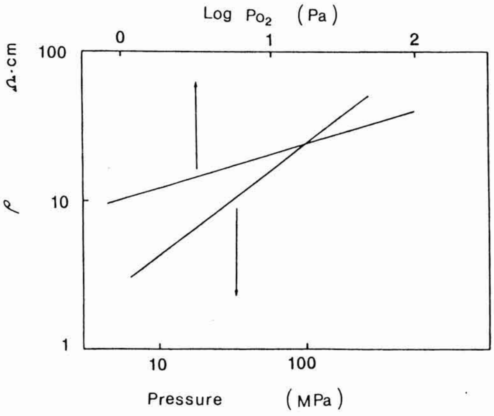

Fig. 8. Comparison of the change of electronic conductivity for 0.5mol%Nb_2O_5-$SrTiO_3$ reduced by HIP and mixed gas with Ar and O_2.

conductivity also depended on the oxygen partial pressure in the reducing atmosphere, decreasing as the partial pressure increased. Therefore, the higher the HIP pressure, the higher the oxygen partial pressure, causing the lower electrical conductivity.

The results shown in Figs.6 and 7 are combined in **Fig.8**, indicating that reduction during the HIP treatment corresponded to that at $P_{o2}=10$Pa under normal pressure, as shown by the light transmittance results.

3-3. Effective Oxygen Partial Pressure

The results of both light transmittance and electrical conductivity measurements indicated that increasing the HIP pressure prevented reduction by increased oxygen partial pressure. One of the causes of this was the oxygen present as an impurity in the argon pressure medium. Increasing the total pressure 1000 times increased the partial pressure of the impurity 1000 times, regardless of the quantity. The Ar gas used in this study contained about 2ppm of oxygen, which corresponded to 10^{-1}Pa under normal pressure and to 10^{2}Pa under 100MPa. Furthermore, the Ar gas contained traces of reducing gases, such as H_2 and CH_4, at almost the same level as oxygen, with the result that the oxygen partial pressure below which the sample was reduced would be lower than 10^{2}Pa. This accounts for the reduction during HIP treatment under 100MPa corresponding to that effected at P_{o2}=10Pa under normal pressure.

Therefore, the effective oxygen partial pressure depends on the concentration of oxygen present as an impurity in the pressure medium in a HIP system using a heating source and refractory insulation which do not contribute to oxidation/reduction.

The reduction of the sample was predictable at high HIP pressures from the impurity oxygen content in the pressure medium, but unexpectedly accelerated at low pressure, showing there were factors other than oxygen partial pressure that affected the reduction.

One of the possible causes for the accelerated reduction at low pressure is organic compounds present in the HIP system, such as piping. A small quantity of oxygen under low pressure would be appreciably consumed by oil and other organic compounds, sharply accelerating the reduction of the sample. At high pressure, on the other hand, this effect is diminished because of the increased quantity of oxygen in the system, with the result that the oxygen partial pressure in the pressure medium then depends mainly on the concentration of impurity oxygen.

4. Conclusions

Sintered $SrTiO_3$ was HIP-treated at 1300°C and also reduced under normal pressure, to correlate the reduction conditions of these processes. Light transmittance and electrical conductivity were used to assess the extent of the reduction. The reduction depends on the HIP pressure, decelerating as the pressure is increased. The extent of reduction at a HIP pressure of 100MPa corresponds to that obtained at Po_2=10Pa under normal pressure. This level coincides with the oxygen partial pressure predicted from the concentration of impurity oxygen present in the Ar pressure medium. The effective oxygen partial pressure under the HIP conditions depends mainly on the concentration of impurity oxygen present in the pressure medium.

References::

1) H. Hardtl, Amer. Ceram. Soc. Bul., 54 (1975) 201-207.
2) M. Shimada, Bul. Ceram. Soc. Japan 22, 483-88 (1987).
3) N-H. Chan, R.KShaa, D.M. Smyth, J. Electrochem. Soc., 128 (1981) 1762-1768.
4) A. Watanabe, H. Haneda, Y. Moriyoshi, S. Shirasaki, M. Tanada and H. Yamamura, Proceedings of 1st International SAMPE Symposium, in print.

This article is a full translation of the article which appeared in Nippon Seramikkusu Kyokai Gakujutsu Ronbunshi (Japanese version), Vol.98, No.6, 1990.

Mechanically Enhanced Open Porous Materials by HIP Process

Kozo Ishizaki, Atsushi Takata and Syojiro Okada*

Department of Materials Science and Engineering, School of Mechanical Engineering, Nagaoka University of Technology
Nagaoka 940-21, Japan
*Japan Grain Institute Co., Ltd.
1047-9 Sue, Ryonan-cho, Ayauta-gun, Kagawa 767-01, Japan

Open porous materials were produced by a hot isostatic press (HIP) process. Cold-isostatically pressed powders were directly heated to a normal sintering temperature under HIPping conditions. The products were characterized by open pores and were almost free from closed pores. Those open pore materials are typically useful as filters, reactor beds, grinding materials and so on. A grindstone of silicon carbide grains with aluminum nitride bridges was discussed as an example. At the sintering temperatures of AlN above 1973K, 20 to 30% of open porosity was maintained in the HIPped samples. On the other hand, normally heated ones were almost fully densified. Since no additives for pore formation were used, uniform pore size distribution and homogeneously dispersed pores were expected by the new HIP process. Normal HIPping effects enhanced the properties of bridge parts by reducing defects and also closed pores in them. Better strength and open porosity were obtained by this method.

[Received November 14, 1989; Accepted February 13, 1990]

Key-words: Open pore, Hot isostatic press (HIP), Filter, Grinding materials

1. Introduction

Recent interest in the development of new materials has resulted in the appearance of a variety of materials with new functions. Porous materials, for example, have applications in various new areas. Porous ceramics, especially closed pore materials, have been used for a long time for many common purposes, including thermal or acoustic insulators, and construction materials such as light walls. On the other hand, materials required to have open pores are mainly used for industrial purposes, such as catalytic converter filters for exhaust gases,[1] electrolytic membranes, filters,[2] various types of gas distributers,[3] bioreactor beds,[4,5] and high-efficiency grindstones.[6]

The conventional methods for producing porous materials are; low-temperature sintering to keep intact the green body pores,[7,8] burning-out combustible organic material (such as phenol resin) added to the green body during the sintering process,[9] thermal treatment of molten glass consisting of soluble and insoluble phases at a temperature at which these phases are formed, followed by chemical dissolution of the former phase,[10,11] and vitrification of a green body consisting of ceramic particles and a vitrified bonding agent to form open pores between the particles.[6]

The two major properties required for recent porous materials are adequate mechanical strength and uniform pore structures. It is however difficult, by the present processes, to simultaneously satisfy the requirements for porosity and strength, because they are frequently contradictory.[6]

The authors have developed a hot isostatic press (HIP) process to improve the mechanical properties of ceramic or metallic materials while retaining adequate porosity, in which no capsule is used. There is no other HIP process, to the best knowledge of the authors, to obtain open-pore materials. The only reported HIP process used was to produce closed-pore metals, and goes as the following: absorb pressurized gas, e.g. argon, in molten metals under HIPping condition, then expand the gas at high temperature under normal pressure.[12] This process mainly forms closed pores. It is much less suitable for producing functional materials with open pores for industrial purposes.

The possible HIP approaches for producing materials with many open pores include the direct method in which powder treated by cold isostatic pressing (CIP) is HIP-treated, and the indirect method in which a combustible organic compound is burnt under an isostatic pressure of, for example, 200MPa, to quickly form a porous body with a more uniform pore distribution. The high-pressure gas in a CIPped green body prevents densification during the sintering process in the former approach, while the combustion gases are prevented from expanding during the sintering process, because most of them undergo solild to super-critical-fluid phase transformation in the latter method.

The method developed in this study falls into the former category, where a CIP-treated green body is directly HIP-treated. It reduces the contradiction between the properties of strength and porocity. The new process also forms easily a porous body with well-controlled pore size and microstructures.[13]

2. Experimental Procedure

2-1. Powder Preparation and Pretreatment for Sintering

This study selected, as a representative example of an open porous material, a grindstone formed of silicon carbide particles (grinding grains) with bridges of aluminum nitride, which was selected for its high thermal conductivity. bridges. The investigation centered on the observation of the bridges forming the porous body. The starting materials were commercial, #60 SiC powder for the abrasive grains,

Table 1. Chemical composition of raw powders

(a) AlN

Impurity					Specific* Surface Area (m^2/kg)	Average** Particle Size (μm)
O(%)	C(ppm)	Ca(ppm)	Si(ppm)	Fe(ppm)		
0.88	210	67	<15	<10	3.7×10^3	1.4

(2) Y_2O_3

Impurity (ppm)							Specific* Surface Area(m^2/kg)	Average** Particle Size(μm)
Dy_2O_3	Ho_2O_3	Er_2O_3	Yb_2O_3	Fe_2O_3	CaO	SiO_2		
<100	<100	<100	<100	<5	<5	20	1.03×10^3	0.93

* B.E.T. method

** Centrifuge particle analysis

Table 2. Typical mixtures of additives.

	Grain and Bridging		AlN Bridging		Marks in
Sample	SiC(vol%)	AlN-Y_2O_3(vol%)	AlN(mol%)	Y_2O_3(mol%)	Figs. 2-4
A	30	70	95	5	Circle ○
A*	30	70	95	5	Triangle △
B	30	70	99	1	Square □
C	70	30	95	5	Diamond ◇

A : Ball mill mixing

A*, B and C : Glass mortar mixing

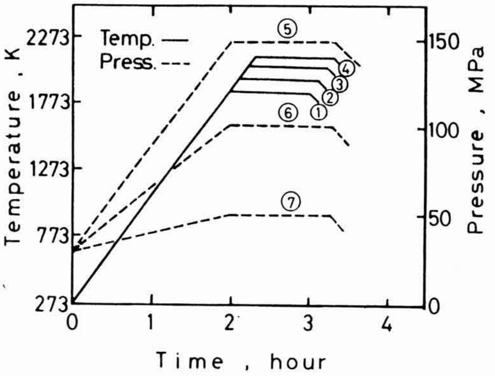

Fig. 1. HIPping schedule. Solid and broken lines represent temperature and pressure respectively.
Temperature: (1): 1873K (2): 1973K (3): 2073K (4): 2123K
Pressure: (5): 150MPa (6): 100MPa (7): 50MPa

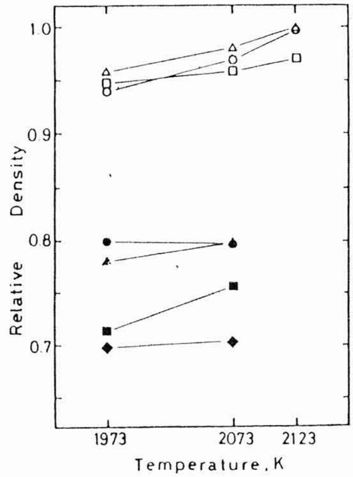

Fig. 2. Relative density vs. sintering temperature, for normal and HIP-treated samples, which were CIPped under pressure of 100MPa for 300ks, and HIPped under 100MPa for 3.6ks. Circles, triangles, squares and diamonds indicate samples A, A*, B and C respectively, as shown in Table 2. Opened and solid marks mean normal and HIP sintering respectively.

thermally conducting AlN powder (Tokuyama Soda, Type F) binder, and Y_2O_3 (Shin-Etsu Kagaku, 0051-SU) sintering aid. The AlN powder was expected to form the bridges for the abrasive grains.

Table 1 gives the compositions and properties of the starting powders, where the average grain size was determined by the centrifugal method and the specific surface area by the BET method. To prepare the standard sinters, a mullite mortar or a ball mill with Si_3N_4 balls were used to mix given quantities of the starting powders in ethanol. **Table 2** gives the compositions of the mixtures.

Samples A, A* and B were used to compare pressureless sintering with HIP sintering, and Samples C for the CIP and HIP tests under various pressure levels.

In ball milling, the powders totalling 0.5kg were mixed in about $200cm^3$ of ethyl alcohol for 24h. The mixture was dried in a drier at 393K for about 12h. In mortar mixing, AlN and Y_2O_3 powders of given quantities were mixed in about $200cm^3$ of ethyl alcohol and dried by a drier, each for about 1h. This mortar mixing was repeated 3 times. The mixture was then dried at 393K for 12h, to remove the ethanol completely. They were then mixed with the SiC grains placed in ethanol, with stirring for about 30min.

Two grams of the mixed powder was placed in a stainless mold, and pressed under a uniaxial compressive pressure of 100MPa for 60s, put in a rubber bag, degassed and CIP-treated under the conditions given in **Table 3** for 5min, to form the green body. The green body thus prepared was coated with boron nitride (BN) powder, and then packed in a carbon sheet, to complete the pretreatment for sintering.

2-2 Sintering and Assessment

The HIP treatment was carried out using a HIP apparatus (Kobe Steel, Dr.HIP) without a capsule in a nitrogen gas atmosphere under the conditions given in **Table 4**, where treatment under 0MPa means normal sintering in a nitrogen

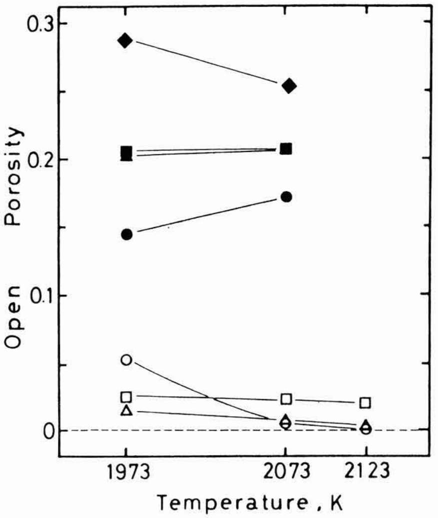

Fig. 3. Open porosity vs. sintering temperature for normal and HIP treated samples, which were CIPped and HIPped by the same condition as indicated in the caption of Fig.2. The marks have the same significance as in Fig.2.

Table 3. CIPping condition.

Sample	A	A*	B	C
CIPping Pressure, MPa	200	200	200	0 (not CIPped) 20 50 100 400

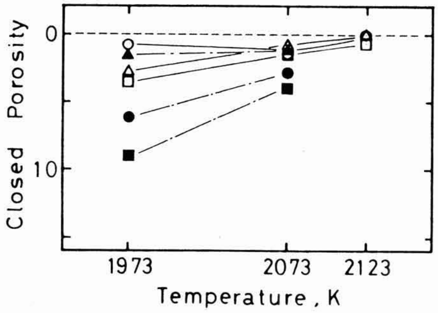

Fig. 4. Closed porosity vs. sintering temperature for normal and HIP-treated samples, which were CIPped and HIPped by the same condition as indicated in the caption of Fig.2. The marks have the same significance as in Fig.2.

gas atmosphere, with a graphite heater as the heating element. The HIP chamber was pressurized first to 30MPa, then heated at a rate of 900K/h and pressurized. It took about 1h to cool the sample from 1800K to room temperature in the furnace. **Figure 1** shows the sintering schedules.

After boron nitride was removed, the apparent density and porosity of sintered samples was measured by the Archimedean method in toluene. The relative density was determined using the theoretical density calculated from the arithmetical average of the density of each component (SiC: 3.20×10^3kg/m^3, AlN: 3.26×10^3kg/m^3, Y_2O_3: 4.84×10^3kg/m^2). Refer to the Appendix for the procedures to determine the apparent density, open porosity and closed porosity.

The fractured surfaces were observed after gold vapor deposition, using a scanning electron microscope (SEM) to examine grain sizes, bond bridges and pores.

Table 4. Sintering condition

Temperature,K	1873	1973	2073	2173
Pressure, MPa	100	0 50 100 150	0 100	0 100
Holding time, hr	1	1	1'	1

3. Results and Discussion

3-1. Sintering

Figures 2, **3** and **4** show the effects of sintering temperature (1873 to 2073K) on the relative density, open porosity and closed porosity of the samples treated by normal or HIP sintering for 1h. The samples marked with, ○, Δ, ❑ and ◆ correspond to the samples A, A*, B and C shown in **Table 2**, where sample A was from starting powders mixed by ball milling and the others mixed by mortar.

Figure 2 indicates that the relative density of the normally sintered samples was in a range from 94 to 100%, whereas that of the HIP-treated ones was fairly lower at 70 to 80%, with a difference of about 20% at the same temperature. Figure 3 shows that the open porosity of the normally sintered samples was fairly low at 6% or less, whereas that of the HIP-treated ones was much higher at 14 to 22%. The former samples, though binary, densified with sintering temperature, as is the case with the samples sintered by the conventional process. The density of the HIP-treated ones, on the other hand, was generally less sensitive to sintering temperature, presumably because pores filled with high-pressure nitrogen gas would not collapse even at high sinter-

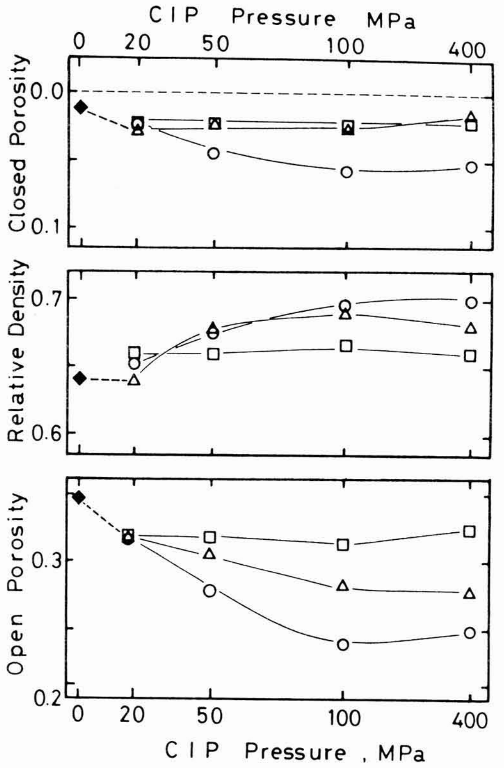

Fig. 5. Open porosity, relative density and closed porosity vs. CIPping pressure. HIPped at 1973K under 100MPa for 3.6ks. The squares, triangles and circles indicate HIPping temperatures as 1873, 1973 and 2073K respectively. The diamonds indicate the samples HIPped at 1973K without CIP treatment. All of the samples were C of Table 2.

ing temperatures. This phenomenon is contrary to those observed in the conventional HIP process, and will be useful for the production of porous materials. However, the HIP treatment destroyed the closed pores to remove the internal flaws, thereby strengthening the bridges and increasing the open porosity of the sample as a whole, as is the case with the conventional HIP process.

No significant difference was observed between 1 and 5mol%, Y_2O_3 addition on relative density (Fig.2) and open porosity (Fig.3) with the normally and HIP sintered samples. However, it should be noted that the normally sintered sample containing 5mol% of Y_2O_3 had a relative density of 100%, when sintered at 2123K, while those containing 1mol% of Y_2O_3 had densities of 94, 95 and 97%, when sintered at 1973, 2073 and 2123K, respectively. Lowering the addition of sintering aid to 1mol%, fine cracks were observed. The HIP-treated samples had no cracks, as far as the visual and SEM observation showed. The formation of cracks indicates that an addition of 1mol% additive was insufficient.

The mixing method seemed to have some effects on the sinter properties. Mortar mixing (Δ) gave a higher relative density for the normally sintered samples, but this trend was reversed for the HIP-treated samples; note that those marked with ● had higher densities (Fig.2). **Figure 3** shows that the samples marked with ▲ (mortar mixing) had 3 to 6% higher open porosity than those marked with ● (ball milling), and **Fig.4** shows that the latter samples had 2 to 5% higher closed porosity than the former. Possibly the SiC abrasive grains and the AlN and Y_2O_3 matrix grains were too different in size to be mixed uniformly with each other by ball milling, as the grindstone was considered to be a binary system, but mortar mixing crushed the SiC particles thus improving sinterability.

Comparing sample A* and sample C, with different compositions, it was found that the porosity could be controlled by the content of the abrasive grains.

Based on the above results, sample C was selected to investigate the effects of CIP and HIP pressure and for SEM observation; it was made from starting powders mixed in a mortar, containing 5mol% of Y_2O_3 and consisting of 70 parts of abrasive grains and 30 parts of bridge grains by volume.

3-2. Effects of CIPping Pressure on Porosity

Figure 5 shows the effects of CIPping pressure on the relative density, open porosity and closed porosity of Sample C, sintered at 1873 to 2073K. The porosity decreased by almost 10% as the CIP pressure increased from 0 to 100MPa for the sample sintered at 2073K. The sample sintered at 1873K, on the other hand, had an essentially constant relative density (66%) and open porosity (33%), irrespective of CIPping pressure. Increasing the CIPping pressure from 20 to 50, and to 100MPa caused the porosity of the samples sintered at 1973 and 2073K to decrease almost linearly, resulting from a decreased distance between the abrasive grains or from an increased contact area. The constant density and porosity of those samples sintered at 1873K, regardless of CIPping pressure, were presumably caused by incomplete sintering at such a low temperature.

The closed porosity was almost constant at about 2%, regardless of CIPping pressure, for the samples sintered at 1873 and 1973K, and at about 5% for those sintered at 2073K under a higher CIPping pressure, showing that increasing the HIPping temperature and CIPping pressure increased the closed porosity, as shown in **Fig.5**. The samples had almost the same relative density, open and closed porosities, when CIP-treated at 20MPa or less, indicating that it is possible to control the porosity by CIP treatment in the above pressure range, because the properties were essentially insensitive of sintering temperature. A porous body of high porosity can therefore, be prepared by lowering CIPping pressure, and increasing the CIPping pressure and sintering temperature result in a porous body of moderate porosity.

3-3. Effects of HIPping Pressure on Porosity

Figure 6 shows the effects of HIPping pressure on relative density, open and closed porosities, where 0MPa HIPping pressure represents normal sintering. Results marked with Δ and ○ are sample C CIP-treated at 50 and 100MPa, respectively, and HIP-treated at 1973K for 1h. The difference in CIPping pressure caused a small difference of 2 to 3% in both relative density and open porosity.

Increasing the HIPping pressure from 0 to 150MPa increased the porosity by 12 to 13% but decreased the relative density by 13%.

Comparing these results with those shown in **Fig.5** for the samples HIP-treated at 1973K with different CIPping pressures reveals that the relative density and other properties of the samples HIP-treated at 150MPa were almost identical to those CIP-treated at 20MPa. This means that increasing the HIPping pressure helps the sample retain its porosity, and the HIPping pressure has larger effects on the pore formation than CIPing pressure.

3-4. Sinterability of Sintered Samples

Figure 7 shows SEM photographs of the fractured surfaces in samples C treated under varying CIPping pressure and then HIP-treated at 1973K under 100MPa for 1h. An increased CIPping pressure accelerated the sintering, presumably because of the decreased inter-grain distance to reduce diffusion distance. A decreased CIPping pressure also increased pore size, and the pores were more rounded as sintering proceeded. The porosity might be affected by pore size.

Figure 8 shows SEM photographs of the fractured surfaces in samples C sintered at various temperatures, with CIPping and HIPping pressures set under 100MPa. A comparison of photographs (a), (b) and (c) suggests that the binder decreased in viscosity as the sintering temperature increased, where sample (a) was sintered insufficiently and sample (c) had excessively low in viscosity and was almost

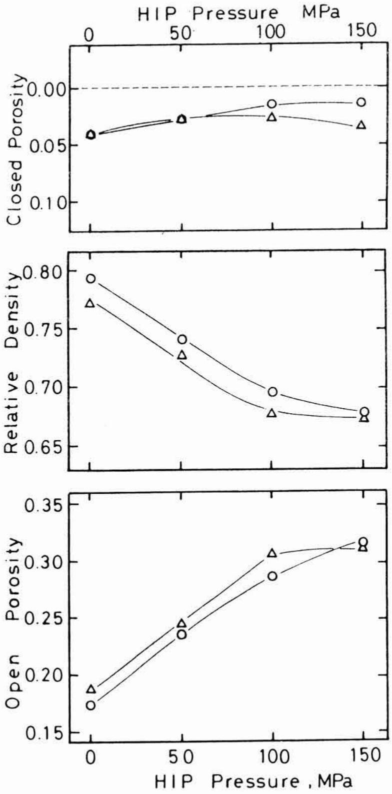

Fig. 6. Open porosity, relative density and closed porosity us. HIPpping pressure. HIPped at 1973K under 50, 100 and 150 MPa for 3.6ks. The zero HIPping pressure represents normal sintering. Triangle and circle marks indicate CIPping prressures, 50 and 100 MPa, respectively. The sampes used correspond to the ones identified as C in Table 2.

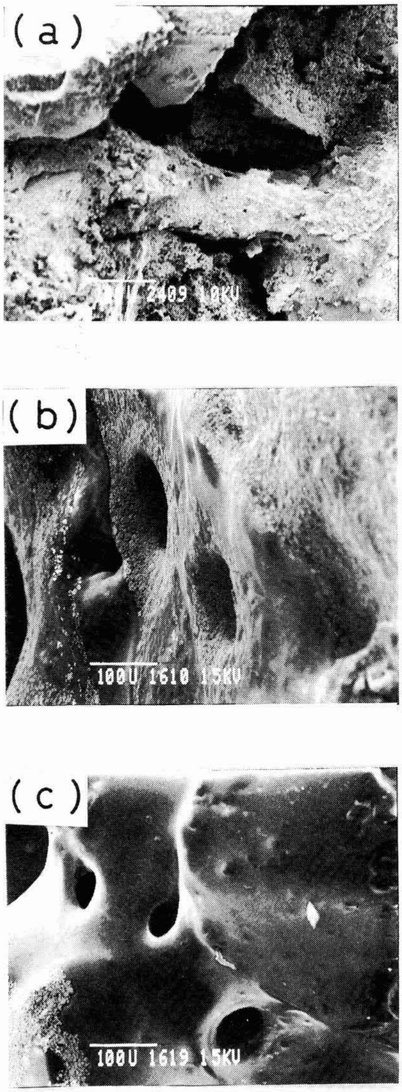

Fig. 7. SEM micrographs of fractured surfaces of HIPped samples for various CIPping pressures. The samples were HIPped at 1973K under 100MPa for 3.6ks, and CIPped under (a) 20, (b) 100 and (c) 400MPa. The scale bars indicate 100µm. The samples used correspond to the ones identified as C in Talble 2.

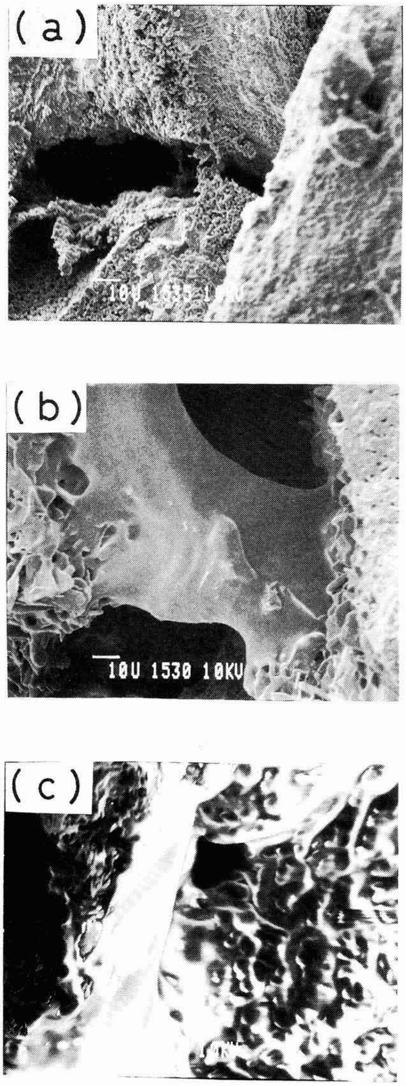

Fig. 8. SEM micrographs of fractured surfaces of HIPped samples for various HIPping temperature. HIPping was performed under 100MPa for 3.6ks at (a) 1873, (b) 1973 and (c) 2073K. All of them were CIPped under 100MPa for 300s. The samples have the same significance as in Fig.5. The scale bars indicate 10μm.

molten, whereas sample (b) had ideal bridges well-sintered to couple the abrasive grains.

Figure 9 shows SEM photographs of the fractured surfaces in samples C HIP-treated at 1973K for 1h under various pressures. The normally sintered treated sample (a) had large cracks running throughout the bond bridge sections, and increasing HIPping pressure improved the sinterability of the bridges. Thus, the increasing HIPping pressure increased the open porosity (**Fig.6**) and improved

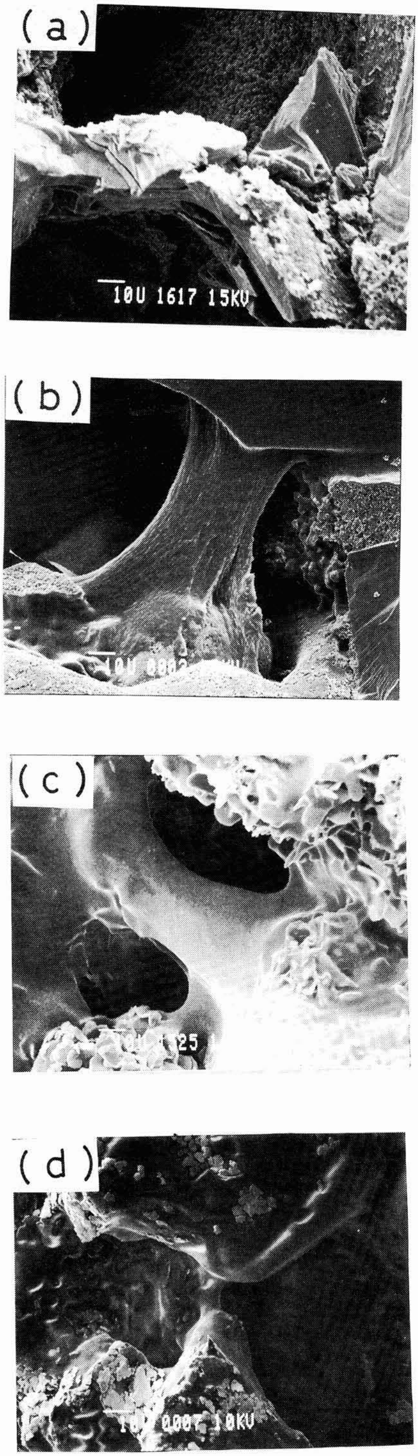

Fig. 9. SEM fractographs of samples HIPped at 1973K for 3.6ks under (b) 50, (c) 100 and (d) 150MPa. Micrograph (a) represents 0MPa or normal sintering. All the samples were CIPped under 100MPa for 300ks. The samples used correspond to the ones identified as C in Table 2. The scale bars indicate 10μm.

sinterability (Fig.9). High isostatic pressure accelerates the diffusion of the grains to be sintered, removes the flaws within the sintered structures, such as cracks, improving sinterability, removes the cracks within the bridges, and increases the pore quantity by pressing the closed pores causing collapse into open pores. The reason why the sintering of bridges was enhanced by the HIPprocess is due to the same reason as the conventional HIP treatment under increased pressure allows the samples to be sintered and densified at lower temperatures than the conventional normal sintering process. These results suggest that increasing HIPping pressure produces a sintered body of higher strength and higher porosity.

4. Conclusions

Porous materials containing large quantities of open pores were prepared using a modified HIP process, and the effects of CIPping and HIPping pressures on the sintered porous materials properties were investigated. The sintered bodies were also compared with those prepared by the conventional normal sintering process.

1) The modified HIP process provides higher open porosity than the normal sintering. Increasing the HIPping pressure increases the open porosity.

2) Increasing the HIPping pressure removes the flaws present within the sinterrd structures and improves the sinterability of the grains.

3) The microstructure can be controlled relatively easily by changing the CIPping or HIPping pressure.

4) The modified HIP process has been shown to be useful for producing porous ceramic materials.

Appendix

Determination of relative density, open porosity and closed porosity

Bulk density and porosity were measured by the Archimedean method, using the following equations:

$$\text{Bulk Density} = [W_1/(W_3 - W_2)] \times \rho_t. \ldots\ldots (1)$$

$$\text{Open Porosity} = (W_3 - W_1)/(W_3 - W_2) \ldots\ldots (2)$$

where W_1 is the weight of the dry sample, W_2 is the weight of the sample placed in toluene for 24h, measured while in suspension, W_3 is the weight of the sample wiped to remove toluene from the surface, and ρ_t is the density of toluene.

Bulk density determined by equation (1) was divided by the theoretical density to find relative density:

$$\text{Relative Density} = (\text{Bulk Density})/(\text{Theoretical Density}) \ldots\ldots (3)$$

Relative density and porosity are considered to follow the relationship, relative density + porosity = 1, from which total porosity is defined as:

$$\text{Total Porosity} = (\text{Open Porosity}) + (\text{Closed Porosity}) \ldots\ldots (4)$$

(Closed porosity is therefore determined by:

$$\text{Closed Porosity} = 1 - [(\text{Relative Density}) + (\text{Open Porosity})] \ldots\ldots (5)$$

Acknowledgments:
The HIP sintering was carried out at the Central Niigata Prefectural Industry Promotion Center.

References:

1) T. Hiki, Seramikkusu, 20, 168-74 (1985).
2) N. Kato, ibid., 23, 726-30 (1988).
3) M. Inagaki, ibid., 19, 104-109 (1984).
4) S. Sakka, Kagaku Kogyo, 2, 159-162 (1982).
5) R.A. Messing, R.A. Oppermann and F.B. Kolot, Biotech. Bioeng., 21, 59-67 (1979).
6) S. Okada, "Development and Applications of Porous Ceramic Materials," edited by S. Hattori, published by CMC (1984), pp.139-48.
7) N. Yamamoto, Proc. of the International Symposium on Fine Ceramics, Arita '87, Society of Fine Ceramics, pp.87-95 (1987).
8) S. Hattori and S. Yamanaka, "New Technologies of High Technological Materials," edited by G. Adachi, G. Shibayama and T. Minami, published by Kagaku Dojin, (1987) pp.117-26.
9) Y. Banno, "Porous Materials," edited by R. Kondoh, published by Gihodo, (1973) pp.227-30.
10) A. Makishima, "Kagaku Sosetsu, Vol.41, Inorganic Amorphous Materials," published by Gakkai Shuppan Center (1983) p.162.
11) T. Nakajima and M. Shimizu, Seramikkusu, 21, 408-12 (1986).
12) M.W. Kearns, P.A. Blenkinsop, A.C. Barber and T.W. Farthing, International J. of Powder Met., 24, 59-64 (1988).
13) K. Ishizaki, S. Okada, T. Fujikawa and A. Takata, Jpn. (Jan. 205421, 1989), U.S. and Germ. Pat. Pending.

This article is a full translation of the article which appeared in Nippon Seramikkusu Kyokai Gakujutsu Ronbunshi (Japanese version), Vol.98, No.6, 1990.

Microstructure and Mechanical Properties of Mullite Ceramics

Hiroshi Ohnishi, Toshio Kawanami, Atsushi Nakahira*[+], Koichi Niihara**

Nippon Kagaku Togyo Co., Ltd., 3-2-24, Oriono-cho, Sakai 590, Japan
*National Defence Academy, 1-10-20, Hashirimizu, Yokosuka 239, Japan
**ISIR, Osaka University, 8-1 Mihogaoka, Ibaraki, 567, Japan
[+]Now with ISIR, Osaka University, 8-1, Mihogaoka, Ibarakio-shi 569, Japan

Microstructural effects on the mechanical and thermomechanical properties of mullite ceramics have been investigated. The mullite ceramics were fabricated by reaction-sintering of mixture of kaolin and Al_2O_3 (M-1) and by pressureless sintering of a powder prepared from Al_2O_3 and SiO_2 sols (M-2) and Al_2O_3 sol-ethylsilicate (M-3) systems from the sol-gel method.
Transmission electron microscopic observation revealed that samples and M-2 contained foreign phases, but that they were much less in M-2. These showed different temperature dependence in mechanical properties such as hardness, Young's modulus, fracture toughness and strength. These differences were explained by the amount of grain boundary impurity phases. Thermal shock fracture behavior was also discussed.
[Received November 16, 1989; Accepted March 12, 1990]

Key-words: Mullite ceramics, Mechanical properties, Sol-gel method, Thermal shock, Grain boundary

1. Introduction

Mullite is an aluminosilicate represented by the formula $3Al_2O_3.2SiO_2$, and is a ceramic material known to be highly resistant to heat and creep.[1]. It is of interest as a high-temperature structural material, because of its resistance to oxidation, being an oxide, and retention of mechanical properties in air at high-temperature.[2,3,4] This sharply distinguishes it from non-oxide ceramics, such as Si_3N_4 and SiC. One of the major disadvantages of conventional mullite material is the poor resistance to high temperatures. It is mainly formed from naturally occurring minerals, such as kaolin, containing impurities which react with Al_2O_3 and SiO_2 to form the glassy phase in the grain boundaries of the sintered ceramics which degrades the mechanical properties at high temperature.[5] Recently, advanced chemical methods, such as the sol-gel,[6] coprecipitation,[7] spray pyrolysis,[2] and alkoxide methods,[8] have been developed to prepared mullite powder with low impurity content and well-controlled Al_2O_3/SiO_2 ratio. Such powders are the starting material for producing high-quality sintered mullite with excellent high temperature resistance. However, some quantity of the glassy phase will be formed in the grain boundaries, even when the theoretical mullite composition consisting of 71.8wt% of alumina and 28.2wt% of silica is achieved.[9]

In this study, three types of mullite ceramics were prepared, one from kaolin and alumina starting materials and two from high-purity powders synthesized by the sol-gel process, to investigate their microstructures and mechanical properties, and to clarify the effects of the impurity glassy phase on the mechanical properties.

2. Experimental Procedure

Three types of mullite sintered samples were fabricated: M-1 from natural minerals, and M-2 and M-3 from the powders prepared by the sol-gel process. For the production of sample M-1, the required quantities of kaolin and alumina were wet-mixed by a ball mill, and formed, after having been dried and granulated. For the production of samples M-1 and M-2, the required quantities of silica and alumina sols (for the former) and ethyl silicate and alumina sol (for the latter) were mixed, and were formed into the powders, after gelation, calcination and grinding.[3,6] Sample M-3 was regarded as the same as sample M-2, except that the former had a lower alkaline impurity content. Each of these powders was pressed by a mold under 98MPa and sintered at 1700°C for 2h in air, to form sintered samples of 40×35×4mm size. Each was cut and ground by a #600 diamond wheel into 3×4×40mm specimens for the strength test. The fracture strength was determined by the 3-point bending test with a span of 30mm, crosshead speed of 0.5mm/min, and temperature in the range from room temperature to 1400°C. The fracture toughness K_{IC} was determined by the controlled surface flaw (CSF) method, under the same conditions as used for the bending test. Microcracks were introduced under a load of 49N by a Vickers indenter. The specimen surface was polished with SiC grinding grains to remove the residual stresses formed around each indent. The shape and size of the cracks in the fractured samples were determined by a scanning electron microscope (SEM). K_{IC} was determined using the following equation[10]:

$$K_{IC} = \sigma M (\pi a / Q)^{1/2} \quad \dots\dots\dots\dots\dots (1)$$

where, σ is the fracture strength by the 3-point bending test, M is a correction term for the free surface, a is crack depth, and Q is the second integral function.

The Vickers hardness was measured by a high-temperature microhardness tester (Nikon QM), at a load of 0.98N and temperatures up to 1300°C for 10sec, under a vacuum of around 1×10^{-5} torr. Young's modulus was measured by the bending resonance method in air at temperatures up to 1400°C, the thermal conductivity by the laser flash method, and the coefficient of thermal expansion by a dilatometer.

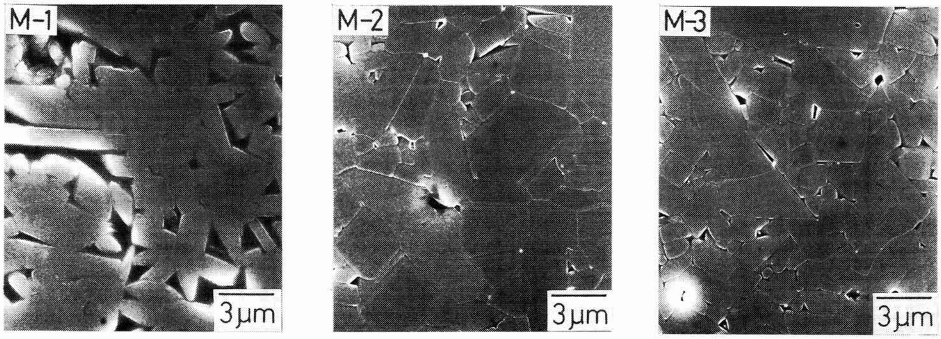

Fig. 1. Scanning electron micrographs of thermally etched-surfaces after polishing for M-1, M-2 and M-3 mullite samples.

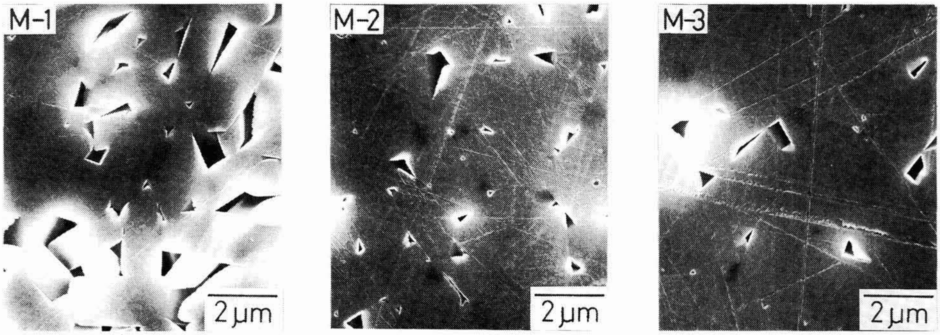

Fig. 2. Scanning electron micrographs of polished surfaces etched by HF solution for M-1, M-2 and M-3 mullite samples.

Table 1. Chemical composition and bulk density for mullites from kaolin and Al_2O_3 (M-1), and by sol-gel method of Al_2O_3 sol-SiO_2 sol (M-2) and Al_2O_3 sol-ethyl silicate (M-3).

Sample	M-1	M-2	M-3
Density (g/㎤)	2.63	3.15	3.15
Al_2O_3/SiO_2 (wt%)	59.2/38.3	71.5/28.5	71.6/28.4
Na_2O (wt%)	0.20	0.05	0.02
K_2O (wt%)	1.05	0.02	0.01
MgO (wt%)	0.10	0.02	0.02

The thermal shock resistance was measured by the water quench method, using the fracture strength of a specimen for the bending test placed in water kept at 20°C after being held at a given temperature for 20min. The microstructures were determined by SEM observation of the polished surfaces (thermally etched or chemically etched with 1% HF) as well as the fracture surfaces. The grain boundaries were observed by a transmission electron microscope (TEM) and an analytical electron microscope (ATEM).

3. Results and Discussion

3-1. Microstructures

Table 1 presents the bulk density, Al_2O_3/SiO_2 ratio, and alkaline and MgO contents of the sintered mullite samples. Samples M-2 and M-3 had compositions very close to the theoretical (71.8% of Al_2O_3 and 28.2% of SiO_2) and only small quantities of alkaline impurities. Sample M-2 contained slightly larger quantities of alkaline impurities than

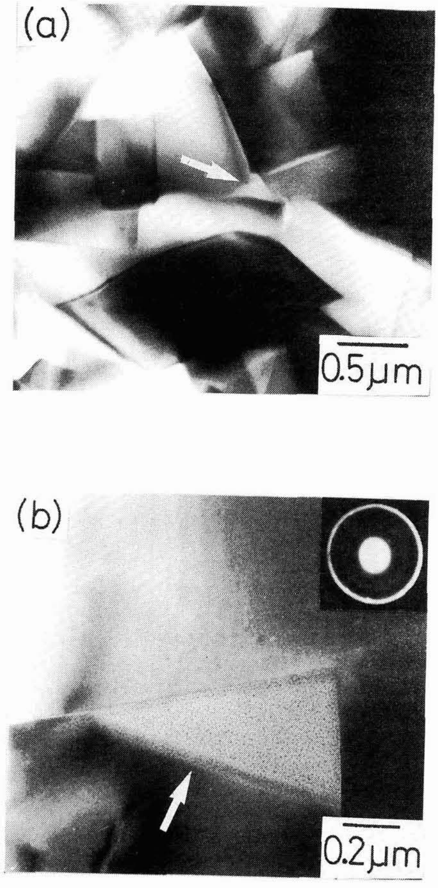

Fig. 3. Transmission electron micrograph (a) and higher magnification of grain-boundary triple point (b) for the M-1 mullite sample. Arrows indicate the impurity phase at the grain-boundary triple point.

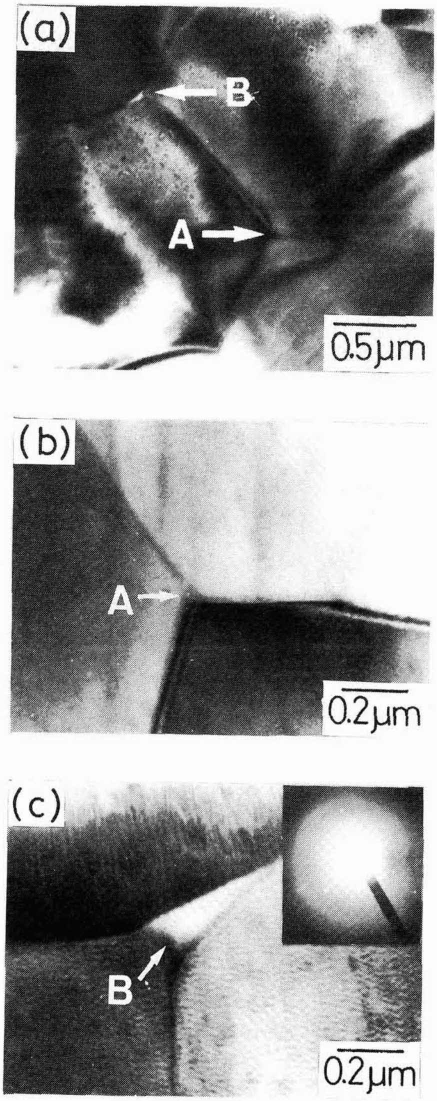

Fig. 4. Transmission electron micrograph for the M-2 mullite sample. The (b) and (c) show higher magnifications of A and B positions in (a), respectively.

sample M-3. Sample M-1 had a lower bulk density than samples M-2 and M-3, and the Al_2O_3/SiO_2 ratio was smaller than the theoretical (it was noted, in the preliminary test, that increasing Al_2O_3 content from the M-1 ratio caused separation of free Al_2O_3). Furthermore, M-1 had larger quantities of alkaline impurities (10 times or higher), resulting from the use of natural kaolin as one of the starting materials. No phase other than mullite was identified in these three samples by X-ray power diffraction.

Figures 1 and 2 show the scanning electron micrographs of the surfaces of the three samples, thermally etched and chemically etched with HF, respectively. Sample M-1 had traces of large quantities of glassy phase in the grain boundaries, and enlonged mullite particles. No significant difference was observed between the microstructures of samples M-2 and M-3; both contained only limited quantities of the glassy phase around the triple points and were characterized by the mixed enlonged and granular particles.

Figures 3 and 4 show transmission electron micrographs of the microstructures of samples M-1 and M-2. Sample

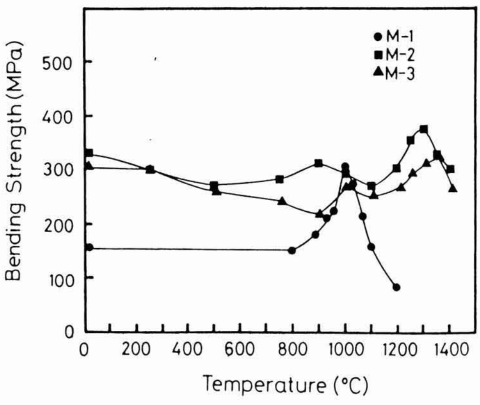

Fig. 5. Temperature dependence of bending strength for M-1, M-2 and M-3 mullite samples.

M-1 had the impurity phase apparently in the grain boundaries, as expected from the SEM photograph of the etched surface (Fig. 3(a)). In particular, a large quantity of wedge-shaped glassy phase can be seen around the triple point (Fig. 3(b)). The glassy phase was composed of SiO_2, Al_2O_3, MgO, and alkaline metal oxides of Na_2O and K_2O, as revealed by ATEM analysis. Sample M-2, on the other hand, had only a limited quantity of the glassy phase around the triple point in the grain boundaries, as shown in Fig. 4 (c).

3-2. Mechanical Properties

Figure 5 shows the temperature dependence of bending strength for each sample. The fracture strength of sample M-1 increased rapidly as the temperature increased, attained a maximum at 1000°C and decreased rapidly thereafter. The maximum strength was about twice the strength at room temperature. The strength of sample M-2 decreased slightly at around 500°C, increased slightly at 900°C, and attained a maximum at 1300°C. The maximum level was about 25% higher than the level at room temperature, and thus the increase rate was much lower than that of sample M-1. It should be noted, however, that M-2 attained a maximum strength at 300°C higher than sample M-1, and the strength decreased thereafter at a much lower rate.

Kanzaki et al.[2] and Kubota et al.[7] discussed the high-temperature strength of high-purity mullite with almost the theoretical composition. Kanzaki et al. reported that the strength of high-purity mullite changes little with temperature in a range from room temperature up to 1300°C, and decreases gradually thereafter.[2] On the other hand, Kubota et al. reported that the strength attained a maximum at a temperature somewhere between 1300°C and 1350°C,[7] as is the case with sample M-2 of this study. The different behavior expectantly results from the different quantity and quality of the impurity glassy phase in the grain boundaries. Kanzaki et al. analyzed the impurity glassy phase by ELLS, finding SiO_2.[9] The glassy phase in sample M-2 was not analyzed in detail, but it would not contain only SiO_2 but silicate containing small quantities of alkaline and alkaline earth metals, as the strength temperature dependence differed from that found by Kanzaki et al.

Figure 5 also shows the temperature dependence of strength of M-3 which contained smaller quantities of alkaline impurities than sample M-2. Samples M-2 and M-3 had similar strength trends at high temperature, but the latter attained the maximum strength at 50°C higher than the former, possibly because of the smaller quantities of alkaline metals in the glassy phase (see Table 1).

Figures 6 and 7 show SEM photographs of the fracture surface of samples M-1 and M-2, respectively, at three temperatures around that at which the strength of each sample attained the maximum; 800, 1000 and 1200°C for the former and 1000, 1300 and 1400°C for the latter. In sample M-1,

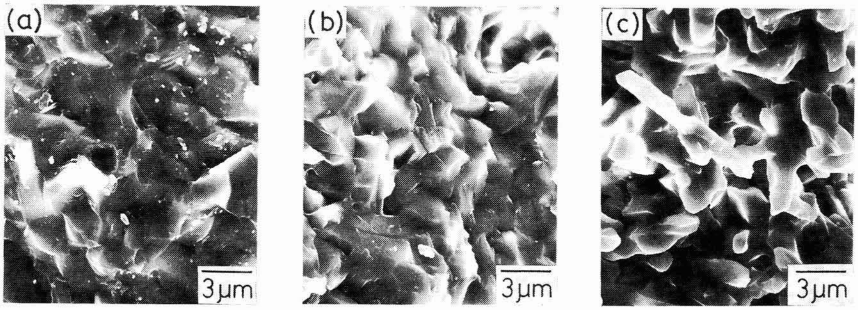

Fig. 6. Scanning electron micrographs of fracture surfaces at 800°C (a), 1000°C (b) and 1200°C (c) for the M-1 mullite sample.

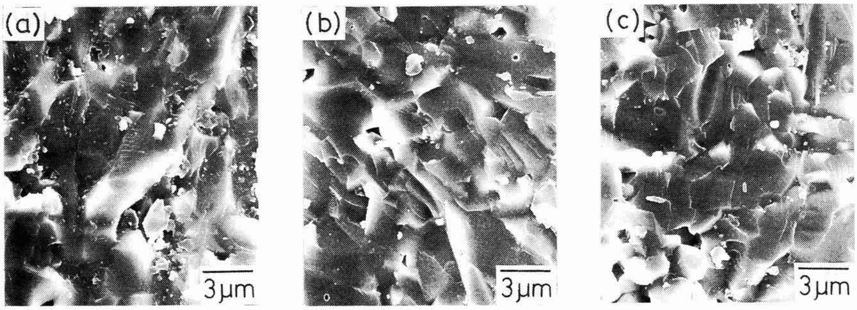

Fig. 7. Scanning electron micrographs of fracture surfaces at 1000°C (a), 1300°C (b) and 1400°C (c) for the M-2 mullite sample.

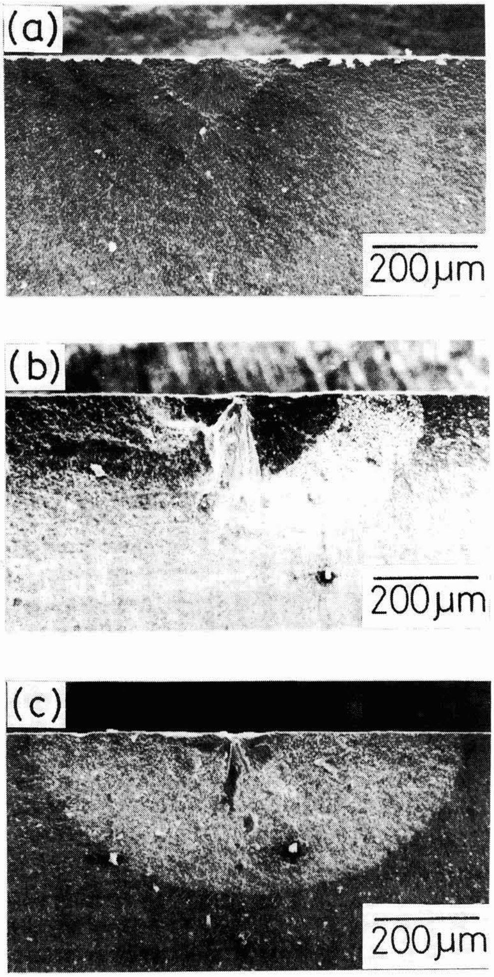

Fig. 8 Scanning electron micrographs of fracture surfaces at 1000°C (a), 1300°C (b) and 1400°C (c) after indenting by Vickers indenter for the M-2 mullite sample.

intragrain fracture was prevalent temperatures below that of maximum strength (Fig. 6(a)), indicating brittle fracture, but intergrain fracture resulting from softening of the glassy phase mainly occurred at a temperature above the maximum strength temperature (Fig. 6 (c)). It is considered, based on these results, that the increased strength of M-1 at high temperature results from decreased viscosity, or from the viscous flow of the glassy phase, blunting the crack tips. In sample M-2, on the other hand, the difference in fracture behavior around the maximum strength temperature was not so conspicuous as in sample M-1, as shown in Fig. 7. Thus, the superior high temperature characteristics of sample M-2 over Sample M-1 can confirmed by SEM observation of the fracture surfaces.

In an attempt to further clarify the above point, the fracture surface during K_{IC} testing by the CSF method were examined by SEM (**Fig. 8**). The fracture surface at 1200°C indicated brittle fracture, showing few traces of slow crack growth, which, however, was notable in the fracture surface at above the maximum strength temperature around 1300°C. As is clearly shown in Fig. 7, no significant difference was observed in the fractures around the maximum strength temperature in those samples in which no precracks were introduced, but there were significant differences for those precracked for the measurement of K_{IC} by the CSF method. The latter samples were characterized, like sample M-1, by intergrain fracture at above the maximum strength temperature.

Figure 9 shows the effects of temperature on the fracture toughness K_{IC} of sample M-2, determined by the CSF method. K_{IC} increased rapidly at 1100°C and above, expectantly resulting from the plastic deformation of the impurity phase in the grain boundaries blunting the crack tips. It was also noted that K_{IC} decreased slightly at around 500°C, a phenomenon also observed by Kubota et al.7) It is not clearly understood at present, but one of the reasons will be the difference between the thermal expansion coefficients of the mullite crystalline phase and the glassy phase.

Figure 10 shows the temperature dependence of Young's modulus for sample M-1 and M-2. Sample M-2 had Young's modulus about 30% higher than sample M-1 at room temperature, resulting from the lower content of

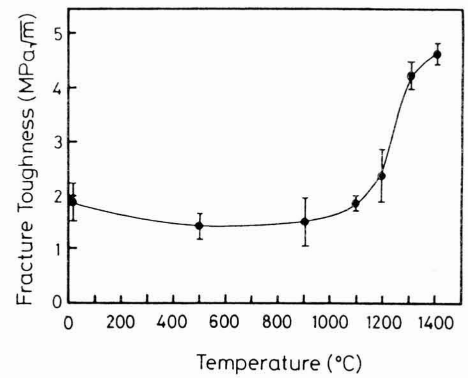

Fig. 9. Temperature dependence of fracture toughness (K_{IC}) for M-2 mullite samples.

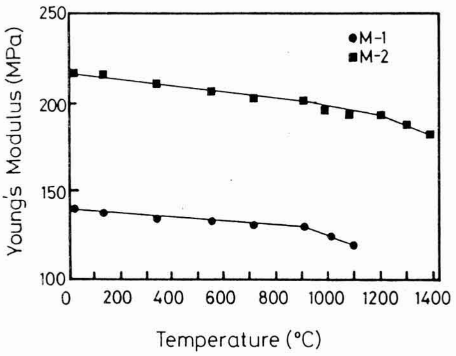

Fig. 10. Temperature dependence of Young's modulus for the M-1 and M-2 mullite samples.

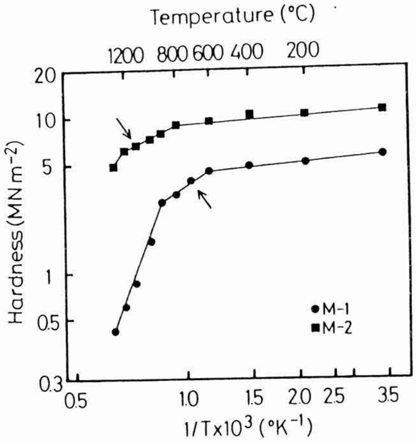

Fig. 11. Temperature dependence of Vickers hardness for the M-1 and M-2 mullite samples.

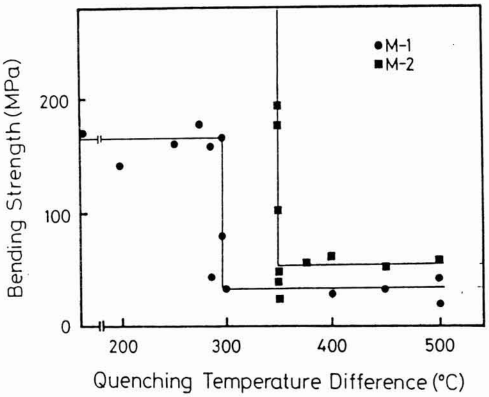

Fig. 12 Bending strength after quenching into water bath for the M-1 and M-2 mullite samples.

glassy phase in the former. Young's modulus began to decrease more rapidly at 900°C in sample M-1, but at 1200°C in sample M-2. This is considered to be caused by the lower contents of alkaline metals and MgO in the latter which increased the softening temperature of the glassy phase. The different temperature dependence of viscosity of the glassy phase presumably results from the different alkaline metal and MgO contents.

Figure 11 shows the temperature dependence of Vickers hardness of samples M-1 and M-2. The latter had a higher hardness than the former at room temperature. The hardness of both samples decreased as the temperature increased, more rapidly with sample M-1. In addition, the change in the hardness of sample M-1 was discontinuous at 600 and 900°C. The corresponding points of sample M-2 were higher at 800 and 1000°C. No cracks initiating from the indent corners were found in the samples at temperatures above the arrows in Fig. 11. The arrows coincide with the temperatures at which the samples started to increase in strength, and are thus considered to be the temperatures above which plastic deformation plays a more important role in determining the temperature dependence.

These results indicate that the effects of temperature on strength, Young's modulus and hardness are closely related to each other. For example, the temperature at which each

Table 2. Thermal conductivity, thermal expansion coeff., bending strength and Young's modulus for M-1 and M-2 mullite samples

	Thermal Conductivity (W/m·K) (400℃)	Thermal Expansion Coeff. (10^{-6}/K) (20-1000℃)	Young's Modulus (GPa) (400℃)	Bending Strength (MPa) (400℃)	R'
M−1	2.1	5.0	140	170	0.39
M−2	3.3	4.8	210	280	0.67

to each other. For example, the temperature at which each sample starts to increase in strength corresponds well to those at which Young's modulus and hardness start to decrease. It may be concluded, therefore, that changes in the mechanical properties with increased temperature are caused by plastic deformation resulting from the softening of the glassy phase in the grain boundaries; a sample having larger contents of alkaline metals and MgO in the glassy phase tends to have a lower critical temperature at which the strength attains the maximum, and Young's modulus and hardness start to decrease. It is also considered that the increased strength depends on the glassy phase quantity.

Figure 12 presents the results of the thermal shock tests. The critical quenching temperature difference (ΔT) of sample M-1 was about 300°C, and that of sample M-2 was about 350°C. The thermal shock resistance is generally assessed by resistance to fracture by thermal shock R′, represented by $R' = \sigma(1-\nu)K/\alpha E$,[11] where σ is the bending strength, ν is Poisson ratio, K is thermal conductivity, α is thermal expansion coefficient, and E is Young's modulus. **Table 2** gives the thermal conductivity, thermal expansion coefficient, strength and Young's modulus of samples M-1 and M-2. The higher Young's modulus of sample M-2 decreases R′ level, which, however, is compensated by the higher strength and thermal conductivity and lower thermal expansion coefficient. The improved thermal shock resistance of sample M-2, therefore, results from the increased strength and thermal conductivity as well as the decreased thermal expansion coefficient.

4. Conclusions

Three types of sintered mullite samples were prepared, one from kaolin and alumina and two from synthesized powders, to investigate the relationship between their microstructures and mechanical properties. The starting powders for the latter two sinter types were of silica and alumina sols, and ethyl silicate and alumina sol, prepared by the sol-gel method.

1) The mullite sample from natural minerals, represented by $Al_2O_3/SiO_2 = 59.2/38.3$ by weight, contained an excess quantity of silica, as compared with the theoretical composition. A glassy phase of high alkalinity was found in the grain boundaries. The mullite samples from the synthesized powders, on the other hand, were characterized by high purity and almost theoretical compositions containing smaller quantities of the glassy phase. The alkaline content of the glassy phase was also lower, 0.07wt% in M-2 and 0.03wt% in M-3.

2) The mullite samples from the synthesized powders had superior bending strength, fracture toughness, Vickers hardness and Young's modulus compared to the sample from natural minerals. The degradation of the mechanical properties at high temperature of the former were well controlled.

3) The temperatures at which the strength attained the maximum and Young's modulus and Vickers hardness started to decrease depended on the glassy phase composition, while the rate of increase of strength and rates of decrease of Young's modulus and Vickers hardness depended on the content of glassy phase.

4) The sintered mullite samples from the powders prepared by the sol-gel method had higher thermal shock resistance, because of their increased strength and thermal conductivity and decreased thermal expansion coefficient.

References:

1) P.A. Lessing, R.S. Gordon and K.S. Mazdiyasni, J. Am. Ceram. Soc., 58 [3-4] 149 (1975).
2) S. Kanzaki, H. Tabata, T. Kumazawa and S. Ohta, J. Am. Ceram. Soc., 68 [1] C6-7 (1985).
3) H. Ohnishi, T. Kawanami, K. Miyazaki and T. Hiraiwa, Proc. of Int. Sympt. of Ceramic Components for Engines. pp. 633-641 (1986).
4) P.C. Dokko, J.A. Pask and K.S. Mazdiyasni, J. Am. Ceram. Soc., 60 [3-4] 150 (1977).
5) T. Kawanami, "New Materials Series, Mullite," edited by S. Somiya, published by Uchida Rokaku-ho, (1986), pp. 123-135.
6) T. Hiraiwa, K. Miyazaki, Y. Kimura, T. Kawanami and H. Ohnishi, The Electrochemical Soc., 169th Meeting (1986).
7) T. Kubota and T. Takagi, Br. Ceram. Proc., 37, 179-88 (1986).
8) T. Mah and K.S. Mazdiyasni, J. Am. Ceram. Soc., 66 [10] 699-703 (1983).
9) S. Kanzaki, O. Abe, M. Ohashi and H. Tabata, Proc. of Int. Sympt. of Ceramic Components for Engines. pp. 625-631 (1986).
10) J.J. Petrovic and M.G. Mendiratta, "Fracture Mechanics Applied to Brittle Materials, ASTM. STP 678", Edited by S.M. Freiman, ASTM, pp 83-102 (1979).
11) J. Nakayama, Seramikkusu, 8 [5], 343 (1973).

This article is a full translation of the article which appeared in Nippon Seramikkusu Kyokai Gakujutsu Ronbunshi (Japanese version), Vol.98, No.6, 1990.

Phase Transition of the Ilmenite Type $NaNbO_3$

Nobuhiro Kumada, Nobukazu Kinomura, Fumio Muto

Institute of Inorganic Synthesis, Yamanashi University
Miyamae-cho 7, Kofu, 400 Japan

The ilmenite type $NaNbO_3$ was prepared by low temperature hydrothermal reaction and had an endothermic phase transition at about 290°C and transformed to the perovskite type structure at about 485°C. The ionic conductivity, the lattice constants at high temperature and the latent heat were measured in order to investigate the phase transition at about 290°C. The crystal structure at 350°C was refined with the X-ray powder Rietveld method and the final R-factors were R_{wp}=24.1, R_p=18.4 and R_B=14.5%. The refinement indicated that partial Na^+ ions moved to the empty octahedral sites along the c-axis. From these results the phase transition at about 290°C was concluded to be the order-disorder transition of Na^+ ions.

[Received November 17, 1989; Accepted February 13, 1990]

Key-words: Ilmenite type, Order-disorder transition, Rietveld method, $NaNbO_3$

1. Introduction

The authors have reported that a low-temperature hydrothermal reaction with the polyacid salt $Na_8Nb_6O_{19}\cdot 13H_2O$ as a starting material forms ilmenite-type $NaNbO_3$, and that ion exchange of the Na^+ ions of this ilmenite-type $NaNbO_3$ with Li^+ ions forms ilmenite-type $LiNbO_3$.[1,2] These ilmenite-type compounds were analyzed by powder X-ray diffraction using the Rietveld method to obtain detailed crystal structures.[3] Ilmenite-type $NaNbO_3$ undergoes an endothermic phase transition at about 290°C, and a further exothermic phase transition at about 485°C from ilmenite-type to perovskite-type $NaNbO_3$.[1] Ilmenite-type $LiNbO_3$ undergoes an exothermic phase transition near 520°C, while no phase transition was detected below that temperature. Moreover, in the case of $CdTiO_3$,[4] which has the ilmenite structure at low temperatures and the perovskite one at high temperature, no phase transition has been reported in the region between these temperatures. In order to study the phase transition of this ilmenite type $NaNbO_3$ near 290°C, the lattice constants at high temperatures were measured as well as the ionic conductivity and latent heat of phase transition. The refinement of crystal structures by powder X-ray diffraction at high temperature using the Rietveld method found that the phase transition near 290°C is the order-disorder transition of Na^+ ions, which is described below in detail. The phase transition of disorder phases to a perovskite structure is also discussed.

2. Experimental Method

Ilmenite-type $NaNbO_3$ was synthesized according to the method reported earlier.[1] For measurement of ionic conductivity, the raw material could not be sintered so it was compacted in a mold glazed with gold paste in advance, the whole of which was used as an electrode. The ionic conductivity was measured by the complex impedance method (Yokogawa-Hewlett Packard, 4226A· 4227AL CZ meter). The latent heat of phase transition was measured by DSC. Powder X-ray diffraction at high temperatures was conducted using CuKα radiation through a Ni filter by attaching a dedicated high-temperature furnace to a powder X-ray diffraction system (RAD-IIC, Rigaku Denki). Lattice constants were obtained by the least squares method with 2θ values from diffraction patterns measured at a scan speed of 0.5°/min. The internal standard was α-Al_2O_3. In order to examine the changes in crystal structures during phase transition, refinement of the crystal structures was attempted by the Rietveld method[5] using powder X-ray diffraction at high temperatures. Long holding times at temperatures even below 500°C will cause phase transition to a perovskite-type phase, so that for powder X-ray diffraction by the step scan method each step was set at 0.05° width for 10 seconds at 350°C in the range from 15° to 80° in 2θ.

3. Results

3-1. Changes in Various Properties at Phase Transition Near 290°C

Figure 1 shows the TG-DTA curve for ilmenite-type $NaNbO_3$. The exothermic peak near 500°C was shown by the powder X-ray diffraction patterns with samples heated over this temperature to be caused by the phase transition from the ilmenite-type to perovskite-type structure.[1] The endothermic peak near 290°C under investigation in this study was formed to give no change in the DTA curve in the cooling process after heating to 350°C, while reheating after cooling to room temperature gave an endothermic peak at about the same temperature, thus proving it to be a reversible change. **Figure 2** shows the temperature-dependence of ionic conductivity obtained by a complex impedance method. The ionic conductivity was nonlinear, and the activation energy was 0.40eV in the low-temperature region and 0.27eV in the high-temperature region. Such an inflection point in the ionic conductivity indicates that the mechanism of ionic conduction is different before and after the process, and it is considered to be caused by the phase transition near 290°C. The temperature of the inflection point is about 50°C lower than that of the en-

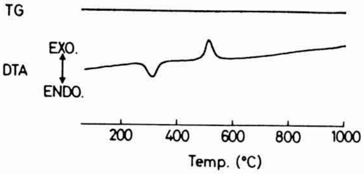

Fig. 1. TG-DTA curves of the ilmenite-type NaNbO$_3$.

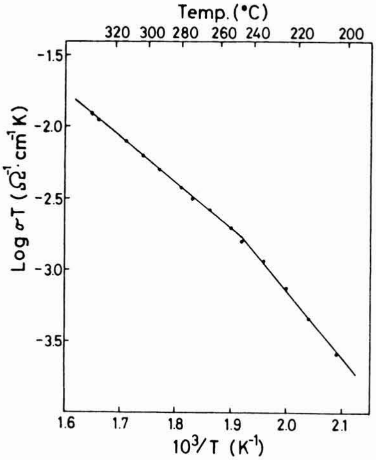

Fig. 2.Ionic conductivity of the ilmenite-type NaNbO$_3$.

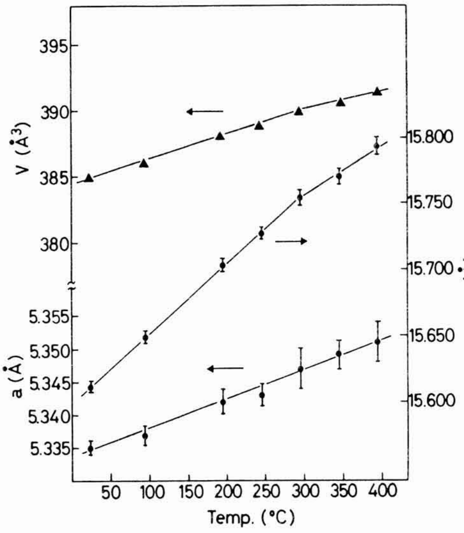

Fig. 3. Temperature dependence of lattice constants and unit cell volume of the ilmenite-type NaNbO$_3$.

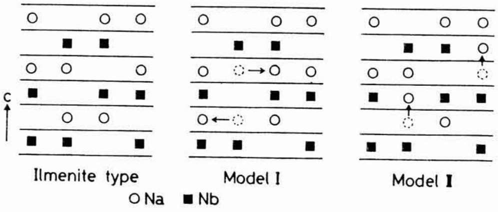

Fig. 4. Models of migration of Na$^+$ ions. Full lines denote the hexagonal close-packed oxygen array.

dothermic peak in the DTA curve, probably because of differences in the heating rate and the accuracy of the temperature measurement, so that the temperature of the phase transition is supposed to be slightly lower than 290°.

3-2. Structural Changes at Phase Transition Near 290°C

In powder X-ray diffraction at high temperatures, each diffraction line shifted to lower angles, but no substantial change was found except for a slight change in diffraction intensity over 300°C. Therefore, the basic ilmenite structure is considered to be maintained even in the temperature range between the endothermic to exothermic peaks. **Figure 3** shows the changes with temperature in the lattice constants obtained by powder X-ray diffraction at high temperatures as well as those in unit volume. The values of the a and c axes increased with the rise in temperature, and in the case of the c axis the gradient changed slightly over 300°C, but no considerable change was detected. Consequently, it is obvious that this phase transition does not alter the basic ilmenite structure, and the change in ionic conductivity suggests that it is a phase transition caused by the movement of Na$^+$ ions. The space group was set to R$\bar{3}$ used in the refinement of crystal structures at room temperature, the two sets of Na$^+$ ions below were assumed to be mobile, and the site occupancy of the Na$^+$ ions was introduced as a parameter before the refinement of crystal structures. The models had the characteristics: i) a part of the Na$^+$ ions moves to vacant octahedral sites in the same plane; and ii) a part of the Na$^+$ ions moves to vacant octahedral sites in the same plane as the Nb^{5+} ions. Each model is schematically shown in **Fig.4.** Refinement was carried out using these models to obtain R factors[6] (R_{wp}, R_p, R_B), atomic parameters, and temperature factors as in **Table 1**. The R factors are almost the same even for different models, but in model I the site occupancy and temperature factors of the Na$^+$ ions moving to vacant octahedral sites in the same plane are negative so that this was not considered to be appropriate. On the other hand, in model II, 7% of the Na$^+$ ions moved from the original octahedral sites of the ilmenite-type structure to vacant octahedral sites in the c-axis direction. **Figure 5** shows the powder X-ray diffraction pattern at 350° in which measurements are expressed by dots, calculated values based on model II by lines, and differences between the former and the latter by ΔY shown below. The above results suggest that in this phase transition Na$^+$ ions migrate as in model II to cause disorder. The reason for the disorder unlike model I but like model II is

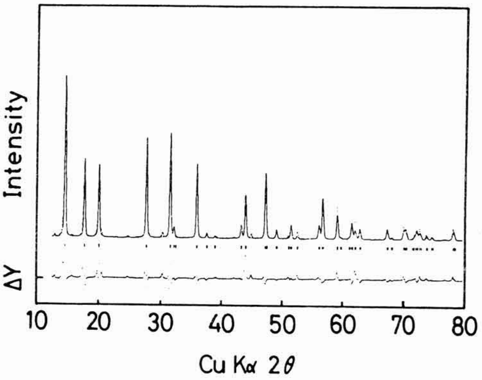

Fig. 5. Rietveld refinement pattern of the ilmenite-type $NaNbO_3$ at 350°C.

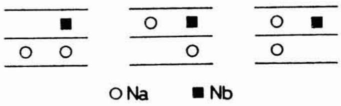

Fig. 6. Models of arrangements of Na^+ and Nb^{5+} ions for the disordered ilmenite-type $NaNbO_3$.

probably as follows. In the case where Na^+ ions move as in model I, they adjoin two Nb^{5+} by sharing octahedral faces. In contrast, in model II, Na^+ ions after movement adjoin two Nb^{5+} ions by sharing octahedral edges. For coordinated polyhedrons of the same ion type, edge sharing is more stable than face sharing so that the Na^+ ions are considered to move to vacant octahedrons sharing edges with Nb^{5+} ions.

3-3. Measurement of Latent Heat at Phase Transition Near 290°C

When Na^+ ions enter the disordered state as in model II, there are three combinations of the arrangement of the two Na^+ ions and a single hole, as shown in **Fig.6**, which leads to $3^{N/2}$ combinations (N: Avogadro's number) per mol. The entropy of the arrangement is expressed by equation (1):

$$S = K\cdot \ln W \quad \ldots\ldots\ldots\ldots\ldots\ldots\ldots (1)$$

where K is Boltzmann's constant. There is only one combination for the regular arrangement, and the entropy change ΔS is given by the following equation:

$$\Delta S = k\cdot \ln 3^{N/2}$$

$$= 4.57\ (\mathrm{J/deg}\cdot\mathrm{mol})$$

Table 1. Atomic parameters of Models I and II.

Model I R_{WP}=24.0%, R_P=18.5%, R_B=14.3%

atom	position	occupancy	x	y	z	B(Å^2)
Na(1)	3a	-0.11(7)	0	0	0	-3(12)
Na(2)	6c	1.05(7)	0	0	0.358(3)	3(1)
Nb	6c	1	0	0	0.1498(7)	0.5(3)
O	18f	1	0.268(8)	0.026(9)	0.228(2)	1(1)

Model II R_{WP}=24.1%, R_P=18.4%, R_B=14.5%

atom	position	occupancy	x	y	z	B(Å^2)
Na(1)	3b	0.14(9)	0	0	0.5	3(8)
Na(2)	6c	0.93(9)	0	0	0.359(3)	1(1)
Nb	6c	1	0	0	0.1493(8)	0.5(4)
O	18f	1	0.268(8)	0.029(9)	0.230(3)	1(1)

Hence, as 563K is the phase transition temperature the latent heat of phase transition is calculated to be 2.57 × 10^3J/mol. This value is in relatively good agreement with 2.19 × 10^3J/mol obtained from DSC. Thus, the latent heat of phase transition also confirmed the order-disorder transition of Na^+ ions.

4. Discussion

Table 2 lists the atomic distances calculated from the atomic parameters obtained by means of model II as well as those at room temperature.[3] The Nb-Nb distance increased from 3.127Å at room temperature to 3.136Å at 350°C (0.3%), while the average atomic distance between Nb and O in the NbO_6 octahedron decreased from 2.02Å at room temperature to 1.96Å at 350°C. Reflecting this, the O-O distance in the NbO_6 octahedron had a range of 2.53-3.09Å at room temperature in contrast to 2.36-3.34Å at 350°C, a broader range. This indicates that the NbO_6 octahedron deforms at 350° much more than at room temperature. On the other hand, the average atomic distance between Na and O in the NaO_6 octahedron was 2.36Å for Na(1) and 2.46Å for Na(2). In comparison with 2.39Å, the average atomic distance between Na and O at room temperature, there was an increase at the Na(2) site where a Na^+ ion was supposed to be present, remained about the same at the Na(1) site. The Na(2)-Na(2) distance (3.19Å) also increased from the Na-Na distance (3.168Å) at room temperature. The O-O distance of the NaO_6 octahedron was 2.63-3.66Å at room temperature, that of Na(1) 2.92-3.70Å at 350°C, and that of Na(2) 2.36-3.79Å, which indicates that the $Na(2)O_6$ octahedron deforms greatly. The increase in Nb-Nb and Na-Na distances is considered to be caused by higher thermal vibration of atoms, as well as the distortion of coordinated polyhedrons by the movement of atoms due to phase transition. The edge sharing O-O distance between NaO_6 octahedra at room temperature is 3.57Å, and increases to 3.79Å at 350°C. This means that the movement of Na^+ ions causes the other NaO_6 octahedron to become vacant, thus leading to longer O-O distances for edge sharing. In contrast, the NbO_6 octahedron shares an edge with the NaO_6 octahedron, and the O-O distance of the shared edge decreased from 3.04Å before sharing to 2.92Å after. As

Table 2. Bond lengths (Å) and angles(°) of the ilmenite type $NaNbO_3$ at 350°C and room temperature.

at 350°C

$Na(1)O_6$ octahedron		$Na(2)O_6$ octahedron	
Na(1)-O	2.36(5)	Na(2)-O	2.45(6),2.46(6)
O-O	2.92(6),3.70(9)		2.46(av.)
	3.31	O-O	2.36(6),3.70(9)
O-Na(1)-O	77(2),103(2)		3.76(6),3.79(7)
	90(av.)		3.40(av.)
		O-Na(2)-O	58(2),97(2)
NbO_6 octahedron			99(2),101(2)
Nb-O	1.86(5),2.06(3)		
	1.96(av.)	Metal-Metal	
O-O	2.36(6),2.37(6)	Nb-Nb	3.136(3)
	2.92(6),3.34(5)	Na(2)-Na(2)	3.19(2)
	2.75(av.)		
O-Nb-O	74(2),79(2)		
	96(2),108(2)		
	89(av.)		

at Room Temperature

NaO_6 octahedron			NbO_6 octahedron		
Na-O	2.38(3),	2.39(3)	Nb-O	1.96(2),	2.07(3)
		2.39(av.)			2.02(av.)
O-O	2.63(3),	3.43(4)	O-O	2.53(3),	2.63(3)
	3.57(4),	3.66(5)		3.04(3),	3.09(4)
		3.32(av.)			2.82(av.)
O-Na-O	67(1),	92(1)	O-Nb-O	78(1),	79(1)
	97(1),	101(1)		100(1),	102(1)
		89(av.)			90(av.)
Metal-Metal	Nb-Nb 3.127(1)		Na-Na 3.168(5)		

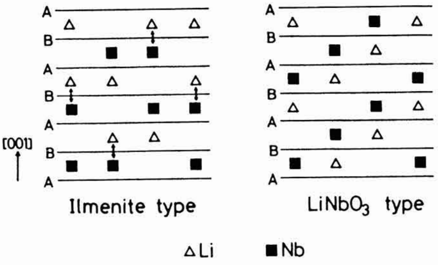

Fig. 7. Cation arrangements for ilmenite-and $LiNbO_3$-type structures. Full lines denote the hexagonal close packed oxygen array.

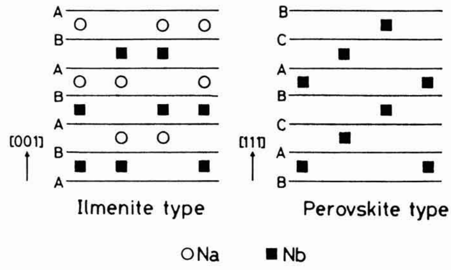

Fig. 8. Cation arrangements for ilmenite-and perovskite-type structures. Full lines denote the hexagonal close packed oxygen array for the ilmenite and the cubic close packed oxygen array for the perovskite type.

stated above, coordinated polyhedrons deformed substantially at the phase transition. The ilmentie-type compounds, $MnTiO_3$[7] and $MnSnO_3$[8] are known to allow order-disorder transition. The disorder phases of these compounds are obtained under high temperatures and pressures, and are formed by the process in which Mn^{2+} ions and Ti^{4+} or Sn^{4+} ions undergo α-Al_2O_3 type arrangement. In this case, the 003 diffraction line disappears in disorder transition while such behavior is not detected in the case of ilmenite-type $NaNbO_3$, so that there seems to be no disorder state as in $MnTiO_3$ and $MnSnO_3$.

In the next step, the mechanism of phase transition of ilmenite-type $NaNbO_3$ with disordered Na^+ ions to a perovskite-type structure is discussed compared to that of ilmenite-type $LiNbO_3$ to the $LiNbO_3$ type. Ilmenite-type $LiNbO_3$ and $NaNbO_3$ undergo phase transitions to $LiNbO_3$-type and perovskite-type structures respectively, the stable phases for each, in exothermic reactions near 500°C. In the pattern of powder X-ray diffraction with ilmenite-type $NaNbO_3$ after heating to 490°C and then cooling, the ilmenite type coexists with the perovskite type, but the peaks of both phases are sharp, indicating high crystallinity. Also, in the case of ilmenite-type $LiNbO_3$, the changes of diffraction peaks before and after phase transition are almost the same. This suggests that both ilmenite-type compounds undergo phase transition to the stable phases without passing through an amorphous state.

The ilmenite- and $LiNbO_3$-type structures adopt the same hexagonal closest packing of oxygens, only with a different arrangement of cations. Consequently, the structural change of $LiNbO_3$ from the ilmenite type to the $LiNbO_3$ type is achieved by half of Li^+ and Nb^{5+} exchanging their sites as shown in **Fig.7**. Also, in the disorder transition of cations at high temperatures and pressures as in $MnTiO_3$ or $MnSnO_3$ above as well as that of cations on phase transition from a wolframite type structure to the α-PbO_2 type structure at high temperatures as in $FeNbO_4$,[9] a site exchange occurs between cations of different types. The ionic radii of the cations for exchange are almost equal among these compounds. The six-coordinated ionic radii of Li^+ and Nb^{5+} ions given by Shannon[10] are as close as 0.76 and 0.64Å, so that $LiNbO_3$ also seems to undergo a similar site exchange between the ions of different kinds, leading to the phase transition from a ilmenite type to the $LiNbO_3$ type.

On the other hand, the structural change of $NaNbO_3$ from an ilmenite type to a perovskite type cannot be explained by the site exchange of cations of two types only as in $LiNbO_3$, since the structures have different oxygen packing. As shown in **Fig.8**, in ilmenite and perovskite types, first the height of Nb atoms is different when projected in the direction of close packing, and moreover, the oxygen packing of the former is hexagonal close packing while that of the latter is cubic close packing including large cations. Consequently, the structural change from ilmenite to

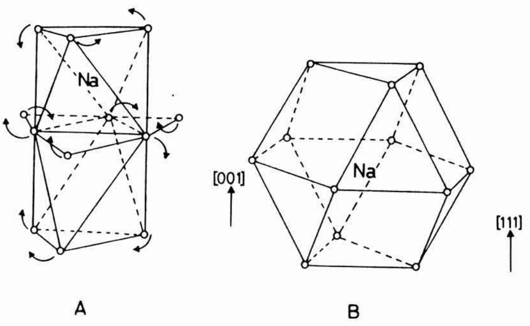

Fig. 9. Transformation of the coordination of the Na^+ ion. (A) octahedral coordination of the $LiNbO_3$ type and (B) 12-fold coordination of the perovskite type.

perovskite types must be discussed in two different ways: the movement of Nb atoms to different oxygen intelayers (height change), and rotation around the axis of close packing to trigger a change from hexagonal to cubic close packing.

In the arrangement of Nb atoms in the direction of close packing, the $LiNbO_3$ type is similar to the perovskite type, and the movement of Nb atoms is considered to be the same as the change from the ilmenite type to the $LiNbO_3$ type. In the case of $NaNbO_3$, Na^+ ions are already in the disordered state at the temperature of phase transition to the perovskite type, and it is possible that an octahedron to be moved into by Nb atoms connected by face sharing is vacant. The possibility that such a movement of ions with relatively high valence occurs at even rather low temperatures has been reported in the case of deintercalation of $NaTiO_2$[11] or $LiVO_2$[12] having α-$NaFeO_2$ type structure. The change in $LiNbO_3$ requiring a similar movement of Nb atoms from the ilmenite type to $LiNbO_3$ type and that of $NaNbO_3$ from the ilmenite type to perovskite type, both occurring at almost the same temperature (500°C), suggest that the Nb atoms are not allowed to move until this temperature. This structure state similar to the $LiNbO_3$ type where Nb atoms moved was encountered transiently in the process of phase transition, and was not detected as an intermediate phase by X-ray diffraction. If it had stayed for a considerable period of time, the intensity of the 003 reflection should have greatly decreased as in the case of disorder phases such as $MnTiO_3$, $MnSnO_3$, $Na_{1-x}TiO_2$ and $Li_{1-x}VO_2$; in reality only ilmenite and perovskite phases were observed by X-ray analysis.

The generated structure similar to the $LiNbO_3$ type further changes into the perovskite type which is the most stable for this compound containing Na^+ ions larger than Li^+ ions, and the example of this structural change is a topotactic one when a perovskite-type $HNbO_3$ is formed by the acid treatment of $LiNbO_3$.[13] That is, perovskite-type structure is framed by a NbO_6 octahedra rotating by about 60 degrees around the c-axis of the $LiNbO_3$ type, and perovskite-type, 12-coordinated A site is formed from two $LiNbO_3$-type octahedra with face sharing as in **Fig.9**. The perovskite-type structure is completed when Na^+ ions arranged at random move to this site. The movement of Nb atoms in the c-axis direction as above changes the face sharing of the NbO_6 octahedra in the ilmenite-type structure into vertex sharing, which is considered to facilitate further rotation around the c-axis.

As stated above, in the structural change of $NaNbO_3$ from the ilmenite type to perovskite type, although occurring rather low temperatures, the generated perovskite-type phase exhibited high crystallinity, which seemed to indicate a topotactic structural change. Nevertheless, the process could be explained without difficulty by combining topotactic structural changes at low temperatures encountered so far in compounds with similar structures.

5. Conclusions

Lattice constants and ionic conductivity at high temperatures were measured to examine the endothermic phase transition near 290°C of ilmenite-type $NaNbO_3$. As a result, changes were detected in the vicinity of the phase transition temperature, indicating that Na^+ ions are liable to move at that temperature. The refinement of crystal structures was conducted by powder X-ray diffraction at high temperatures using a Rietveld method, and this process proved to be an order-disorder transition in which Na^+ ions move from the original octahedral sites to vacant octahedral sites sharing faces in the c-axis direction and shift to a disordered state. The measurements of the latent heat of phase transition also confirmed the theory. The probable explanation for phase transition from ilmenite- to perovskite-type structures is a mechanism by way of the $LiNbO_3$-type rearrangement of Nb^{5+} ions.

References:

1) N. Kinomura, N. Kumada and F. Muto, Mater. Res. Bull. 19, 299-304 (1984).
2) N. Kumada, N. Ozawa, F. Muto and N. Kinomura, J. Solid State Chem., 57, 267-8 (1985).
3) N. Kumada, N. Kinomura, and F. Muto, Seramikkusu Ronbun-shi, (in press).
4) J. Liebertz and C.J. Rooymans, Z. Phys. Chem. Neue Folge, 44, 242-9 (1965).
5) F. Izumi, Kobutsugaku Zasshi, 17, 37-50 (1985).
6) R.A. Young D.B. Wills, J. Appl. Cryst. 15, 430-8 (1982).
7) Y. Syono, S. Akimoto, Y. Ishikawa and Y. Endoh, J. Phys. Chem. Solids, 30, 1665-72 (1969).
8) Y. Syono, H. Sawamoto and S. Akimoto, Solid State Commun., 7, 713-6 (1969).
9) R.S. Roth and J.L. Waring, Am. Mieral., 49, 242-6 (1964).
10) R.D. Shannon, Acta Cryst., A32, 751-67, (1976).
11) A. Maaza, C. Delmas and P. Hagenmuller, J. Inclusion Phenom., 1, 45-51 (1983).
12) L.A. de Picciotto, M.M. Thackeray, W.I.F. David, P.G. Bruce and J.B. Goodenough, Mater. Res. Bull., 19, 1497-506 (1984).
13) C.E. Rice and J.K. Jackel, J. Solid State Chem., 41, 308-14 (1982).

This article is a full translation of the article which appeared in Nippon Seramikkusu Kyokai Gakujutsu ronbunshi (Japanese version), Vol.98, No.6, 1990.

Fabrication and Microstructure of Porous Hexaaluminate Ceramics

Masato Machida, Masaki Sirouzu*, Koichi Eguchi and Hiromichi Arai

Department of Materials Science and Technology, Graduate School of Engineering Sciences, Kyushu University
6-1 Kasuga-koen, Kasuga-shi 816, Japan
*Tokuyama Soda Co., Ltd., Technical Development Laboratory
1-1 Mikage-cho, Tokuyama-shi 745, Japan

Heat-resistant porous ceramics were fabricated by sintering of sol gel-derived hexaaluminate fine powders at 1200-1600°C. Although the sintered samples showed high porosities (ca. 50%), the N_2 permeability is low because of small pore size (< 100nm). The packing of planar particles of hexaaluminate formed two kinds of peaks in their pore size distribution at < 10nm and 100nm. Second-stage sintering of the crushed powders significantly enhanced the N_2 permeability. In the samples after second-stage sintering, the loose packing of large agglomerates formed macro-pores (10μm) besides the voids of primary particles. These macropores are effective for high gas permeation. Consequently, the second-step sintering of hexaaluminate attains the mixed structure of micropores and macropores, which is a possible microstructure for application to filtration catalysts.

[Received November 17, 1989; Accepted February 13, 1990]

Key-words: Hexaaluminate, Porous Ceramics, Gas Permeation, Sintering

1. Introduction

Porous ceramic materials have wide applications in filters for filtration and separation processes.[1,2] More recently, simultaneous separation and catalytic functions have been required for membrane-type catalysts and diesel particulate purification catalysts.[3,4] To develop functional materials for specific purposes, it is necessary to precisely control the physicochemical properties, including pore characteristics (size, shape and distribution) and surface characteristics (catalytic properties and surface modification). In addition, they should have high heat resistance.

The authors have attempted to use heat-resistant, ultrafine particles of hexaaluminate compounds for combustion catalysts.[5-9] Hexaaluminate powders are (1) very difficult to sinter,[5,6] and hence suitable as starting materials for heat-resistant, microporous ceramics, and (2) are capable of high catalytic activities, when the Al sites in the lattices are partially substituted by a transition element.[8,9] These characteristics make them desirable materials for heat-resistant filter catalysts.

However, preparation of porous ceramics from ultrafine hexaaluminate particles and controling their pore characteristics have been little investigated, because these particles are very difficult to sinter.

In this study the authors investigated, as part of basic research on the application of hexaaluminate compounds to filter materials, the effects of preparation conditions on the microstructure. Of particular interest for clarifying the relationship between the microstructures and gas permeability were the effects of calcination and sintering temperature, pore size of the starting materials, and secondary sintering, which were studied in order to improve the gas permeability of these materials.

2. Experimental Procedure

2-1. Preparation of Powdered Hexaaluminate

Hexaaluminates ($BaAl_{12}O_{19}$ and $BaMnAl_{11}O_{19-\alpha}$) were prepared by the hydrolysis of metal alkoxides.[8] The required quantities of metallic barium and aluminum isopropoxide ($Al(OC_3H_7)_3$) were mixed with 2-propanol at 80°C for 3h with stirring. Hydrolysis was performed by intrtoducing distilled water or an aqueous solution of manganese nitrate ($Mn(NO_3)_2 \cdot 6H_2O$) into the alcohol solution.. The resultant gel was dried, thermally decomposed and calcined at 1200° to 1600°C. The product was confirmed to be hexaaluminate by a powder X-ray diffractometer (Rigaku Denki 4011).

2-2 .Preparation of Porous Ceramics

The hexaaluminate powder which was pressed into a disk was sintered at 1200°C to 1600°C for 5h (primary sintering). The sintered ceramics were crushed, and the particles thus obtained were classified into 3 groups by size, 44μm and below, 45 to 74μm, and 75μm and above. Each powder was presented into a disk, after a given quantity of liquid paraffin was added, and sintered again at 1450°or 1600°C (secondary sintering).

2-3. Gas Permeability and Microstructure Measurement

The dimensions and weight of each sintered sample was measured to determine the apparent density. The Archimedean method was used to determine the true density. The pore size distribution was determined by nitrogen adsorption and mercury porosimeter (Carlo Erba 2000), and the gas permeability by a flow system with nitrogen at room temperature and a differential pressure in the range from 100 to 400mm H_2O. The following equation was used to find the nitrogen gas permeability:

$$Q = K \cdot \Delta p \cdot S/l$$

where, Q: flow rate of permeated gas (mol/sec), K: permeability of gas ($mol \cdot m \cdot sec^{-1}m^{-2}Pa^{-1}$), Δp: differential pressure (Pa), S: sample surface area (m^2), l: sample thickness (m).

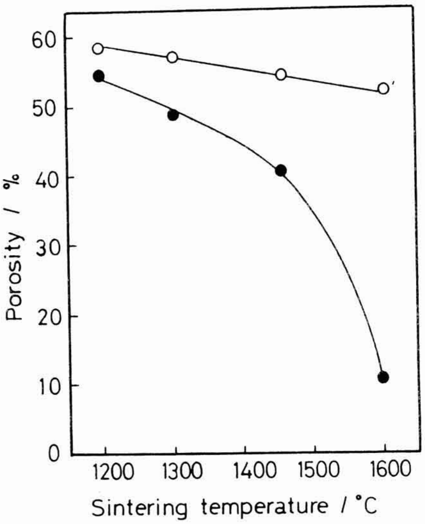

Fig. 1. The porosity of hexaaluminate sintered at elevated temperatures. Powders were calcined at 1300°C prior to sintering.
○ $BaAl_{12}O_{19}$, ● $BaMnAl_{11}O_{19-\alpha}$

The microstructures were observed with a scanning electron microscope (SEM, JOEL, JSM-T330A, JSM-840F), and a transmission electron microscope (TEM, JOEL, JEM-200CX). The samples for TEM analysis were prepared by ion thinning (JOEL, JIT-100).

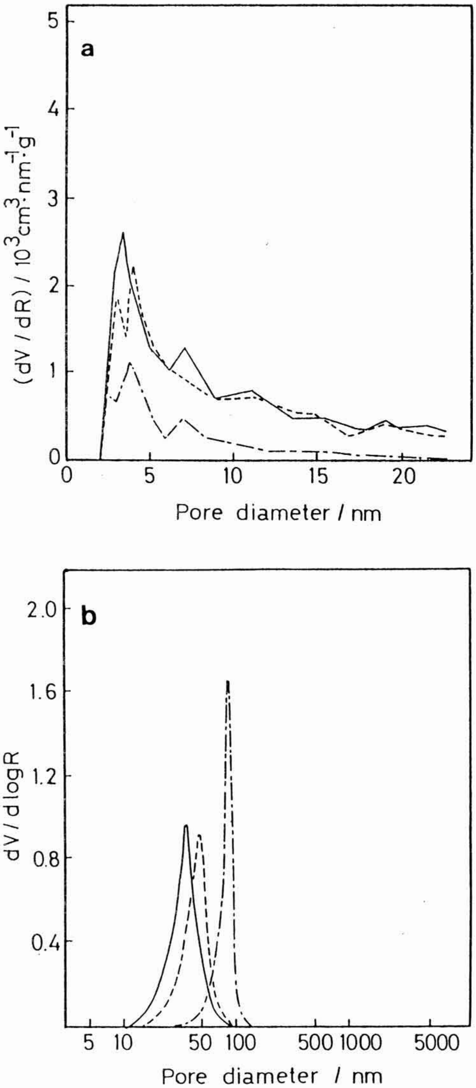

Fig. 2. Pore size distribution of $BaMnAl_{11}O_{19-\alpha}$ sintered at elevated temperatures measured by a) volumetric nitrogen adsorption and b) porosimeter.
—— 1200°C ...... 1300°C -·—·1450°C

3. Results and Discussion

3-1. Microstructures and Porosity of Sintered Hexaaluminate

The effects of sintering temperature on the porosity of $BaAl_{12}O_{19}$ and $BaMnAl_{11}O_{19-\alpha}$ were investigated. The Mn substituted in the hexaaluminate lattice acted as a active catalytic component. **Figure 1** shows the effects of sintering temperature on porosity of sintered hexaaluminates.The porosity decreased with increase in temperature. The porosity of $BaAl_{12}O_{19}$ was relatively insensitive to temperature, retaining a porosity of 50% or more, even when sintered at 1600°C. On the other hand, the porosity of $BaMnAl_{11}O_{19-\alpha}$ decreased more rapidly, when sintered before 1450°C or more, indicating that densification proceeded drastically by sintering. The difference in sinterability between these samples resulted from the lowering in melting point of $BaAl_{12}O_{19}$ from 1915°C, due to partial substitution with Mn. The pore size distributions of the hexaaluminate samples were characterized by two peaks at diameters of 10nm or less (**Fig.2a**) and 30 to 100nm (**Fig.2b**), except for the sample sintered below 1600°C, which had no peak and smaller microstructures, as a result of rapid sintering. For the samples sintered at 1450°C, micropores of several tens of nm increased in size from 40 to 90nm as the sintering temperature increased, while micropores of several nm remained essentially unchanged in size, irrespective of the sintering temperature. The total volume of these two types of micropores corresponded to the pore volume estimated by porosity, indicating that these pores accounted for essentially all of the pores present in the sinters and there were few macroscopic, secondary pores.

Figure 3 presents the SEM images of the fracture surfaces of the sintered $BaMnAl_{11}O_{19-\alpha}$ samples. The sample sintered at 1300°C had primary grains of 0.1 to 0.2μm dis-

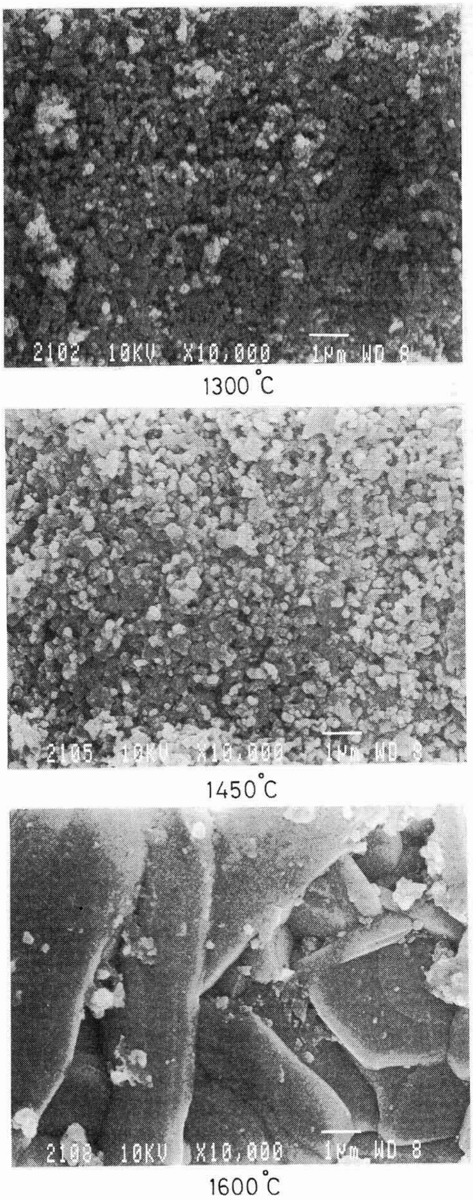

Fig. 3. SEM images of BaMnAl$_{11}$O$_{19-\alpha}$ sintered at elevated temperatures. Powders were calcined at 1300°C prior to sintering.

tributed evenly in the sintered body, and pores were formed as voids of these grains. Increasing the sintering temperature to 1450°C caused the grains to grow to 0.5 to 1μm in size, and the necks also grew as a result of the sintering of the grains. Increasing the temperature further to 1600°C accelerated sintering so that the hexaaluminate samples prepared by the sol-gel process consisted of thin plate-like microcrystals with orientation along the (001)plane.[8]

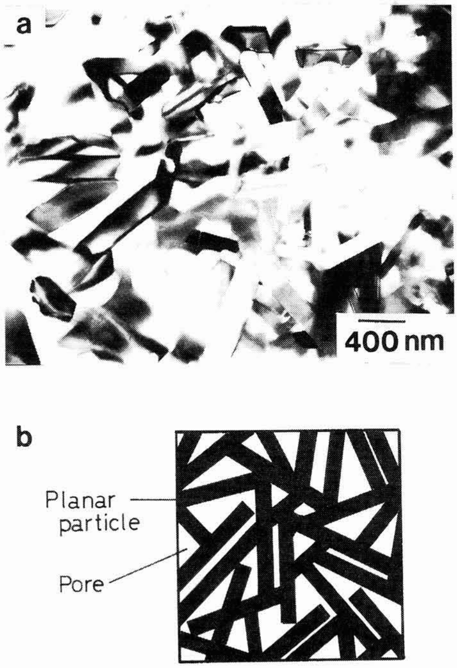

Fig. 4. a) TEM image of BaMnAl$_{11}$O$_{19-\alpha}$ sintered at 1450°C.
b) Schematic pore structure of sintered hexa-aluminate. hexaaluminate.

Uniformly sized, plate-like grains of 100nm thickness were observed in the sample prepared at 1450°C, as revealed by TEM observation (**Fig.4a**). Rod-shaped grains appeared in the photograph, because many of the bottom faces of the plate-like grains were oriented at right angles to the fractured faces. The grains contacted each other at the sides and bottoms, causing neck growth. For this reason, the sintered hexaaluminate sample had micropores in the voids, which were formed when the plate-like grains were placed one on another, as shown in the model (**Fig.4b**). These pores had sizes almost corresponding to the peak sizes (10nm or less, and several tens of nm) observed in the pore size distribution analysis (Fig.2).

3-2. Effects of Primary Grain Size on Porosity of Ceramics

Figure 5 shows the effects of calcination temperature on porosity and nitrogen gas permeation of the BaMnAl$_{11}$O$_{19-\alpha}$ powders, calcined at various temperatures and sintered at 1450°C. Both porosity and N_2 permeation increased as the calcination temperature increased up to 1450°C. The pore size of the sintered samples, on the other hand, increased and the distribution became broader as the calcination temperature increased (**Fig.6**). The observed increase in pore size, contributed little to gas permeation, and the porosity (total pore volume) is considered to be a more important factor.

Figure 7 presents the SEM images of the BaMnAl$_{11}$O$_{19-\alpha}$ powders calcined at various temperatures. Almost all of the primary grains grew to 1μm or more in the sample

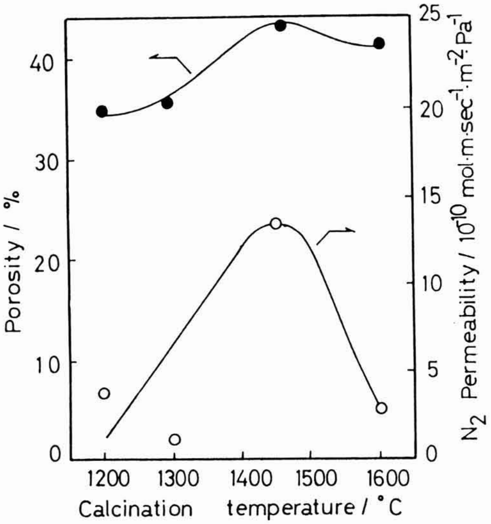

Fig. 5. Effect of calcination temperature of powders on the porosity and N_2 permeation of $BaMnAl_{11}O_{19-\alpha}$ sintered at 1450°C.
● Porosity ○ Permeability

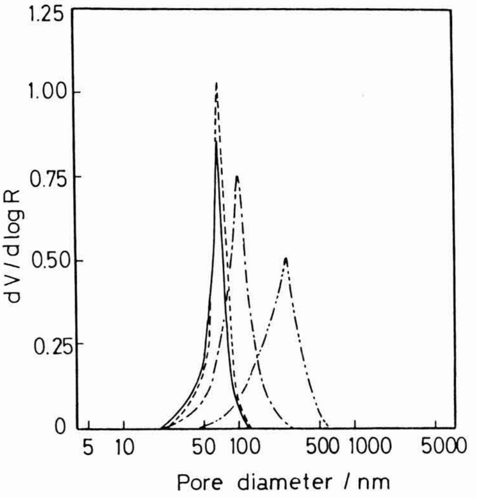

Fig. 6. Effect of calcination temperature of powders on the pore size distribution of $BaMnAl_{11}O_{19-\alpha}$ sintered at 1450°C.
—— 1200°C ...... 1300°C —·— 1450°C —··—1600°C

calcined at 1600°C. The sinter from this powder, therefore, had a broader grain size distribution, increased density, and thus decreased pore volume. This seems to be a reason why the nitrogen permeation in the sample from the powder calcined at 1600°C decreased in spite of having the largest pore size among the samples prepared in this study.

These results indicated that the gas permeation characteristics of the porous body of sintered hexaaluminate were closely related to the pore volume. The primary pores in the sintered hexaaluminate samples were considered to be mostly continuous, because they were formed as voids of the plate-like grains, as discussed in Fig.4. Many of these pores were so small (0.1μm or less) that it was very difficult to drastically increase the permeation rate by controlling the pore volume because the Knudsen diffusion is dominant in these micropores. It was essential to provide secondary macropores of 10μm or larger to improve the permeation properties.

3-3. Preparation of Porous of Hexaaluminate Ceramics by Secondary Sintering

The primary sintered hexaaluminate was sintered again (secondary sintering), after crushing and granulating to improve the gas the permeation characteristics by producing macropores of ca.10μm. **Table 1** summarizes the effects of grain size of the primary sintered $BaMnAl_{11}O_{19-\alpha}$ samples on porosity and nitrogen permeability of the secondary-sintered samples. The secondary-sintered sample showed 2 to 3 orders higher gas permeability than the primary-sintered sample. Both the porosity and gas permeability of the secondary-sintered samples increased as the grain size

Table 1. Effect of grain size regulation on porosity and N_2 permeability of $BaMnAl_{11}O_{19-\alpha}$ after second-stage sintering at 1600°C.

	1450 °C a)		1600 °C a)	
grain size /μm	porosity /%	N_2 permeability /mol·m·sec^{-1}·m^{-2}Pa^{-1}	porosity /%	N_2 permeability /mol·m·sec^{-1}·m^{-2}Pa^{-1}
<44	50.4	5.12 X 10^{-8}	39.7	1.41 X 10^{-7}
45-74	45.4	0.91 X 10^{-8}	43.1	9.04 X 10^{-7}
75-149	44.1	2.59 X 10^{-8}	43.9	15.00 X 10^{-7}

a) First-stage and second-stage sintering temperature.

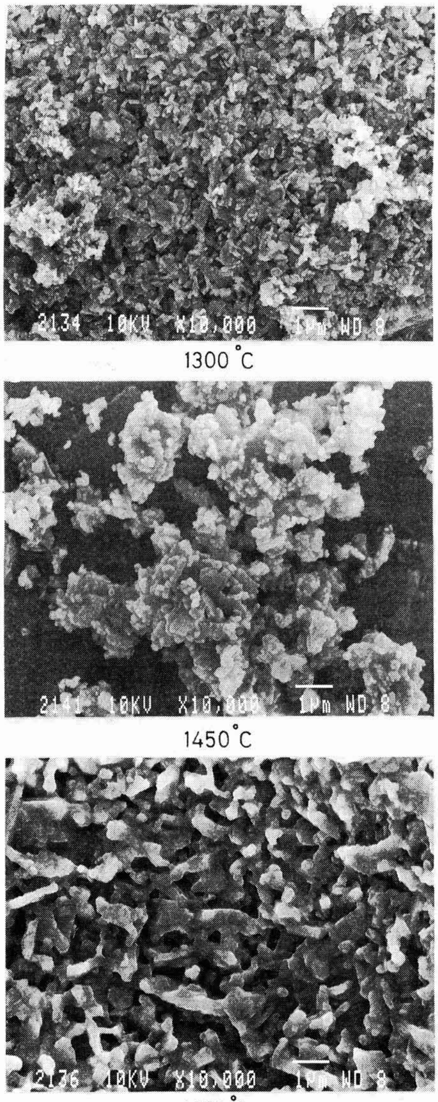

1300 °C

1450 °C

1600 °C

Fig. 7. SEM images of the $BaMnAl_{11}O_{19-\alpha}$ powders calcined at elevated temperatures.

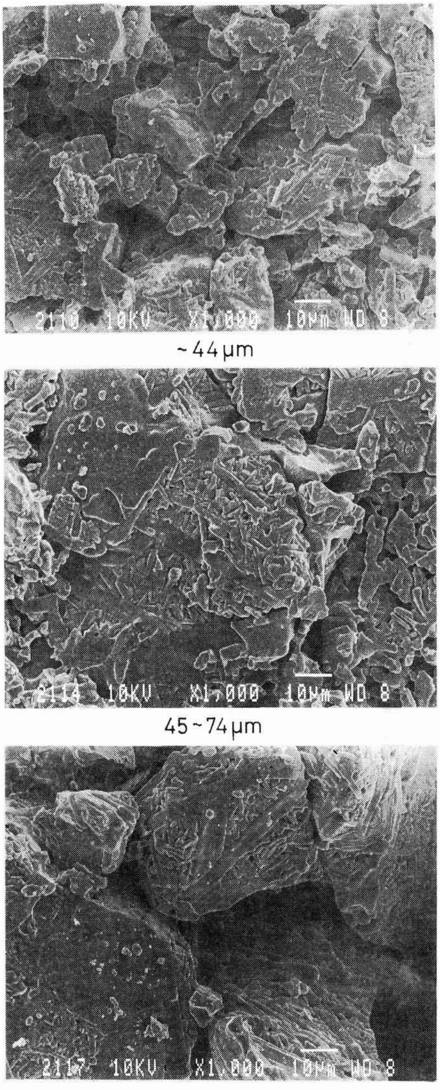

~44 μm

45~74 μm

75~149 μm

Fig. 8. SEM images of $BaMnAl_{11}O_{19-\alpha}$ after second-stage sintering.
First-stage sintering : 1600°C
Grain size regulation : 44μm, 45-74μm, 75-149μm
Second-stage sintering : 1600°C

of the crushed primary-sintered sample increased, for those primary and secondary samples sintered at 1600°C. **Figure 8** shows the SEM images of the sample secondary-sintered at 1600°C, indicating that the sample consisted of secondary grains of several tens μm. Increasing the size of the grains produced larger macropores that provided paths for gas molecules. For the sample secondary-sintered at 1450°C, on the other hand, the effects of grain size of the primary-sintered sample on porosity and gas permeability were less conspicuous, partly because the $BaMnAl_{11}O_{19-\alpha}$ sample was not adequately sintered at 1450°C. The submicron primary grains were weakly bonded to each other and no secondary grains of several tens μm size were found. These results indicated that the weakly agglomerated grains during the primary sintering step collapsed due to rearrangement of particles and neck growth during the secondary sintering step. As a result, the effects of primary sintering were not sufficiently developed.

Figures 9 and **10** show the effects of primary sintering temperature on the porosity and nitrogen gas permeability, respectively, of the secondary-sintered samples from the

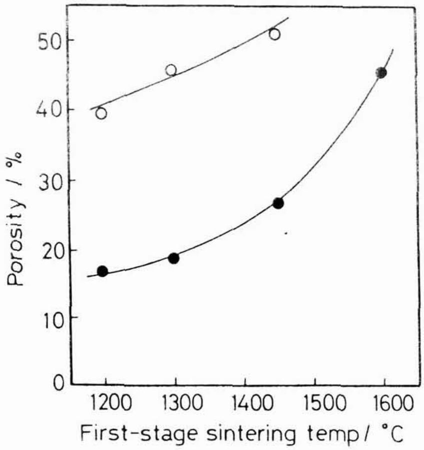

Fig. 9. Porosity of $BaMnAl_{11}O_{19-\alpha}$ after second-stage sintering. Grain size was regulated to 45-75μm after first-stage sintering.

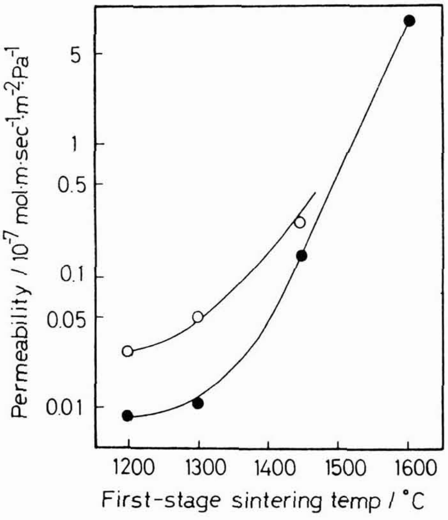

Fig. 10. Nitrogen permeability of $BaMnAl_{11}O_{19-\alpha}$ after second-stage sintering. Grain size was regulated to 45-75μm after first-stage sintering.
○ 1450°C ● 1600°C

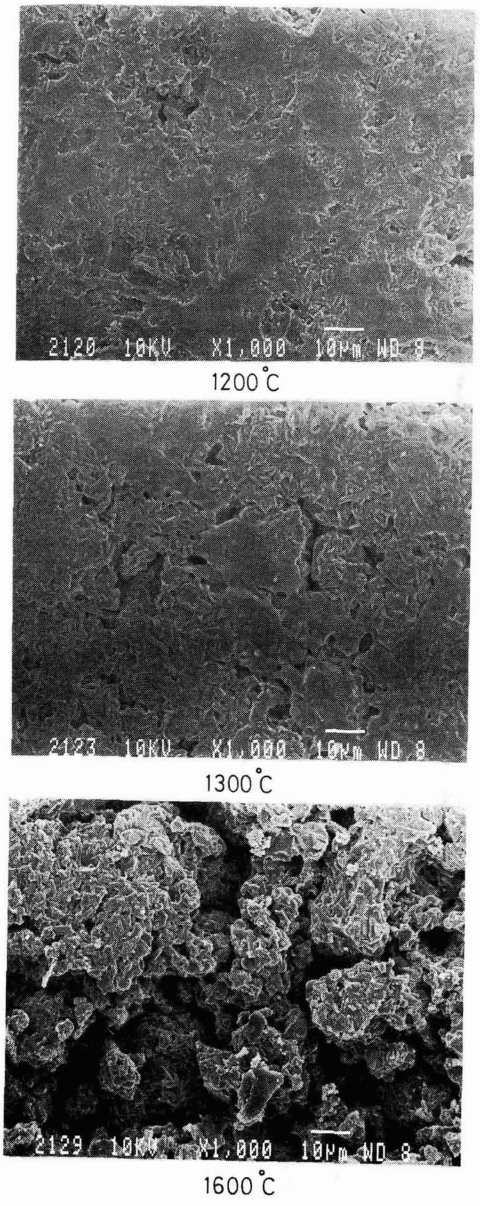

Fig. 11. The effect of the first-stage sintering temperature on the microstructure of $BaMnAl_{11}O_{19-\alpha}$ after second-stage sintering at 1600°C.
Grain size was regulated to 45-75 μm after first-stage sintering.

powder of 45 to 74μm. **Figure 11** shows their SEM photos of these hexaaluminate ceramics. The porosity of the samples secondary-sintered at 1450°C and 1600°C increased as the primary sintering temperature increased. The SEM analysis of the samples sintered at 1200°C and 1300°C during the primary sintering step also revealed that there were micropores of several μm, but no macropores larger than 10μm or secondary grains of 45 to 74μm. As discussed earlier, in the primary sintering at lower temperature were formed samples consisting of weakly agglomerated grains, and the secondary macropores as well as the primary micropores of several μm disappeared in the second-stage sintering process.

The sintered samples with high gas permeation, on the other hand, had macropores of about 10μm between the porous secondary grains of several tens μm formed by the sintering of the primary grains, to provide paths for gas permeation.. Thus, the secondary-sintered of hexaaluminate is mainly characterized by coexistence of micropores (several μm)and macropores (several ten μm).

For a porous filter to have a catalytic function, it is necessary to form macropores for gas permeation and micropores where the catalytic reaction takes place. The porous body of hexaaluminate can have two types of pores, when sintered at 1400°C or higher. Sintered $BaMnAl_{11}O_{19-\alpha}$ itself is a catalyst, and has the potential for a heat-resistant filter catalyst or other functional material, when sintered at the optimum conditions for gas permeation and catalytic characteristics.

4. Conclusions

Ceramic porous bodies of hexaaluminate micrograins were investigated to identify microstructures and the effects of preparation conditions on their gas permeation characteristics.

1) Primary sintered hexaaluminate micrograins consist of plate-like grains randomly placed one on another, with micropores of several nm to several tens of nm between the grains formed when the necks are grown.

2) Gas permeability of the primary sintered hexaaluminate depends on the total pore volume.

3) Sintering the primary sintered sample, after crushing, forms macropores of 10μm or larger, which drastically increase the gas permeability.

4) The secondary-sintered hexaaluminate samples have both micropores and macropores. These microstructurers are quite useful for catalytic filters.

References:

1) T. Hioki, Seramikkusu, 20, 168 (1985).
2) S. Sakka, ibid., 23, 702 (1988).
3) T. Shirota, Shokubai, 29, 646 (1987).
4) J. Abthoff, H.D. Shuster, H.J. Langer, G. Loose, SAE paper, No.850015, 1985.
5) M. Machida, K. Eguchi, and H. Arai, J. Catal., 103, 385 (1987).
6) M. Machida, K. Eguchi, and H. Arai, Bull. Chem. Soc. Jpn., 61, 3659 (1988).
7) M. Machida, K. Eguchi, and H. Arai, J. Am. Ceram. Soc., 71, 1142 (1988).
8) M. Machida, K. Eguchi, and H. Arai, Chem. Lett., 1988, 1461 (1988).
9) M. Machida, K. Eguchi, and H. Arai, Chem. Lett., 1987, 767 (1987).

This article is a full translation of the article which appeared in Nippon Seramikkusu Kyokai Gakujutsu Ronbunshi (Japanese version), Vol.98, No.6, 1990.

Microstructure and Thermal Conductivity of Thermal Barrier Coating

Yoshiyasu Ito, Yutaka Ishiwata and Hideo Kashiwaya

Toshiba Corporation, Heavy Apparatus Engineering Laboratory
2-4 Suehiro-cho, Tsurumi-ku, Yokohama-shi 320, Japan

The microstructure of plasma sprayed coating of zirconia stabilized with 8wt.% of yttria was analysed by the electrochemical technique. Porosity of 15.9% was mostly opened pores which consisted of cracks by cooling and the incomplete bonding of sprayed particles. The thermal properties of plasma sprayed coating of zirconia and NiCrAlY were studied by a laser flash method. The thermal conductivities measured were related to the microcracked structures described above. Also, thermal conductivities of the two-layer composites (the plasma sprayed coatings) were determined by the laser flash method using Bulmer's technique. The thermal contact resistance at the zirconia/SUS304 interface showed a large amounts of scatter without NiCrAlY bond coating. This tendency was observed in the bonding strength of sprayed coatings. Namely, a better correlation between the thermal contact resistance and the bonding strength is obtainable.

[Received December 11, 1989; Accepted March 12, 1990]

Key-words: Thermal barrier coating, Microstructure, Plasma sprayed coating, Thermal properties, Bonding strength, Stabilized zirconia, NiCrAlY bond coating

1. Introduction

Production equipment conventionally used under severe working conditions such as high temperature, high pressure and corrosive atmospheres has recently been required to operate under even more severe conditions, at which metal materials are close to the limit of their characteristics, in order to further improve the efficiency of production processes, and equipment is being developed for such specifications. Since ceramics generally have various superior properties such as heat, corrosion and abrasion resistance, the commercial application of ceramics in the form of a coating on the surface of metal parts is rapidly increasing. Ceramics coatings applied by the plasma spraying technique have proved useful as thermal barrier coatings on various types of equipment for high temperature service, including the typical example of the gas turbine, so this coating process is one of the processes most often used. Zirconia (ZrO_2) is frequently used as the material for the thermal barrier coating mentioned above. However, the microstructures and characteristics of zirconia ceramics as coatings differ considerably from those of zirconia in bulk. For instance, zirconia coatings contain a lot of pores and microcracks (defects),[1,2] and the crystalline phases in zirconia coatings consist of a mixture of cubic and tetragonal phases as shown by X-ray diffraction analysis,[1,3] laser Raman spectroscopy,[4] and neutron diffraction analysis.[5] The thermal conductivity and linear thermal expansion coefficient of plasma sprayed zirconia coating have been investigated.[6,7,8] However, these investigations were carried out on the sprayed coating itself, but not the characteristics of the composite body of a sprayed ceramics coating on a substrate (composite layer structure), except in a few cases.

Consequently, the authors intended in the present study to clarify the microstructure of the plasma sprayed ZrO_2 coating, and to investigate the thermal conductivity of this sprayed coating with special attention to the interface between the substrate and ceramic coating.

2. Experimental Procedure

The samples used in the experiments were prepared by the plasma spraying technique. ZrO_2 powders stabilized with 8wt% Y_2O_3 in particle sizes of 10 to 44μm were sprayed and NiCrAlY alloy powders with particle sizes of 10 to 44μm were used as bond coating material. **Table 1** shows the chemical compositions of the materials. To prepare a test sample, the surface of a disk-shaped metal substrate of 10mm diameter and 1.5mm thickness was cleaned of grease, roughened with white alundum (WA#54),

Table 1.Chemical compositions of powders used for spraying.

Materials	Chemical compositions					
NiCrAlY (wt %)	Ni	Cr	Al	Y	Fe	Si
	Bal.	22.43	10.70	1.06	0.074	0.071
8%Y_2O_3-ZrO_2 (wt %)	ZrO_2	Y_2O_3	TiO_2	SiO_2	Fe_2O_3	CaO
	Bal.	7.9	0.18	0.14	0.08	0.06

Table 2. Chemical compositions of substrate.

Material	Chemical compositions (wt%)						
	C	Si	Mn	P	S	Ni	Cr
SUS304*	0.06	0.68	1.00	0.027	0.005	8.29	18.09

* S.S.T. (1120°C, 1.2 min. W.C.)

Table 3. Plasma spraying parameters.

Plasma gun	Metco 7M
Nozzle type	Metco GP
Current	750 A
Voltage	49 V
Spray distance	140 mm (NiCrAlY) 100 mm (ZrO_2)
Traverse speed	10 m/min.
Powder feed	30 g/min.
Primary gas	Argon
Secondary gas	Helium

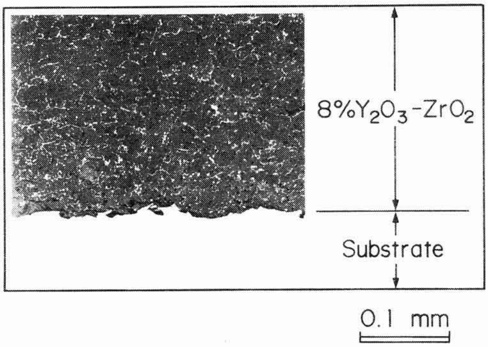

Fig. 1. Microphotograph of plasma sprayed coating.

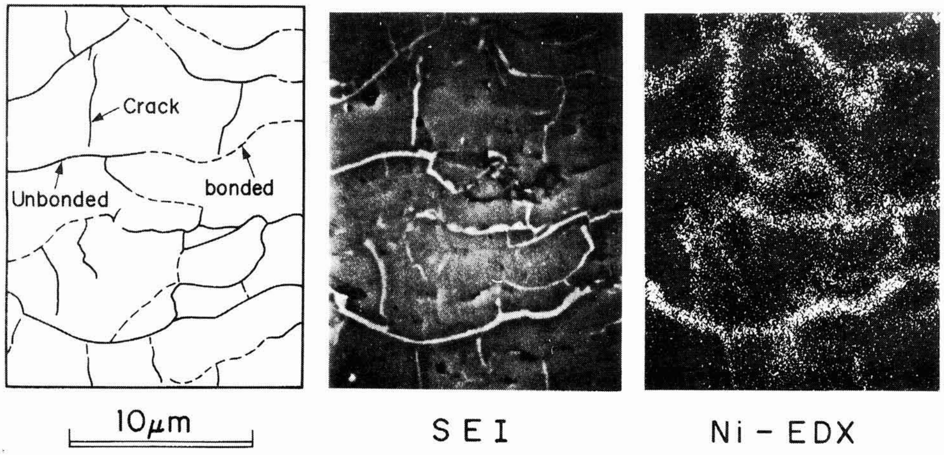

Fig. 2. Microstructure of plasma sprayed zirconia obtained by electrochemical technique.

and plasma-sprayed with the materials. The chemical compositions of the SUS304 substrate are shown in **Table 2**, and the plasma spraying parameters in **Table 3**. In order to investigate the effect of the bond coating on the thermal conductivity of the sprayed coating, a sample without bond coating and one with a bond coating of 100μm thickness were prepared. The ZrO_2 coating was applied in three different thicknesses of 250μm, 500μm and 1mm on the samples above, and these samples were used in the experiments.

To investigate the microstructure of the sprayed coating, the sample was electrochemically treated[9] and then the microstructure of the coating observed in a vertical section. The surface conditions of the coating were also observed using a SEM and the micropore distribution measured in the coating by the mercury adsorption technique, and the crystalline phases of ZrO_2 in the coating were observed by X-ray diffraction technique. A porosimeter (model 1-70, Carlo Erba Co.) was used for the mercury adsorption test, and an X-ray diffraction apparatus (PW 1710-1729, Phillip Co.) with a Cu source (source voltage-current: 40kV-20mA) was used for the X-ray diffraction analysis. A thermo-constant measurement apparatus (TC-3000, Shinkuu-Rikoh Co.) was used to measure the thermal conductivity and specific heat of the plasma sprayed ZrO_2 coating. This measurement was carried out in an Ar atmosphere in the range from room temperature to 1500K.

3. Microstructure of Thermal Barrier Coating

Figure 1 shows a typical photograph of the cross-sectional microstructure of plasma sprayed ZrO_2 coating, which was preliminarily electro-chemically treated (nickel plating), applied to a substrate. The photograph clearly shows that open pores in the coating were penetrated by Ni from

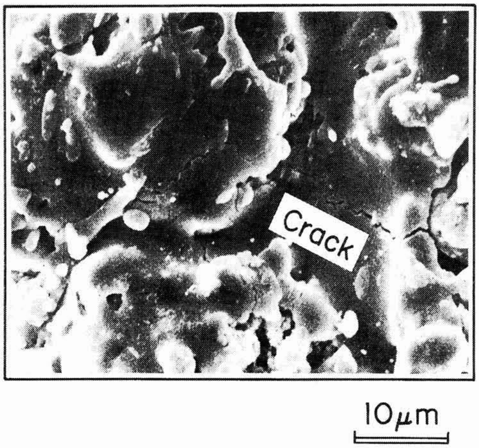

Fig. 3. Microcracks observed on the surface of zirconia coating.

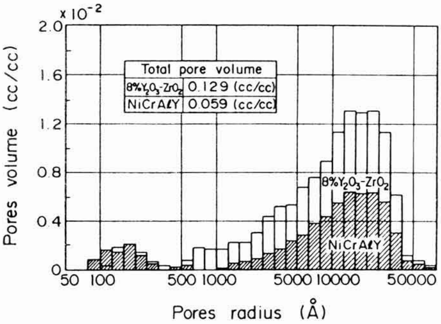

Fig. 4.Pore size distribution of sprayed coatings.

the substrate surface toward the coating surface, so the microstructure of the sprayed ZrO_2 coating is easier to observe with the application of Ni plating. The plasma sprayed ZrO_2 coating contains a lot of small defects which consist of narrow cracks. **Figure 2** shows these microcracks enlarged for more detailed observation. Because of the mechanism of formation of the plasma sprayed ceramic coating, the cracks observed were classified into two types, cracks generated parallel to the layer structure of the sprayed coating, and those generated perpendicular to the layers. The parallel cracks are those generated in areas where the fused ZrO_2 particles sprayed did not bond well with the previously formed ZrO_2 coating when deposited, so these cracks are better understood as defects caused by incomplete bonding, rather than as cracks in the ordinary sense. The perpendicular cracks are generated by thermal stress, and have shorter lengths and narrower widths, compared with the parallel cracks. The cracks in both parallel and perpendicular directions to the coating layer were also observed on the surface of the ZrO_2 coating, as shown in **Fig.3**. Presumably the thermal barrier coating of ZrO_2 ceramics is strongly resistant to deformation caused by thermal stress, etc., and is much more flexible compared to the bulk ceramic because of the presence of these fine cracks of two types. The presence of these cracks naturally acts to reduce the thermal conductivity of the sprayed ceramic coating. Figure 1 apparently indicates that Ni is almost uniformly distributed in the sprayed ZrO_2 coating from the surface of the SUS304 substrate to the surface of the ZrO_2 coating. This phenomenon suggests that almost all of the cracks in the plasma sprayed ZrO_2 coating are direct pores which pass through the surface of the ZrO_2 coating to the surface of the substrate.

The pore size distribution in the sprayed ZrO_2 coating was measured by the mercury adsorption method, and the results are shown in **Fig.4**. The same distribution was also measured in the sprayed NiCrAlY bond coating, and the results are given in Fig.4 for comparison. The figure shows that the porosity (pore volume) in the sprayed ZrO_2 coating is apparently higher than in the sprayed NiCrAlY coating. The porosities of the sprayed coatings measured by the mercury adsorption method agreed relatively well with those of 3.6% for the NiCrAlY coating and of 15.9% for the ZrO_2 coating measured by the water submersion technique using a sample retreated with paraffin. These results suggest that almost all of the pores in the plasma sprayed coatings are open pores.

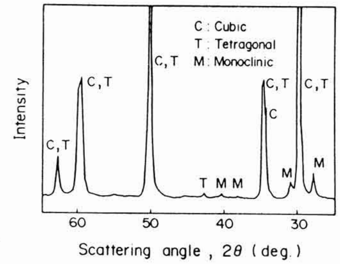

(a) Starting powder,

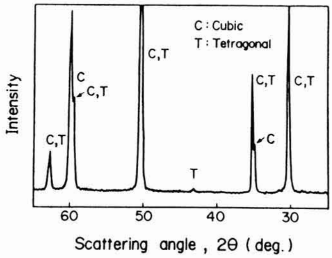

(b) Sprayed coating

Fig. 5. X-ray diffraction patterns of stabilized zirconia
(a) Starting powder, (b) Sprayed coating

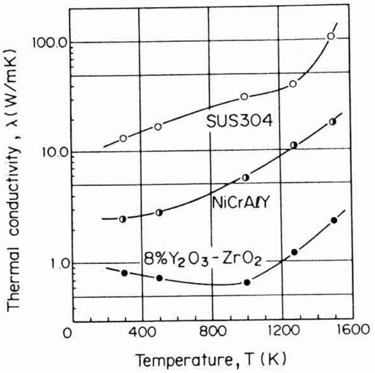

Fig. 6. Thermal conductivities of stabilized zirconia, NiCrAlY and SUS304.

The characteristics of plasma sprayed ceramics coating are due to the microstructure which contains a lot of crack shape defects, and the crystalline structure which results form the spray coating process as described below. The crystalline structure of ZrO_2 is monoclinic at room temperature, but is transformed to tetragonal in the temperature range from 1273 to 1373K, and further to cubic at around 2604K. The ZrO_2 powders stabilized with 8wt%Y_2O_3 used in the experiments were prepared by the fusion-and-pulverizing technique. The starting powder before plasma spraying consisted of a mixture of the monoclinic, tetragonal and cubic phases, as clearly shown in **Fig.5(a)** by X-ray diffraction analysis. Since the crystalline structure of the starting ZrO_2 powders strongly depends on the preparation process, it is reasonable that they should contain the monoclinic phase which is stable at low temperature. However, according to the results of X-ray diffraction analysis of the surface of the plasma sprayed ZrO_2 coating, as shown in **Fig.5(b)**, the crystalline structure consisted of a mixture of tetragonal and cubic phases, both of which are stable at high temperature, with no monoclinic phase. Presumably the crystalline phases stable at high temperature were detected at room temperature because of the rapid cooling of the material during the spray coating process.

4. Thermal Conductivity of Thermal Barrier Coated Parts

4-1. Thermal Conductivity of the Coating

The thermal conductivity of the plasma sprayed coating was measured by the laser flash method, and the results are given in **Fig.6**. Even a sintered bulk of ZrO_2 with a high density has a low thermal conductivity of about 2W/mK at room temperature. In the case of a plasma sprayed coating of ZrO_2 with a high porosity, the thermal conductivity was reduced still lower, as seen in Fig.6. A similar result was obtained for a sprayed coating of NiCrAlY alloy in that its thermal conductivity was lower than that of same alloy in the ordinary metallic state. It is assumed that this decrease in thermal conductivity was caused not only by the presence of pores in the plasma sprayed coating, but also by the partial oxidation of metal and the formation of a layer structure of oxidized metal during the spraying process. The thermal conductivity of SUS 304 which was used as the substrate is also shown in Fig.6 for comparison. None of these three materials shows a remarkable temperature dependence of thermal conductivity in the lower temperature

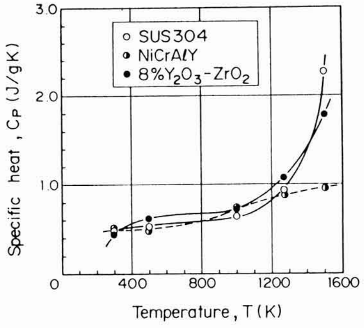

Fig. 7. Heat capacities of stabilized zirconia, NiCrAlY and SUS304.

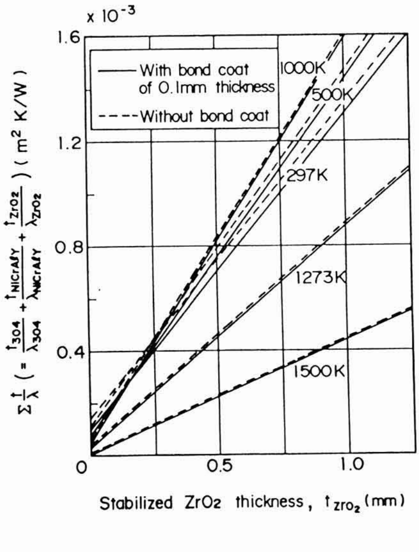

Fig. 8. Calculated heat resistance of plasma sprayed coatings

range below 1000°C, but thermal conductivities increased with increasing temperature at higher temperatures. The specific heats of these three materials were measured as shown in **Fig.7**. A remarkable temperature dependence of specific heat cannot be observed at temperatures lower than 1000°C, and there was no significant difference between them, but a trend of specific heat increases with increasing temperature in the range higher than 1000°C.

If the thermal conductivities of the various materials are obtained, the thermal conductivity characteristics of the composite materials with plasma-sprayed ceramic coating can be calculated by assuming one-dimensional steady thermal conduction through a multi-layer plate. In the case of a composite material with a plasma sprayed ZrO_2 coating applied on the top surface of SUS 304 substrate, the heat resistance was calculated using equation (1) given below, and the results are shown in **Fig.8**.

$$\sum \frac{t}{\lambda} = \frac{t_{304}}{\lambda_{304}} + \frac{t_{NiCrAlY}}{\lambda_{NiCrAlY}} + \frac{t_{ZrO_2}}{\lambda_{ZrO_2}} \quad \cdots\cdots\cdots \quad (1)$$

t_{304}, $t_{NiCrAlY}$ and t_{ZrO_2} are the thickness of the SUS 304 substrate, plasma sprayed coating of NiCrAlY, and plasma sprayed coating of ZrO_2, and λ_{304}, $\lambda_{NiCrAlY}$ and λ_{ZrO_2} are the thermal conductivities of the materials. Assuming the thickness of the SUS304 substrate to be 1.5mm and the thickness of the bond coating of NiCrAlY to be 0.1mm, we calculated the effect of the thickness of ZrO_2 coating on the heat resistance of the composite material was calculated as shown in Fig.8. It is clear from the figure that the presence of the NiCrAlY bond coating has only a relatively small effect on the heat resistance of the whole composite with the plasma sprayed ceramic coating.

4-2. Thermal Conducting Characteristics of Layer-Structured Composite

In this section, the calculated results for the heat resistance of the plasma sprayed coating composite given in Fig.8 are compared with the experimental results. Parker et al.[10] proposed the flash method, in which a sample with an even thickness is heated by a pulse on the upper surface, and the heat flow proceeds toward the lower surface. The thermal conductivity and specific heat of the sample are calculated from the rate of change of temperature with time at the lower surface when the whole sample is heated at a uniform temperature. This method is frequently used because of the simple procedure. However, the flash method of Parker et al. is based on thermal analysis of a single solid body sample of homogeneous quality, and does not hold when directly applied to layer-structured composite consisting of different kinds of materials. Some investigations[11,12,13] have been carried out on techniques for measuring the heat constant of layer-structured composites using the flash method.

The flash method was applied to the composite material of the thermal barrier coating in these experiments by adopting a technique proposed by Bulmer et al.[12] and the thermal conductivity of plasma sprayed ZrO_2 coating calculated. We adopted the measured values of thermal conductivity, specific heat, density and thickness of the SUS304 substrate, and those for the specific heat, density and thickness of plasma sprayed ZrO_2 coating, and in addition, measured the time required before the temperature at the lower surface of the thermal barrier coating composite reached a half of the maximum temperature when the upper surface of the composite was heated by the pulse. All of the measured values described above were introduced into a non-steady thermal analysis equation, obtaining the thermal conductivity of the plasma sprayed ZrO_2 coating.

Using the composite samples prepared by direct plasma spraying of ZrO_2 on a SUS304 substrate without bond coating, their heat resistances were measured, and the results in **Fig.9** were compared with the calculated results with the same samples given in Fig.8. It is seen that some of the measured values are rather higher than the calculated ones. Composite samples were prepared by plasma spraying of

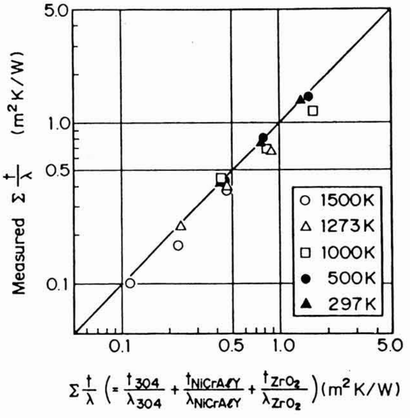

Fig. 9. Correlation between measured and calculated heat resistance without bond coating.

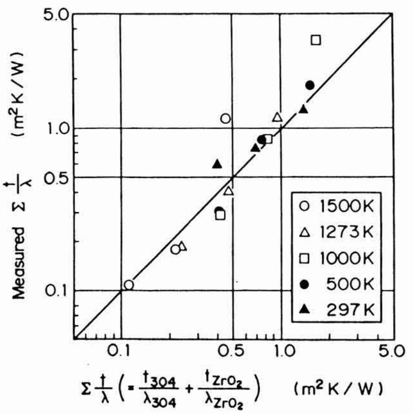

Fig. 10. Correlation between measured and calculated heat resistance with bond coating.

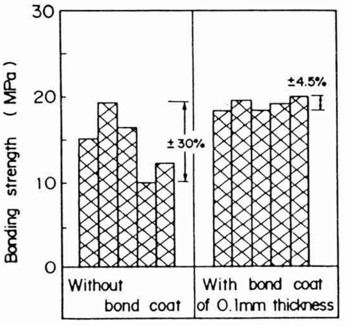

Fig. 11. Effect of bond coating on bonding strength.

NiCrAlY as a bond coating and ZrO_2 as a top coating on SUS304 substrate, and their heat resistances were measured, and the measured results were compared with the calculated ones in **Fig.10**. In the process of analyzing these experimental results, the presence of the intermediate layer of NiCrAlY can be neglected and the thermal conductivity based on the simple assumption of a two-layer structured composite was determined. . It is seen in Fig.10 that the measured values and the calculated ones agreed relatively well with each other. Presumably the measured heat resistance of the composite is higher than the calculated one in Fig.9 because of the thermal contact resistance at the interface between the substrate and the plasma sprayed ZrO_2 coating. Therefore, i t is assumed that when ZrO_2 is plasma-sprayed on a substrate without bond coating, the thermal contact resistance widely fluctuates, but then ZrO_2 is sprayed on a substrate with a bond coating of NiCrAlY, the thermal contact resistance at the interface is negligible.

5. Discussion

Bond coating is generally used to improve the bonding strength between the plasma sprayed coating and substrate. It is also used for the purpose of relaxing the thermal stress generated by different linear expansion coefficients of the top coating and substrate in the case of equipment for high temperature use, and for this purpose, a material having an intermediate linear expansion coefficient is used as the bond coating. The experimental results obtained in the preceding section proved that the bond coating effectively decreased the fluctuation as well as the value of the thermal contact resistance between the plasma sprayed ceramic coating and substrate. As a result of the above mentioned effects, the bond coating can relax the thermal stress at the interface between the sprayed ceramic coating and substrate. The value of the thermal contact resistance is assumed to be closely related with the bonding strength of the sprayed ceramic coating with the substrate.

The bonding strength between the sprayed ceramic coating and substrate was measured by the bonding test,[14] the results of which are shown in **Fig.11**. We prepared test samples having coating thicknesses of 100μm NiCrAlY bond coating and 300μm ZrO_2 top coating, and applied a pulling rate of 0.5mm/min in this bonding test. As is obvious in the figure, the samples with bond coating showed relatively stable bonding strength of around 20MPa, but those without bond coating had widely-fluctuating bonding strength, including a maximum strength of 20MPa and lower. It is assumed that when the thermal contact resistance is high, the contact area between the sprayed coating and substrate is small, so the bonding strength of the sprayed coating decreases since it mainly depends on the anchor effect between the coating and substrate. The authors previously proposed[15] a non-destructive detection technique for interface defects in ceramic coatings, in which infrared thermography was used to detect the thermal distribution generated when the coating was heated at the top surface. As the thermal contact resistance at the interface between the plasma sprayed ceramic coating and substrate is closely correlated with the bonding strength of the sprayed ceramic coating, as confirmed in the present experiment, it is possible that not only the isolation of sprayed ceramic coating from the substrate but also the bonding strength distribution of the sprayed ceramic coating can be determined by the infrared thermography analisis.

6. Conclusions

1) Plasma sprayed coatings of ZrO_2 stabilized with 8wt%Y_2O_3 and of NiCrAlY had porosities of 15.9% and 3.59%, and the pores were mostly open pores.

2) By observing plasma sprayed ZrO_2 coatings after electrochemical treatment, it was shown that the open pores in the sprayed ZrO_2 coating mostly corresponded to incompletely bonded areas in ZrO_2 particles sprayed and formed in a layer structure, or to the cracks generated during rapid cooling and solidification.

3) When ZrO_2 particles were spray-coated directly on the surface of the SUS304 substrate without bond coating, the thermal contact resistance at the interface between the substrate and ZrO_2 coating widely fluctuated. However, it was shown to become stable and to decrease by application of a bond coating of NiCrAlY prior to the ZrO_2 coating.

4) The thermal contact resistance at the interface between the SUS304 substrate and plasma sprayed ZrO_2 coating was found to be closely correlated with the bonding strength of the sprayed ZrO_2 coating. By application of a bond coating of NiCrAlY, the plasma sprayed ZrO_2 coating had a less variable and lower thermal contact resistance, and had a stable bonding strength value of around 20MPa.

References:

1) K. Shinohara, K. Nakagiri and H. Yoshioka, Bulletin of Engineering Department of Ehime University, 11-1, 397-403 (1980).
2) N. Kawamura, WELTEC, 6, 10-7 (1987).
3) H.A. Miller, R.G. Garlick, J.L. Smialek, Ceramic Bulletin, 62-12, 1355-1358 (1983).
4) N. Iwamoto, N. Umesaki, S. Endo, Thin Solid Films, 127, 129-137

(1985).

5) N.R. Shank, H. Herman, S.P. Singhal, C.C. Berndt, Thin Solid Films, 119, 159-171 (1984).
6) L. Pawlowski, D. Lombard, A. Mahlia, C. Martin, P. Fanchais, High Temperature – High Pressure, 16, 347-359 (1984).
7) P. Morrell, R. Taylor, High Temperatures – High Pressures, 17, 79-88 (1985).
8) L. Pawlowski, D. Lombard, P. Fauchais, J. Vac. Sci. Technol A3-6, 2494-2500 (1985).
9) Y. Arata, A. Oomori, R. Nagayama, H. Kawamura and C. Li, Japan Welding Society, Annual Proceedings Abstract, 40, 192-3 (1987).
10) W.J. Parker, R.J. Jenkins, C.P. Butler, G.L. Abbott, Journal of Applied Physics, 32-9 (1961) 1679-1684.
11) K.B. Larsen, K. Koyama, Journal of Applied Physics, 39-9 (1968) 4408-4416.
12) R.F. Bulmer, R. Taylor, High Temperature – High Pressures, 6 (1974) 491-497.
13) P. Morrell, R. Taylor, High Temperature – High Pressures, 17 (1985) 79-88.
14) ASTM Designation C633-69.
15) Y. Ito, M. Saito, H. Kashiwaya, M. Ohishi and T. Kaneko, Ceramics Society of Japan, Gakujutsu Ronbun-shi, 97-11, 1358-64 (1989).

This article is a full translation of the article which appeared in Nippon Seramikkusu Kyokai Gakujutsu Ronbunshi (Japanese version), Vol.98, No.6, 1990.

Preparation of $ZrSiO_4$ Powder Using Sol-Gel Process (1) – Influence of Starting Materials and Seeding –

Hidehiko Kobayashi, Toshiyuki Takano, Toshiyuki Mori,* Hiroshi Yamamura* and Takashi Mitamura

Department of Applied Chemistry, Faculty of Engineering, Saitama University,
255 Shimo-ohkubo, Urawa-shi 338, Japan
*, Advanced Materials Research Laboratory, TOSOH Co., Ltd.
2743-1 Hayakawa, Ayase-shi 252, Japan

The effect of temperature, heating rate and addition of $ZrSiO_4$ seed crystals on the preparation of $ZrSiO_4$ powders by the sol-gel process was studied using X-ray powder diffractometry. $ZrSiO_4$ powders have been prepared by different precursors in $Zr(OPr^i)_4$–Si $(OEt)_4$, $Zr(OPr^i)_4$-SiO_2 sol, $ZrOCl_2 \cdot 8H_2O$ -Si $(OET)_4$ and $ZrOCl_2 \cdot 8H_2O$ -SiO_2 sol groups. The formation rate of $ZrSiO_4$ was higher in Si $(OEt)_4$ than in SiO_2 sol. The formation rate was influenced by heating rate, and, in particular, increased remarkably below 2.5K/min. When a small amount of commercial $ZrSiO_4$ was added to the powder for precursor composition as seed crystals, $ZrSiO_4$ powder with a purity of 94 to 96% was formed at 1600°-1650°C. It was found that the addition of seeds results in lowering of the formation temperature of $ZrSiO_4$ by about 100°C. On the other hand, a $ZrSiO_4$ powder of 94 to 96wt% purity was obtained by heating the powder of precursor composition at 1300°C for 1h, followed by reheating at 1650°C for 1h. The results have suggested that the preparation of $ZrSiO_4$ powder of nearly single phase is possible using the sol-gel process by controlling the seedings and/or the two-stage heating.

[Received December 25, 1989; Accepted February 13, 1990]

Key-words: Preparation of $ZrSiO_4$, Sol-gel process, Two-stage heating, $ZrSiO_4$ seeding

1. Introduction

Zircon ($ZrSiO_4$) is a composite oxide of low thermal expansion coefficient and high resistance to thermal shocks, like mullite ($3Al_2O_3 \cdot SiO_2$). Somiya et al. have recently reviewed the research on zircon, mostly the natural type, to investigate its potential as a structural material.[1] For zircon to fully exhibit its inherent advantages, it is considered necessary to prepare a high-purity powder as the starting material. However, few researchers have discussed the preparation of high-purity zircon powder, except Roy et al.[2] and Kanno ;[3-7] the former reviewed most zircon synthesis processes, including the sol-gel and hydrothermal method, and the latter discusses zircon formation mechanisms in the sol-gel process.[3-7]

In this study, the authors investigated the effects of the combination of the starting materials, calcination heating rate and addition of seed grains, in an attempt to prepare high-purity zircon powder by the sol-gel process.

2. Experimental Procedure

2-1. Sample Preparation

The starting materials were $ZrOCl_2 \cdot 8H_2O$ (Kanto Kagaku, special grade), $Zr(OPr^i)_4$ (Kojundo Kagaku Kenkyusho, 99.99% pure), $Si(OEt)_4$ (Kojundo Kagaku Kenkyusho, 99.999% pure), and silica sol (Nissan Kagaku, Snowtex-0, containing 20wt% of SiO_2). The following four types of samples were prepared using the starting materials.

(a) $ZrOCl_2 \cdot 8H_2O$ and ethanol were mixed, with stirring, at 40° to 50°C to form a solution, to which $Si(OEt)_4$ was added stoichiometrically to form $ZrSiO_4$. The mixture was stirred for 1h to form a sol, which was added, after the pH was adjusted to 2 with HCl, dropwise to doubly distilled water (10 times the molar quantity of $ZrOCl_2$) for hydrolysis, to form a gel. The solvent was evaporated, the gel dried at 200°C, and crushed in an agate mortar. The dried gel was then treated at 300°C to remove remaining moisture and chlorine, and again crushed in an agate mortar, to form the powdered sample (referred to as sample (a)).

(b) $Zr(OPr^i)_4$ was dissolved, with stirring, in iso-BuOH (with a given quantity of 2-methyl-2, 4-pentanediol added as the chelating agent), as required at 50°C in a flow of nitrogen, and refluxed for 10h. $Si(OEt)_4$ was then added, with stirring, to a mixed solution of doubly distilled water and ethanol adjusted to pH 2 with HCl, in the stoichiometric quantity required to form $ZrSiO_4$. This mixture solution of $Si(OEt)_4$, H_2O and EtOH (1:1:1 molar ration) was used as the starting solution for the partial hydrolysis of $Si(OEt)_4$. It was made into a sol by adding it, with stirring, to $Zr(OPr^i)_4$ dissolved in i-BuOH, and then hydrolyzed with a mixture of doubly distilled water and ethanol, adjusted to pH 2 with HCl, into a gel. The mixed solution had a composition of 1 mol of $Zr(OPr^i)_4$, 8 mols of water and 1 mol of ethanol. The effluent was evaporated to remove the solvent, crushed by an agate mortar, dried again at 200°C, and then crushed again by an agate mortar, to form the powdered sample (sample (b)). This sample was prepared by referring to the conditions for hydrolyzing Zr-O-Si alkoxide, reported by Nogami et al.[8]

(c) The same procedure as used for preparing sample (a) was repeated, except $ZrOCl_2 \cdot 8H_2O$ and silica sol were used, to form a powdered sample (sample (c)).

(d) The same procedure as used for preparing sample (b) was repeated, except $Zr(OPr^i)_4$ was dissolved in ethanol, which was added dropwise to the silica sol containing equimolar SiO_2 and $ZrSiO_4$, to form the powdered sample (sample (d)).

Furthermore, 1 to 5wt% of commercial $ZrSiO_4$ powder

(Kojundo Kagaku Kenkyusho, 98% pure, containing 0.3% of Hf, 0.06% of Fe, Ti and Al, and 0.03% Y impurities) was added, as the seed for promoting $ZrSiO_4$ formation, to sample (a), in order to investigate the seeding effects.

2-2. Calcination and Measurement of $ZrSiO_4$ Yield

Calcination was performed by a box-type high-temperature air oven (NECCO, with Kanthal super heating elements), where the powdered sample was heated at 20K/min to 900°C, then at a given heating rate (1.25 to 10K/min) to a given temperature level (1200° to 1650°C), at which it was held for 1h, cooled at the same rate as used for heating down to 900°C, and then allowed to stand in the oven.

The $ZrSiO_4$ yield was measured by an X-ray diffractometer (Rigaku Denki, RAD-C). The X-ray diffraction patterns of the powdered samples, calcined at 1200° to 1650°C, were processed in such a way that the areas of the four peaks of $ZrSiO_4$ (200), m-ZrO_2 (111,111), t-ZrO_2(101) appearing at 2θ of 26 to 32° were used to determine relative intensities, which were then used to determine $ZrSiO_4$ yield α_{ZrSiO}, by the equation $\alpha_{ZrSiO4} = I_{ZR(200)}/(I_{ZR(200)} + I_{M(111)} + I_{M(111)} + I_{T(101)})$,[3,9] where ZR stands for $ZrSiO_4$, M for m-ZrO_2, T for t-ZrO_2, and numbers in parentheses for the face indices.

3. Results and Discussion

3-1. Relationship between Starting Material Composition and $ZrSiO_4$ Yield

Combinations of Zr alkoxide or $ZrOCl_2$ zirconia component and Si alkoxide or silica sol silica component were used to prepare the powdered precursors for $ZrSiO_4$.

In order to investigate the effects of the Zr-O-Si bond on the relationship between the precursor composition and $ZrSiO_4$ yield, the IR spectra of the commercial $ZrSiO_4$ powder and the equimolar mixture of SiO_2 and ZrO_2 powders were measured. Absorption, presumably due to the Zr-O-Si bond in the $ZrSiO_4$ precursor compositions, was observed at around 1000cm^{-1}. Nogami et al. suggested that the absorption at 1018cm^{-1} is probably due to the Zr-O-Si bond.[8,10] Kanno et al., rejecting the above explanation, consider that the unidentified peak at 1028cm^{-1} is due to the bond.[5) Based on these discussions, samples (a) through (d) were investigated to confirm whether the Zr-O-Si bond was present or not in these samples. It was found that there was no possibility of the presence of the bond in samples (c) and (d), and they were merely mixtures of SiO_2 and ZrO_2. Sample (a) had an absorption peak shoulder at around 1000cm^{-1}, and sample (b) an absorption peak at around 1000cm^{-1}, suggesting the presence of the bond. Though the presence of the bond was not positively confirmed, the four sample types used in this study were considered to fall into two general categories. Samples (a) through (d) were calcined at a given temperature (1300° to 1650°C), to investigate the relationship between the starting material composition and $ZrSiO_4$ yield. Figure 1 shows the effects of calcination temperature on the $ZrSiO_4$ yield for the four samples, where each was heated at 10K/min to a given temperature, at which it was held for 1h. Samples (a) and (b), containing $Si(OEt)_4$, had notably higher yields than samples (c) and (d), containing silica sol. In addition, the former samples started to be converted into $ZrSiO_4$ at lower temperature. This resulted presumably from the use of $Si(OEt)_4$ which acted to increase the reactivity of silica by the Hedvall effects associated with transformation of silica from the amorphous state to the crystalline state,[4,11) or else from relatively uniform mixing producing good precursor powder. In any case, the critical factors for increasing the $ZrSiO_4$ content are, as pointed out by Kanno et al.,[4) a uniform mixture of ZrO_2 and SiO_2, and desirable interfacial conditions of SiO_2. Sample (a) prepared by the sol-gel process and sample (b) prepared by the alkoxide process were found to be preferable over the others. It should be noted, however, that all the samples prepared from the starting materials containing organic matter had a lower $ZrSiO_4$ content, though slightly, when calcined at 1650°C. It was also observed that sample (a) had a higher $ZrSiO_4$ content than sample (b), conceivably because the latter sample was heated at the relatively high rate of 10K/min so the Zr-O-Si bond could not be maintained at the given temperature, with the result that the inherent efficiency of the alkoxide process was not achieved.

3-2. Effects of Addition of Diol to Metal Alkoxide

The difference in the liability of metal alkoxides to

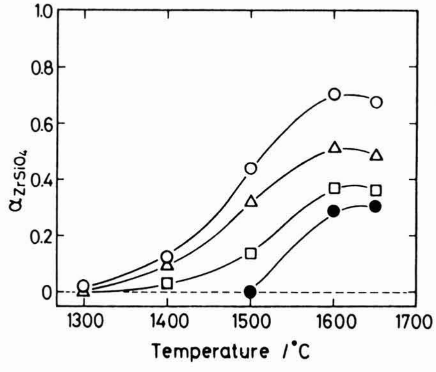

Fig. 1. Effect of starting materials on the preparation of zircon.

○ : $Si(OEt)_4$-$ZrOCl_2$, △ : $Si(OEt)_4$-$Zr(OPr^i)_4$,
□ : SiO_2 sol-$Zr(OPr^i)_4$, ● : SiO_2 sol-$ZrOCl_2$

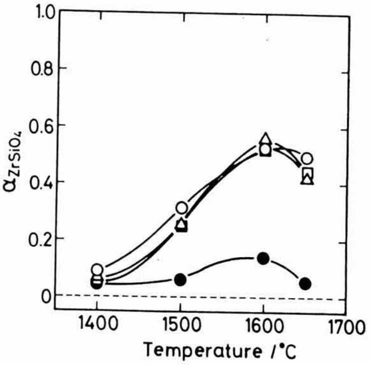

Fig. 2. Effect of diol addition on the preparation of zircon.

○ : (b_0), △ : (b_1), □ : (b_2), ● : (b_3)

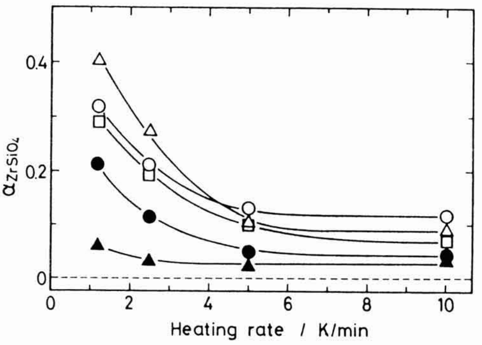

Fig. 3 .Effect of heating rate on the preparation of zircon.

○ : $Si(OEt)_4$-$ZrOCl_2$, △ : (b_0), □ : (b_1), ● : (b_2), ▲ : (b_3)

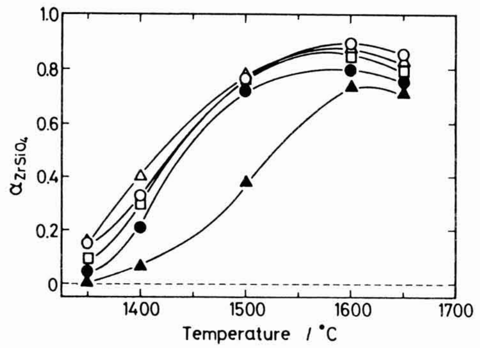

Fig. 4. Effect of heat-treatment temperature on the preparation of zircon. Heating rate : 1.25K/min. Holding time: 1h.

○ : $Si(OEt)_4$-$ZrOCl_2$, △ : (b_0), □ : (b_1), ● : (b_2), ▲ : (b_3)

hydrolysis causes a major problem when two or more metal alkoxides are used as the starting materials to prepare a homogeneous sol. This problem may be solved by adding a diol to a solution of the more active metal alkoxide, to control the hydrolysis.[12] For example, adding 2-methyl-2, 4-pentadiol (referred to as diol) as a chelating agent to a $Zr(OPr^i)_4$ solution produces a chelate compound with a structure corresponding to the mixed molar ratio.[13] This compound may be used to control hydrolysis, when the mixed molar ratio is carefully controlled. A given quantity of diol was added to $Zr(OPr^i)_4$, in an attempt to control the hydrolysis, and so to prepare a homogeneous powder as the precursor for $ZrSiO_4$, and the effects of diol addition on $ZrSiO_4$ yield were investigated.

Figure 2 shows the effects of calcination temperature in a range from 1400° to 1650°C on the $ZrSiO_4$ yield for sample (b) containing various quantities of diol, where samples containing 0, 1, 2 and 3 mol/$Zr(OPr^i)_4$ are referred to as (b_0), (b_1), (b_2) and (b_3). The other calcination conditions were 10K/min heating rate and 1h holding time. At 1600°C calcination temperature, the yields of $ZrSiO_4$ decreased in the order of (b_1) (56%), (b_2) 52%, (b_0) 51% and (b_3) 14%. It should be noted that (b_3) had a much lower yield than the others. Addition of 3 mol or more diol to $Zr(OPr^i)_4$ caused the 6-coordination position of Zr to be totally occupied by the diol ligands, preventing the formation of $ZrSiO_4$. At 1650°C, on the other hand, the $ZrSiO_4$ yield was decreased, as a result of an equilibrium between the formation and thermal dissociation of $ZrSiO_4$. An increased quantity of diol tended to accelerate the thermal dissociation of $ZrSiO_4$, presumably by the action of the carbon component of the diol remaining in the sample as an impurity. Thus, addition of an excessive quantity of diol decelerated, rather than accelerated, the formation of $ZrSiO_4$ because of the increased quantity of impurity remaining in the $ZrSiO_4$ product formed.

3-3. Effects of Heating Rate during Calcination on $ZrSiO_4$ Yield

It is known that nucleation in a solid-phase reaction is affected considerably by the heating rate. The heating rate, therefore, was varied from 1.25 to 10K/min, in order to investigate its effects on $ZrSiO_4$ yield.

Figure 3 shows the effects of heating rate on $ZrSiO_4$ yield at 1400°C for the combinations of $Si(OEt)_4$/$ZrOCl_2$ and $Si(OEt)_4$/$Zr(OPr^i)_4$ and samples (b1), (b_2) and (b_3). The $ZrSiO_4$ yield increased significantly as the heating rate decreased below 5K/min, but it was little affected by heating rates in the range from 5 to 10K/min, for all the samples tested. Sample (b_0), prepared by the alkoxide method, was affected by the heating rate more significantly than the others; the yield at 10K/min was about 31% higher than that at 1.25K/min. Similar trends were observed for the other calcination temperature levels tested, although the effects of heating rate tended to diminish as the calcination temperature increased.

Figure 4 shows the effects of calcination temperature on the $ZrSiO_4$ yield at a heating rate of 1.25K/min, where each sample was held for 1h at each temperature level. All the samples, except sample (b_3), followed similar trends, attaining a maximum at 1600°C. At the same time, the temperature at which $ZrSiO_4$ started to be formed was shifted to lower temperatures down to 1350°C. The preparation method (samples (a), and (b_0) through (b_3) had more effect during the initial stage of $ZrSiO_4$ formation (at 1300° to 1400°C), and at a low heating rate. Therefore, it may be concluded that decreasing the heating rate, particularly down to 2.5K/min or less, increases the $ZrSiO_4$ yield, indicating the importance of nucleation in formation of $ZrSiO_4$.

3-4. Effects of Seeding

As discussed in the previous section, the solid-phase synthesis of $ZrSiO_4$ is greatly affected by nucleation. Commercial $ZrSiO_4$ powder was added to the precursor $ZrSiO_4$, to investigate the seeding effects on $ZrSiO_4$ yield. The conditions were:1, 2.5 and 5wt% of commercial $ZrSiO_4$ added to sample (a), heating rate; 10 K/min, calcination temperature; 1200° to 1650°C, and holding time; 1h.

Figure 5 shows the effects of calcination temperature on $ZrSiO_4$ yield for each seeding rate. The results with the seed-free sample are also shown, for comparison. Seeding allowed the initiation of $ZrSiO_4$ formation at 1200°C, lowering the initiation temperature by at least 100°C. The $ZrSiO_4$

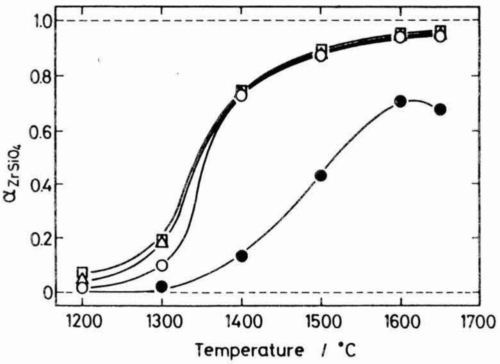

Fig. 5. Effect of heat-treatment temperature on the preparation of zircon with the addition of commercial zircon powder.
○ : 1 wt%, △ : 2.5 wt%, □ : 5 wt%,
● : no added (a)

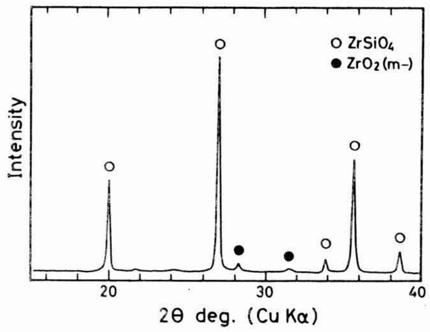

Fig. 6. X-ray diffraction pattern of the sample (a) powder with the addition of 1wt% commercial zircon powder heated at 1650°C for 1h. Heating rate : 10K/min.

product became almost a single phase ($ZrSiO_4$: 94 to 96%), when calcined at 1600° to 1650°C. **Figure 6** shows an example of the X-ray diffraction patterns of the $ZrSiO_4$ powder prepared under the above conditions. Seeding apparently increased the $ZrSiO_4$ yield, particularly notable at calcination temperatures in the range between 1200° and 1500°C. The seeding effects depended on the quantity of the seed added at 1200° to 1300°C, but were almost independent of the quantity above 1400°C. A small quantity of the $ZrSiO_4$ powder, about 1wt% in the precursor composition, acted as the seed to initiate the formation of $ZrSiO_4$ at 1200°C and produce almost only the single phase of $ZrSiO_4$ at 1600°C. No significant effects were observed with higher seed contents.

3-5. Effects of Two-Stage Calcination

Seeding with a small quantity of commercial $ZrSiO_4$ powder has been proved to be an effective means of increasing $ZrSiO_4$ yield. The commercial powder contained traces of impurities, which, however, might decrease the thermal dissociation temperature of $ZrSiO_4$.[14,15] An attempt was made, therefore, to use the synthesized powder as the seed by two-stage calcination, where a synthesized sample was calcined to form the $ZrSiO_4$ nuclei and then calcined again, after adequate crushing in an agate mortar. The first-stage calcination conditions were 1.25K/min heating rate, 1350°C calcination temperature, and 1h holding time, to form fine, evenly distributed $ZrSiO_4$ nuclei. The produce was again calcined at a heating rate of 1.25K/min and calcination temperature of 1600°C for 1h.

Table 1 summarizes the $ZrSiO_4$ yields of samples (a) and (b_0) through (b_3) by the two-stage calcination process. Similar effects to those discussed in Section 3.4 were observed, and almost only single phases of $ZrSiO_4$ (94 to 96%) were produced. It was also found that the final $ZrSiO_4$ yield was almost independent of the first-stage yield. These results were similar to those with commercial $ZrSiO_4$ powder, showing no additional effects in the presence of an excessive quantity of the powder.

The two-stage calcination results also suggested the possibility of producing high-purity $ZrSiO_4$ by the sol-gel approach without using an additive. A purity of the product below 100% might result either from a slight deviation of the starting material composition from the stoichiometric or inadequate synthesis conditions, in particular those causing insufficient homogeneity of the precursor composition. These are now under scrutiny.

4. Conclusions

Four types of precursor compositions were prepared by the sol-gel process, in an attempt to synthesize high-purity $ZrSiO_4$ powder. The effects of calcination temperature, heating rate and seed addition on $ZrSiO_4$ yield were investigated.

1) The silica component derived from $Si(OEt)_4$ precursor gave a higher $ZrSiO_4$ yield than that prepared from the silica sol. Addition of diol chelating agent to the metal alkoxide decelerated the formation of $ZrSiO_4$, when used in excess of 3 mol. eq. of $Zr(OPr^i)_4$. The carbonaceous matter formed as a result of diol addition remained in the $ZrSiO_4$, which may have acted as an impurity to cause the thermal dissociation of $ZrSiO_4$ calcined at 1650°C.

2) Formation of $ZrSiO_4$ was affected by the heating rate during the calcination process, and accelerated as the heat-

Table 1. Preparation rate of zircon by two-stage heating.

Sample	Relative preparation rate 1st stage	 2nd stage
(a)	0.16	0.96
(b_0)	0.14	0.96
(b_1)	0.09	0.95
(b_2)	0.05	0.96
(b_3)	0.01	0.94

ing rate decreased, particularly at 2.5K/min or less. It was further observed that the precursor derived from the metal alkoxide tended to give a higher $ZrSiO_4$ yield, as the heating rate and calcination temperature decreased.

3) Addition of a small quantity of commercial $ZrSiO_4$ powder (about 1wt%) to the synthesized precursor achieved the formation of almost pure single phase of $ZrSiO_4$, when the calcination temperature was increased from 1600° to 1650°C. Thus, seeding the precursor powder is an effective method of producing high-purity $ZrSiO_4$.

4) Two-stage calcination with the second stage temperature of 1600°C formed almost only the single phase of $ZrSiO_4$. This approach has opened up for the sol-gel process the possibility of producing high-purity $ZrSiO_4$ without the use of additives.

(Presented to the 2nd Symposium of the Japan Ceramic Society, October, 1989)

Acknowledgments:

The authors thank Miss. M. Takada (now at Toshiba Corp.) for her cooperation, and Nissan Kagaku Kogyo for providing silica gel.

Reference:

1) Zircon, Science and Technology," edited by S. Somiya, published by Uchida Rokaku-ho, (1989), pp. 25-313.
2) S. Komarneni and R. Roy, Reference 1), pp289-98.
3) T. Suzuki and Y. Kanno, Yogyo-Kyokai-shi, 95, 1018-22 (1987).
4) Y. Kanno and T. Suzuki, Zairyo, 37, 378-84 (1988).
5) Y. Kanno and T. Suzuki, Hyomen Kagaku, 9, 207-12 (1988).
6) Y. Kanno and T. Suzuki, J. Mater. Sci. Lett., 8, 41-43 (1989).
7) Y. Kanno, J. Mater. Sci., 24, 2415-20 (1989).
8) M. Nogami and K. Nagasaka, Seramikkusu Ronbun-shi, 96, 925-29 (1988).
9) Y. Kadogawa and Y. Yamate, Yogyo -Kyokai-shi, 93, 338-40 (1985).
10) H. Nogami and Y. Moriya, Yogyo-Kyokai-shi, 85, 59-65 (1977)).
11) M. Kunugi, A. Konisahi, S. Manabe, Zairyo, 15, 615-20 (1966).
12) Y. Abe, N. Sugimoto, Y. Nagao and T. Misono, Yogyo- Kyokai-shi, 95, 1141-44 (1987).
13) A. Yamamoto and S. Kambara, J. Am. Chem. Soc., 81, 2663-67 (1959).
14) T. Uetsuki, Reference 1), pp. 115-41.
15) Y Kanno, ibid., pp. 143-48.

This article is a full translation of the article which appeared in Nippon Seramikkusu Kyokai Gakujutsu Ronbunshi (Japanese version), Vol.98, No.6, 1990.

Wetting and Joining of SiC by Ag-Cu-x%Ti Brazing Alloys

Young-Soo Chung and Takayoshi Iseki

Research Laboratory for Nuclear Reactors, Tokyo Institute of Technology
12-1, O-okayama 2-chome, Meguro-ku, Tokyo 152, Japan

Wetting behavior of 72Ag-28Cu-x%Ti alloys on SiC was investigated in a vacuum of 10^{-3}Pa. Ti-free Ag-Cu alloy did not wet SiC and the contact angle became about 160°. With more than 0.5%Ti, the alloy wetted SiC well. Wetting of SiC by Ag-Cu-x%Ti alloy was thought to proceed by the adsorption of active metal Ti at the interface. In Ag-Cu-0.2%Ti alloy, the wetting angle became about 130° in a vacuum of 10^{-3}Pa, but the alloy reacted with SiC.

Microstructure and composition at the surface and bulk of each alloy after wetting experiment were analyzed by SEM and EDX. Non-wetting behavior of Ag-Cu-0.2%Ti alloy on SiC was thought to have resulted from the presence of atmospheric oxygen. Thus, Ti was consumed by the reaction with the atmospheric oxygen at the surface of the alloy leaving little Ti available to wet SiC. But for more than 0.5%Ti, a considerable amount of Ti for adsorption remained and wetted SiC. When the amount of atmospheric oxygen was increased, the reaction between oxygen and Ti in the brazing alloy became active and therefore the alloy could not wet SiC even in the case of Ag-Cu-2%Ti.

The state that brazing alloy contacts with atmospheric oxygen is much different between the cases of wetting and joining experiments. Ag-Cu-0.2%Ti alloy could join SiC successfully, even though the contact angle was about 130° in wetting experiment, probably because it was difficult for Ti to react with the atmospheric oxygen in joining experiment and Ti could adsorb at interface.

[Received December 25, 1989; Accepted February 13, 1990]

Key-words: SiC, Ag-Cu-x%Ti, Atmosphere, Active metal, Wetting, Joining

1. Introduction

The active metal method is frequently used for the joining of ceramics brazing In this method, brazing alloys with a small content of an active metal such as Ti are placed between the two materials to be joined, and heated to form the joint. The necessary condition in this joining process is the wetting of the materials to be joined by the brazing alloy. Brazing alloys of the Ag-Cu system, which are effective for the brazing of metals, do not wet almost all types of ceramics, so the addition of a small amount of active metal is required. The authors previously reported[1] that, when joining SiC with brazing alloys of the Ag-Cu-Ti system, the wetting of SiC by these alloys was improved by the addition of active metals such as Ti to the alloys because the active metals were adsorbed well at the interface. In practice, several wt% of Ti is often added to brazing alloys.[2-6] However, if we assume the improvement of wetting behavior simply depends on the adsorption of the brazing alloy on the ceramic to be joined, a smaller amount of Ti added will be enough to achieve a good joint. In the case of adsorption of P on Fe, or in the adsorption of Ti on Al_2O_3 ceramics in the reaction between Al_2O_3 and Ni-Ti system brazing alloys,[7,8] it has been reported that the addition of P or Ti in a small amount, less than 1%, was sufficient to achieve the adsorption of P or Ti required for the reduction of interface energy. When larger amounts of Ti were added to the brazing alloys, a thicker reaction layer between the brazing alloy and SiC was formed. The reaction products which constitute the reaction layer are reported to be Ti_5Si_3, TiC, etc. The formation of such reaction products may cause the following problems. Ti_5Si_3 is a weak material with a four-point bending strength as low as 70MPa,[1] and Ti_5Si_3, TiC and Ti_3SiC_2 have large thermal expansion coefficients, about twice as large as that of SiC.[1] Therefore, when a thicker reaction layer is formed, it is possible that fairly large thermal stresses are formed between the brazing alloy and SiC. In fact, it was reported[2-4] that the joining strength of SiC decreased with an increase of Ti content in the alloy.

In the present study, the authors investigated the effects of the Ti content in Ag-Cu-Ti system brazing alloys and the furnace atmosphere on the wetting and the joining of SiC, in order to clarify the relationships between wetting and atmosphere, and wetting and joining when the Ti content in the brazing alloys was reduced.

2. Experimental Procedure

2-1. Measurement of Contact Angle

The contact angles of brazing alloys of the (72Ag-28cu)-xwt%Ti system (x=0 to 2.0) were measured using pressureless sintered SiC (Kyocera Co., SC-201) with a density of 3.13g/cm^3 and a low content of B and C sintering aids, cut to 10×10×1.5mm^3 and polished on one surface using 1μm diamond paste.

The brazing alloys were prepared by mixing the three metal powders forming the alloy composition, and by press-forming the mixture. The powders were Ag powder (99.9%, particle size −300mesh, Rare Metallic Co.), Cu powder (99.99%, fine particle, Rare Metallic Co.), and Ti powder (99.1%, particle size −350mesh, Osaka Titanium Co.). Five compositions of brazing alloys were made by adding Ti 0.0, 0.2, 0.5, 1.0 and 2.0wt% to the eutectic alloy composition of 72Ag-28Cu, and powders for these compositions were mixed in acetone. After mixing, about 0.2g of powder was press-formed under about 80MPa to form pellets 4mm in

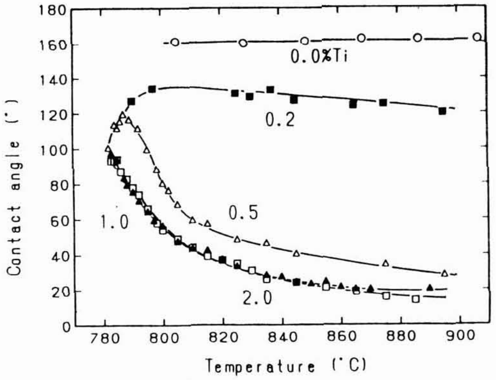

Fig. 1. Variations of the contact angle of Ag-Cu-xwt%Ti alloys on pressureless sintered(PLS)-SiC while heating at a rate of 10°C/min.

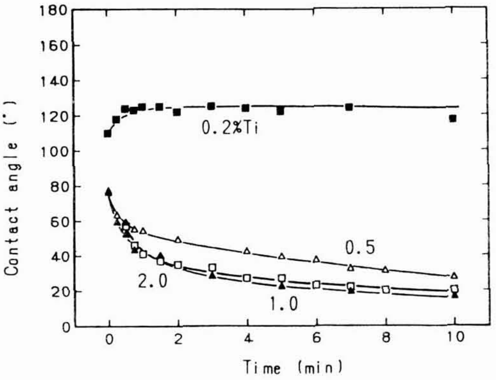

Fig. 2. Variations of the contact angle of Ag-Cu-xwt%Ti alloys on PLS-SiC as a function of holding time at 820C.

diameter and about 2.5mm in height.

A SiC substrate was placed inside the graphite heating elements of a high frequency electric furnace, and a pellet of brazing alloy was placed on the polished surface of the SiC substrate. Starting from around 780°C, the melting point of the brazing alloy, photographs of the sample were taken from about 30cm using a 800mm telephoto lens. From the photographs taken, the contact angles of alloy on both left and right sides were measured and the mean value calculated.

2-2. Joining

Brazing alloy foils were used in the SiC joining experiments. The foil (Tanaka Kikinzoku Co.) had a thickness of 100μm and two different Ti contents, 0.2 and 2wt%, and were cut to about 10×10mm.^{2} The SiC samples used were the same quality as used in the measurement of wetting angles, and were 10×10× 9mm.^{3} The surface of the sample to be joined was polished with 1μm diamond paste.

Two SiC samples were joined by placing a sheet of brazing alloy foil between them and heating at 850° C or 950°C for 30min in a high vacuum in the high frequency furnace. The heating rate of 40°C/min and cooling rate of 80°C/min were used in this joining process.

2-3. Analysis and Measurement of Strength

We analyzed the microstructures and compositions of both the joined sample and the sample used for the measurement of wetting behavior by SEM and EDX. The joined sample was cut, the cut face polished with 1μm diamond paste and the microstructure and distribution of Ti at the joined interface investigated. For the sample used for measurement of wetting behavior, the microstructure and the composition of brazing alloys at the surface and in the inside were analyzed.

The four-point bending strength of the as-received SiC and joined SiC samples were also measured. The samples were cut to about 3.5× 2.5×18mm.^{3} A jig with an upper span of 7mm and lower span of 14mm were used for this measurement.

3. Results and Discussion

3-1. Change in Contact Angle of Ag-Cu-x%Ti Alloys on SiC with Temperature and Time

Figures 1 and **2** show the changes in the contact angle of a Ag-Cu-x%Ti alloy drop on SiC with temperature and time using alloys with various Ti contents from 0 to 2.0wt%. Figure 1 shows the results when the temperature rose at 10°C/min, starting from 780°C. Figure 2 shows the change in the contact angle as a function of time when the temperature was kept constant at 820°C. The pressure was controlled at a high vacuum of 10^{-3}Pa in both experiments.

These results indicate that the contact angle is about 160° when no Ti is added to the alloy, but decreases when Ti is added, and that where Ti content was 1.0 and 2.0wt%, the wetting of SiC by the alloys progresses with increased temperature, or with time. The wetting was fairly good even when the Ti content was as low as 0.5wt%. When the Ti content was lowered to 0.2wt%, poor wetting resulted, but it was confirmed that the brazing alloy and SiC reacted at the interface, which should result in good joining of SiC. By comparing Figs.1 and 2, we find that the contact angle θ depends on the temperature, which is one of the important factors, but once SiC is wetted, it strongly depends on the Ti content and time, rather than on the temperature.

3-2. Relationship between Contact Angle and Joining Strength

The joining strength is affected by thermal stress and by the reaction products formed in the reaction layer, but a simple relationship between joining strength and contact angle can be assumed for discussion. The contact angle θ should satisfy equation (1) shown below, in which γ_{SV} is the surface tension of SiC (1840mJ/m^2),[9] γ_{LV} is the surface tension of the brazing alloy drop (947mJ/m^2 at 820°C),[10] and γ_{SL} is the interface energy between the SiC and brazing alloy drop.

$$\gamma_{SV} = \gamma_{SL} + \gamma_{LV}\cos\theta \quad \ldots\ldots\ldots\ldots\ldots (1)$$

When Ti is not added to the brazing alloy of the Ag-Cu

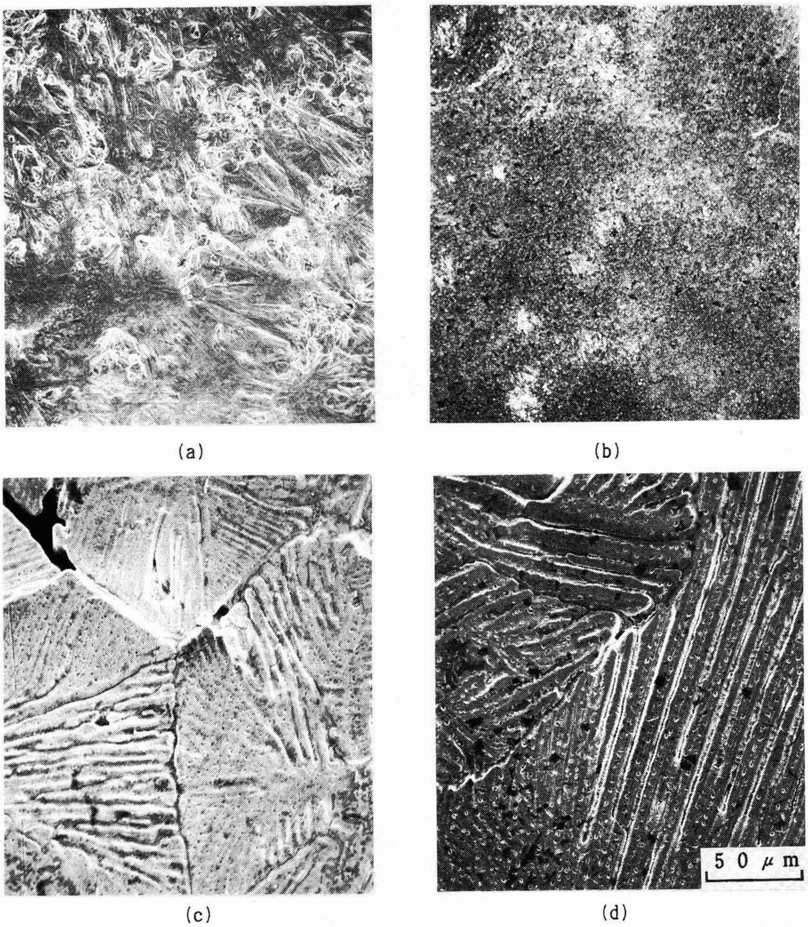

Fig. 3. Scanning electron micrographs of the surfaces of Ag-Cu-xwt%Ti drop after wetting experiment under a vacuum of 10^{-3}Pa

system, the interface energy γ_{SL} between the alloy and SiC is calculated from equation (1) to be as great as about 2730mJ/m^2 in the case of a contact angle of 160° at 820°C. But when a small Ti content is added to the alloy, the contact angle is reduced to 20° and γ_{SL} is calculated to be as small as about 950Jm/m^2. The decrease in interface energy between the liquid and solid mentioned above means that a large energy as calculated in equation (2) below is required for the separation of the joined interface.

$$W_a = \gamma_{SV} + \gamma_{LV} - \gamma_{SL} = 1837\text{mJ/m}^2 \quad \ldots\ldots (2)$$

(W_a : work of adhesion)

Here, the value of the surface tension of the brazing alloy γ_{LV} used in equation (2) for work of adhesion is that for no adsorption of Ti at the interface. When Ti is adsorbed at the interface, the composition of the alloy changes, as in our present experiment, and the surface of the alloy obtained by separation at the interface is different from the surface of the original alloy. Since the surface of the alloy obtained by separation at the interface contains an increased amount of Ti which was adsorbed at the interface, the value of γ_{LV} at this surface is increased. As a result, the energy required for separation at the interface increases. Therefore, the decrease of contact angle caused by the adsorption of Ti at the interface implies an increase of joining strength, as expected from the calculation of equation (2) for work of adhesion.

The interface energy between the SiC and brazing alloy γ_{SL} is reduced by the adsorption of Ti at the interface. Since adsorption is a two-dimensional phenomenon, we can assume that even a very small amount of Ti will be sufficient for the reduction of γ_{SL} due to its adsorption. In order to survey the possibility of joining SiC by using a brazing alloy with a low Ti content of 0.2wt%, we carried out a wetting experiment, but did not observe good wetting behavior between SiC and Ag-Cu-0.2wt%Ti alloy. Accordingly, we

Table 1. Weight ratio of Ag:Cu:Ti at the surface and inside of the Ag-Cu-xwt%Ti alloys after wetting experiment under a vacuum of 10^{-3}Pa.

	Ti%	Region	Ag	Cu	Ti
(a)	0.2	Surface	56.8 (3.7)	30.5 (3.3)	12.7 (0.4)
		Inside	69.7 (0.0)	30.3 (0.0)	0.0 (0.0)
(b)	0.5	Surface	36.5 (0.8)	42.0 (0.4)	21.5 (0.5)
		Inside	70.7 (0.4)	28.9 (0.4)	0.4 (0.2)
(c)	1.0	Surface	78.0 (4.1)	21.1 (3.4)	0.9 (0.7)
		Inside	68.3 (1.5)	30.6 (1.3)	1.1 (0.1)
(d)	2.0	Surface	82.2 (0.9)	17.6 (0.9)	0.2 (0.1)
		Inside	73.3 (1.7)	26.3 (1.6)	0.4 (0.3)

( ) : Standard deviation

investigated the causes of this behavior, as described below.

3-3. Effect of Atmosphere on Contact Angle

In the wetting experiments, a vacuum was maintained in the furnace of 10^{-3}Pa, but the effect of a minor amount of oxygen on the contact angle leaking into the furnace atmosphere during the experiment was examined, in addition to the effect of the oxygen originally present in the atmosphere.

In both reaction equations (3) and (4) shown below, the free energy of reaction ΔG° depends on the absolute temperature T.[11] From the calculation of ΔG° using these equations, we find that complete prevention of oxidation of Ti at 820°C requires either the reduction of the oxygen partial pressure P_{O_2} to as low as about 4×10^{-35}atm, or the introduction of H_2 gas into the furnace atmosphere to keep the partial pressure ratio of P_{H_2}/P_{H_2O} higher than 2×10^{8} . Ti is so reactive to oxygen that it is practically impossible to completely prevent oxidation.

$$Ti + O_2 = TiO_2 \quad \ldots\ldots\ldots\ldots\ldots\ldots (3)$$

$$\Delta G^\circ = -909.8 + 0.1732T\ (kJ/mol)$$

$$2H_2 + O_2 = 2H_2O \quad \ldots\ldots\ldots\ldots\ldots\ldots (4)$$

$$\Delta G^\circ = -492.8 + 0.1096T\ (kJ/mol)$$

Thermodynamically, the complete prevention of oxidation of Ti is considered to be practically impossible. From the quantitative consideration of the reaction, however, the amounts of oxygen originally present in the furnace and that leaking into the furnace during the experiment are small, and such a limited amount of oxygen only participates in the oxidation of Ti. A Ti content of 0.2wt% in the Ag-Cu system brazing alloy is large to satisfy the adsorption of Ti on SiC, and for the resultant wetting of SiC by Ti, but good wetting did not result. We assume the reason for this is the effect of the minor amount of oxygen present in the reaction atmosphere. Thus, Ti migrated toward the surface of the alloy drop and was oxidized, instead of migrating toward the interface between the alloy drop and SiC to be adsorbed there.

Figures 3(a) to **(d)** show the SEM photographs of the sufaces of Ag-Cu-xwt%Ti system brazing alloy drops with various Ti contents of 0.2, 0.5, 1.0 and 2.0wt% after the wetting experiment under a high vacuum of 10^{-3}Pa. **Table 1** shows the average compositions in an area of about 200μm×200μm in the surface region and in the inside of the same brazing alloys after the wetting experiment under a vacuum of 10^{-3}Pa, which were analyzed by EDX and expressed as the weight ratio Ag: Cu: Ti. Figures 3(c) and (d) show the microstructures in the surface region of the alloys with Ti contents of 1 and 2wt%. They appear to be similar to those in the inside of the alloys, which have the eutectic microstructure of Ag-Cu alloy. The data given in Table 1 show little difference in Ti content between the surface region and the inside, although we are not sure that the results measured by EDX in our experiments indicate the chemical analyses right at the surface, because the compositions obtained were an average over a certain depth. Figures 3(a) and (b) show the microstructures in the surface region of the alloy with Ti contents of 0.2 and 0.5wt%. They differ widely from those inside. The data given in Table 1 indicate that Ti is concentrated in the surface region in both (a) and (b). We assume that such a concentration of Ti was caused by the migration of Ti toward the surface, and that Ti was oxidized and formed an oxide film. In the case of high Ti contents of 2.0 or 1.0wt% in the alloy, Ag evaporated vigorously out of the alloys at high temperature, obscuring the observation window of the furnace, but in the case of a Ti content of 0.2wt%, little evaporation of Ag was observed. We suppose the Ti oxide films formed on the surface of the alloy disturbed the evaporating of Ag.

With Ti contents of 1.0wt% and higher, since the wetting experiments used the same conditions as for the Ti content of 0.2wt%, there should not be a difference in the amount of oxygen in the atmosphere. If Ti migrates toward the surface of the alloy drop and is oxidized in the cases of Ti contents of 0.2 and 0.5wt%, Ti must react with oxygen in the atmosphere in the cases of higher Ti contents of 1.0 and 2.0wt%. However, no Ti oxide layer was detected in the surface region in the latter cases by EDX survey, as shown in (c) and (d) in Table 1. Presumably these results are due to the dissolution of oxygen or Ti oxide into Ag-Cu-xwt%Ti alloys in the case of high Ti content. No phase diagram for the Ag-Cu-Ti-O system is available, but, according to the phase diagram of the Ti-O system available,[12] we expect that Ti oxide will precipitate when the oxygen content in the liquid Ti is increased. Since Ti has a stronger affinity with oxygen than Ag and Cu in the brazing alloy, Ti is assumed to react with most of the oxygen and to precipitate out at the surface in the form of Ti oxide. Therefore, the solubility of oxygen in the Ag-Cu-x%Ti system alloys is assumed to increase with increased Ti content in the alloys. We will consider this relationship by comparing the cases of Ti contents of 0.2 and 2.0wt% in the alloys. In the case of a Ti content of 0.2wt%, almost all the Ti was oxidized at the surface of the liquid alloy drop, instead of being adsorbed at the interface between the alloy drop and SiC, resulting in a small Ti content x remaining in the alloy drop. With the decrease of Ti content in the alloy, the solubility of oxygen in the alloy decreases and Ti oxide precipitates out at the surface of the alloy. As shown in (a) in Table 1, Ti was not detected in the inside. In the case of a Ti content of 2.0wt% in the alloy, a fraction of the Ti is oxidized consuming the small oxygen content in the atmosphere, and after that, no further oxidation of Ti takes place. As a result, a good

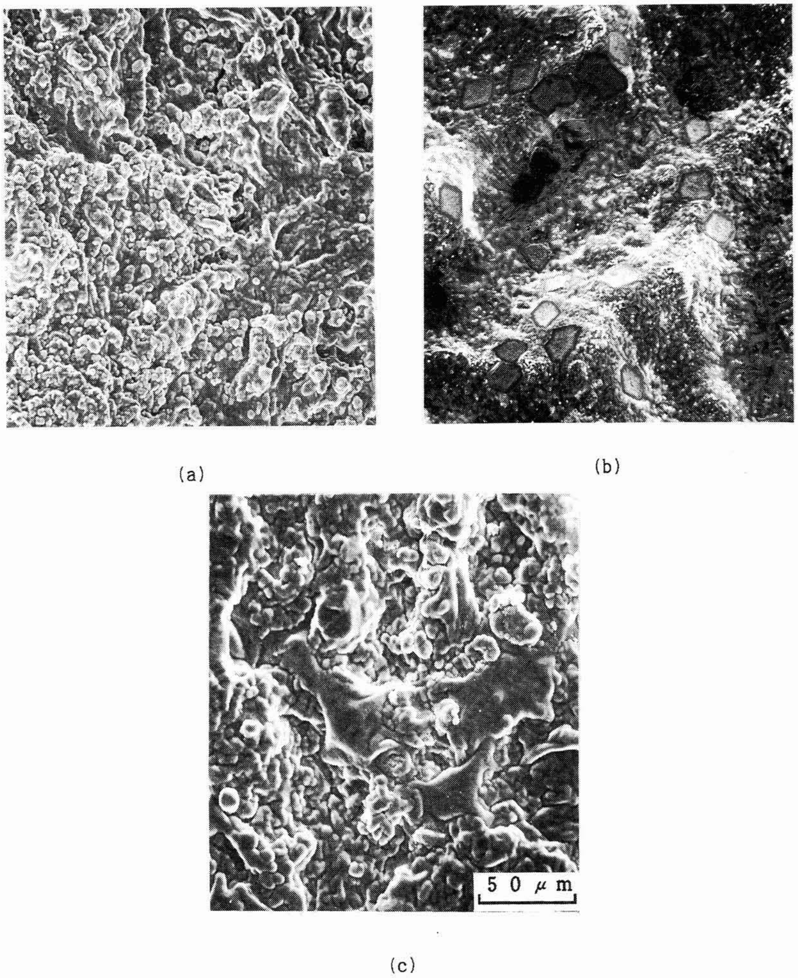

Fig. 4. Scanning electron micrographs of the surfaces of Ag-Cu-xwt%Ti drop after wetting experiment. (a) 0.5wt%Ti, 2×10^{-2}Pa. (b) 2.0wt%Ti, 7×10^{-2}Pa, (c) 2.0wt%Ti, 1.5×10^{-1}Pa.

amount of Ti was found to have remained unreacted in the alloy. Therefore, an alloy with a high Ti content starts to dissolve oxygen, and the Ti contents at the surface and in the inside are little different, as shown in Table 1. It is also assumed that a good amount of Ti was adsorbed at the interface, resulting in the good wetting behavior. It is seen in (d) in Table 1 that the Ti content inside the alloy decreased to less than 2wt%. We assume that this decrease of Ti content was caused by the reaction of a fairly large amount of Ti at the interface with time in the experiment.

As a consequence of the reasoning above, it might be expected that if oxygen content in the atmosphere increases, the amount of Ti oxidized increases, and the Ti content x decreases so that Ti oxide precipitates out of the liquid alloy because the content in the liquid alloy exceeds the solubility limit even in the case of a high Ti content of 2.0wt%, resulting in poor wetting behavior at the interface. The causes for deterioration of wetting behavior are assumed to be an insufficient Ti content in the alloy to be adsorbed or the generation of too much Ti oxide layer at the surface of the liquid alloy drop, resulting in a loss of fluidity of the liquid

Table 2. Weight ratio of Ag:Cu:Ti at the surface and bulk of the Ag-Cu-xwt%Ti alloys after wetting experiment.

	Ti%	Vac. (Pa)	Ag	Cu	Ti
(a)	0.5	2×10^{-2}	3.5 (0.5)	17.6 (1.1)	77.9 (0.7)
(b)	2.0	7×10^{-2}	60.9 (1.1)	32.3 (0.8)	6.7 (0.4)
(c)	2.0	1.5×10^{-1}	0.8 (0.1)	2.2 (0.1)	96.8 (0.3)

( ) : Standard deviation

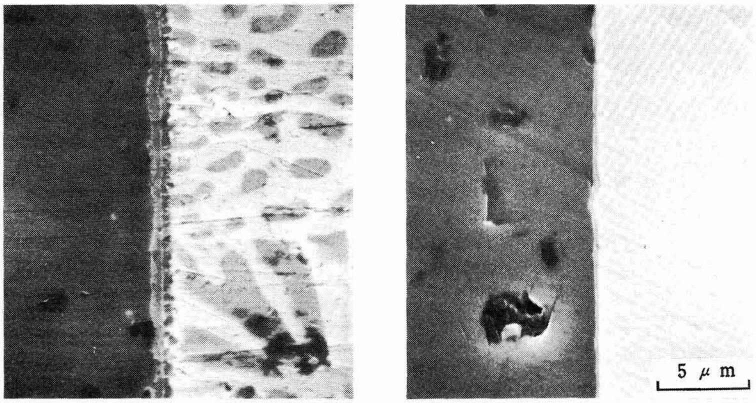

(a) (b)

Fig. 6. Scanning electron micrographs of the joined interfaces between SiC and (a) Ag-Cu-2.0wt%Ti, (b) Ag-Cu-0.2wt%Ti brazing alloys. (850°C, 30min)

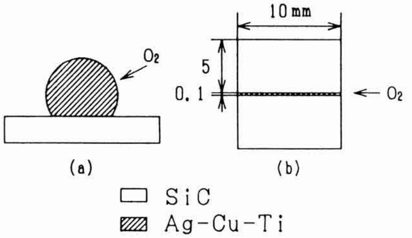

Fig. 5. Schematic diagram for the state of brazing alloys exposed to the atmospheric oxygen during (a) wetting and (b) brazing experiment.

alloy drop. We previously mentioned that a limited amount of oxygen can participate in the oxidation of Ti, but, as a matter of course, this amount of oxygen increases with higher vacuum pressures, the increase of furnace volume, and the increase of experiment time.

Figures 4(a), **(b)** and **(c)** show the change in the surface state of solidified alloys with Ti contents of 0.5 and 2.0wt% when the pressure was increased, so increasing the oxygen content in the atmosphere. In this wetting experiment, the contact angle θ was found to become larger with increased pressure. **Table 2**(a), (b) and (c) shows the compositions of the alloy surface analyzed by EDX with the same Ti contents as in Fig.4. They indicate high Ti contents at the surface. With a content of 2.0wt%, good wetting was found under a pressure of 10^{-3}Pa, but the contact angle increased under an increased pressure of 7×10^{-2}Pa, and the wetting behavior became poor in addition to the increase in contact angle under a further increase in pressure of 1.5×10^{-1}Pa. If the converse of these results is true, an alloy with a low Ti content of 0.2wt% will have good wetting if a lower pressure is applied or if conditions are used which hinder the reaction of Ti with oxygen in the reaction atmosphere, although this alloy did not show a good wetting behavior under a vacuum of 10^{-3}Pa.

3-4. Joining of SiC using a Ag-Cu-0.2wt%Ti Brazing Alloy and Measurement of Four Point Bending Strength of the Joined SiC

In the proceeding section we showed that, with a Ti content of 0.2wt%, the brazing alloy did not display good wetting behavior due to the effect of a minor amount of oxygen in the atmosphere, but it will possibly give good wetting using conditions which hinder the oxidation of Ti in the brazing alloy. The amount of Ti to be oxidized in the brazing alloy is related to the surface area of the alloy in contact with oxygen in the atmosphere. **Figure 5** schematically illustrates the contact conditions of the brazing alloy with oxygen in the atmosphere in the wetting experiment and in the joining experiment. In the wetting experiment (Fig.5(a)), Ti in the brazing alloy is rather easily oxidized because the surface ares of the alloy in contact with oxygen is large. During joining experiment (Fig.(b)), however, the surface area of the alloy is smaller, so Ti will be less oxidized and more probably adsorbed at the interface between the alloy and SiC. Consequently, we think that the poor wetting behavior of the brazing alloy with 0.2wt% Ti content in the wetting experiment does not always imply difficultly in SiC joining using this alloy.

Figure 6 (b) shows a SEM photograph of a joined interface of SiC when a foil sheet of brazing alloy of Ag-Cu eutectic composition with 0.2wt% Ti was used for joining. An SEM photograph of a joined interface of SiC in shown in Fig.6(a) when the same eutectic brazing alloy with 2.0wt%Ti was used for comparison. The SiC was joined well in both cases. The only difference observed is the

Table 3. Four point bending strength of as-received and joined SiC.

Specimen		Strength (MPa)
As-received		312 (23)
Joined at 850℃	by Ag-Cu-0.2%Ti	100 (24)
	by Ag-Cu-2.0%Ti	94 (34)
Joined at 950℃	by Ag-Cu-0.2%Ti	0 (0)
	by Ag-Cu-2.0%Ti	293 (60)

( ) : Standard deviation

thickness of the reacted layer formed at the interface of SiC, as thick as about 0.9µm in the case of 2.0wt% Ti content, but very thin in the case of 0.2wt% Ti content. Presumably the thin layer in the latter case was caused by the small Ti content in the brazing alloy used.

The results of measurement of the four point bending strength of the joined SiC using brazing alloy with 0.2wt% Ti content are shown in **Table 3**. It was also measured for as-received SiC and joined SiC using brazing alloy with 2.0wt% Ti content, and the results are compared in Table 3. SiC joined at 850°C using brazing alloy with 0.2wt% Ti content had a similar bending strength to that of SiC joined using alloy with 2.0wt% Ti content. However, observation of the fractured surfaces of the joined SiC samples after the bending strength test showed that the sample joined using brazing alloy with 2.0wt% Ti content was smoothly separated along the interface between the brazing alloy and SiC, but the sample joined using brazing alloy with 0.2wt% Ti content was strongly bonded at some parts of the interface. SiC joined at 950°C using brazing alloy with 0.2wt% Ti content indicated a trace of reaction at the contact surface between the two SiC pieces, but had no joining strength at all. These results suggest that the joining of SiC is sensitive to such conditions as atmosphere, temperature, etc., where the Ti content in the brazing alloy is small. In the ideal conditions where oxygen is completely excluded from the reaction atmosphere, we assume that good wetting behavior is present and good joining is achieved even when the Ti content in the brazing alloy is only 0.2wt%. However, since the effect of oxygen on the joining of SiC is unavoidable in practice, we think that a higher Ti content than 0.2wt% is necessary to achieve joined SiC with a high and uniform strength. Our results demonstrate the same trends in the relationship between the wetting behavior and joining strength as those reported by Nicholas using Al_2O_3 ceramics and Cu-Ti system brazing alloys,[13] with alloys of various Ti contents[13] He showed that with an increase in Ti content, the contact angle decreased, but the joining strength did not, and when Ti content was decreased until the contact angle was 150° and wetting was poor, the highest joining strength was obtained. He also reported that when the Ti content was further decreased, the joining strength began to decrease.

4. Conclusions

The authors investigated the contact angles of Ag-Cu-xwt%Ti system brazing alloys on SiC under a pressure of about 10^{-3}Pa and obtained good wetting behavior when the Ti content in the alloy was more than 0.5wt%. We assumed that the poor wetting behavior shown in the case of Ti content of 0.2wt% in the alloy was due to oxygen present in the atmosphere reacting with almost all the Ti at the surface of the alloy leaving insufficient Ti for adsorption at the interface between the SiC and the alloy. In the case of Ti contents of more than 0.5wt% in the alloy, Ti is partly oxidized, but this is limited by the amount of oxygen present in the atmosphere. Oxygen solubility in the Ag-Cu-xwt%Ti system alloys is estimated to increase with increased Ti content x in the alloy, so we assume that even after part of the Ti was oxidized, an adequate amount of Ti was present in the alloy for dissolution of the Ti oxide produced by oxidation and the Ti oxide dissolved into the alloy, allowing Ti to be adsorbed at the interface between SiC and alloy, resulting in good wetting. When the pressure was increased, increasing the amount of oxygen in the atmosphere, much of the Ti was oxidized and so the alloy did not wet the SiC even when the Ti content in the alloy was as high as 2.0wt%.

Since the contact conditions between brazing alloy and atmosphere oxygen differ in the wetting experiment and the joining experiment, oxidation of Ti and wetting of Ti on a ceramic substrate do not show the same behavior. Because of such different behaviors, a brazing alloy with a large contact angle and therefore a poor wetting behavior in the wetting experiment, is not always ineffective in the joining of SiC. For example, a brazing alloy with 0.2wt% Ti content had a contact angle of about 130° in our wetting experiment, but it effectively joined SiC by heating at 850°C for 30min obtaining a four-point bending strength of about 100MPa.

Acknowledgments:

The research was supported by Engineering Research Association for High Performance Ceramics, by a Grant-in-Aid for Scientific Research on Priority Areas from the Ministry of Education, Scinece and Culture and by the Inamori Foundation.

References:

1) T. Iseki, T. Yano and Y.S. Chung, Seramikkusu Ronbun-shi, 97, 710-4 (1989).
2) T. Iseki, H. Matsuzaki and J.K. Boadi., Am. Ceramc. Soc. Bull., 64, 322-24 (1985).
3) H. Mizuhara and E. Huebel, Welding J., 65, 43-51 (1986).
4) H. Okamura, Y. Sakamoto, T. Funamoto and A. Shida, Japan Welding Society, 15th Research Committee Meeting on Interface Joining, No.IJ-34-88 (1989).
5) R.E. Loehman, Am. Ceram. Soc. Bull., 68, 891-96 (1989).
6) R.R. Kapoor and T.W. Eagar, J. Am. Ceram. Soc., 72, 448-54 (1989).
7) J. Benard, "Adsorption on Metal Surfaces", Elsevier, Amsterdam (1983) p.54.
8) B.C. Allen and W.D. Kingery, Trans. Met. Soc. AIME, 215, 30-37 (1959).
9) M.W. Barsoum and P.D. Ownby, "Surfaces and Interfaces in Ceramic and Ceramic-Metal Systems", Mater. Sci. Res. Vol.14, Ed. by J. Pask and A. Evans, Plenum Press, New York (1981) p.463.
10) L.E. Murr, "Interfacial Phenomena in Metals and Alloys", Addison-Wesley, Reading, Mass. (1975) p.104.
11) D.R. Gaskell, "Introduction to Metallurgical Thermodynamics", McGraw-Hill, New York (1973) pp.497-98.
12) M. Hansen and K. Anderk, "Constitution of Binary Alloys", McGraw-Hill, New York (1958) p.1069.
13) M.G. Nicholas, Brit. Ceram. Trans. J., 85, 144-146 (1986).

This article is a full translation of the article which appeared in Nippon Seramikkusu Kyokai Gakujutsu Ronbunshi (Japanese version), Vol.98, No.6, 1990.

Powder Characteristics of Strontium Ferrite by Solid State Reaction

Zenji Kato, Nozomu Uchida, Keizo Uematsu and Katuichi Saito

Nagaoka University of Technology
Department of Material Science and Technology, Kamitomioka 1603-1, Nagaoka, Niigata

Strontium ferrite granules of powder particles having various fractional reactions were prepared by solid state reaction between 750 and 1250°C for 0.1 to 16h. Aggregate formation among particles was characterized by the die pressing test at 0 to 49MPa. At reaction temperatures below 1100°C, the strength of aggregates increased with reaction time and increasing temperature. At a given fractional reaction, the strength of aggregates did not depend on the reaction conditions. These results suggest that both aggregated formation and solid state reaction have the same temperature dependence. Above 1150°C, reaction was completed in a short time. Strength of granules increased as grain growth proceeded in the granule.

[Received December 27, 1989; Accepted February 13, 1990]

Key-words: Powder compaction, Granule, Strontium ferrite, Solid state reaction, Aggregate

1. Introduction

Most ceramic powders used for the production of formed ceramic products are manufactured by a solid state reaction process, in which the raw material powders are mixed, calcined and crushed. The formation of new compounds from raw materials by solid state reaction is the main target in the calcination process, but the formation of aggregated particles by sintering occurs simultaneously. The essential requirements for ceramic powders to be used in the production of formed ceramic products are, (1) homogeneous chemical composition (2) fine particle size, and (3) non-aggregated particles. It is therefore necessary to consider both the solid state reaction and aggregated particle formation during calcination, if ceramic powders with superior characteristics are to be synthesized. Many studies have been made of the reaction mechanism in the field of solid state chemistry.[1] Concerning aggregate formation, however, very few studies have been reported.

In our present study, the authors intended to independently evaluate the chemical reaction and aggregate formation of ceramic particles during calcination in the synthesis process of ceramic particles by solid state reaction, and to obtain basic conditions for the synthesis of particles with superior characteristics. The reaction model used in our study was the solid state reaction between ferric oxide and strontium carbonate to form strontium ferrite. We evaluated the solid state reaction by the measurement of weight change and powder X-ray diffraction analysis, and evaluated aggregate formation by the die pressing test. The die pressing test investigates the change in relative density of particles with change in pressure when the particles are compacted, and is based on the theoretical analyses of aggregated particles reported by Arakawa[2] and Nietz et al.[3] The die pressing test is frequently used in studies on the press-forming of ceramics[4] to investigate the compaction behavior of ceramic granules which contain organic binder, but we found no studies in which this test was used for the evaluation of the aggregation behavior which accompanies the solid state reaction of ceramic powders.

2. Experimental Procedure

The starting materials were ferric oxide (over 98.8%) and strontium carbonate (96.4%), both of which were commercial products. The starting materials were weighed to make non-stoichiometric composition of strontium ferrite ($SrO\cdot 5.8Fe_2O_3$), distilled water was added, and the solids mixed and crushed using an attriter, and then dried and granulated using a spray-drier. About 20g of the granulated material was placed on a platinum boat, and the boat placed in a horizontal electric furnace with SiC heating elements previously heated to given temperature. After holding at this temperature for a given time in air, the sample was rapidly cooled. A Pt-Pt13%Rh thermocouple and a PID type temperature controller were used for control and temperature measurement in the furnace.

The fractional reaction was found by the powder X-ray diffraction and gravimetric methods. For the X-ray diffraction method, a calibration curve which gave the relationship between peak area and chemical composition was used. The samples used for this calibration curve were prepared by the following procedures. First materials were prepared, one was a granulated sample from which the binder was removed by heating at 500°C for 1h, at which temperature no solid state reaction took place, and the other was a granulated sample in which the strontium ferrite phase was completely formed by repeating two cycles of heating at 1250°C for 1h and crushing. Secondly, the two materials were mixed in various weight ratios. The peak areas in the vicinity of diffraction angles $2\theta=43.5$ (ferrite), 42.1 (iron oxide) and 30.6 (strontium carbonate) were measured using an X-ray diffraction apparatus (model 2038, Rigaku Denki Co.) and FeKα radiation. The fractional reaction of the heated sample was determined by the gravimetric method using the following procedures. The raw material was heated until the strontium carbonate contained in the mixture was completely decomposed, and the weight loss of the material was taken as the theoretical weight loss. Then, the ratio of the weight loss of a sample against theoretical was used as the fractional reaction of this sample. An autograph

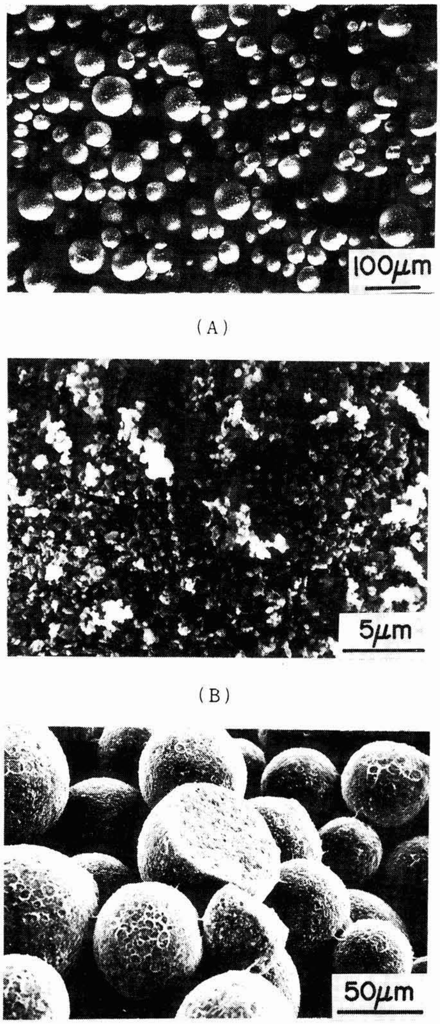

(A)

(B)

(C)

Fig. 1. SEM micrographs of specimens (A) Size distribution (B) Packing of powder particles (C) Internal structure of granules.

(model DSS-500, Shimazu Seisakusho Co.) was used in the unidirectional pressing test of powders. In this test, about 0.5g of powder was placed in a cemented carbide die with a 1cm inside diameter, and was compacted at rate of 0.05mm/min until the maximum pressure of 49MPa was reached. The relative density of the compacted powder sample was determined based on the theoretical density of ferrite of 5.00g/cm^3 and by correcting for the deformations of die and jigs. To evaluate the microstructure of the samples, we used a scanning electron microscope (model JSM-T100, Nippon Denshi Co.).

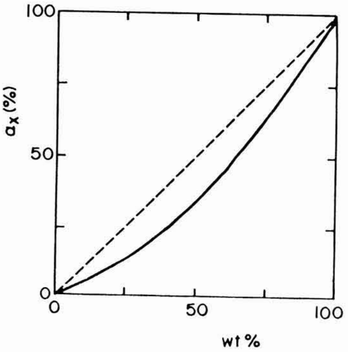

Fig. 2. Calibration curve of strontium ferrite system by X-ray diffraction analysis.

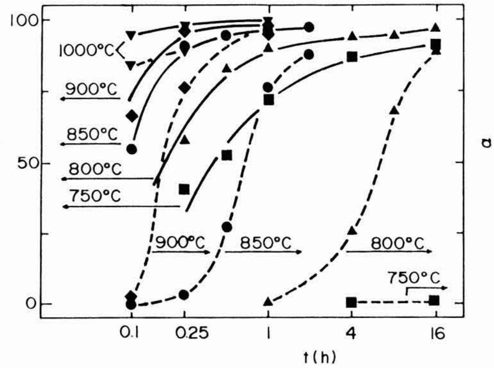

Fig. 3. Change of fraction reacted determined from weight loss αx with time at various temperature.

3. Results

Figure 1 shows SEM micrographs of the granulated raw materials used in our tests. **Figure 1(a)** shows that the granules are spherical and of suitable size distribution of the order of several tens of microns. Under a high magnification in Fig. 1(b), the granulates are aggregates of submicron size particles. The cross-sectional micrograph of a granule in Fig. 1(c) shows that the granule is closely packed with fine particles inside.

Figure 2 shows the calibration curve of the strontium ferrite system, prepared for the determination of fraction reaction. The relationship between peak area in the powder X-ray diffraction diagram and ferrite content in the sample is not linear.

Figure 3 shows the relationship between fractional reaction determined from both the weight loss and X-ray diffraction pattern and the reaction time at various temperatures. Fractional reaction at any temperature increased with time, and rate of change in fractional reaction increased considerably with increased reaction temperature.

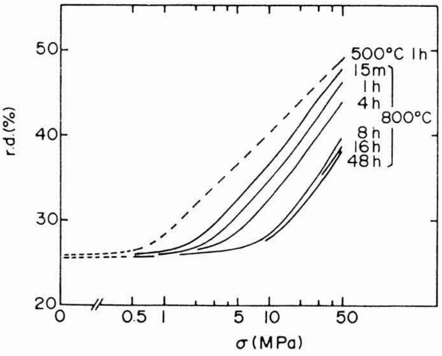

Fig. 4. Compaction behavior of samples reacted at 800°C. Broken line is non-reacted sample. Relative density (r.d.) is plotted against forming pressure.

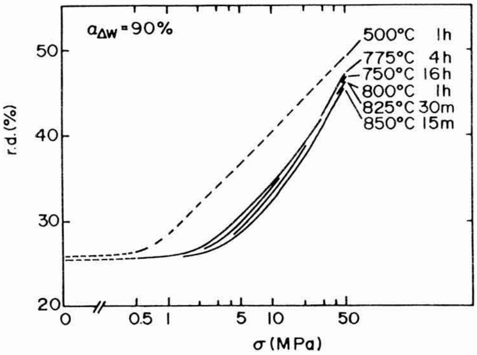

Fig. 5. Compaction behavior of samples with at constant α w = 90%. Broken line is non-reacted sample. Relative density (r.d.) is plotted against forming pressure.

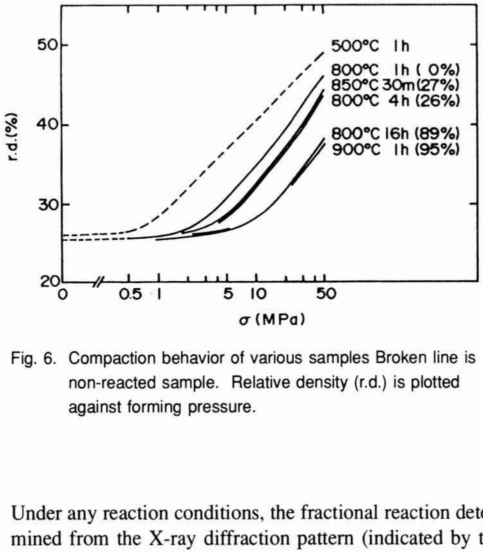

Fig. 6. Compaction behavior of various samples Broken line is non-reacted sample. Relative density (r.d.) is plotted against forming pressure.

Under any reaction conditions, the fractional reaction determined from the X-ray diffraction pattern (indicated by the broken lines in Fig. 3) is lower than that determined from weight loss (indicated by the solid lines in Fig. 3), and the difference between the two is especially larger in the low fractional reaction region. Since strontium carbonate does not decompose spontaneously at any temperature we used, such a large difference of fractional reaction is presumably caused by the formation of intermediate reaction products in the initial period of reaction, which are not clearly indicated by X-ray diffraction peaks.

Figure 4 shows the compaction behaviors of non-reacted particles calcined only at 500°C for 1h, and of reacted particles heated at 800°C for various times from 15min to 48h. The compaction of the reacted samples changed considerably compared to the non-reacted sample, even when the heating time at 800°C was short (15min), and continued to change even move with reaction time up to 8h, beyond which there was little change. When the sample was heated at temperatures other than 800°C, the time required for the change in compaction differed depending on the temperature, but the change of compaction with increased heating time showed similar trends to that in Fig. 4.

Figure 5 shows the results of the die pressing test of the granules prepared using various reaction conditions obtaining the same fractional reaction (90%) determined by weight loss. The heating time required to obtain this fractional reaction depends the reaction conditions, for instance, a heating time of 15min was required at 850°C, and 16h was required at 750°C. As apparently observed in this figure, all of these granule samples had nearly the same compaction behavior. Similar results were obtained with granule samples prepared under various conditions to obtain fractional reactions lower than 90%. This result can be interpreted as follows. In the initial period of solid state reaction when the fractional reaction determined from weight loss was less than 90% and little ferrite formation identified by X-ray diffraction analysis, the compaction behavior of calcined particles depended on the fractional reaction, but not on the reaction conditions.

Using various reaction temperatures and times, we prepared granular samples in which ferrite formation was identified, in other words, which had various fractional reactions determined by the X-ray diffraction technique. The results of compaction of these granular samples are given in **Fig. 6**. As observed in this figure, samples with nearly the same fractional reaction had nearly the same compaction as in the case of samples prepared at 850°C for 30min and at 800°C for 4h. Therefore, compaction behavior depends on the fractional reaction, but does not depend on the reaction conditions, if the reaction temperature is lower than 1000°C.

Figure 7 shows the SEM micrographs of compacted granular samples. Among the four compacted granular samples shown here, the one compacted to a relative density of 27.2% at 4.9MPa showed a partial fracture. With the increase of applied pressure, the fracture of granules progressed more. Although the contour of granules was still recognizable when the granular sample was compacted to a relative density of 28.2% at 9.8MPa, it disappeared when the sample was compacted to a relative density of 36.8% at 49MPa.

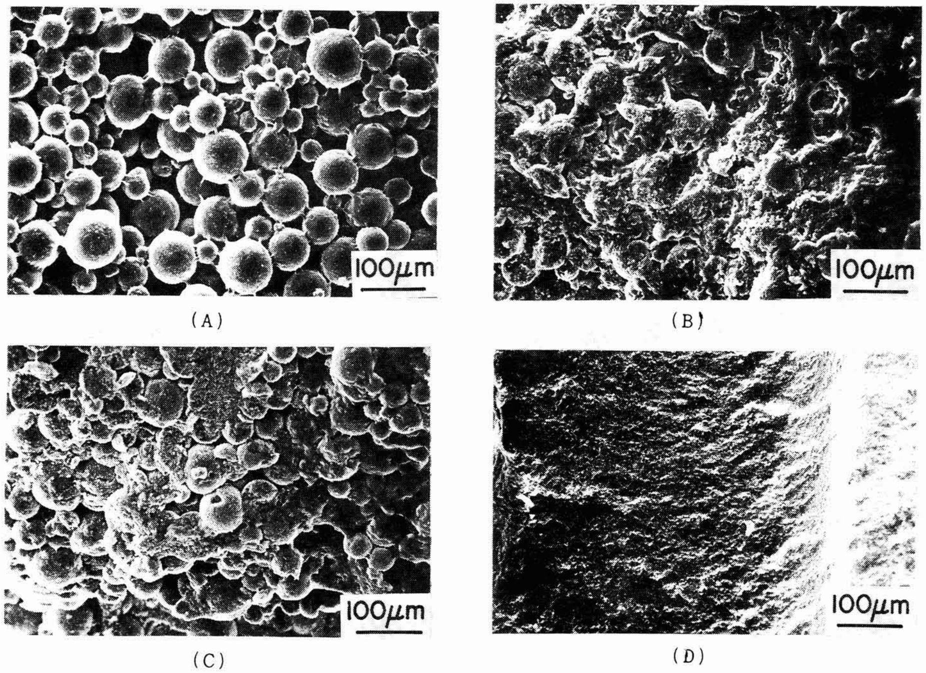

(A) (B) (C) (D)

Fig. 7. SEM micrographs of compressed specimens (A) 0.49MPa (B) 4.9MPa (C) 9.8MPa (D) 49MPa.

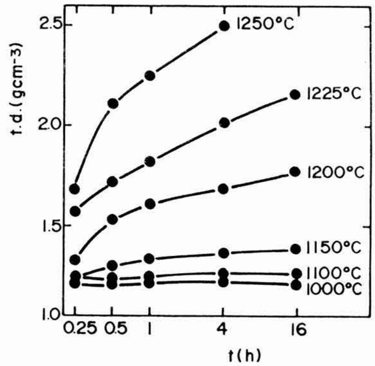

Fig. 8. Change of tapping density with time at various temperature.

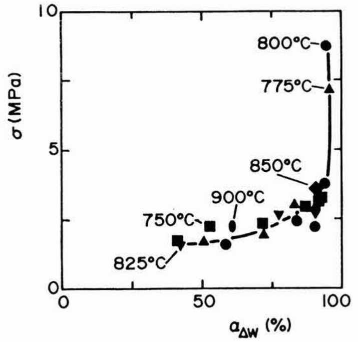

Fig. 9. Relationship between fraction reacted by weight loss and the pressure of break point in compaction curve.

Figure 8 shows the relationship between reaction time and tapping density of the samples prepared at reaction temperatures higher than 1000°C. The tapping density rapidly increased with increased reaction time when the reaction temperature was higher than 1000°C, but increased little when the reaction temperature was 1000°C even when heated for as long as 16h. When granular samples were heated at higher temperatures than 1000°C, the ferrite formation reaction was almost complete (more than 90%), and the SEM observation carried out separately revealed that the rapid increase in tapping density at high temperature was caused by the shrinkage of granules caused by the sintering of ferrite particles in the granules.

4. Discussion

The aggregate strength of particles in a compacted sample was determined from the pattern of the compaction

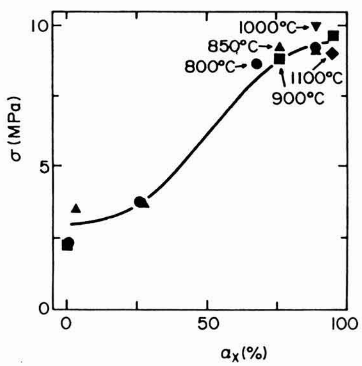

Fig. 10. Relationship between fraction reacted by X-ray diffraction analysis and the pressure of break point in compaction curve.

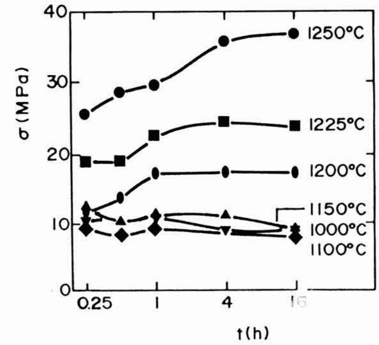

Fig. 11. Pressure of break point in compaction curve at various reaction time and temperature.

curve of the particles. According to Arakawa,[2] the break point in the compaction curve corresponds to the pressure initiating the fracture of aggregation among particles. All the compaction curves obtained in our present study showed a break point, which is assumed to be the initiation pressure for the fracture of granules. This is proved in **Fig. 7** by the fracture of granules at compacting pressures in the range of 4.9 to 9.8MPa, and by the change in the compaction curve in the same compacting pressure range. Consequently, we decided to take the pressure at the break point in the compaction curve as the strength of the granules, following Arakawa.

Figure 9 shows the relationship between the strength of granules and the fractional reaction determined from weight loss, using the granular samples prepared at various reaction temperatures. As shown in the figure, the strength of the granules does not depend on the reaction conditions, but gradually increases with the increase in fractional reaction in the range less than 90%, and rapidly increases with the increase in fractional reaction of more than 90%. In the case of fractional reaction less than 90%, no formation of ferrite phase was identified by the X-ray method, and the materials showed interesting phase changes, but we do not consider them important in the synthesis of the powder particles.

Figure 10 shows the relationship between the fractional reaction determined by X-ray diffraction and the strength of granules. It shows that the strength of granules increased with increased fractional reaction determined by the X-ray method, in other words, with the increase in ferrite formation, until it was almost saturated at the fractional reaction of 70% and higher. It also shows that the strength of granules was little affected by the reaction temperature when the fractional reaction was the same.

Figure 11 shows the relationship between heating time and strength of granules at high heating temperature. When the heating temperature was lower than 1100°C, the strength of the granules changed little with the increase of heating time, remaining at a value of around 10MPa, which is nearly equal to the strength of the granules prepared by adequate reaction at 900°C, as shown in Fig. 10. We therefore assume that, when the heating temperatures was lower than 1100°C, sintering among the particles did not progress after the ferrite formation reaction was finished, even if heating was continued. When the heating temperature was 1200°C, the strength of the granules increased almost linearly with increased heating time in the early period, but increased little with heating time after sintering of the intragranular particles. The tapping density increased considerably when the heating temperature was higher than 1200°C, as shown in Fig. 8. The strength of the granules achieved a fixed saturation value with increased reaction temperature.

At the beginning of this study, we expected that the activation energies for reaction and for aggregate formation would be different, and that temperature would have different effects on the rates of reaction and aggregate formation. However, our experimental results suggest that reaction and aggregate formation depend similarly on temperature. This can be interpreted in another way in that neither of reaction nor aggregate formation are rate limiting. Another observation is that an extended heating time has little effect on aggregation among particles after ferrite formation is completed, except in the case of extremely long heating times. We consider this is important in the synthesis of ceramic powder, because aggregation among the particles does not depend on the reaction conditions as long as the reaction temperature is not extremely high and reaction for a little longer time than necessary does not cause problems, therefore, we can choose reaction condition within wider tolerances.

Yamaguchi[5] reported similar results in the synthesis of ferrite. He determined the compaction coefficient by using particles prepared by calcination and crushing, and evaluated the aggregation of the particles by this coefficient. He confirmed that this coefficient decreased with increased calcination temperature in the lower range, had a constant value in the range beyond a certain calcination temperature, and increased with calcination temperature in the range beyond 1400°C. He defined the calcination temperature at which the compaction coefficient began to stabilize as the recrystallization temperature, and concluded that it was important for the preparation of raw material powders with superior properties. In our present study, we analyzed the same phenomenon from the viewpoint of the strength of granules, and succeeded in quantifying it.

In our present study, strontium carbonate disappeared in the early stage of reaction, but the formation of strontium ferrite was not identified by X-ray diffraction analysis at this stage. We assume that these phenomena are caused by the formation of intermediate reaction products which do not have clear X-ray diffraction peaks. These intermediate products eventually react with ferric oxide to form strontium ferrite. Many reports are available on the solid state reaction between ferric oxide and strontium carbonate, among which Naik et al.[6] examined the mechanism of this reaction, and obtained similar conclusions to the present study.

5. Conclusions

To investigate the solid state reaction and aggregation of particles, the authors synthesized calcined particles of strontium ferrite, obtaining the conclusions as follow.

1)The reaction is completed in a short time when the reaction temperature was higher than 1000°C, but took a long time when the temperature was lower.

2) Fractional reaction determined from the weight loss of the sample and that determined from X-ray diffraction analysis widely differed.

3) When the reaction temperature was lower than 1100°C, aggregation among the fine particles in granules progressed with the reaction in the early stage, but stopped in the end stage, in which ferrite was formed at 90% or more.

4) When the reaction temperature was higher than 1200°C, sintering among the particles progressed, and the strength of granules increased with the increase of heating temperature.

References:

1) "Kotai no Kanyosuru Muki-Hanno", edited by Nippon Kagaku-kai, published by Gakkai Publishing Center (1975).
2) M. Arakawa, Zairyo, 34, 1245-8 (1985).
3) D.E. Niesz, R.B. Bennett, and M.J. Snyder, Am. Ceram. Soc. Bull., 51, 677-680 (1972).
4) J.S. Reed, "Introduction to the Principle of Ceramic Processing", John Wiley & Sons (1988).
5) T. Yamaguchi, Funtai Oyobi Funmatsu-Yakin, 10, 7-12 (1963).
6) I.K. Naik and A.R. Das, Trans. Indian Ceram. Soc., 40, 199-205 (1981).

This article is a full translation of the article which appeared in Nippon Seramikkusu Kyokai Gakujutsu Ronbunshi (Japanese version), Vol.98, No.6, 1990.

Relation between AE and Integrity on Machining with Surface Grinder in New Ceramics

Kazuhisa Kinoshita, Daisuke Imanaka,* Itsuo Korenaga and Noritsugu Kawabata*****

Department of Mechanical Engineering, Faculty of Engineering, Oita University, 700 Dannoharu, Oita-shi 870-11
*Division of Mechanical Engineering, Graduate School of Engineering, Oita University, (as above)
**Wakamatsu works, Hitachi Metals Ltd., 1-9-1 Kitahama, Wakamatsu-ku, Kitakyushu-shi 808
***Noritake Diamond Industries Co., Ltd., 210 Takeno Tanushimaru-cho, Ukiha-gun, Fukuoka-ken 839-12

The machining test with a surface grinder was carried out on new ceramics to investigate the relation between AE, grinding force and machining integrity.
As a result of fundamental test, both amplitudes and continuous-times of AE signals were distinctly affected by the difference of base materials in which the AE sensor was mounted.
In grinding test, the distinguishable amplitude of AE took place in coincidence with the place of the slit of test pieces, which was considerably higher than that of the bulk. In the case of new ceramics, the order of the magnitude of the amplitude of AE showed the opposite tendency compared with that of the grinding force. Especially, the integrity of SiAlON was superior to that of WA and 2A, in correspondence with the degree of the AE count numbers.

[Received September 7, 1989; Accepted February 13, 1990]

Key-words: New ceramics, Grinding, Integrity, Cracks, Acoustic emission, Grinding force

1. Introduction

The rising needs for industrial diversification, higher accuracy and higher quality in products has stimulated demand for new ceramics. While new ceramics are highly resistant to wear, heat and corrosion, they are hard to grind because of the high hardness and brittleness, and products such as machine parts lack reliability.[1-4] Thus, there is a strong demand for the establishment of precision machining, methods for evaluating machining performance and the improvement of reliability of parts. Recently, studies have been made on new ceramics and signal analysis during machining.[5-7] However, because of the complexity, the relationship between product quality and machining methods and conditions as well as dynamic factors such as grinding force, vibration and grinding, and dust scattering have not been explained and still remain for investigation. By grinding new ceramics, we measured the acoustic emission (AE) signals during machining and studied their relationship with the ground surfaces.

2. Study of AE Measurements

In the evaluation of AE signals, signal characteristics are expected to vary considerably with the AE sensor installation conditions (base material, thickness, shape, distance from the vibration source, etc.) Thus, before measuring AE signals during grinding, the AE propagation characteristics must be studied by conducting basic tests in simplified environments.

First, to investigate the effect of sensor installation conditions on AE waves, we prepared base samples out of three materials: steel, acrylic resin and plywood, 56×395×22mm 80×365×5mm and 60×415×9mm, respectively. The signal source was obtained by rupturing a carbon 0.5mm in dia. on the base. The elastic wave generated was passed through a sensor, preamplifier and discriminator to amplify the signal and eliminate noise. Then it was displayed as an AE wave form on the digital oscilloscope. At the same time, the AE duration was measured by inputting the signal from the discriminator into a dual counter. Between the signal source and the sensor, three distances were chosen: 5, 10 and 15cm. The maximum waveform amplitude, rising time and duration were defined as shown in Fig. 1. The results of the basic tests (figures omitted) showed that with a larger distance between the signal source and the sensor, the maximum amplitude was smaller, and particularly prominent with acrylic and plywood plates. This may be because spread and internal friction losses vary with materials.

With all materials, as the distance increased, the rising time increased nearly proportionally. The literature shows that, as an elastic wave, AE has longitudinal and transverse waves and surface waves generated by the first and second waves hitting against interfaces and the propagation velocity of longitudinal waves is highest, those of transverse and surface waves being about 60%.[8] In terms of energy, the surface waves are highest, transverse waves have about half the energy of surface waves and longitudinal waves have very low energies compared with the others. Thus, a delay in rising time can be understood by considering that the transverse and surface waves at high energy levels reach the sensor later than the longitudinal wave which is fastest and has low energy.

Secondly, the AE duration can be read from the dual counter by determining a suitable discriminative level for threshold level. For discriminative level, with two levels V_H and V_L determined as shown in **Fig. 1**, the interval between the rising AE signal passing V_H and the falling AE signal passing V_L is counted as a duration. The results of our test proved that with the steel plate, the duration is much

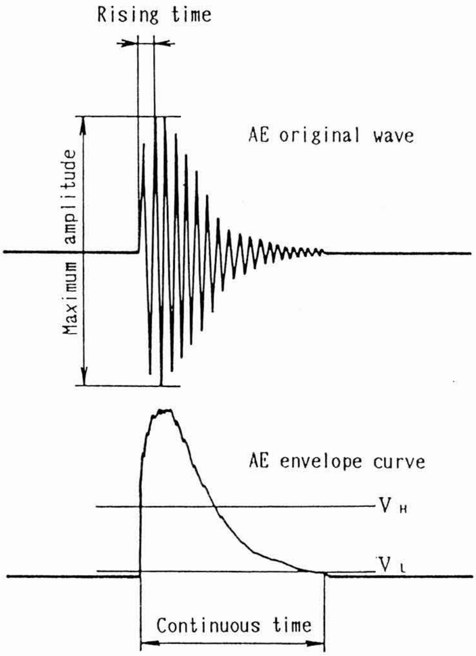

Fig. 1. Definition of analysis of AE signal.

longer than with the acrylic and plywood plates. Generally, with a medium which is sufficiently large to enable the effect of reflection to be neglected, the attenuation of elastic waves is almost completely governed by spread and internal friction losses. If the medium is a finite flat plate, there is also the effect of multireflection involved, causing elastic waves to attenuate slowly. Thus, it is considered that with steel plates, the effect of multireflection is larger than with other materials.

In actual grinding, such tools as vises are often used to secure the workpieces. In such settings, the work pieces are not simple flat plates and the effect of multireflection may be considerably complicated. However, it is expected that if the results of basic tests are taken into account, variations of AE waveforms with the workpiece materials can be adequately studied in actual grinding tests.

3. Experimental

To detect AE in grinding, a sensor was mounted on the table of a surface grinding machine as shown in **Fig. 2**. Using samples (S45C, 2A) notched as shown in **Fig. 3** and a WA grinding wheel, we conducted tests making a specific

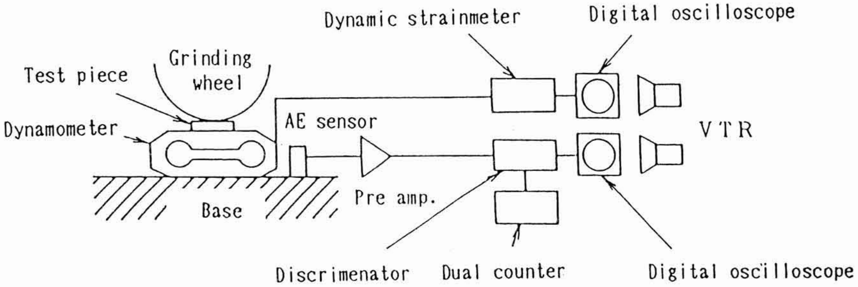

Fig. 2. Measuring circuit of AE signal and grinding resistance.

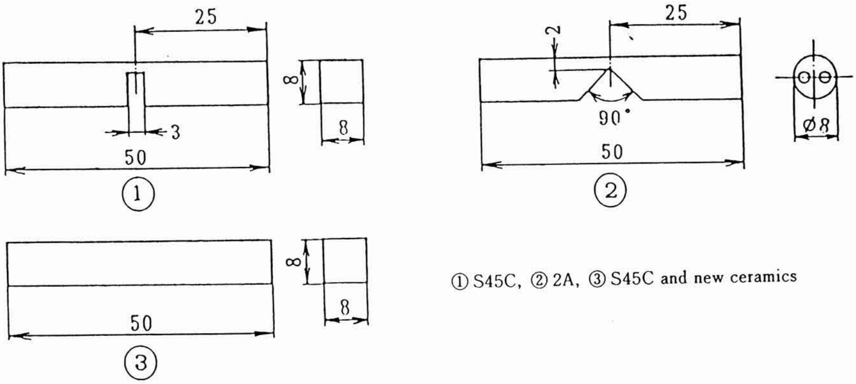

① S45C, ② 2A, ③ S45C and new ceramics

Fig. 3.Test pieces.

dry cut per pass with a circumferential wheel speed of 25.6m/s until the workpiece was ruptured.

In ordinary grinding, using a dynamometer, we also detected the grinding resistance in the tangential and vertical directions. Because of the performance of the analysis system, dynamometry and AE signal detection were alternated in about 10 cycle steps in grinding.

Table 1 shows the grinding conditions. The materials of the workpieces were 2A, WA and SiAlON; S45C was also used for comparison.

Table 1. Data for grinding condition.

Grinding wheel	SDC170N75B, 300×25×76.25 WA60H6V, 275×25×76.25
Test piece	S45C 2 A W A SiAlON
Wheel speed	SDC : 28.1m/s W A : 25.6m/s
Table speed	26m/min
Depth of cut	6, 20, 40μm
Grinding fluid	Solution type (JIS-W2)

4. Results and Discussion

Figure 4 shows AE waveforms. In each frame, the top represents the original waveform and the bottom, the envelope. The horizontal and the vertical axes represent sweep time and amplitude respectively. In (a) and (b) for workpieces material S45C, loads on both side of the sample without notches fluctuate so impulsively that the amplitude of the AE waveform was increased. Also, there is a rise in the waveform at the center corresponding to the notch. (c) and (d) are for 2A. Without notches, there are no variations in the AE waveform over the full area of the sample. The AE waveform obtained at the moment of fracture is shown in (d). When the notch ruptures, the AE waveform is greatly increased.

Figure 5 shows AE waveforms and grinding resistance of new ceramics being ground and surface conditions and roughness after grinding. The conditions for grinding new ceramics are the use of a diamond wheel, dry, and depth of

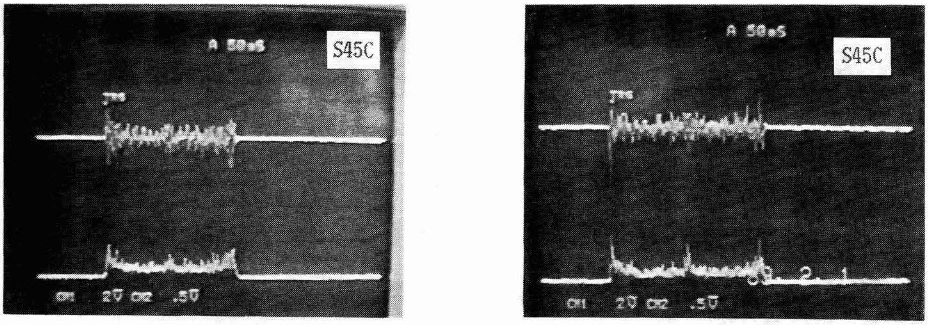

(a) Notchless (b) Notched

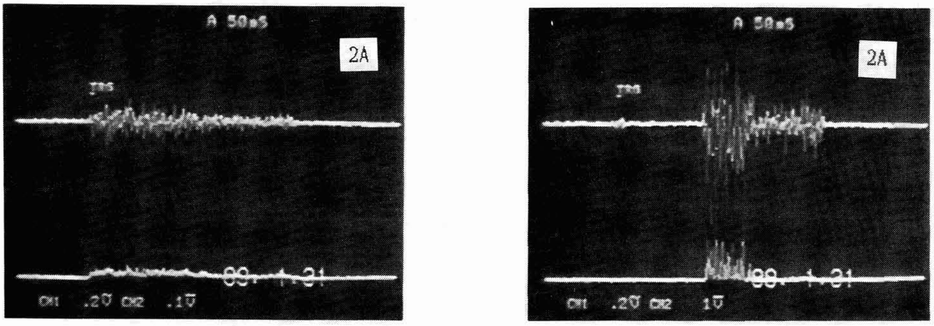

(c) Notchless (d) Notched

Fig. 4. Comparison of AE signal between S45C and 2A.

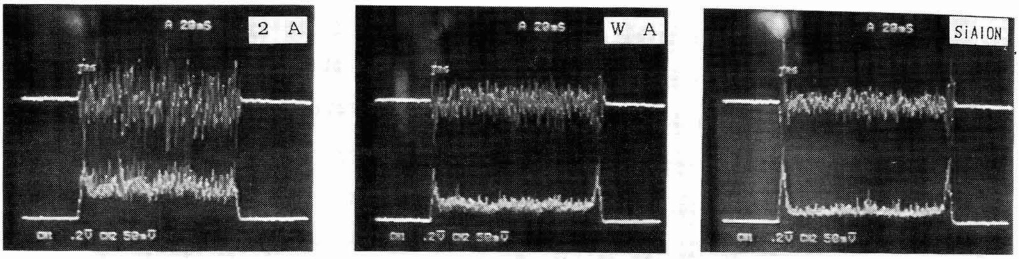

(A) AE signal

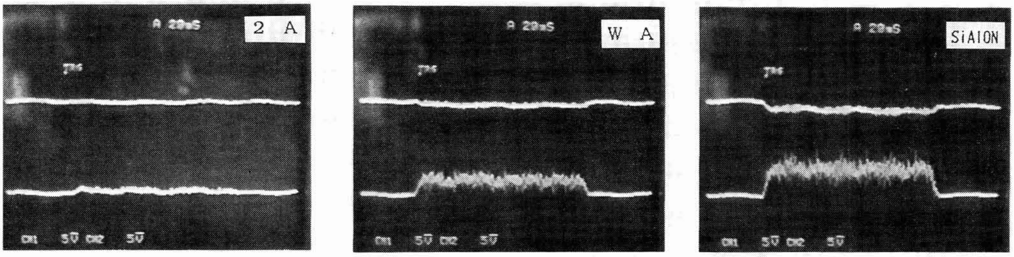

(B) Grinding force

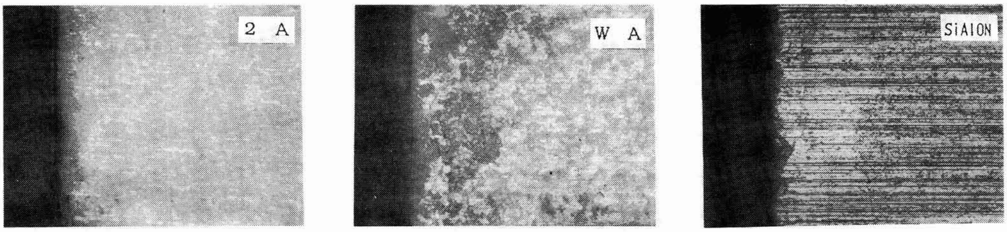

(C) Typical surface state and chipping

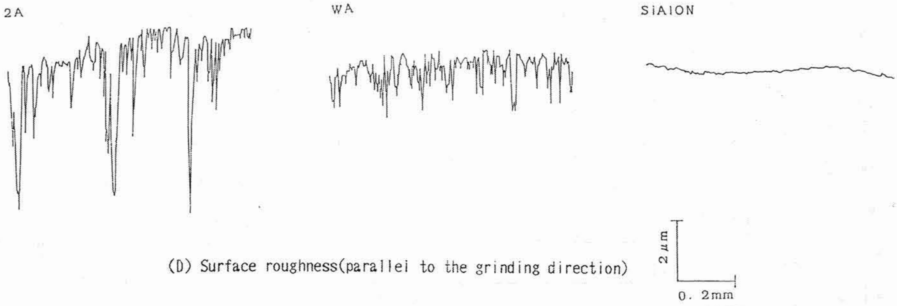

(D) Surface roughness(parallel to the grinding direction)

Fig. 5. Comparison of dynamic behavior and surface integrity among 2A, WA and SiAlON.

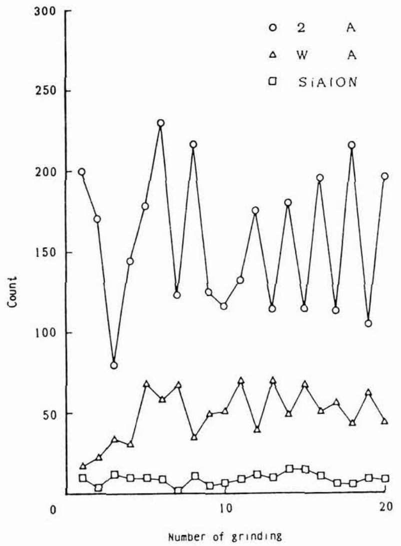

Fig. 6. Variation of AE count.

cut constant at 6μm. The grinding resistance of the materials is in the order: SiAlON, WA and 2A. The AE levels are the reverse: 2A, WA and SiAlON. The end faces of the samples show increased amplitudes due to impact loads, which are particularly prominent with SiAlON and WA. With 2A it is not prominent because the fracture was considerable throughout the sample.

The photographs of surfaces and the graphs of surface roughness for 2A and WA show signs of decay like little fractures. In contrast, the data for SiAlON shows machining marks (grinding streaks), and signs of material removal like plastic deformation as with metallic materials, which proves the remarkable deformation ability for the material.

Concerning AE signal processing, it is generally recognized that while sudden AE signals are generated with brittle materials, continuous AE signals are generated in fatigue fracture of metal materials.[9] However, the machining of brittle materials as in the present study covers wide areas from normal grinding involving fine fracture to so-called brittle fractures of materials. Thus, because of treating data like continuous AE in precision machining, it is important to measure AE counting rates.

Figure 6 shows AE counting with new ceramics. Compared with SiAlON and WA, 2A shows much higher AE counts. WA shows counts about 5 times higher than those for SiAlON, suggesting SiAlON suffers fewer fractures due to cracks. In addition, with all materials, counts fluctuate with cycles of grinding. This is partly because of internal scatter of crystal grain size, porosity and bonding state in the materials and variations of AE energy accumulation and release level with materials. Thus, it was proved that if continuous fractures also occur in brittle materials, an effective method is to measure counting rates often used for ductile materials.

All the results above proved that AE signals were closely related with surface conditions (roughness) or fracture patterns. We have not yet studied cracks in sample surfaces or interiors. An investigation using electron microscopy, etc., will be carried out in the future.

5. Conclusions

Through surface grinding of new ceramics, we found the following results:

1) AE amplitudes and durations varied with the media carrying the AE sensors.

2) The amplitudes of the AE waveforms during grinding were increased pulsewise corresponding to the notches in the samples. Such signals can be easily discriminated from those obtained in grinding flat materials.

3) With new ceramics, it was proved that among various materials, increases in grinding resistance were not always consistent with those in AE amplitude.

4) In summary, AE analysis is an useful method. It is further necessary to determined quantitatively the relationship between the surface and internal conditions of materials and the dynamic behavior of the materials during grinding. This will be done in the along with the analysis of cracks in samples.

Acknowledgments

In the present study, Prof. Miyagawa at Oita University and Prof. Matsuo, Dean of the Engineering Dept., Kumamoto University gave us a great deal of help. Technicians Goto and Arita and final year students Niizawa and Sagara helped us manufacture the test apparatus and conduct tests. We express our sincere thanks to them.

References:

1) K. Sakai and M. Ito, Journal of Japan Society of Lubrication Engineers, Vol. 33, No. 1, p509 (1988).
2) T. Nishida and E. Yasuda, Evaluation of Dynamic Characteristics of Ceramics, Nikkan Kogyo Shinbun, p185 (1986).
3) M. Koizumi and M. Yanagida, Basics of Fine Ceramics, Ohm Publishing, p18 (1987).
4) H. Saito, Utilization of Fine Ceramcis, Part I, Taiga Publishing, p137 (1986).
5) T. Matsuo and K. Oobuchi, Precision Molding and Grinding of Fine Ceramics, data by Ceramics Study Group, p1 (1988).
6) Y. Kakino, H. Eda and K. Kishi, Detection Using AE of Start of Contact between Grinding Wheel and Workpiece, preprint for the Japan Society of Precision Engineers, p106 (1981).
7) H. Eda, K. Kishi, S. Natsu and M. Ogura, Inprocess Detection Using AE of Grinding Cracks in Fine Ceramics, Transactions of the Japan Society of Mechanical Engineers, Vol. 55, No. 511, p797 (1989).
8) M. Onoe, K. Yamaguchi, H. Nakasa, K. Sano, E. Isono and T. Watanabe, Basics and Applications of Acoustic Emission, Corona Pub., p16 (1976).
9) M. Onoe, K. Yamaguchi, H. Nakasa, K. Sano, E. Isono and T. Watanabe, ibid., p72 (1976).

This article is a full translation of the article which appeared in Nippon Seramikkusu Kyokai Gakujutsu Ronbunshi (Japanese version), Vol.98, No.6, 1990.

Precise Control of Shrinking Rate during Sintering

Osami Abe

Government Industrial Research Institute, Nagoya
1-1 Hirate-cho, Kita-ku Nagoya 462, Japan

A technique for precise control of shrinking rate up to high densities during sintering has been developed using a specially designed dilatometer. The detected shrinkage was periodically fed into a microcomputer system to calculate heating rate as a control parameter by a function optimized for densification behavior. By improving the accuracy of shrinkage measurement and optimizing the control function, the shrinking rate could be controlled within the accuracy of ±3% up to high densities above 95%. It was possible to reduce the grain size of sintered bodies remarkably by this precise control. This technique also contains the multi-step and functional controls of shrinking rate according to preset profiles as a function of time or shrinkage, where the accuracy was ±5% up to a density of more than 96%.

[Received November 1, 1989; Accepted March 12, 1990]

Key-words: Shrinking rate, Precise control, Accuracy, Alumina, Grain size

1. Introduction

It is well known that in order to improve the properties of ceramics for either structural or functional applications, reduction of the grain size and limiting the formation of defects are important. Thus, high-purity fine powders are often used as the starting materials for sintering. With fine powders, however, sintering by heating to a sufficiently high temperature to produce highly densified sintered bodies greatly promotes grain growth and may also induce defects during rapid densification.

To eliminate the development of such unfavorable microstructures in heating, Palmour et al. have developed a rate-controlled sintering method which controls the shrinking rates to relatively low levels.[1-4] Reportedly, magnesia-containing alumina and spinel obtained by this method have smaller grain sizes than those made by ordinary sintering methods.[1-3] However, for high-purity alumina, the grain size is much the same as that obtained with a short hold time after heating at a constant rate, not showing as good results as expected.[1] The method of Palmour et al. feeds the measured shrinkage directly back to the temperature controller and controls the temperature so that the shrinking rate will be constant. The controllable range by this method is below 90% relative density.[1,2] The above results are due to the fact that the latter part of the sintering process, closely related to the grain growth and the microstructural development in particular, was uncontrolled. Additionally, in their reports, the density increasing curves during control showed fluctuations, which suggests that control was inadequate. The performance of sintered products will be increased by the rate-controlled sintering method by improving the drawbacks mentioned above and optimizing the conditions for the easily sinterable powders available today.

Thus, we studied methods for controlling the shrinking rates up to a relative density of 95% or above, at which the microstructure develops particularly rapidly, by improving the accuracy of shrinkage measurement and controlling the shrinking rates with the help of a microcomputer. In the method reported here, the shrinking rates are not only controlled constantly but also in several steps to cope with microstructural development estimated during sintering or by some functions determined beforehand.

2. Equipment

The equipment used in the rate-controlled sintering method consisted of a shrinkage measurement section and an operation and control section. **Figure 1** shows the outline of the shrinking measurement section. It is a constant

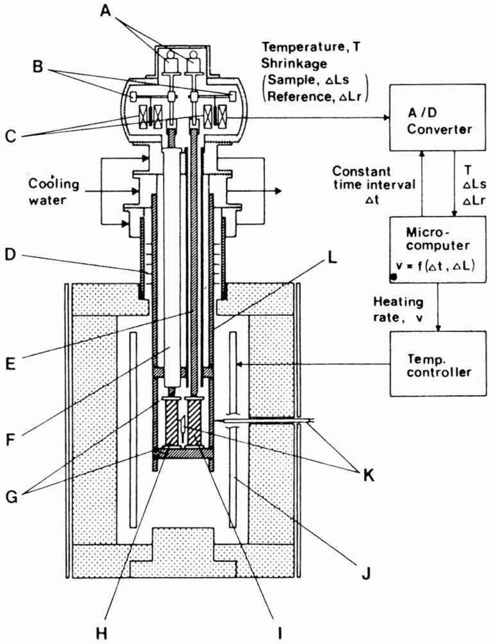

Fig.1. Inside view of dilatometer for controlling shrinking rate. A: Weight, B: Counterweight, C: Transducer, D: Radiation shield, E: Detector, F: Sleeve, G: Spacer, H: Reference, I: Sample, J: Heating element, K: Thermocouple, L: Sample holder.

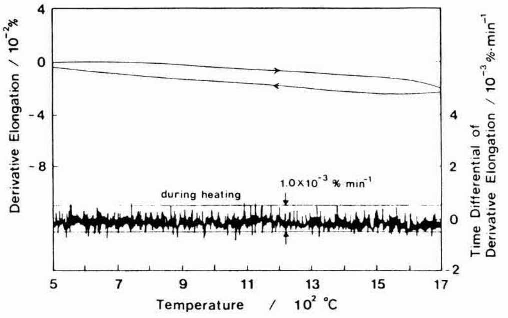

Fig. 2. Measurement accuracy of shrinkage and shrinking rate. The accuracy of detecting shrinkage and shrinking rate was expressed as the derivative elongation and the time differential of the derivative elongation, respectively. Sample: α-Al_2O_3, Heating rate: 5K min^{-1}, Load: 10g.

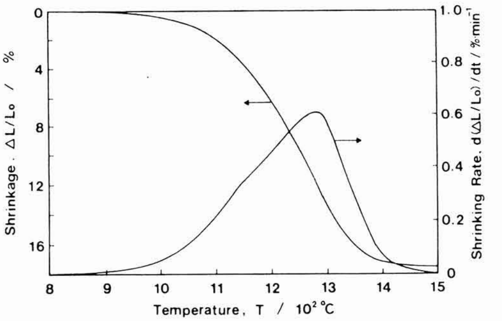

Fig. 3. Temperature dependence of shrinkage and shrinking rate of high-purity alumina at the constant heating rate. Heating rate: 5K min^{-1}, Load: 10g.

load differential pushrod type with a similar shrinkage detection mechanism to the shrinking rate measurement system for non-oxides reported previously.[4] Sample (I) and a standard sample (H, high-purity sintered alumina) were placed in the sample holder (L). The shrinkage was detected by differential transformer (C) via detector bar (E) in contact with the top of the sample. The weight of the detector bar was balanced with counterweight (B) of the balance at the top of the equipment and the load during measurement was kept constant by weight (A). The sample system (E-G, L) was made of high-purity alumina. The thermocouple (K) was Pt-Rh(6-30). The highest heating temperature was 1750°C and the maximum heating and cooling rates were 80K min^{-1} (above 500°C) and 40K min^{-1} (down to 1100°C), respectively. The maximum size of samples accepted was 50×20×20mm, which enabled the preparation of test bars for the JIS flexural strength test after rate-controlled sintering.

The shrinkage(ΔL_s) of the sample, the thermal expansion(ΔL_r) of the reference material and temperature(T) were A/D converted and input into a microcomputer at a constant time interval(Δt). The microcomputer corrects the shrinkage referring to the thermal expansion of the standard sample, computes a heating rate (or cooling rate, V) to control the shrinking rate to a preprogrammed value, outputs the results to the temperature controller and records the data obtained. To correct shrinkages, the coefficient of thermal expansion of the standard sample (sintered high-purity alumina) approximated by a 5th power function was used.

3. Method for Controlling Shrinking Rates

In the equipment used, the shrinking rate was controlled by obtaining the shrinking rate: (R) as estimated after time Δt from the measured and corrected shrinking rate (linear shrinking rate: $d(\Delta L/L_0)dt$; ΔL: corrected shrinkage, L_0: length of the sample), further obtaining the heating rate(ν) as a function of R and controlling heating.

The estimated shrinking rate(R) was obtained from the data on the shrinking rates (Rn to Rj = $[d(\Delta L/L_0)/dt]_n$ to $[d(\Delta L/L_0)/dt]_j$) for total j+1 measured values j steps backward from the latest measured value (Rn) by using the following equations:

$$R = R_n + \sum_{i=1}^{j} \frac{2^{j-i} \cdot (R_{n-j+1} - R_{n-i})}{C} \quad \ldots\ldots (1)$$

$$C = \sum_{i=1}^{j} 2^{j-i} \quad \ldots\ldots\ldots\ldots\ldots\ldots (2)$$

Equation (1) has a correction factor using a shrinking rate difference added to Rn. Here 2^{j-1} is the weighting for each shrinking rate difference and C is a constant to equate the sum of weightings to 1.

When obtaining a heating rate as a function of an estimated shrinking rate, it is important to correctly estimate the response of the shrinking rate to heating rate variations. Such response can to some extent be estimated from several sintering rate equations.[6-8] In practical sintering processes, however, the response may vary in a complicated way beyond estimation by variations in sintering mechanisms and microstructure due to phase transition and the rate of chemical reactions and sintering. Thus, on the basis of the item proportional to the yth power (y: integer 1 or above) of the relative deviation between the shrinking rate setting (R_p) and the estimate (R), we obtained controlled heating rate (V_p) by making the following corrections expected from sintering rate equations.

(a) According to Kingery, the shrinking rate during the initial sintering at a constant temperature can be given by

$$\frac{d[\Delta L/L_0]}{dt} = k \cdot r^{-m} \cdot t^{-n} \quad \ldots\ldots\ldots\ldots (3)$$

(k: rate constant, r: grain size, m and n: positive constants)

This equation shows that as the grain size r and time t increase, the shrinking rate decreases. With the estimated shrinking rate in equation (1), on the other hand, no such decreases are taken into account. Even if there is no devi-

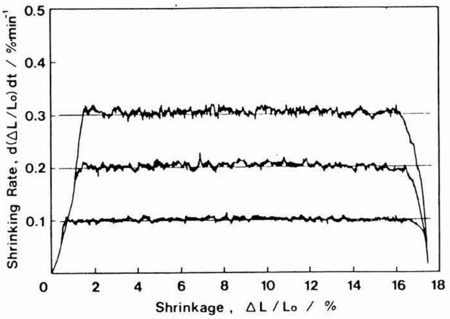

Fig. 4. Shrinking rate of high-purity alumina as a function of shrinkage. The shrinking rate was controlled to constant values (0.1–0.3% min^{-1}). Load: 10g.

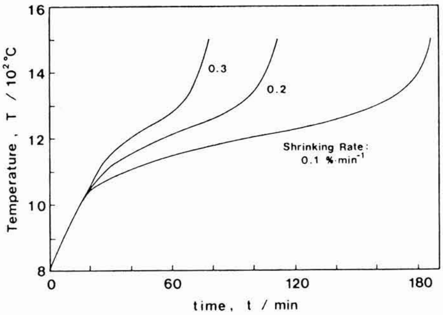

Fig. 5. Temperature profile during control of shrinking rate.

ation between the predetermined and estimated shrinking rates, the shrinking rate decreases must be compensated for by continuously raising the temperature.

(b) It is considered that the effect of grain size is small in the initial sintering but increases during sintering and that in the final stage of sintering, the shrinking rate is further reduced by the influence of variations in particle shape in addition to grain growth and the generation of closed pores. It is also considered that generally, the closer the shrinking is to its theoretical value, the less the driving force for densification becomes. Thus, while the greater the density becomes, the greater the temperature rise that is needed to increase the shrinking rate, in contrast with a slight temperature fall is necessary to reduce the shrinking rate.

From this reasoning, for the effect in (a), we made corrections by adding a certain heating rate to the term of the shrinking rate difference. For the effect in (b), which is related to the progress of sintering, we added a correction term which shows that as the theoretical shrinkage is approached, the heating rate increases and thus we obtained the following basic control equation:

$$V_p = C_1 \cdot \left[\left(\frac{R_p - R}{R_p} \right)^y \cdot (V_m - V_0) + V_0 \right]$$

$$+ C_2 \cdot \left[\frac{(\Delta L/L_0)}{(\Delta L/L_0)_{th}} \right] \cdot (V_m - V_0) \; . \; . \; . \; . \; . \; . \; . \quad (4)$$

where C_1 and C_2 are constant, $(\Delta L/L_0)_{th}$ is theoretical shrinkage and V_m is the limit of heating rates. This limit value was used to prevent heating rates from exceeding the control range of the apparatus (maximum heating and cooling rates: 80 and 40 $Kmin^{-1}$, respectively). The term with coefficient C_1 is the conversion term for the deviation between the setting and the estimate $[(R_p\text{-}R)/R_p]$. It is a function of yth power which passes V_0 when $(R_p\text{-}R)/R_p$ is zero. With R=0, its maximum is $C_1 \cdot Vm$. The term with coefficient C_2 is a correction term by shrinkages. When the theoretical shrinkage is reached, the second term is at its maximum $C_2 \cdot (V_m - V_o)$. Thus, V equals $C_1 \cdot V_m$ at the start of sintering and $(C_1+C_2) \cdot V_m - C_2 \cdot V_0$ at the end of sintering.

To further optimize the controlled heating rate in equation (4), following ordinary PID control, we obtained the following integral and differential components (V_I and V_D):

$$V_I = V_I^0 + V_p \cdot \Delta t \cdot (I_0/100) \; . \; . \; . \; . \; . \; . \; . \; . \; . \; . \; . \quad (5)$$

$$V_D = V_D^0 - V_D \cdot (D_0/100) \; . \; . \; . \; . \; . \; . \; . \; . \; . \; . \; . \; . \quad (6)$$

where V_I^0 and V_D^0 are the settings of the components Δt before and I_0 and D_0 are the weights of the components. From the equation above, we calculated the controlled heating rate by using the following equation:

$$V = V_p + V_I + V_D \quad . \; . \; . \; . \; . \; . \; . \; . \; . \; . \; . \; . \; . \; . \quad (7)$$

The representative values of the control constants for controlling shrinking rates at relatively low levels were y=1, C_1=C_2=1, V_m=10 to 40$Kmin^{-1}$, V_0=2 to 5$Kmin^{-1}$, I_0 =5 to 15 and D_0=2 to 10. The end of control was determined as either when the shrinkage previously specified is reached or when the specified temperature is reached. When the end of control was detected, the sample was heated up to the final temperature setting. The sample was held at that temperature for a certain time and was then cooled.

4. Accuracy for Measurements of Shrinkage and Shrinking Rate

Figure 2 shows the measurement accuracy for shrinkages and shrinking rate with the use of sintered high-purity alumina for both standard and test samples, represented by derivative elongation and the time differentials, respectively. Here, no corrections in reference to the standard sample were made. The maximum drift of the derivative elongation was -2.4×10^{-2}%. This value can be converted into a linear thermal expansion coefficient of $-2 \times 10^{-7}K^{-1}$, which when compared with that of quartz glass ($5.5\times10^{-7}K^{-1}$/<1000°C[9]) suggests that the measurement accuracy is sufficiently high. The scatter of the time differential of differential displacements was within $\pm5\times10^{-4}$ % min^{-1} and its standard deviation was 1.1×10^{-4}% min^{-1}. Even if the shrinking rate is con-

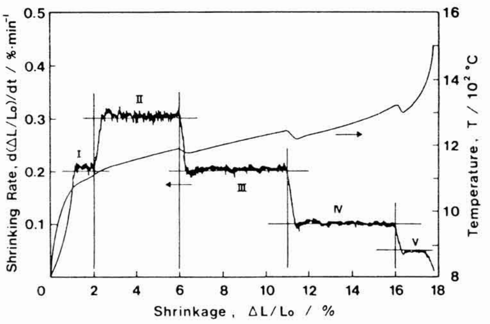

Fig. 6. Shrinking rate and temperature profile during multi-step control of shrinking rate of high-purity alumina. Load: 10g. Programmed values: Step 1 (0.2% min^{-1}, –2% shrinkage), Step II (0.3% min^{-1}, 2-6%), Step III (0.2% min^{-1}, 6-11%), Step IV (0.1% min^{-1}, 11-16%), Step V (0.05% min^{-1}, 16%–).

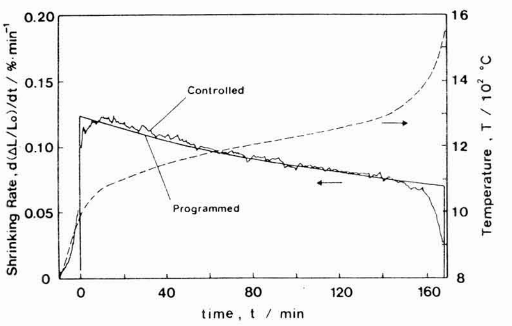

Fig. 7. Shrinking rate and temperature profile of high-purity alumina during controlling shrinking rate as a function for a constant rate of increasing density. Load: 10g.

trolled to 0.1% min^{-1}, this value is about 1/200 of the setting, sufficiently small to enable the influence on shrinking rate control to be neglected.

5. Rate-Controlled Sintering of Alumina

Using the equipment and the control technique described above, we conducted rate-controlled sintering of high-purity alumina (Tamicron TM-D, Taimei Kagaku, purity: 99.9%, specific surface area: 13.6m^{2}g^{-1}). The green compacts were prepared by die-pressing alumina powder into 45 ×15×15mm blocks and then further CIP- molding under 300MPa. The relative density and the theoretical shrinkage of the green compacts were 55.71% and 17.72%, respectively. Initially, the compact was sintered by heating at a constant rate of 5Kmin^{-1} and obtained the temperature dependence of shrinkage and shrinking rates as shown in **Fig.3**. Although a shoulder is observed at 1130°C, the shrinking rate curve is relatively smooth. After holding for 10 min at 1500°C, a sintered body with a relative density of 96.4% was obtained.

Figures 4 and **5** show the relationships between shrinking rates or shrinkages and temperature profiles for the alumina compact being sintered under rate control. Three shrinking rate settings between 0.1 and 0.3% min^{-1} were chosen referring 1/2 of the shrinking rate peak (0.6% min^{-1}) in Fig.3. For control the following parameters are used: y=1, V_m=10Kmin^{-1}, V_0=3Kmin^{-1} and C_1=C_2=1. The other control parameters were chosen as appropriate within the range mentioned above. Figure 4 shows that the control accuracy was within ±3% of the settings and that shrinking rates were well controlled with shrinkages to16.7% (setting: 0.1% min^{-1}) or16.2% (0.3% min^{-1}). The shrinkages here suggest that control is possible up to 96 and 95% relative density. Reflecting the high accuracy of shrinking rate control, the temperature profiles are smooth upward curves. Also, the inclinations of the temperature profiles show that the heating rates rise rapidly in temperature ranges over 1300°C. With low shrinking rate settings, however, the slopes vary slightly around 1300°C, causing the maximum of the relative density effective for shrinking rate control to rise.

6. Multi-Step and Functional Controls for Shrinking Rates

For better control of sintering, we studied multi-step control of shrinking rates and functional control using the shrinking rate-time (or shrinkage) profiles. For multi-step control, the control steps were specified in terms of shrinkages. The determination of the end of each step was the same as in controlling shrinkages to a constant level. **Figure 6** shows the control accuracy levels and temperature profiles in controlling the shrinking rates of high-purity alumina compacts by 5 steps within the range from 0.3 to 0.05% min^{-1}. The control constants were the same as in controlling shrinking rate to a constant level. In any step, the scatter was within about ±3% of the setting. The time needed for transfer from one step to another was about 1 or 2 min and a shorter time was needed when the setting was decreased than when it was increased. Directly after a setting was achieved, there was a positive (when the setting was increased) or negative (when the setting was decreased) fluctuation, although it was not so large as to cause the control accuracy to fall significantly. Also, the setting for the final step was determined as 0.05% min^{-1}, allowing the maximum relative density to rise to 97%.

Functional control was achieved by determining the point when the shrinking rate reached the initial setting (R_0) as t=0 and rewriting setting (R_p) at each time interval Δt. When controlling shrinking rates as a function of time or shrinkage, R_p is determined by the optional functions:

$$R_p = f(t) = f(n\times\Delta t) \quad \ldots\ldots\ldots\ldots\ldots \quad (8)$$

$$R_p = g(\Delta L/L_0) \quad \ldots\ldots\ldots\ldots\ldots\ldots \quad (9)$$

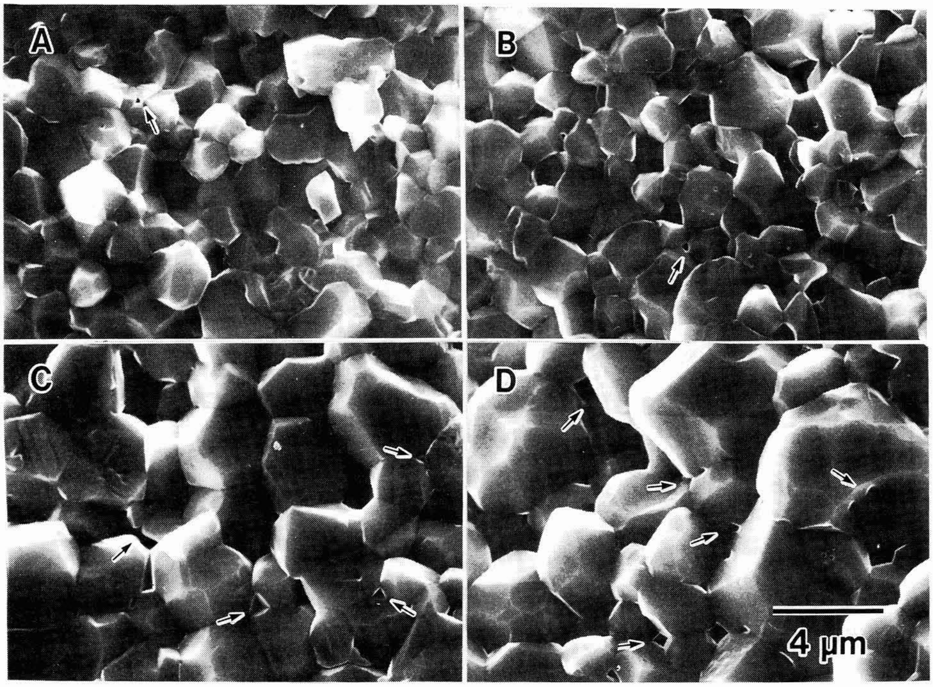

Fig. 8. Microstructure of sintered bodies prepared by rate controlled sintering (A and B) and constant heating rate (C and D). Final heating condition: 1500°C, 10min. A: Shrinking rate: 0.1% min^{-1}, Grain size: 1.07±0.36μm, B: 0.3% min^{-1} 1.23±0.38μm, C: Heating rate: 5Kmin^{-1}, 2.34±0.81μm, D: 60K min^{-1}, 2.98±1.30μm. The grain size values were obtained from SEM photographs as averages for 200 grains.

For control as a function of shrinkage, it is necessary to use an estimate at a point Δt after for $\Delta L/L_0$ in equation (9) but we did not use such estimates on the assumption that if the shrinking rate is not very high, the error in the correction term including C_2 in equation (4) as a coefficient was corrected by V_1 and V_D.

As an example of functional control, **Fig.7** shows the control accuracy and the temperature profiles in controlling the shrinking rate of a high-purity alumina compacts as a function of time which keeps a constant increasing rate in density. If the density increasing rate ($d\rho/dt$) is constant (s), with green density written as ρ_0, R_p is given by

$$R_p = \frac{1}{3} \cdot \frac{s \cdot \rho_0^{1/3}}{\rho_0 + s \cdot t} \quad \dots\dots\dots\dots\dots\dots \quad (10)$$

In Fig.7, the density increasing rate (s) and initial setting (R_0) at the start of control were determined as 0.25% min^{-1} and 80% of R_p (0.123% min^{-1}) obtained with t=0 in equation (10), respectively.

Although the results showed a control value fluctuation of about 5% of the setting directly after the start of control, they subsequently showed a high control accuracy and control was possible within ±5% of the setting with relative density up to 96% (160 min).

7. Microstructure of Sintered Materials

Figure 8 shows the microstructures at the centers of samples sintered by heating at rates of 5 and 60K min^{-1} and samples sintered with shrinking rates controlled to constant levels. To compare the grain size of sintered samples obtained by a rate-controlled sintering method with that obtained by an ordinary method, the diameters of 200 grains were measured. Figure 8 shows clearly that the grain size and the width of grain size distribution of sintered bodies can be reduced even by controlling only the shrinking rates to constant values. Also, the size and the number of the remaining pores indicated by arrows in Fig.8 were reduced. This suggests the possibility to control the microstructure precisely by extending the range of shrinking rate control towards higher density.

More data will be necessary to discuss the effect of control parameters and heating rates on grain size but such discussions are beyond the scope of this report and will be dealt with separately. When shrinking rates were placed under step control (Fig.6) or function control (Fig.7), similar decreases in grain size were observed. However, further studies are necessary to optimize the control steps and functions in accordance with microstructures.

In sintering with a heating rate of 5Kmin^{-1} (Fig.3) grains grew prominently at temperatures above 1300°C (relative density 85% or up). By the rate-controlled sintering method, on the other hand, shrinking rate control is possible in high density ranges above 95%. This suggests that the control method described here can be used to control the microstructures of sintered products by optimizing the relationship between shrinkages and shrinking rates in high density ranges.

8. Conclusions

A method to control shrinking rate during sintering up to high densities more than 95% with high controlling accuracy have been studied. A high-accuracy dilatometer applicable up to 1750°C have been developed for this purpose. The control of shrinking rate was performed by controlling heating rate according to the values obtained by a microcomputer processing of shrinkage data measured in a constant time interval. The control functions were optimized by referring the practical densification behavior. The control of shrinking rate to more than 95% theoretical density with the accuracy of ± 3% was enabled by the increased measuring accuracy of shrinkage and the optimized control functions. Multi-step control and functional control of shrinking rate according to the programmed shrinking rate-time (or shrinkage) profiles were also enalbed. By the precise control up to high densities, it was possible to eliminate severe grain growth.

Acknowledgments

The author thanks Mr. K. Kuwabara and Mr. M. Naruo for their assistance. The present study was supported in part by Research and Development Project of Basic Technology for Future Industries, AIST, MITI, Japan.

References:

1) H. Palmour III and M.L. Huckabee, "Rate-Controlled Sintering", Proc. Intl. Symp. on Factors in Densification and Sintering of Oxide and Non-oxide Ceramics, Eds. by S. Somiya and S. Saito, Hakone (Japan) 1978, pp.278-297.
2) M.L. Huckabee and H. Palmour III, "Rate-Controlled Sintering of Fine-Grained Al_2O_3", Am. Ceram. Soc. Bull., 51, 574-576 (1972).
3) H. Palmour III and D.R. Johnson, "Fine Cubic Microstructure Uniquely Achieved by Strain Induced Recrystallization During Sintering of Spinel", Am. Ceram. Soc. Bull., 49, 767 (1970).
4) S. Abe, S. Kanzaki, High-Temperature Dilatometer for Nonoxide Ceramics, J. Ceram. Soc. Japan, 97, 187-191 (1989).
5) JIS R1601-1981 for Testing Bending Strength of Fine Ceramics.
6) W.D. Kingery, "Study of the Initial Stages of Sintering Solids by Viscous Flow, Evaporation-Condensation, and Self-Diffusion", J. Appl. Phys., 26, 1205-1212 (1955).
7) W.D. Kingery, "Densification during Sintering in the Presence of a Liquid Phase. I. Theory", ibid., 30, 301-307 (1959).
8) "Sintering-Case Studies," eds. by S. Somiya and Y. Moriyoshi, Uchida Rokakuho, Tokyo, 1987.
9) "Kagaku-Binran, Kiso-hen II," ed. by Chem. Soc. Japan, Maruzen, Tokyo, 1975, p. 686.

This article is a full translation of the article which appeared in Nippon Seramikkusu Kyokai Gakujutsu Ronbunshi (Japanese version), Vol.98, No.6 , 1990.

Bias Effect on the Formation of Carbon Films by RF-Plasma CVD

Masatoshi Nakayama, Kunihiro Ueda, Masanori Shibahara, Kazunori Maruyama*, Kiichiro Kamata*

Basic Laboratory of Research Center, TDK Corporation, Nenei 113, Saku-city, Nagano 385, Japan
*Nagaoka University of Technology, Department of Chemistry, Nagaoka-city 940-21, Japan

This paper is concerned with the bias effect of additional DC voltage, which is applied between the reaction chamber and the substrate, on the properties of carbon films prepared by RF-plasma CVD. Hard carbon films (Hv≤2500) of 50 to 100nm thick were synthesized by the plasma CVD method with negative DC voltage to the substrate. The deposition rate, refractive index and microhardness of the films increased with increasing negative voltage at −140V or above. Their Raman spectra showed two broad peaks at 1350cm^{-1} and 1550 to 1580cm^{-1}. These facts suggested that the additional negative bias promoted the formation of i-carbon and/or diamond-like structures in the films.

[Received October 31, 1989; Accepted February 13, 1990]

Key words: Carbon film, RF-plasma CVD, DC bias effect, Diamond-like structure, i-carbon, Raman spectra

1. Introduction

Carbon films of various properties have been formed by RF-plasma chemical vapor deposition (CVD).[1-6] To obtain a hard film, a method employing only self-bias is commonly used. The application of a DC current in parallel with an RF-power supply has also been reported, causing the formation a phase similar to cubic diamond around room temperature.[1] However, no reports have been published on systematic studies of the changes in properties, including hardness in particular, of films produced with an added bias by DC voltage impression. The self-bias varies with the RF power, the vapor pressure and the electrode area. If the DC voltage is impressed in parallel or in series when studying the effect of the DC bias only, it is difficult to single out this effect.

Applying a DC voltage between the chamber and the substrate (the bias voltage), independent of the RF power between the parallel plates used to excite reactions, and varying it with a fixed reaction gas pressure, RF power and substrate temperature, we studied the effect on film formation rates and the refractive indices and hardnesses of the films produced.

2. Experimental

The carbon films were formed from CH_4 and H_2 using a parallel plate RF-plasma CVD system designed to apply a DC bias independently to the electrodes as shown in **Fig.1**.

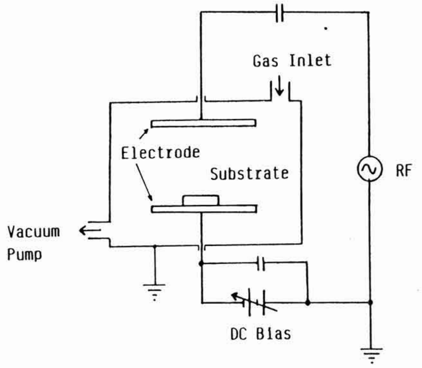

Fig. 1. Schematic diagram of RF-Plasma reactor.

The parallel electrode plates were 27×27cm and 4.0cm apart. The voltage was applied with the substrate as the negative pole. The substrates were Si(100). The synthesis conditions and properties of the samples formed are shown in **Table 1**.

An ellipsometer was used to measure the refractive indices and thicknesses of the carbon films produced. The hardnesses of the films were measured with a microhardness meter (MHA-400, NEC) which measured the Vickers hardness from the depths made by the indenter (indenting load: 5 to 15mg). To analyze the structure of the films, a laser Raman analyzer (NR-1100 Ar laser, JEOL, 514.5nm, 2W) was used. The textures were observed with a scanning electron microscope (JSM-890, JEOL).

3. Results and Discussion

Run Nos.1 to 17 in Table 1 show the experimental conditions and results using various bias voltages with a constant material feed. **Figure 2** shows the effect of the bias voltage on the film formation rates and refractive indices under the conditions mentioned above.

When the bias voltage was 0V, the carbon film formation rate was about 4nm min^{-1}. As the absolute value of the voltage increased, the film formation rate also increased. When the bias voltage was −250V, it was around 7 to 8nm min^{-1}, about twice that achieved with voltage 0V. The increases in film formation rates by bias voltage impression are considered to be due to the controlled diffusion of positive ions produced from CH_4 or H_2 and increased ion velocities, which resulted in an increase in material deposi-

Table 1. Experimental conditions and observed properties of carbon films obtained.*)

Run No.	Bias Vol. (V)	Flow rate		R.F. Power (W)	Reaction Time (min)	Film Thickness (nm)	Deposition Rate (nm min⁻¹)	Refractive Index (at 6328Å)	Vickers Hardness (kg mm⁻²)
		CH₄ (cm³ min⁻¹)	H₂ (cm³ min⁻¹)						
1	0	7.5	5	500	10	45	4.5	1.65	380
2	0	7.5	5	500	30	120	4.0	1.71	330
3	0	7.5	5	500	30	110	3.7	1.70	
4	-140	7.5	5	500	10	50	5.0	1.96	700
5	-150	7.5	5	500	60	340	5.7	2.00	
6	-250	7.5	5	500	10	80	8.0	2.15	1750
7	-250	7.5	5	500	60	410	6.8	2.10	
8	0	60	20	500	10	50	5.0	1.64	
9	-250	60	20	500	10	90	9.0	2.25	2500
10	-300	60	20	500	10	92	9.2	2.25	2500

*)The total pressure and substrate temperature were maintained at 0.025Torr and 200℃, respectively. The distance between two electrode plates (27×27cm) was 4.0cm.

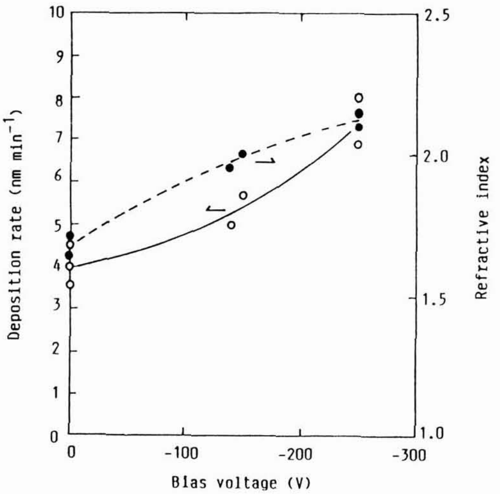

Fig. 2. Effect of bias voltage on deposition rate (○) and refractive index (●) of carbon films obtained.

tion on the substrate. Run Nos. 8 to 10 in **Table 1** show the results with an increased material flow rate, which at the same bias voltage level gave consistently higher film formation rates.

When the bias voltage was 0V, the refractive index was about 1.7. As the bias voltage rose, the refractive index also increased. When the bias voltage was −250V, it was around 2.10 to 2.15 (Run Nos. 6 and 7), close to that of diamond (2.40). If the Lorenz-Lorentz equation related to refractive indices and densities is taken into account, an increase in the refractive index of a carbon film implies an increase in the density of the film. Thus, Fig.2 implies that as the bias voltage rises to −250V, the density of the film increases. As with increases in film forming rates, the positive ions are accelerated by the applied voltage and gain translational energy. As the ions impact on the substrate, the film is compacted, causing the refractive index to increase. Also, as shown in Table 1, the hardness was greatly increased up to 2500kg mm⁻²)In addition, if a higher bias voltage over −300V is applied, the plasma is unstable. Thus, such high bias voltages were excluded from our tests.

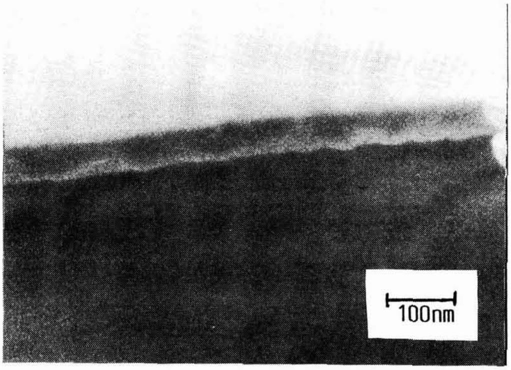

Fig. 3. SEM photograph of carbon film No.6 in Table 1.

Figure 3 shows a typical microstructure of the samples prepared. Clearly, the surface is flat and composed of very small particles. The surface and cross-sectional microstructures of the carbon films produced varied little with the bias voltage. The film thickness measured with an ellipsometer agreed, within ±1nm, with those obtained from SEM photographs.

Figure 4 shows the Raman spectra of carbon films formed with various bias voltages. The carbon film produced without a bias voltage had no characteristic peaks in the range from 1000 to 2000cm⁻¹ (Fig.4(A)). The carbon film formed with a bias voltage of −140V had broad peaks at 1580 and 1350cm⁻¹ (Fig.4(B)). With the carbon film produced with a bias voltage of −250V, the peak at 1350cm⁻¹ was weaker and the broad peak at 1550cm⁻¹ stronger compared with the previous film.

The Raman spectra of natural diamond has a sharp peak at 1332.5cm⁻¹ and the carbon film named i-carbon by Weissmantel et al. has a broad peak at 1550cm⁻¹.[9,10] Also, the Raman spectra of graphite crystals and defective graphite have peaks at 1575 and 1360cm⁻¹, respectively.[11] However, the Vickers hardness of graphite is in the range from 8 to 20(kg mm⁻²) and that of the carbon films produced with a bias voltage is above 700kg mm⁻²), which is much

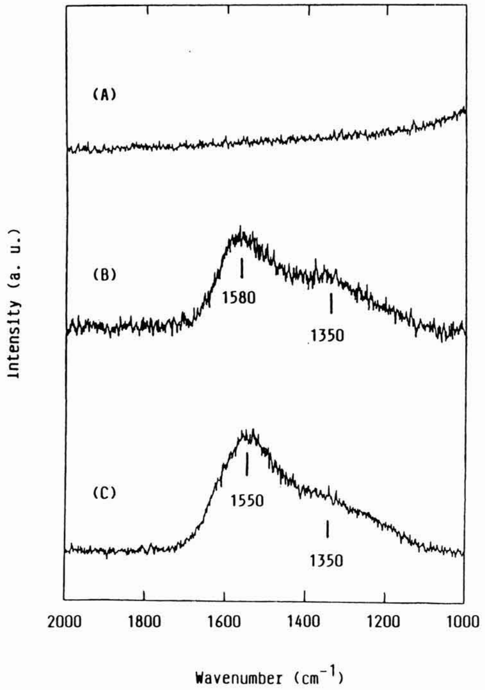

Fig. 4. Raman spectra of carbon films obtained under various bias voltages; 0V(A), −140V(B), −250V(C).

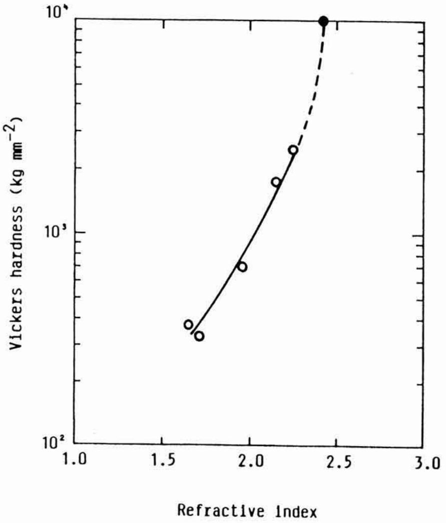

Fig. 5. Relationship between refractive index and Vickers hardness of carbon films obtained.

higher.[12] This suggests that there is very little graphite structure present. According to Sedaka et al., even if a diamond structure is detected by X-ray diffraction analysis, the sharp peak at 1333cm^{-1} is reduced and the peak at 1500cm^{-1} increased in the Raman spectrum by segregation in the crystal grain boundaries and the existence of amorphous carbon in the surface layer. Thus, in Fig.4, it is assumed that without a bias voltage, amorphous-carbon films are produced, but with a bias voltage, an i-carbon or diamond structure or a mixture is produced.

Figure 5 shows the hardnesses and refractive indices of the carbon films produced in the present test. The black dot (λ) shows the hardness and refractive index of natural diamond. This plot shows that there is a good correlation between the refractive indices and the Vickers hardnesses of the carbon films produced. Since the increases in refractive index are related to the increases in density of the films, as mentioned earlier, the trend in the figure can be understood as increases in Vickers hardness due to density increases and variations in chemical bonding.

The present study can be summarized as follows:

1)Applying a DC bias voltage in series with the PF power supply on the substrate when forming a carbon film using the RF-plasma CVD method caused the film formation rate, refractive index (max. 2.25) and Vickers hardness (max. 2500) of the film to increase greatly.

2)The structure of the films produced is considered to be the result of the generation of an i-carbon or diamond structure or a mixture accelerated by the bias voltage.

References:

1) H. Vora and T.I. Moravec, J. Appl. Phys., 52 (1981) 6151.
2) R. Mania, L. Stobierski and R. Panpuch, Cryst. Res. & Tech., 16 (1981) 785.
3) B. Dischler, A. Bubenzer and P. Koidl, Appl. Phys. Lett., 42 (1983) 636.
4) A. Bubenzer, B. Dischler, G. Brandt and P. Koidl. J. Appl. Phys., 54 (1983) 4590.
5) J.M. Mackowski, R. Pignard, N. Vendovotto, P. Robert and A. Donnadieu, J. Non-Crystalline Solids, 77 & 78 (1985) 837.
6) S. Matsumoto, J. Mater. Sci. Lett., 4 (1985) 600.
7) K. Kobayashi, N. Mutsukura, K. Yamamoto and Y. Machi: Powders and Powder Metallurgy, 34 (1987) 402.
8) H.A. Lorentz, Wied. Ann., 9 (1880) 641: L. Lorenz, ibid., 11 (1880) 70.
9) S.A. Solin and A.K. Ramdas, Phys. Rev. B 1 (1970) 1687.
10) C. Weissmantel, G. Reisse, J. Erler, F. Bewilogu, V. Ebersbach and C. Schmidt, Thin Solid Films, 63 (1979) 315.
11) F. Tuinstra and J.L. Koenig, L. Chem. Phys., 53 (1970) 1126.
12) T. Oku and E. Eto, Carbon, 12 (1974) 477.
13) Diamond Film Forming Technique, ed. by N. Sedaka, General Technology Center (1988) p.264: Y. Sato, M. Kamo and N. Sedaka, Proc. 9th Symp. on ISIAT (1985); M. Nakamizo, K. Tamai: Carbon 117 (1984) 94.

This article is a full translation of the article which appeared in Nippon Seramikkusu Kyokai Gakujutsu Ronbunshi (Japanese version), Vol.98, No.6, 1990.

Crystal Phase and Thermistor Constant of Mn-Co-Ni Oxide in Cooling Process after Firing

Takashi Yokoyama, Takeshi Meguro, Tadashi Sasamoto*, Nobuyuki Hirai, Yoshiaki Abe and Naochika Torikai**

Department of Materials Chemistry, Yokohama National University
156 Tokiwadai, Hodogaya-ku, Yokohama-shi 240, Japan
*Department of Chemical Technology, Kanagawa Institute of Technology
1030 Shimoogino, Atsugi-shi 243-02, Japan
**Technol Seven Co., Ltd.
1-3-10 Kamoi, Midori-ku, Yokohama-shi 226, Japan

Changes in crystal phase and thermistor constant of Mn-Co-Ni oxide, a thermistor material, in cooling process below 1000°C after firing at 1400°C were studied. The starting oxide was made of nitrates of Mn, Co and Ni with a molar ratio of 3.0:1.9:1.1 by firing at 1400°C. Samples were prepared by annealing the above oxide at various temperatures between 250° and 1000°C for 24 hours followed by quenching into water. Precise X-ray diffraction analysis of quenched samples revealed a good correlation between the thermistor constant B and the fractional ratio of crystal phases, such as cubic spinel, tetragonal spinel of low-temperature form and tetragonal spinel of high-temperature form, in the sample. It seemed that, in the temperature range between 560° and 650°C, there existed very complicated crystal structures in which the fractional ratio of cubic spinel and tetragonal spinel of high-temperature form varied intricately. Therefore, it is assumed that the change in thermistor constant observed at around 550° to 650°C in the previous paper[4] can be attributed to the very complicated changes of fractional ratio of cubic spinel and tetragonal spinel of high-temperature form in annealed samples.

[Received October 30, 1989; Accepted February 13, 1990]

Key-words: Mn-Co-Ni oxide Phase transition Spinel Thermistor Thermistor constant

1. Introduction

The annealing conditions, crystal structure and electric properties of transition metal oxide thermistor materials have already been investigated by the authors.[1-7] However, unclarified points still remain about the relationship between the thermistor properties and crystal structures.

The previous paper[4] reported that the thermistor constant (constant B) of Mn-Co-Ni oxide changed considerably at around 600°C in the cooling process after firing at 1400°C. It was also assumed that, since around this temperature a crystal structure change from tetragonal spinel of the low temperature form to the high temperature form was observed, the above change in constant B might be partly attributable to the crystal structure change in the tetragonal spinel.[4] However, another cause of the change in constant B night be the change in the fractions of low temperature and high temperature tetragonal spinel, and this study investigates this possibility. In particular, precise X-ray diffraction analysis in the vicinity of (311), the maximum peak of spinel, was conducted, followed by peak separation, to obtain the frctions of cubic spinel, tetragonal spinel of the low and high temperature forms, and the relationship between crystal change and the change in constant B.

2. Experimental

The starting material was made of nitrates of Mn, Co and Ni with a molar ratio of 3.0:1.9:1.1. After weighing, mixing and evaporation to dryness, it was calcined at 1000°C for 3hr and fired at 1400°C for 1hr, then allowed to cool in the furnace. The starting material, thus obtained, was again annealed for 24hr at a temperature between 250°C and 1000°C followed by quenching to prepare specimens for X-ray diffraction analysis. The preparation of the starting material and specimens for X-ray diffraction all used the same conditions as reported in the previous paper.[4]

To investigate the fractions of tetragonal spinels of low and high temperature form and cubic spinel in the annealed specimens, precise X-ray diffraction analysis in the vicinity

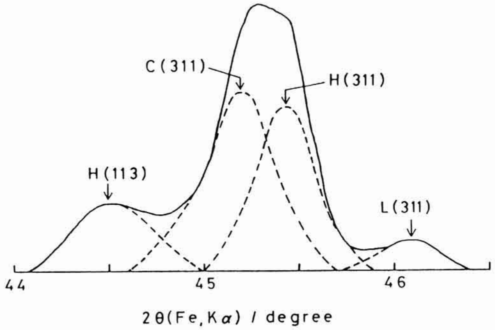

Fig. 1. Peak separation of X-ray diffraction profile (311) in the oxide heat-treated at 590°C.
C:Cubic spinel,
H:High-temperature form of tetragonal spinel,
L:Low-temperature form of tetragonal spinel

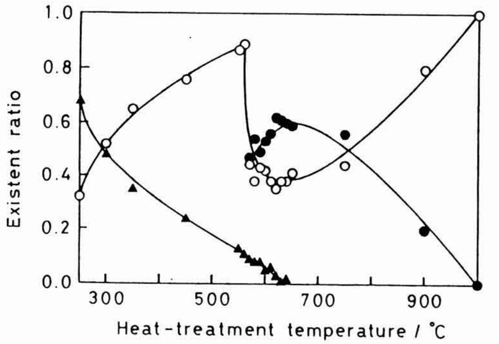

Fig. 2. Relationship between heat-treatment temperature and existent ratios of cubic and tetragonal spinels in Mn-Co-Ni oxide.
○:Cubic spinel,
●:High-temperature form of tetragonal spinel,
▲:Low-temperature form of tetragonal spinel

of (311), the highest peak of specimens, was conducted, followed by peak separation, as shown in Fig.1, with the peak areas used to calculate fractions. Considering the multiplicity factor of X-ray diffraction analysis,[8] the peak areas of low- and high-temperature form tetragonal spinels were calculated by adding peak areas of (113) and (311). In EPMA observation, the crystal phase of rock salt structure in the specimen distributed separately like as islands[4] and their content was small. Therefore, we considered that their contribution to electical properties of the specimen was nearly negligible. The conditions of X-ray diffraction were Fe target, 20kV, 10mA, time constant 8 sec and scanning rate 1/8°/min.

3. Results and Discussion

Figure 2 shows the relationship between fractions of cubic spinel and tetragonal spinels of low temperature and high temperature forms contained in the samples and the annealing temperatures. There is a tendency for the fraction of tetragonal spinel of the low-temperature form to gradually decrease in the temperature range between 250°C and 600°C, reaching zero at 650°C. On the other hand, the fraction of tetragonal spinel of the high temperature form appears in the vicinity of 570°C, inreasing with annealing temperature, but decreasing over 650°C. The fraction of cubic spinel increases with temperature in the range between 250°C and 560°C but sharply decreases in the range between 560°C and 600°C, increasing again in the range between 650°C and 1000°C.

Here, the change in fraction of the spinels with the increase in annealing temperature will be discussed.

In the previous paper[4], the authors investigated the crystal structures and compositional changes of Mn-Co-Ni oxide in the cooling process after firing at 1400°C using X-ray diffraction analysis and EPMA. The results showed that the crystal structure of the Mn-rich phase forming the matrix was mixed crystal of cubic spinel and tetragonal spinels, indicating that in this composition of the Mn-rich phase, the Mn, Co and Ni contents remained almost constant at temperatures below 450°C while the Mn content tended to decrease with an increase in annealing temperature over 450°C with the Co and Ni contents increasing.[4] Considering the above point, the increase in cubic spinel in the temperature range between 250°C and 560°C as confirmed in this study is attributable to the low temperature tetragonal spinel undergoing a phase change to cubic spinel which is a high-temperature stable phase.[6] On the other hand, the increase in cubic spinel in the temperature range between 650°C and 1000°C is attributable to the tetragonal spinel of high temperature form undergoing a crystal change to cubic spinel and the tetragonal spinel of high temperature form undergoing a phase change to cubic spinel that is a high-temperature phase[6] due to the decrease in Mn content in the Mn-rich phase with the increase in annealing temperature[4] in the temperature range between 650°C and 900°C. Also, the large decrease in cubic spinel at around 600°C is due to the decrease in Mn content in the Mn-rich phase in the temperature range between 450°C and 650°C.[4] It is assumed that the crystal change mentioned above corresponds to the change in Mn^{3+} ion concentration on octahedral sites in the spinel phase.[2-4]

Next, the relationship between the abundance of each spinel and the constant B will be discussed.

As mentioned in the introduction, the authors confirmed in the previous paper[4] that the constant B of Mn-Co-Ni oxide measured in the cooling process after firing at 1400°C changed considerably at around 600°C. Because of the crystal change from low-temperature tetragonal spinel to the high-temperature form at around this temperature, it was assumed that the large change in the constant B was attributable to the crystal change of tetragonal spinels.[4] As other causes for the change in the constant B such as the fractions of tetragonal spinels of low temperature and high temperature form could be also involved, this study confirmed that the fractions of cubic spinel and tetragonal spinel of the high temperature form varied in a complicated way in the temperature range between 570°C and 650°C as shown in Fig.2. In this case, it seems that hopping conditions vary either for cubic spinel or for tetragonal spinel of the high-temperature form.[5,9-11] Thus, the results of this study seem to show that constant B varies with the complicated change in the fractions of the spinels forming the matrix phase. Further, it is inferred that, since the fraction of low-temperature tetragonal spinel is very small at around 600°C, it is not related to the change in constant B.

From the above, it is assumed that the large change in constant B of Mn-Co-Ni oxide at around 600°C can attributed to the change in fractions of cubic spinel and tetragonal spinel of the high-temperature form forming the matrix phase, as shown in this study, besides the large change in the axis ratio of tetragonal spinel.[4]

Since the relationship of the crystal structures and the electrical properties of Mn-Co-Ni oxide is complicated, it is necessary to conduct various measurements using the single phases of spinels to investigate it thoroughly. As the preparation of single phase samples is very difficult, none of them has been obtained. However, the results obtained from this study will increase our knowledge of the manufacturing process of thermistors.

References:

1) T. Meguro, T. Sasamoto, T. Yokoyama, T. Yamada, Y. Abe and N. Torikai, Yogyo-Kyokai-shi, 95, 336-340 (1987).
2) T. Meguro, T. Sasamoto, T. Yokoyama, M. Hayashi, H. Horiuchi, Y. Abe and N. Torikai, Yogyo-Kyokai-shi, 95, 1095-1100 (1987).
3) T. Meguro, T. Sasamoto, T. Yokoyama, K. Shiraishi, Y. Abe and N. Torikai, Nippon Seramikkusu Kyokai Gakujutsu Ronbunshi, 96, 338-341 (1988).
4) T. Yokoyama, T. Meguro, T. Sasamoto, S Yamada, Y. Abe and N. Torikai, Nippon Seramikkusu Kyokai Gakujutsu Ronbunshi, 96, 985-989 (1988).
5) T. Sasamoto, T. Meguro, T. Yokoyama, M. Hayashi, H. Horiuchi, Y. Abe and N. Torikai, Nippon Kagaku Kaishi, 1988, 1612-1617.
6) T. Meguro, T. Sasamoto, T. Yokoyama, K. Suzuki, Y. Abe and N. Torikai, Nippon Seramikkusu Kyokai Gakujutsu Ronbunshi, 96, 1163-1166 (1988).
7) T. Yokoyama, T. Meguro, T. Sasamoto, K. Ito, Y. Abe and N. Torikai, Nippon Seramikkusu Kyokai Gakujutsu Ronbunshi, 97, 427-431 (1989).
8) L.V. Azaroff and M.J. Buerger, "The Powder Method in X-ray Crystallography", McGraw-Hill Book Company, New York (1958) 181-209.
9) Y. Kumashiro, Denki Kagaku -Kyokai-shi, 38, 862-868 (1970).
10) N.M.B.E. Badramany, E.F. Mina, H.D. Merchant, S. Arafa and R.P. Poplawsky, J. Am. Ceram. Soc., 62, 113-116 (1979).
11) M. Suzuki, J. Phys. Chem. Solids, 41, 1253-1260 (1980).

This article is a full translation of the article which appeared in Nippon Seramikkusu Kyokai Gakujutsu Ronbunshi (Japanese version), Vol.98.No.6, 1990.

Crystallization of Li_2O-K_2O-Al_2O_3-SiO_2 -F Glasses Prepared by Rapid Quenching

Susumu Kawai and Muneyuki Motoyama

Hyogo Prefectural Institute of Industrial Research
3-1-12, Yukihira-cho, Suma-ku, Kobe-shi 654, Japan

The crystallization process of the rapidly quenched glasses in the system Li_2-O-K_2O-Al_2O_3-SiO_2-F has been investigated. Batches of the lepidolite composition were melted at 1773K for 10 minutes and quenched with a twin roller apparatus. Lepidolite and β-eucryptite were precipitated at 773K and 873K, respectively. However, it was necessary to keep the glass at 773K for more than 1 hour for the precipitation of lepidolite. The thermal conductivity of the glass ceramics heated at 773K for 1 hour and then at 973K for 2 hours was larger than fluorphrogopite glass ceramics, and its thermal expansion coefficient and dielectric properties were similar to those of fluorophrogopite glass ceramics.

[Received November 30, 1989; Accepted February 13, 1990]

Key-words: Glass ceramics, Crystallization, Rapid quenching, Lepidolite, Eucryptite

1. Introduction

When glasses are heated under suitable conditions, fine and homogeneous crystal phases are precipitated, synthesizing glass ceramics with good heat resistance and excellent mechanical properties. In particular, glass-ceramics containing fluorine mica crystal phases are known as electrically insulating and machinable materials. Typical crystal phases are fluorotetrasilicic mica and fluorophrogopite in which fluorine substitutes the hydroxyl group of mica. The molten phase of the fluorotetrasilicic mica system ($KMg_{2.5}Si_4O_{10}F_2$) becomes a transparent glass when quenched and forms aggregates of mica microcrystals by heating, to form glass-ceramics.[1] In contrast, the molten phase of the fluorophrogopite ($KMg_3AlSi_3O_{10}F_2$) system becomes polycrystalline containing mica crystals by slow cooling but glasses are not obtained even by rapid quenching because the molten substance is rapidly crystallized. Also, if cations are substituted for other ions in the composition, it rapidly crystallizes in the cooling process without forming glasses.[2,3] Recently, various amorphous materials have been developed by allowing molten substances to pass between two metal rollers followed by quenching.[4] However, few reports have discussed aluminosilicates containing fluorine, which are difficult to vitrify, as mentioned above.

In this study, lepidolite ($K(LiAl)_3(AlSi_3O_{10})F_2$)[5] is used as a substitute mica for fluorophrogopite or fluorotetrasilicic mica, and the results of the investigation on the conditions of formation of Li_2O-K_2O-Al_2O_3-SiO_2-F glasses by the twin roller method as well as crystals precipitated by heating will be reported.

2. Experimental Procedures

To prepare the glasses, batches of the system KF·LiF·Al_2O_3·3SiO_2 corresponding to the lepidolite composition were melted at 1773K for 10 min in a platinum nozzle after melting at 1473K followed by cooling. The molten materials were rapidly quenched by pouring onto the twin roller under an argon gas flow. The roller rotation rate was varied in the range between 2000 and 4000 rpm.

To investigate the crystallization process of the glasses obtained and the properties of glass ceramics, a differential thermal analyzer (Rigaku Denki, 8076), an X-ray diffraction apparatus (Rigaku Denki, RAD-3C, CuKα), an analytical electron microscope (Nihon Denshi, JEM-2000FX), a thermal conductivity measuring apparatus (Kyoto Denshikogyo, TC-22) and a Q-meter (YHP, 4342A) were used.

3. Results and Discussion

The molten lepidolite composition crystallized readily by ordinary quenching with LiF crystals precipitated to form cloudy glass, but became transparent homogeneous glass in flake form by rapid quenching at a roller rotating rate of 3000rpm under an argon gas pressure of 0.2MPa. If the melting temperature was lower than the above (1773K), the ejection of molten substance was impossible even under a higher argon gas pressure because the viscosity was too high. The cooling rate decreased when both the roller rotating rate and gas pressure were low, obtaining glass in a part of which LiF crystals were precipitated.

Table 1 shows the results of differential thermal analysis measured at 10K/min. The samples A, B and C were prepared at a melting temperature of 1773K and under a gas pressure of 0.2MPa and at a roller rotation rates of 2000,

Table 1. Results of DTA.

specimen	Tg/K	Tc_1/K	Tc_2/K	Tm/K
A	649	992	1138	1470
B	655	1014	1138	1486
C	686	1031	1138	1495

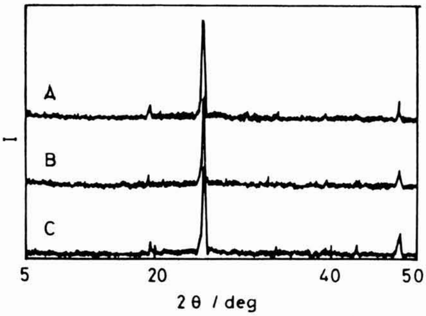

Fig. 1. X-ray diffraction patterns of glasses heated at 1073K for 1 hour.
A: 2000rpm., B: 3000rpm., C: 4000rpm.

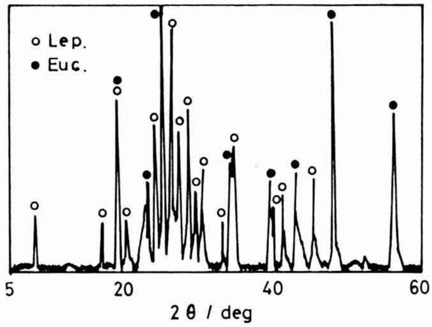

Fig. 3. X-ray diffraction pattern of glass ceramics.

3000 and 4000rpm, respectively, and were all transparent homogeneous glasses. The glass transition temperature (Tg) of the glasses increased with an increase in roller rotation rate. This indicates that, since Tg is the transition temperature of a super cooled liquid to a vitreous solid, the molten substance was quenched and solidified at higher temperature with increased roller rotation rate. Both the exothermic temperature peak (Tc_1) resulting from crystallization and the endothermic temperature peak (Tm) assumed to result from melting showed a tendency to increase with increased rotation rate, that is, cooling rate.

Glass powders were pressed to a size of 10(dia)×1mm and heated at 1073K for 1hr, and the crystal phases precipitated were identified by the X-ray diffraction method. As shown in **Fig.1**, for each sample only β-eucryptite was formed, and the absence of lepidolite was confirmed. To investigate the precipitation process of lepidolite crystals, the sample was heated at a fixed temperature in the range between 673 and 1273K for 1hr, and the peak intensity of the principal X-ray diffraction line of precipitated crystals measured. Since the peaks overlapped, the peak for β-eucryptite was measured at 2θ=47.8° and that for lepidolite at 2θ=8.7°. The results are shown in **Fig.2**. For β-eucryptite, the crystals started precipitating at temperatures over 773K, with the precipitation reaching a maximum at 973K and then decreasing with further increases in temperature. On the other hand, for lepidolite, crystals did not precipitate at temperatures below 723K with the precipitation reaching the maximum at 773K and decreasing to a very low level at 873K. When the heating time was 0.2hr at 773K, where the precipitation amount of lepidolite reached the maximum, β-eucryptite precipitated but no lepidolite crystal was confirmed. This indicates that the temperature range in which the nucleation and the growth of lepidolite crystals take place is narrow while the crystal growth rate is also low and heating at 773K for more than 1hr will be necessary to precipitate lepidolite.

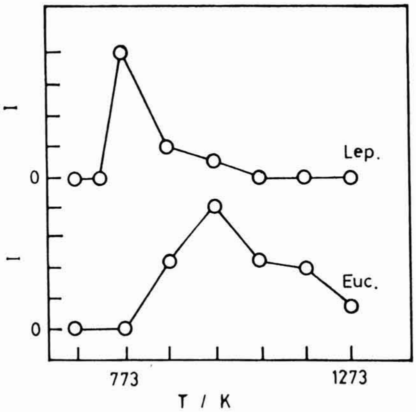

Fig. 2. Relative intensities of X-ray diffraction lines of lepidolite and β-eucryptite in the specimens heated at various temperatures for 1 hour.

Heating the glass B at 773K for 1hr and then at 993K for 2hr resulted in the precipitation of lepidolite and β-eucryptite as shown in **Fig.3**. **Figure 4** shows the TEM of the samples by an analytical electron microscope and the selected-area electron diffraction pattern. It was confirmed that the plate crystals seen by TEM were 1μm in size and were twin crystals of lepidolite as revealed by selected-area electron diffraction pattern analysis.

Table 2 shows the properties of the glass ceramics obtained by annealing under the above conditions. It also shows the properties of fluophrogopite glass ceramics for comparison.[6] The thermal expansion coefficient is similar to that of fluorophrogopite glass-ceramics so the effect of the larger thermal expansion coefficient and the residual

Table 2. Properties of glass ceramics.

Properties	Present	Others
Apparent density (g/cm^3)	2.35	2.52
Thermal expansion coefficient ($\times 10^{-7}/K$) (293-993K)	113	123
Thermal conductivity ($cal/cm \cdot s \cdot K$)	0.008	0.004
Dielectric constant (1MHz)	4.8	5.8
Dielectric loss (1MHz)	0.005	0.003

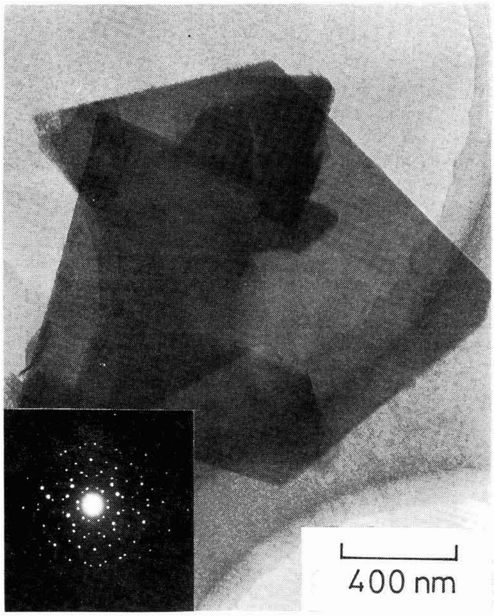

Fig. 4. Transmission electron micrograph of lepidolite in glass ceramics.

glasses of lepidolite more than compensates for that of β-eucryptite which has a negative value. The Tg and glass softening point were apparently due to the residual glass observed in the thermal expansion curve. The thermal conductivity was larger than that of fluorophrogophite glass ceramics while the dielectric properties were almost the same.

4. Conclusions

Glasses of the system Li_2O-K_2O-Al_2O_3-SiO_2.F were prepared by the rapid quenching method using a twin roller apparatus, and the crystallization process and the properties of the glass-ceramics obtained by heating were investigated with the following results.

1) The molten lepidolite composition tended to rapid crystallization by ordinary quenching and became an opaque glass with LiF crystals precipitated, but became a transparent homogeneous glass in flake form by rapid quenching at a roller rotation rate of 3000rpm under an argon gas pressure of 0.2MPa after melting at 1773K.

2) The crystals that precipitated in the glass by heating were lepidolite and β-eucryptite, with the precipitations being greatest at 773K for lepidolite and at 873K for β-eucryptite.

3) Although the precipitation of lepidolite was greatest at 773K, the range of temperature in which crystal nucleation took place and the crystals grew seemed to be small. It was necessary to heat the glass at 773K for more than 1hr for the precipitation of lepidolite.

4) The thermal expansion coefficients of the glass ceramics obtained by heating were composed of β-eucryptite with a thermal expansion coefficient of a negative value, and lepidolite and residual glasses with a large thermal expansion coefficients which resulted in a value of 113×10^{-7}/K. The thermal conductivity was larger than that of fluorophrogopite glass-ceramics and the dielectric properties were similar to those of fluorophrogopite glass-ceramics.

References:

1) H. Steinfink, Am. Mineral, 47, 886-896 (1962).
2) R.M. Hazen and D.R. Wones, ibid, 57, 103-129 (1972).
3) W.H. Daniels and R.E. Moore, J. Am. Ceram. Soc., 58, 217-221 (1975).
4) T. Minami, Ceramics Japan, 17, 278-283 (1982).
5) A.A. Levinson, Am. Mineral, 38, 88-107 (1953).
6) M. Sakamoto, S. Iwata, Kogyo Zairyo, 26, 93-98 (1978).

This article is a full translation of the article which appeared in Nippon Seramikkusu Kyokai Gakujutsu Ronbunshi (Japanese version), Vol.98, No.6, 1990.

Synthesis and Sintering of SiC-C Powder Mixture from $Si(OCH_3)_4$ and Phenol Resin

Hidehiko Tanaka, Jin Koazhe and Kazushi Hirota

National Institute for Research in Inorganic Materials
1-1 Namiki, Tsukuba-shi, Ibaraki-ken 305, Japan

Tetramethoxysilane and phenol-formaldehyde condensate, both in liquid state, were polymerized with water. The polymer was carbonized and heated at 1750-1850°C. Then, a mixture of fine β-SiC and C powder was synthesized. Hot pressing of this powder using B as a sintering aid yielded a SiC-C composite. The composite had a higher fracture toughness than sintered monolithic SiC. The crack bridging mechanism by the C particles increased the fracture toughness of the SiC-C composite.

[Received January 6, 1990; Accepted March 12, 1990]

Key-words: SiC, C, Powder synthesis, SiC composite

1. Introduction

A variety of approaches have been proposed for the synthesis of fine SiC powder for sintering including solid- and vapor-phase processes.[1-3] The commercial method, however, is based on the reduction of powdered silica (SiO_2) with carbon (C). It is a heterogeneous solid/vapor phase process, and the reaction rate depends on the SiO and CO partial pressures. For a homogeneous process to be viable, the starting SiO_2 and C powders should be fine to provide large surface areas and they should be well mixed.[1] We attempted to prepare an organic precursor for highly sinterable SiC powder using well mixed organic liquid compounds as the SiO_2 and C sources.[4] This process forms synthesized SiC powder free of unreacted SiO_2 and C residues, so that further treatment to remove the residual SiO_2 and C by oxidation or acid treatment can be eliminated.

The above process can give SiC powder containing residual carbon when an excess of carbon is used for the organic precursor. In this study, the SiC-C powder mixture was prepared using liquefied tetramethoxysilane and phenol resin as the SiO_2 and C sources, and it was sintered into a composite material in which the carbon particles were uniformly dispersed. This article discusses the forms of the synthesized particles and the fracture toughness of the sintered composite material.

2. Experimental Procedure

Tetramethoxysilane ($Si(OCH_3)_4$, (Trichemical Lab.) and phenol resin, a condensate of resol-type phenol and formaldehyde (Dai-Nippon Ink), were mixed in the presence of ethylalcohol solvent, to which water was slowly added to form a gel. It was dried, to form a resin-like polymer, which was carbonized at 1000°C in a flow of argon gas. It was further heat treated at 1600° to 1850°C, also in a flow of argon gas, to synthesize the SiC-C powder mixture. The carbon content was determined by a carbon analyzer (TC-136, Leco, Michigan).

The SiC powder, after an adequate quantity of boron (0.2 to 2wt%) was added, was hot-pressed under the conditions of 2100° to 2200°C and 20MPa. The fracture toughness of the C-dispersed composite (SiC-C) thus prepared, was measured by the Vickers indentation (IF) method[5,6] and the SENB (SEPB) method involving precracked samples.[6,7]

3. Results and Discussion

3-1. Synthesis of SiC-C Powder Mixture

Tetramethoxysilane and phenol resin were mixed uniformly, and then polymerized and solidified. A gray, transparent resin resulted. The major reactions responsible for the solidification of the liquefied starting materials were hydrolysis of tetramethoxysilane and the condensation/polymerization of the phenol resin.

The SiO_2 and C components were considered sufficiently fine to be uniformly mixed in the liquid phase, because no separation was observed during the reaction process.

The polymerized resin was carbonized at 1000°C into a black, bright, glassy carbonaceous solid of uniform composition. Heating the carbonized resin at a higher temperature produced powdered SiC or a SiC-C mixture. The reaction between SiO_2 and C started at 1600°C and was completed at 1700°C or higher. The oxygen content in the synthesized powder was fairly constant at 0.7wt%, almost irrespective of the synthesis conditions. **Figure 1** shows the effects of the C/SiO_2 ratio in the precursor (carbonized resin) on the yield and C content of the synthesized powder prepared at 1750°C. A single phase SiC powder resulted when the C/SiO_2 ratio was decreased to about 2 mol/mol or less. The product yield increased in proportion to the C/SiO_2 ratio. The reaction was considered to be represented by:

$$SiO_2 + (1+2\alpha)C = \alpha SiC + (1-\alpha)SiO + (1+\alpha)CO,$$
$$0<\alpha<1$$

where it was assumed that excess SiO_2 was evaporated as SiO.[4]

The yield shown in Fig. 1 was in fairly good agreement with that predicted from the α level. Carbon remained in the synthesized powder when the C/SiO_2 ratio was above 2, resulting in the formation of a SiC-C mixture. The yield of SiC was fairly constant at 31 to 32%, and no longer controlled by the above equation. The oxygen might partly volatilize as SiO_2.

The SiC powder synthesized was the β-cubic phase. The particle size depended on the synthesis temperature and the quantity of residual carbon.

Figure 2 shows the shapes of the particles, where a) and b) are photographs of the powders containing residual carbon, and c) and d) are single phase SiC powders, all synthesized at 1750° to 1850°C. The grains grew when synthesized at high temperature, particularly in the single phase powders. The residual carbon seemed to control the growth of the SiC grains. The secondary agglomeration of the grains was very weak and it had no effect on the later sintering process. It is therefore considered that directly sinterable fine powders may be prepared by controlling the C content and temperature.

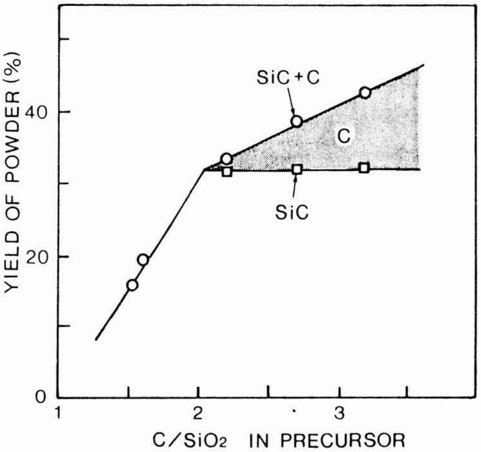

Fig. 1. Yield of SiC from carbonized polymer (SiC precursor). The carbonized polymer where $C/SiO_2>2$ produces SiC and C powder mixture. Shadowed area shows C yield.

3-2. Sintering and Fracture Toughness of SiC-C Composite Materials

SiC-C powder mixtures of various carbon contents were prepared at 1750°C by the method described in the previous section, and boron was added before hot-pressing. The powders were densified to almost the theoretical density. **Figure 3** shows the microstructures of the sintered composites and **Table 1** their densities and mechanical properties. Each composite sample consisted of a matrix in which carbon particles were dispersed. The SiC matrix was of the β phase, consisting of the particles somewhat expanded in plates. The carbon particles, 0.9 to 1.4μm in size, were present in the grain boundaries of SiC. The size increased slightly in proportion to the content.

The Young's modulus and hardness of the SiC-C composite decreased in proportion to the carbon content. These properties were between those of SiC and C, following the rule of mixtures. The fracture toughness was measured mainly by the IF method, although samples 1, 2 and 5 shown in Table 1 were measured by the SEPB method. It increased in proportion to C content; the fracture toughness of the sample containing 23wt% of C was 1.6 times higher than that of the single phase SiC. The fracture toughness deter-

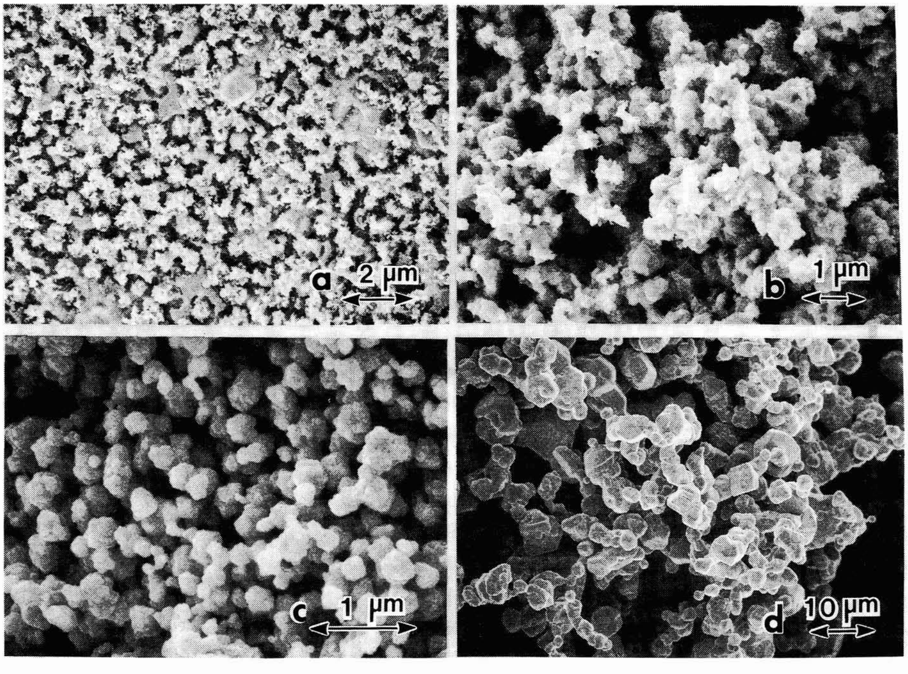

Fig. 2. Powder synthesized from carbonized polymer. (a) and (b) were synthesized at 1750°C and 1850°C from the carbonized polymer with $C/SiO_2=1.6$. C content is 23wt% in (a) and 22wt% in (b). (c) and (d) were synthesized at 1750°C and 1850°C from $C/SiO_2=3.2$. No residual C exists in (c) and (d).

Table 1. Material and mechanical properties of SiC-C composite.

Sample No.	W_P	d^R %	Hv	E GPa	ν	r μm	K_{IC} $MN/m^{1.5}$
1	0.00	97.2	2519	414	0.16	-	2.75(2.03)
2	0.088	98.9	2394	355	0.15	1.09	2.98(2.26)
3	0.11	100	1942	342	0.15	1.05	3.55
4	0.13	100	1990	337	0.14	0.90	3.14
5	0.18	94.7	1199	220	0.13	0.84	3.67(2.71)
6	0.21	99.3	1410	288	0.13	1.29	4.11
7	0.23	100	1552	289	0.13	1.43	4.28

W_P : Content of C grains in the composite.
d^R : Relative density.
Hv:Vickers hardness.
E and ν: Young's modulus and poisson's ratio.
r:Mean grain size of C.
K_{IC} :Fracture toughness which was measured by IF method.
The K_{IC} in the parenthesis was measured by SEPB method.

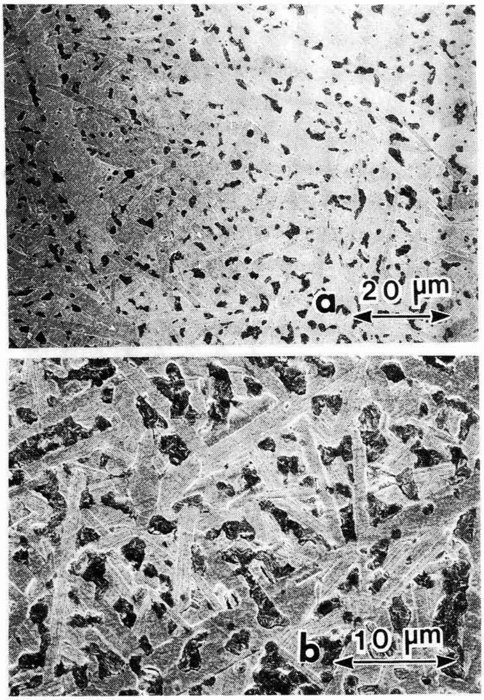

Fig. 3. Microstructure of SiC-C composite
(a) C=11wt%, (b) C=21wt%.

mined by the SEPB method tended to be lower than that determined by the IF method. Although it was difficult to decide which method provided better results, both methods demonstrated the common trend that fracture toughness increased as carbon content increased.

It may be therefore concluded that SiC can have increased toughness when containing dispersed carbon particles.

Figure 4 shows the fracture surface of the SiC-C composite and the cracks running through the surface, introduced by the Vickers hardness tester. As can be seen, these

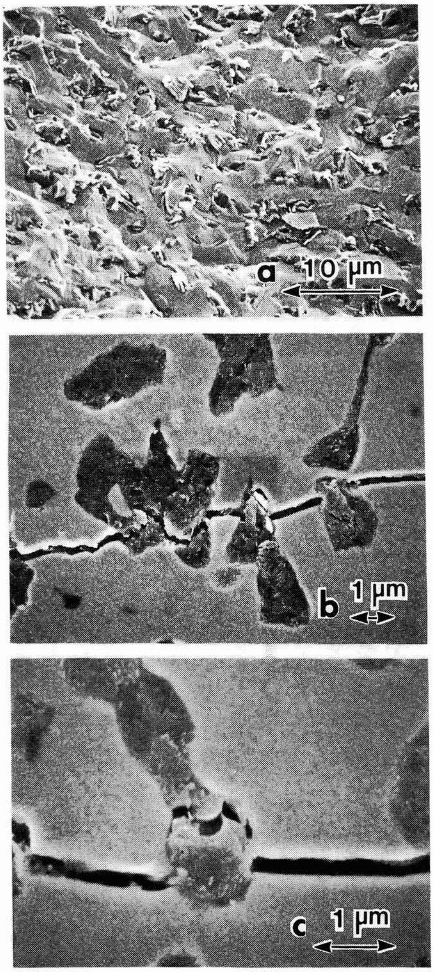

Fig. 4. C pull-out behind the crack tip in SiC-C composite.
(a) Fracture surface, (b) and (c) cracks propagating from indentation site. C content is 21wt%.

cracks were straight, cutting and pulling out the carbon particles. The traces of the carbon particles pulled out were observed. A number of researchers have discussed the reinforcement of SiC sinters with dispersed particles. In particular, significant improvements in toughness were observed in the SiC matrix with dispersed $TiB_2$$^{8)}$ or TiC,$^{9,10)}$ both known for a high modulus of elasticity and hardness. It was suggested that the reinforcement is caused by the dispersed particles which deflect the cracks.$^{11)}$ This was not the case with the composite systems prepared in this study, because the dispersed carbon particles were not strong enough to deflect the cracks and the cracks were not deflected in the SiC matrix. Judging from the reinforcement mechanisms for fiber-reinforced composite materials,$^{12,13)}$ it is considered that the carbon particles are pulled out behind the crack edges, creating friction which prevents the cracks from opening. This reinforcement mechanism is called the bridging mechanism in whisker-reinforced composite ceramics.$^{13)}$ The bridging mechanism of the carbon particles for the cracks may account for the reinforcement of the SiC matrix.

4. Conclusions

A mixture of tetramethoxysilane and phenol resin was solidified and carbonized to form the SiC precursor in which SiO_2 and C were mixed well. A SiC-C powder mixture resulted when the precursor was heat treated at high temperature. The carbon particles controlled the growth of the synthesized SiC grains, keeping them fine. The mixture contained no residual SiO_2, and could be highly densified when hot pressed in the presence of boron, without crushing or post-treatment process. The fracture toughness of the carbon-dispersed SiC composite was higher than that of the single SiC phase. It was considered that the composite system was reinforced by the dispersed carbon particles, which produced a frictional force when they were pulled out by cracks.

References:

1) S. Somiya and K. Inomata, "Silicon Carbide Ceramics," published by Uchida Rokaku-ho (1988), pp.273-268, pp.373-382.
2) K. Kijima and M. Konishi, Yogyo Kyokai-Shi, 93, 511-16 (1985).
3) Y. Suyama, R.M. Marra, J.S. Haggerty and K. Bowen, Am. Ceram. Soc. Bull., 64, 1356-59 (1985).
4) H. Tanaka and Y. Kurachi, Ceramics International, 14, 109-15 (1988).
5) G.R. Anstis, P. Chantikul, B.R. Lawn and D.B. Marshall, J. Am. Ceram. Soc., 64, 533-38 (1981).
6) "Survey Results of the Standardization of Fine Ceramics," by the Fine Ceramics Society of Japan, March, 1985, pp.96-201.
7) T. Nose and T. Fujii, J. Amer. Ceram. Soc., 71, 328-33 (1988).
8) C.H. McMurtry, W.D. G. Boecker, S.G. Seshadri, J.S. Zanghi and J.E. Garnier, Am. Ceram. Soc. Bull., 66, 325-29 (1987).
9) G.C. Wei and P.F. Becher, J. Am. Ceram. Soc., 67, 571-74 (1984).
10) H. Endoh, M. Ueki and T. Kubo, FC Report, 6, 301-302 (1988).
11) K.T. Faber and A.G. Evans, Acta Metall., 31, 565-76 (1988)
12) D.B. Marshall, B.N. Cox and A.G. Evans, ibid., 33, 2013-21 (1985).
13) P.F. Becher, C.H. Hsueh, P. Angelini and T.N. Tiegs, J. Am. Ceram. Soc., 71, 1050-61 (1988).

This article is a full translation of the article which appeared in Nippon Seramikkusu Kyokai Gakujutsu Ronbunshi (Japanese version), Vol.98, No.6, 1990.

Effect of B_2O_3 Addition on Synthesis of Superconducting Oxide Bi-Sr-Ca-Cu-O

Seiji Adachi, Osamu Inoue and Syunichiro Kawashima

Central Research Laboratory, Matsushita Electric Industrial Co., Ltd.
3-15 Yagumo-Nakamachi, Moriguchi, Osaka 570, Japan

Bi-Sr-Ca-Cu-O ceramics with B_2O_3 additive were synthesized. The magnetic shielding effect for the sample containing B_2O_3 was larger than that without B_2O_3. However, the XRD intensities of 2223 phase for both samples were almost the same. Therefore, it is considered that 2223 phase surrounds a non-superconductive phase in the B_2O_3-containing sample.

[Received January 29, 1990; Accepted March 12, 1990]

Key-word: Oxide superconductor, Bi-Sr-Ca-Cu-O, B_2O_3, Addition, Liquid Phase

1. Introduction

Obtaining a single-phase sample of superconducting oxide $Bi_2Sr_2Ca_2Cu_3O_y$. (2223 phase) is difficult and the synthesis of single-phase samples of it has been a problem since it was discovered.[1] The method of firing a mixture with an excess of Ca and Cu compounded and fired for a long time[2] and the possibility of synthesizing a sample containing a large amount of 2223 phase in a comparatively short time with grinding and forming processes during sintering to improve homogeneity[3], have been reported. Also, the 2223 phase has been successfully formed as a single phase by substituting Pb for part of Bi.[4,5] Hatano et al., investigating the forming process of 2223 phase in Bi-Pb-Sr-Ca-Cu-O, reported that the liquid phase of Pb forms a mass transfer path, promoting the formation of 2223 phase.[6] Honda et al. indicated that the liquid phase of K takes part in the particle growth of 2223 phase in Bi-Sr-Ca-K-Cu-O.[7]

This work assumes that B_2O_3 might also form a liquid phase constituent promoting the formation of 2223 phase.

2. Experimental Procedures

Samples were prepared by the solid phase method using Bi_2O_3, $SrCO_3$, $CaCO_3$, CuO and B_2O_3 as raw materials. The compound composition was $Bi_2Sr_2Ca_6Cu_7O_y$. The raw materials were wet-mixed with an oscillating mill in ethanol using ZrO_2 of 5mm diameter and the dried powder was calcined twice at 750°C for 5hr and once at 800°C for 5hr in air. The calcined powder was ground in the same way as the raw materials. Two samples using the obtained powder with or without 0.08wt% B_2O_3 added by mixing in a mortar were granulated, formed and fired in the temperature range between 850° and 880°C for 72hr in air. The crystal structures of the samples obtained were investigated by powder X-ray diffraction. The evaluation of superconductive properties was by electrical resistance measurements by the DC four-terminal method and AC magnetic susceptibility measurements (a simple method of measuring inductance on coiled samples, the samples being almost the same in size) were conducted in the temperature range between room temperature and the temperature of liquid nitrogen

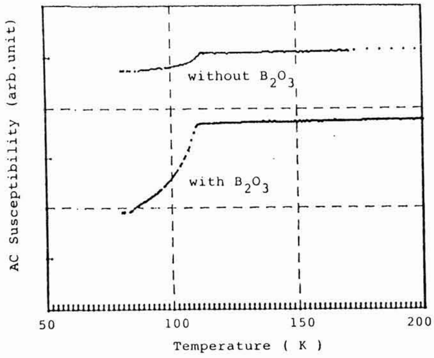

Fig. 1. Temperature dependence of AC susceptibility for the Bi-Sr-Ca-Cu-O with and without B_2O_3 sintered at 870°C for 72 hrs in air.

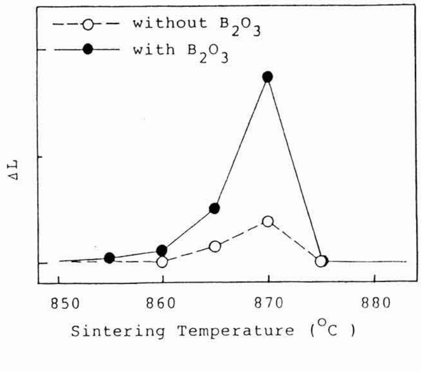

Fig. 2. Sintering temperature dependence at ΔL (ΔL=Inductance (at shift start temperature)- Inductance (at 77K))

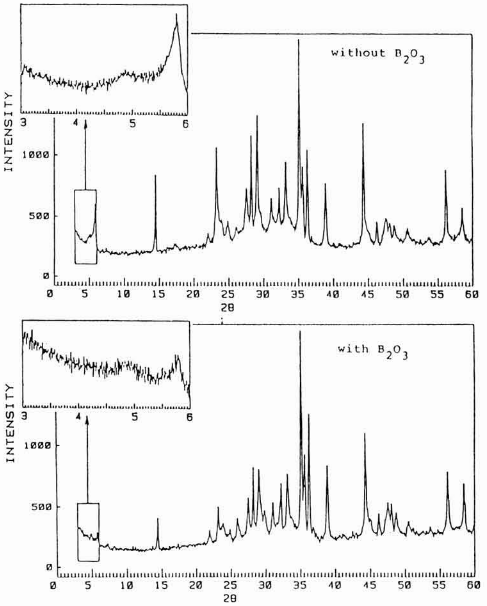

Fig. 3. Powder X-ray diffraction patterns for Bi-Sr-Ca-Cu-O with and without B_2O_3 sintered at 870°C for 72 hrs in air.

(300-77K).

3. Results and Discussion

Figure 1 shows the magnetic susceptibility of the samples fired at 870°C. For samples both with and without B_2O_3 addition, a magnetic shielding effect was indicated at temperature below 110K. The apparent volume percentages of superconductive phase were larger for the samples with additives. **Figure 2** shows the relationship between the firing temperature and the magnetic shielding effect. ΔL on the ordinate is the difference between the inductance at the starting point of decrease and that at 77K. It indicates that the optimum firing temperature does not shift by adding B_2O_3. The sample with B_2O_3 addition has a larger magnetic shielding effect.

Figure 3 shows the X-ray diffraction patterns of the samples fired at 870°C. Although the broad peaks at 2θ=4.8 and 24.0 are attributable to 002 and 0010 of 2223 phase, for both samples with and without B_2O_3 addition almost the same peak intensities were obtained. Assuming that the volume percentage of the formed 2223 phase is proportional to the X-ray diffraction intensity, the volume percentage of 2223 phase formed even with B_2O_3 addition is almost the same as that without B_2O_3.

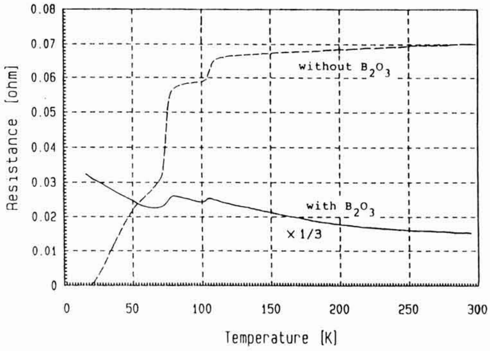

Fig. 4. Temperature dependence of electrical resistance for the Bi-Sr-Ca-Cu-O with and without B_2O_3 sintered at 870°C for 72 hrs in air.

A difference of three times in the magnetic shielding effect appears to be due to the phase present even though the volume percentage was almost the same. A larger shielding effect is obtained if a superconductive phase precipitates surrounding a non-superconductive phase. It is considered that the liquid phase formed by adding B_2O_3 wetted the crystal particles as if surrounding each of them, to become a mass transfer path, resulting in the formation of 2223 phase on the surface of crystal particles.

Figure 4 shows the temperature dependence of electrical resistance. For the sample without B_2O_3 addition, two step onsets at 106K and 76K are indicated with the resistance decreasing to zero at 20K. For the sample containing B_2O_3, the resistance decreased at 105K and 77K but did not became zero, with a constituent which shows a semiconductive behavior behaving as if connected with a superconductive phase in series. This seems to be because the liquid phase formed by adding B_2O_3 entered the grain boundary between the superconductive phases cutting off the passage of the superconductive current.

4. Conclusions

Bi-Sr-Ca-Cu-O ceramics with a small amount of B_2O_3 were synthesized. The magnetic shielding effect for the sample containing B_2O_3 was larger than that without B_2O_3. The X-ray diffraction pattern indicated no increase in the volume percentage of 2223 phase due to B_2O_3 addition. Therefore, it is considered that 2223 phase is formed surrounding a non-superconductive phase in the B_2O_3-containing sample.

References:

1) H. Maeda, Y. Tanaka, M. Fukutomi and T. Asano, Jpn. J. Appl. Phys., 27, L209 (1988).
2) N. Kijima, E. Endo, J. Tsuchiya, A. Sumiyama, M. Mizuno and Y. Oguri, Jpn. J. Appl. Phys., 27, L821 (1988).
3) O. Inoue, S. Adachi, Y. Takahashi, H. Hirano and S. Kawashima, "Powder and Powder Metallurgy", 35, 937 (1988).
4) M. Takano, J. Takada, K. Oda, H. Kitaguchi, Y. Miura, Y. Ikeda, Y.

Tomii and H. Mazaki, Jpn. J. Appl. Phys., 27, L1476 (1988).
5) U. Endo, S. Koyama and T. Kawai, Jpn. J. Appl. Phys., 27, L1476 (1988).
6) T. Hatano, K. Aota, S. Ikeda, K. Nakamura and K. Ogawa, Jpn. J. Appl. Phys., 27, L2055 (1988).
7) T. Honda, T. Wada, M. Sakai, M. Miyajima, N. Nishikawa, S. Uchida, K. Uchinokura and S. Tanaka, Jpn. J. Appl. Phys., 27, L545 (1988).

This article is a full translation of the article which appeared in Nippon Seramikkusu Kyokai Gakujutsu Ronbunshi (Japanese version), Vol.98, No.6, 1990.

Information & communications

News

Fine Ceramics Technology Conference Held in Nagoya

The Association of Japanese Industrial Particle Technology opened its "Fine Ceramics Technology Conference" at Aichi Prefectural Welfare Pension Hall in Nagoya city. The market for fine ceramics, now worth one trillion yen annually, is expected to be as large as 6 trillion yen in 2000, when the quality and function of fine ceramics will have reached a new level. Researchers who are actively in the forefront of research in various fields delivered lectures on such themes as "Development of New Usage and Technology of Fine Ceramics" and "Higher Functions and Particle Technology of Fine Ceramics."

The list of speakers and topics is as follows. "New Development of the Ceramics Industry" (Mr. S. Nagamune, Chief of Fine Ceramics Section, Consumer Goods Industries Bureau, the Ministry of International Trade and Industry), "Development and Problems of Structural Ceramics" (Mr. R. Kato, Head of Research Department, Nihon Special Ceramics Industry Co., Ltd.), Prospects for High-Temperature Superconductive Oxide Manufacturing Technology (Mr. T. Shiobara, Chief of the 4th Research Section, Superconductive Engineering Laboratory, International Superconductive Industrial Technology Research Center and Chairman, Mr. S. Sotoyama, Prof. of Nagoya University), "Technology for Membrane Manufacture Utilizing Static Electricity" (Mr. H. Yamamoto, Prof. of University of Tokyo), "Existing Trends of Metallic Ceramic Composite Materials" (Mr. I. Yamai, Prof. of Nagoya Industrial University), "Precision Processing Technology for Ceramics of Complicated Shape" (Prof. O. Saito, Toyota Industrial University and Mr. Y. Kawahara, Chief of the Section for Basic Structural Material Ceramics, Industrial Technology Research Laboratory of the Agency of Industrial Science and Technology), "Functional Design of Particle Materials" (Mr. M.Arakawa, Vice Chairman of Particle Engineering Association), "Functionalization of Fine Ceramics by the Sol-Gel method" (Prof. S. Sakka, Kyoto University), "Agglutination and Dispersion of Fine Particles of Ceramic Materials" (Prof. K. Tohatani, Kyushu Industrial University and Chairman, Mr. J. Tsubaki, Deputy Chief of the Fine Ceramics Center Department), "Particle Properties and Sintering (Mr. S. Abe, Chief Researcher of the Department for Basic Ceramics, Nagoya Industrial Technology Research Laboratory), "Gradient Function Materials and Particle Technology" (Mr. K.Hirano, Chief Researcher, Material Engineering Department, Mechanical Technology Research Laboratory of the Agency of Industrial Science and Technology) and "Superautomization of Particles and Its Utilization (Prof. N. Ichinose, Waseda University and Chairman, Mr. R.Itoh, Executive Director of The Association of Japanese Industrial Particle Technology)

Ceramic Composites of High Strengths

A joint study group of Kyoto Polytechnic Textile University and Osaka Cement Co., Ltd. have developed ceramics of the zirconia system (TZP) whose flexural strength is 3000 MPa on the average and 3440 MPa at maximum. The study group aimed to increase the strength of ceramics of the zirconia system by combining two kinds of ceramics with different sintering properties. In other words, a composite was manufactured by sintering a mixture of easily diffusible zirconia powder with a crystal diameter of 10 nm and scarcely diffusible alumina with a particle diameter of about 0.5μ.

In this composite, alumina crystal particles of 0.5 to 1.0μ are wrapped by zirconia crystal particles of 0.1 to 0.2μ. Flexural strength is 1.5 times higher than that of conventional ceramics which show a maximum strength of about 2000MPa. Since mass production of this product is relatively easy, its use is expected to spread into many fields where higher strength and hardness are required.

Composite Functions Given to Ceramic Particles

Nagoya Institute of Industrial Technology of the Agency of Industrial Science and Technology is planning to develop ultra-particles with gradient functions, which can be used to produce thin silica membranes on the surface of alumina ceramics, etc. The idea is to allow the particle itself to have composite functions and the key to this development is the utilization of hydrolytic response. A water membrane is produced on the surface of ceramic particles before coating and then membranes are made on the ceramic surface when metallic alkoxide reacts with this water in an organic solvent. Fatty acids are used as the reactive catalyst and ceramic particles are uniformly diffused in the solvent by combining oil-soluble surface-active agents. Membrane thickness ranges from about twenty to several hundreds of Å. Other compounds can be finely coated on the surface of the ultra-particles while the membrane thickness is being controlled. Composite functions are then given to the ultra-particles that are being produced by controlling the composition ratio at 0.1%/W. Attempts are being made to use materials other than silica for coating and make compound thin membranes of 2 to 3 layers. This product is scheduled to be marketed as part of a 5-year plan, and it will have many uses in sensors, semiconductors, etc.

Multiple Crystal Transparent YAG

Kurosaki Ceramics Co., Ltd. announced that they have successfully developed a method of synthesizing ceramic elements of multiple crystal transparent YAG (yttrium aluminum garnet) using normal temperature sintering technology based on the solid phase reaction method. YAG powder is mixed by the company's newly developed method and then molded by CIP (cold isostatic press) and sintered in atmospheric gas at about 1700°C under normal or reduced pressure. The largest products available at present are 15 × 15 × 80mm., but several units can be synthesized at the same time in one sintering furnace. The optical properties of the product are almost comparable to those of single-crystal YAG. There is no inferiority in wavelength-dependence. When compared with the lift-up method and single crystal growth method, the production cost can be considerably reduced because of the simple procedure that takes from 3 to 4 days, one tenth the time needed for conventional methods. The company is planning to find practical applications for this neodymium-added YAG in laser processing, laser knives, communication apparatus, high-temperature glass instruments, etc., and it is expected that this product will be highly marketable.

Manufacture of Fine Ceramics by Injection Molding

Miyagawa Kasei Industrial Co., Ltd. is reportedly launching all-out efforts to find new market demands for fine ceramic products after establishing their manufacturing technology for injection molding. More precise and delicately-shaped ceramic products can be manufactured by injection molding than by common pressmolding. However, only a few companies can do mass-production, because of required molding conditions and difficulty in the mold making.

Miyagawa Kasei has been researching the techniques in this area since 1973 and have successfully achieved a dimensional accuracy as small as a few microns. Screws, tiny holes of 0.1mm diameter, cross holes, etc. that are very difficult to press-mold are now available. Consequently the company is planning to carry out increased sales activities in industries such as electronics, electricity machinery, foodstuffs, textiles, etc.

Application of Far-Infrared Ceramics to Agriculture

A forum on the theme of "Application of Far-Infrared Ceramics to Agriculture" was held on March 28 for the purpose of applying far-infrared rays not only to the fields of textiles and food but also to the field of agriculture.

On the basis of studies on infrared rays applied to the cultivation of rice plants, orchids, and golf course lawns, the mechanism and effects of these rays have been clarified as follows:

Special water having a sterilizing power is produced by means of a far-infrared ceramic combined with ozone. An active aquatic plant, known as "Green Savior", is raised by using this special water instead of agricultural chemicals. Lawns derived from the active aquatic plant, when used for golf courses, grow faster by 5 times than the conventional lawns and can be kept in the best condition at all times.

"Kenko Ikubyo Sheet" is a far-infrared seedling culture sheet used on a seedbed to promote the growth of rice plants and increase the ear-forming rate. It is also helpful in decreasing the disease of orchids.

Electro-Optical Ceramics of Ne Type

A study group led by Asst. Prof. K. Uchino of the Department of Science and Engineering of Jochi University has developed highly durable electro-optical ceramics of a new type for light display. This new material is mainly composed of magnesium niobic acids (PMN) with a small amount of titanium, and becomes transparent like PLZT when sintered at about 1200°C. PMN is heat-resistant and can be switched on and off with a third less voltage than is needed for PLZT. PMN was originally developed for ceramics actuators and its mechanical strength is as high as twice that of PLZT with much less expansion, contraction and distortion. PMN shows most promise as a material for projection TVs. Cathode-ray tubes and liquid crystal display are now used for this type of television, but it is difficult to reduce the size of CRTs, and LCDs are too sensitive to heat. However, a compact and heat-resistant projection television can be manufactured with PMN.

Striation in Ceramics

Mr. S. Horibe, Chief Researcher of the Tsukuba Branch of the Institute of Metallic Material Technology of the Agency of Industrial Science and Technology, has discovered striation in ceramics which is similar to metal fatigue. No report has ever been made on the finding of such striation in ceramics, which are fragile and seldom show plastic deformation. Mr. Horibe used the Vickers hardness test in which a diamond indenter was repeatedly pressed into a silicone carbide sample which had been sintered under normal pressure, and he observed the surface damage with an electron microscope. He confirmed intracrystal striation of a few μm diameter which is quite comparable to that found in metals.

Although only a striped pattern was seen in the crystal he judged that it was striation similar to metal fatigue because of the right angle in the advancement of the fissure of striation and the number of stripes which corresponded to the pressure. Mr. Horibe also confirmed that it is a common phenomenon since such a stripe has been recognized in other ceramics as well. Thus, this discovery may well contribute to the general understanding of the breakage mechanism of ceramics.

Preproduction Line of 8-inch Wafers

Toshiba Ceramics will complete a preproduction line for mass-production of 8-inch wafers in September. This line will be installed in the control laboratory.

In this laboratory, a prototype line is already producing 500 wafers monthly but the preproduction line will produce 2000 8-inch wafers monthly. The total investment will reach 500 million yen.

Japanese semiconductor manufacturers have been hesitating to install 8-inch wafer facilities, because of immature technology for 8-inch wafer manufacturing.

Shin-Etsu Handotai Co., Ltd., however, has established a prototype line and Japan Silicon Co., Ltd. will establish one by summer. Therefore, Toshiba Ceramics will sooner or later be supplying samples in competition with them.

Low Pollution Ceramic Reciprocating Engine

Isuzu Motor Co., Ltd. is to invest 6 billion yen for development of a ceramic reciprocating engine, contrary to the current world trend.

Isuzu expects that their ceramic engine will meet pollution control standards for diesel engines effective from 1993 and 2000, which demand a reduction of up to 65% of NO_x in exhaust gas. Isuzu has proven that its ceramic engine has achieved a reduction of 30% of fuel consumption. The company is now constructing a new laboratory at its Fujisawa works to establish volume production technology for ceramic engines by the end of 1991. Initially the company use ceramics for piston rings, exhaust valves, etc., but now the employment of ceramic materials is expanding.

Free Electron Laser

A free electron laser generates a laser beam by the interaction between light and electrons. This light is emitted by the electrons through the magnetic field in vacuum from an electron beam accelerator vibrated by "wiggler" equipment. This laser is essentially different from a solid or gas laser, and can provide large output because there is no medium intervening and no upper limit of output caused by destroying the medium. The wavelength of the laser beam can be varied simply by changing the energy of the beam. It can also be varied by changing the direction of the magnetic field of the wiggler periodically along the optical path.

The free electron laser consists of two opposite mirrors with the wiggler placed between them as shown in Fig.1. A beam reacts with electrons in the wiggler field and it is amplified while it goes back and forth between these mirrors to oscillate.

The free electron laser provides a beam with a high power output ranging from short wavelengths to long wavelengths. This it is a powerful research tool for a

Table 1. Parameters of 35MeV DS microtron

Maximum energy	35MeV
Beam current	300μA
Bunch beam peak current*	2 – 5A
Incident energy	5MeV
Energy gain per rotation	6MeV
Rotation count	5
Klystron**	4
Frequency	2,450MHz
Output	50kW cw (continuous)
Accelerating tube	DAW type
Electromagnet	
Magnetic flux density	0.1867T
Maximum track radius	616mm
Minimum track radius	81mm

* For high-frequency acceleration an electron group becomes a block of about 1mm in the forward direction per high-frequency cycle. The current value of this block is called the bunch beam peak current.

** Vacuum tube used for high frequency power amplification.

Table 2. Sample free electron laser by 35MeV DS microtron

	Mirror interval	6.1m (50 wavelength)
Wiggler	Length	1.6m
	Cycle	35mm
	Format	Helical
Bunch beam	Peak current	3A
	Maximum amplification rate	7%
	Laser wavelength	4μm
	Peak output	580kW
	Average output	58W

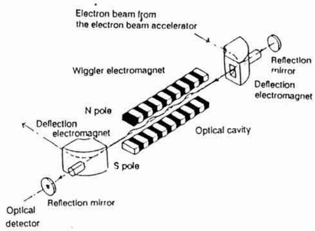

Fig. 1. Principle of a free electron laser

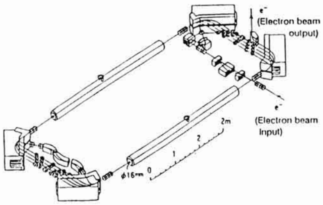

Fig. 3. Bird's-eye view

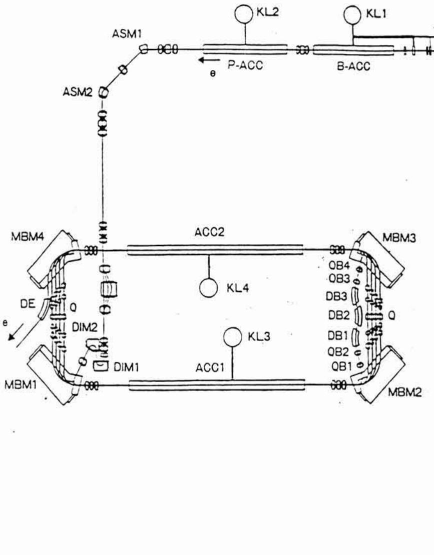

Incident equipment:	
Electron gun (GUN)	100KeV
Chopper (CP)	
Buncher accelerating tube (B-ACC)	2m × 1
Preaccelerator accelerating tube (P-ACC)	2m × 1
Klystron (KL)	500kW × 2
Beam transport system	
Analytic electromagnet (ASM)	2
Deflecting incident electromagnet (DIM)	2
DSM	
Accelerating tube (ACC)	4m × 2
Klystron (KL)	50kW × 2
Main deflecting electromagnet (MBM)	2t × 4
Phase correction deflecting electromagnet (DB)	3
Phase correction 4-pole electromagnet (QB)	4
5 unit, 4-pole electromagnet (Q)	8 sets
Fetching electromagnet (DE)	1

Fig. 2. DS microtron configuration

wide variety of fields including electronics, high-performance materials, and biology. Conventional material processing by a particle beam such as ion, electron, or molecule beams cannot meet the needs of high-performance materials due to the charge effect, while SOR cannot provide enough power. In Japan, the Institute of Laser Engineering Osaka University, has completed a laser with an output of 10MW and a wavelength of 100 to 1000μm. The Electrotechnical Laboratory have also installed a free electron laser.

The Laser Technology Research Institute will be installing a high-performance free electron laser with a wavelength of 100 to 500nm and a peak output of 100MW in Osaka. The budget for this installation is 8 billion yen. This laser will simultaneously generate 3 high power short wave length pulse beams. It will consist of an electron accelerator with an output of 350MeV and a wiggler magnet with a length of 8m. According to the plan, the new laser will be designed during 1990 and completed by 1993. Then it will be used to establish various techniques such as pattern formation, etching, CVD impurity diffusion, crystal growth, and catalytic reaction. With these techniques, the following will be developed: (1) electron devices such as ULSI, super lattice, and 3-dimensional quantum well, (2) materials such as super high-purity advanced ceramics, (3) new chemical synthetic materials, (4) biotechnology, (5) uranium concentration, and (6) communications, medical and space technologies. The Research Institute will develop IQRM (Integrated Quantum Processing Manufacturing) technology by 1998.

At the same time, the Foundation of Osaka Science & Technology Center have compiled a detailed design specification of a free electron laser. This is a preparation to invite a national laser research base.

Apart from this, Nihon University has succeeded in developing an electron accelerator for a free electron laser. The newly developed DC microtron was constructed to prove the assumption that rotating a liniac beam would be the most suitable accelerator for a free electron laser. The principles of operation are as below:

When an electron beam is preaccelerated by an incident unit and injected into the accelerator, a resonance condition occurs between the magnetic field and an electric field of a high enough frequency, and by this, acceleration is performed. Electron energy is increased by placing an electromagnet to change the direction of the electron beam 180 degrees at the entry and exist of each of two accelerating tubes to return the accelerated electrons to the entry of the accelerating tubes and so repeat this procedure.

The DS microtron is such that a single accelerator offers a combination of features such as the continuous beam that a cyclotron provides, the large current acceleration of a linear accelerator, and the phase stability and constant an energy width of a synchrotron. Parameters are listed in Table 1. A disk and washer (DAW) type of acceleration structure is used, originally proposed by a Soviet scholar and characterized by good acceleration efficiency. The length of the accelerating tube is 4m and it accelerates an electron to 3MeV. A group of 70 cavity resonators are contained in the accelerating tube, and the DS microtron uses two such tubes through which an electron beam rotates five times. The electron beam is given 5MeV by the preliminary acceleration and is accelerated to 30MeV by the DS microtron itself, to give 35MeV in total.

In addition to serving as the accelerator for a free electron laser, this DS microtron can provide a relatively strong radiative beam from several μm to milliwaves.

Abstracts of Articles on Ceramics from the Selected Journals of the Learned Societies

Zairyo
Vol.39, No.443
Aug. 1990
1076-1081

Evaluation of Fracture Toughness and Resistance of High Strength Graphite

Hideo KOBAYASHI*, Yoshio ARAI*, Tooru ARAKI**
and Tatsuo OKU***

Effects of specimen size and initial notch on fracture toughness and fracture resistance characteristics were examined for three high strength graphite materials, IG-11, IG-110 and IG-110U. A characteristic R-curve behavior and specimen size requirements for fracture mechanics parameters were discussed. An effect of elevated temperature environment on the fracture toughness was also examined at elevated temperatures from room temperature upto 820°C in a vacuum environment. The temperature effect was discussed in comparison with the result at room temperature in an air environment. The results obtained are summarized as follows :

(1) Graphite materials show a characteristic R-curve behavior in which the fracture resistance increases in the initial stage of crack extension near the initial notch tip, takes a constant value in the intermediate stage, and then decreases in the final stage near the specimen back face. The effect of initial notch is caused by an underestimation of the stress intensity factor, K, for a corner crack. It is shown that the true fracture resistance is constant and equals to the fracture toughness.

(2) The stress intensity factor, K, is valid as the fracture mechanics parameter for the fracture toughness testing. A well-known specimen size requirement for the metallic materials can be extended to the graphite materials by replacing the yield stress by the tensile strength.

(3) The fracture toughness increases slightly with increasing temperature in the vacuum environment and it has a larger value than that obtained at room temperature in the air environment. So, the fracture toughness and the fracture resistance obtained at room temperature in air can give conservative estimations for the evaluation of the structural integrity of the high temperature gas cooled reactor.

Key words : Fracture mecanics, Fracture toughness, Fracture resistance, Graphite material

Zairyo
Vol.39, No.443
Aug. 1990
1082-1088

Impact Damage of SiC and Si_3N_4 Ceramics by Solid Particles

Seiichi HAMADA* and Tetsuo TERAMAE**

Ball contact damages were investigated on pressureless sintered SiC and Si_3N_4 ceramics. Impact tests were carried out using the air gun system. Three kinds of balls ; steel, SiC and Si_3N_4, the size of which was 3 mm in diameter, were used as projectiles, and four kinds of ceramics were used as target specimens of size 7.5×10×85 mm. After the impact tests, three point bending tests were carried out to evaluate the residual strength of the specimens, and differences in failures with ball contact were discussed taking the results of numerical analyses into consideration.

The results are summarized as follows ;

(1) The residual strength could not be estimated by the diameter of the ring crack.

(2) SiC specimens with steel ball impact, and Si_3N_4 specimens with SiC ball impact showed the largest degradation of strength.

(3) Distinction of fracture between SiC and Si_3N_4 specimens seemed to be caused by the differences in strength and fracture toughness of these materials.

Key words : Gas turbine, Ceramics, Impact strength, Brittle fracture

Zairyo
Vol.39, No.443
Aug. 1990
1089-1094

Behavior of Ductile Crack Initiation from a Crack under Mixed Mode Loading

Keiichiro TOHGO*, Akio OTSUKA** and Hong-Wei GAO***

Behavior of ductile crack initiation from a crack under mixed mode I-Ⅱ loading has been investigated on a weldable structural steel SM41A. Elastic-plastic fracture toughness tests were carried out on the single-edge-cracked specimens subjected to bending moment and shearing force. The ductile crack initiation from the mixed mode crack occurred in two types — fibrous-type and shear-type — depending on the loading mode. When the mode I component was more predominant, the fibrous-type crack was initiated by the coalescence of microvoids. On the other hand, under the mode Ⅱ predominant loading, the shear-type crack initiation occurred by large shear deformation. The applicability of J-integral concept to the ductile crack initiation from a mixed mode I-Ⅱ crack was examined. The condition of ductile crack initiation from a mixed mode crack was shown by contour line on the J_I-J_{II} diagram, J_I and J_{II} being the mode I and Mode Ⅱ components of J-integral, respectively. The condition of crack initiation for mode Ⅱ crack, J^i_{II}, was different in value from the condition of crack initiation for mode I crack, J^i_I.

Key words : Ductile fracture, Crack initiation, Mixed mode crack, J-integral, Fibrous-type crack, Shear-type crack

Nihon Kinzoku Gaku Kaishi
Vol.54, No.7, 1990
758-763

Numerical Analysis of Compositional Distribution Change in Functionally Gradient Materials*

Tomoyasu Aihara**, Mikio Kaji*** and Tadashi Igarashi**

Thermomigration is a mass transport phenomenon under the influence of a temperature gradient. This effect has been found in the applications of high temperature heat transfer to have a pronounced influence on the thermal stability of functionally gradient materials (FGM). FGM consists of two or more compositions and phases having continuously changing distributions. The numerical analysis by the finite difference method is applied to the compositional distribution change induced by the thermomigration in two-phase βTi/TiC and V/V_2C FGM's or alloys having a uniform compositional distribution. The results show a considerable difference in the compositional distribution change between the two alloy systems, with a proportional relationship between the temperature conditions and the duration time for βTi/TiC FGM's.

Keywords: *temperature gradient, thermomigration, metal/carbide alloy, functionally gradient material, finite difference method, thermal stability*

Zairyo
Vol.39, No.443
Aug. 1990
1101-1105

A Stress Singularity Parameter Approach for Evaluating Reliability of LSI Plastic Package

Toshio HATTORI*, Asao NISHIMURA** and Gen MURAKAMI***

The stress and displacement fields at the close vicinity of a bonding edge show approximately the following singular behaviors.

$$\sigma(r)=K/r^{\lambda} \quad (1)$$

$\sigma(r)$: stress
r : distance from singularity point
K : intensity of stress singularity
λ : order of stress singularity

Formerly we presented a new adhesive strength evaluation method using these two stress singularity parameters K and λ. In this paper, the strength estimation on resin cracking at the tab edge of LSI plastic package was attempted by using these stress singularity parameters. Crack initiation criteria using stress singularity parameters were measured on 90° notch specimens, plain specimens, fracture toughness tests and so on. Crack initiation behaviors of three types LSI plastic packages were analysed using these crack initiation criteria. These analytical results cf delamination and crack initiation behaviors were compared with the heat-cycle experimental results.

From these studies it was found that the intensity of stress singularity at the tab edge increased in accordance with the increase of delamination area of tab bottom, and this delamination area depended strongly on the tab size.

Key words : Plastic encapsulation, Resin cracking, Delamination, Thermal stress, Stress singulality parameter, Crack initiation, Delamination propagation

---

Zairyo
Vol.39, No.443
Aug. 1990
1106-1112

Effect of Stress Components on Fatigue Crack Growth Rate under Multiaxial Stress Condition

Toshimitsu A. YOKOBORI*, Takeshi ISOGAI**, Takeo YOKOBORI***
and Yukihisa KOIZUMI****

Multiaxial fatigue tests were carried out to investigate the effect of stress components ($\Delta\sigma$, $\Delta\tau$, $\sigma_{st.}$, $\tau_{st.}$) on fatigue crack growth.

The test method was the combined tension and tortion one in phase loading by using thin-walled hollow cylindrical specimens with pre-cracks. The experiments were carried out under the condition of equal equivalent stress amplitude, $\Delta\sigma_{eq}=\sqrt{\Delta\sigma^2+3\Delta\tau^2}$

Under the condition of mixed modes, the fatigue crack growth rate increases remarkably with increasing stress ratio. This characteristics is due to the effect of static tensile stress $\sigma_{st.}$ on $\Delta\tau$.

In this paper, the effect of static tensile stress was incorporated in the constitutive equation of fatigue crack growth rate under the mixed mode fatigue condition of $\Delta\sigma$ and $\Delta\tau$. Then, the following constitutive equation of fatigue crack growth rate including the effects of $\Delta\sigma$, $\Delta\tau$, $\sigma_{st.}$ and $\tau_{st.}$ was obtained.

$$db/dN=A(\Delta K_{1b})^{m}$$

$$A=(A_{R=0})^{1/r^*}$$

$$r^*=\begin{cases} 1+(\sigma_{st.}/\Delta\tau)^{1/2}/7 & \text{(Region IIa)} \\ 1 & \text{(Region IIb)} \end{cases}$$

$$A_{R=0}=\begin{cases} 2.16\times10^{-5}\times0.230^{m} & \text{(Region IIa)} \\ 3.64\times10^{-5}\times0.147^{m} & \text{(Region IIb)} \end{cases}$$

$$m=\begin{cases} f(\sigma_2/\sigma_1) & \text{(Region IIa)} \\ g(\sigma_2/\sigma_1) & \text{(Region IIb)} \end{cases}$$

Key words : Multiaxial fatigue crack growth rate, Effect of stress ratio, Effect of static tensile stress, Effect of static torsional stress, Effect of stress component

Nihon Kinzoku Gaku Kaishi
Vol.54, No.8, 1990

Effect of Alloying Elements on ZrC Particurate Dispersion in Liquid Aluminum*

Makoto Kobashi**, Takao Choh*** and Yasutaka Horibe**

SiC particules are mainly used as reinforcement of metal matrix composites. However, it is impossible to incorporate SiC particles with small size (<1 μm) into molten aluminum and difficult to get a good distribution of particles. ZrC is more suitable as reinforcement than SiC, because of its thermal stability and low surface energy, so the effect of alloying elements on dispersion of ZrC particles into molten aluminum was investigated. Good wettability between ZrC particle and molten aluminum is essential for particulate incorporation. A number of reports have shown the dependence of wettability between ceramics and metals upon chemical reactions. $ZrAl_3$ was detected in the matrix of ZrC/pure Al composite by using EPMA. The time required for incorporation of ZrC particles into molten aluminum was defined as an incorporation time. The incorporation time of ZrC was shortened by alloying Si, Ti or Bi which has strong affinity for ZrC. In this case, metallic compounds including these alloying elements were detected in the matrix. On the other hand, the incorporation time was not so influenced by adding Pb, Cu or Zn which has weak affinity for ZrC and it was prolonged by adding Zr, a constituent of ZrC particle.

The incorporation time was shortened by alloying Mg, Ca and Li, although no metallic compound including these elements was detected in the matrix,

The microstructure of the composite shows the particulate concentration along grain boundaries of matrix, because of its slow solidification rate. However, under the condition of rapid solidification rate by casting, the uniform particulate distribution was obtained.

Keywords: *composite, zirconium carbide particle, alloying elements, incorporation time, solidification rate, particulate distribution*

Nihon Kinzoku Gaku Kaishi
Vol.54, No.7, 1990
764-771

Improvement of Mechanical Properties by Microstructure Controlling of Ti-6Al-4V Alloy without Processing Strain

Akira Nozue*, Keiji Ohki** and Tadatsune Okubo*

The purpose of the present study is to improve the mechanical properties of the beta-quenched and beta-annealed specimens with little strain due to processing, only by heat-treatment. Control of volume fraction, morphology and distribution of alpha is of great importance in achieving desired mechanical properties with a good combination of yield strength, elongation and fracture toughness. Accordingly, a special (S) solution treatment has been proposed to obtain bimodal structures of equiaxed and acicular alphas. The microstructures of the specimens subjected to the S solution treatment consisted of nearly equiaxed and acicular alphas with the matrix of the tempered martensite. As a result, the mechanical properties became almost equivalent to the specimens of the double solution treatment, which has been widely known to exhibit an optimum combination in the specimens with the strain due to forging and rolling. The fracture toughness for the S solution treatment was found to increase due to zone shielding and crack deflection. Finally, the S solution treatment was applied to welded materials.

Keywords: *titanium-6 aluminum-4 vanadium alloy, mechanical properties, microstructure control, solution treatment*

Zairyo
Vol.39, No.442
Sept. 1990
852-858

Numerical Analysis for Torsional Stress and Rigidity of Nonsymmetrical Three-Layered Beams Subjected to Torsion

Hiromi DEWA*

In this paper, numerical analyses of torsional stress and rigidity were carried out on two types of nonsymmetrical three-layered sandwich and covered beams subjected to torsion, by utilizing the exact and briefly arranged analytical solution. The following different features of these beams became clear from the numerically calculated results.

(1) The maximum shear stress in the sandwich beam with hard core appeared at the middle point of the thicker layer of the outer elastic layers, and for the beam with soft core it appeared at the same point of the thinner outside layer. But for the covered beam, it appeared always in the thicker outside layer.

(2) Shear stress in the core of the sandwich beam became highest at both the top and bottom interfaces, and it was highest in the symmetrical beam composition. The maximum stress for the covered beam, which did not appear at the interface, was lowest in the symmetrical beam composition.

(3) An appropriate core layer thickness existed in order to reduce shear stress at the interface of two-layered beam by core insertion. In this case, the saturation of stress reduction was induced by inserting a thicker core, and moreover, higher stress than that of the original two-layered beam was induced sometimes at the interface.

(4) Torsional rigidity of the symmetrical sandwich beam was lowest for the soft core and highest for the hard core. On the other hand, for the covered beam it was lowest in the symmetrical and highest in the two-layered beam composition. These characteristics for torsional rigidity are controlled by the increase of torsional rigidity of the elastic layer of each beam created by bonding.

Key words : Nonsymmetrical three-layered beam, Torsion, Stress analysis, Torsional rigidity, Sandwich beam, Convered beam

Nihon Kainzoku Gaku Kaishi
Vol.54, No.8, 1990
861-869

Self-Accommodation Structure in the Ti-Ni-Cu Orthorhombic Martensite*

Youichi Watanabe**1), Toshio Saburi**2), Yutaka Nakagawa**3) and Soji Nenno**4)

Self-accommodation process and the resulting structure of the orthorhombic martensite in a Ti-Ni-Cu shape memory alloy were investigated.

Observations of the self-accommodation process of habit plane variants of the orthorhombic Ti-Ni-Cu martensite were made by transmission electron microscopy, and the three-dimensional configuration of the variants resulting from self-accommodation was analyzed.

The results obtained are as follows.

(1) The fundamental unit of the self-accommodation structure in three-dimensions is cuboidal, consisting of six different variants. This structure appears to be a triangular when observed in the $\langle 111\rangle_P$ direction (P: Parent).

(2) The six variants are twin related with each other and two types of twin relations exist among them. One is the $(111)_M$ $[211]_M$ type I twin and the other is the $(011)_M$ $[011]_M$ compound twin (M: Martensite).

Then, on the basis of the observed relations among the variants the deformation process of the orthorhombic martensite was discussed.

Keywords: *martensitic transformation, shape memory alloy, titanium-nickel alloy, titanium-nickel-copper alloy, electron microscopy, self-accommodation, variant configuration*

Nihon Kinzoku Gaku Kaishi
Vol.54, No.8, 1990
870-877

Formation of Austenite and Martensite in the Surface Layer of Pure Iron due to Ion-Nitriding Hardening*

Naoki Yasumaru**

Pure iron was ion-nitrided in a mixed gas (80 vol% N_2+20 vol% H_2) under a reduced pressure of 665 Pa at 803, 923 and 1013 K and then quenched in water for the elucidation of the ion-nitriding behaviour accompanied with phase transformations above the eutectoid transformation temperature of 863 K for the Fe-N system.

When nitrided at 803 K, the nitrided case consists of two layers as usual nitrided cases do; (i) a compound layer with a hardness of about Hv 700 which is mainly composed of γ'-Fe_4N, and (ii) a diffusion layer of about Hv 250.

When nitrided at 923 K, the nitrided case consists of; (i) a compound layer of about Hv 750, mainly composed of γ'-Fe_4N, under which are (ii) an inner layer of γ austenite of about Hv 400 and (iii) a diffusion layer.

When nitrided at 1013 K, the nitrided case consists of; (i) a thin compound layer, (ii) an inner hardened layer of γ and α' martensite, of which the hardness increases from Hv 400 to Hv 700 toward the inside corresponding to the content of the α' phase, and (iii) a diffusion layer.

To explain the formation of the relatively thick hardened layers of austenite at 923 K and martensite at 1013 K, the nitrogen concentration at each temperature and the degree of the stability of the γ phase when quenched in water after nitriding were examined.

Keywords: *ion-nitriding, pure iron, nitrided case, phase transformation, austenite, martensite, compound layer, diffusion layer*

Nihon Kinzoku Gaku Kaishi
No.54, Vol.8, 1990
878-887

High Strain Rate Superplasticity and Role of Dynamic Recrystallization in Duplex Stainless Steel*

Kaneaki Tsuzaki**, Hirohisa Matsuyama***, Mamoru Nagao**** and Tadashi Maki**

Superplasticity and microstructural change during deformation of a 25Cr-7Ni-3Mo α/γ duplex stainless steel having a microduplex structure have been studied. The specimen of microduplex structure with fine α and γ grain sizes (~1 μm) showed high strain rate superplasticity at 1273 K. Elongation over 1700% was obtained at a strain rate of 1.7×10^{-2} s^{-1}. Even at 1.7×10^{-1} s^{-1} elongation was near 1000%. α/α boundaries were low angle ones before the superplastic deformation and were changed to high angle ones by dynamic recrystallization in the early stage of deformation. During deformation up to 1300% elongation after the recrystallization of the α phase, dislocations were scarcely observed in the whole of the specimen. It was concluded that the grain boundary sliding is a predominant deformation mode during superplastic flow in the present steel and the role of dynamic recrystallization is to make the structure suitable for the grain boundary sliding in the early stage of deformation. The mechanism of dynaimic recrystallization was briefly discussed.

Keywords: *duplex stainless steel, superplasticity, high strain rate superplasticity, microduplex structure, fine grain structure, dynamic recrystallization, continuous recrystallization, grain boundary sliding*

Zairyo
Vol.39, No.442
Sept. 1990
864-870

Surface Roughening of Polymers during Plastic Deformation

Takeji ABE*, Hideaki NAKANISHI** and Satoru UMEMOTO***

The surface roughening during tensile and compressive plastic deformations of polymers was investigated with a stylus instrument. The surface roughness of nylon, grey polyvinyl chloride and polyethylene increased with increasing applied strain. The surface roughness of polypropylene and transparent polyvinyl chloride increased in the early stage of tensile deformation, and it remained almost constant in the later stage. Surface roughening was hardly observed for polycarbonate.

To investigate the mechanism of surface roughening, the deformed surface was observed by a scanning electron microscope. It was found that the development of fibrous structure, the break of the fibrous structure near the surface and the formation of craze contributed to the surface roughening.

Key words : Polymers, Plastic deformation, Surface roughness, SEM

Zairyo
Vol.39, No.442
Sept. 1990
871-877

Experimental Study on Crater Configurations by Hypervelocity Impact with Relation to their Material Properties of Titanium Alloys and Aluminum Alloys

Akira NAKAMURA*, Yuuichi MATSUMOTO*, Hideaki KASHII**
Yoshio TAKANEZAWA***, Toshikatsu MAYAMA**, Kenji KOIDE****
and Yoshihisa KITAGAWA****

Hypervelocity-impact experiments were performed on the titanium alloys and aluminum alloys to study relation between the crater configurations and the static material properties. The copper projectiles were accelerated by means of a two-stage light-gas gun at averagely 2000 m/sec, and were impacted on the zero oblique specimens. The crater configurations (crater depth, crater volume and mean crater diameter) were observed, and the relation to their static material properties (density, proof stress, elongation) were studied. As a result, several correlations between the deformation by the hypervelocity impact and the static material properties were found, as follows ;

(1) The crater depth of the both materials was dependent on their density and proof stress, and was expressed by the next equation.

$$\lambda=37.8\rho_t^{-0.671}\sigma_{0.2}^{-0.175}$$

(2) The crater volume of the both materials decreased with an increase of the product of proof stress by elongation.

(3) The aspect ratio of the crater of the both materials decreased with an increase of proof stress.

(4) The crater configurations of the titanium alloys were different from these of the aluminum alloys. Decreasing the product of proof stress by elongation resulted in the increase of the mean crater diameter of the titanium alloys, whereas for the aluminum alloys, it resulted in the increase of the crater depth and the mean crater diameter, particularly the crater depth.

Key words : Hypervelocity impact, Crater, Titanium alloy, Aluminum alloy, Material property, Two-stage light-gas gun

---

Zairyo
Vol.39, No.442
Sept. 1990
844-846

Binder Extraction and Sintering of Metal Injection Molding Parts

Katsuyoshi SAITOH* and Yasunari KANEKO**

The testing of metal injection molding of SUS316L powders using a PE (polyethylene)-PP (polypropyrene)-sesame oil binder system was carried out. When the green parts were immersed in a THF (tetrahydrofuran) solvent at 50°C for 2 hr. the sesame oil was all extracted. The residual parts were debound in nitrogen gas. The debound parts were sintered at 1320°C in vacuum for 1 hr. The relative density of the sintered specimen was 95.1%. The carbon and oxygen contents of the sintered specimen were 0.001 wt% and 0.03 wt%.

Key words : Metal injection molding, SUS316L powder, Extractive debinding, Sintering

---

Zairyo
Vol.39, No.442
Sept. 1990
878-882

High Temperature Strength of Fiber-Reinforced Ni_3Al-Mo in situ Composite

Chengguo WANG*, Shiomi KIKUCHI**, Yoshitaka OKITSU***
and Masahiro KOIWA****

The strength of directionally solidified Ni_3Al-Mo alloys was investigated in tension at temperatures ranging from room temperature to 1273 K. The 0.2% flow stress showed the positive temperature dependence. The flow stress increased with increasing temperature, reached a peak at 973 K and then decreased. The effect of Mo fiber on the strength was dominant at temperatures lower than 973 K, but it became weaker above 973 K because the strength of Mo fiber decreased.

The microstructures of deformed Ni_3Al matrix changed at test temperatures. Below the peak temperature long straight dislocations, which appear be formed by cross slip, were found in the matrix. At temperatures higher than 973 K three-dimensional networks of dislocations were formed, which indicates that the recovery process is more active.

Key words : Ni_3Al-Mo alloy, Fiber reinforced material, In situ composite, High temperature strength, High temperature deformation

Nihon Kinzoku Gaku Kaishi
Vol.54, No.8, 1990
895-902

Mechanical Alloying of Al-20 mass%Ti Mixed Powders

Shunichi Abe*, Shigeoki Saji** and Shigenori Hori***

Alloying processes, formation of amorphous phase and hardening of Al-20 mass% (12.4 at%) Ti mixed powders during mechanical alloying with an Attritor type of ball mill, have been investigated by means of optical, scanning and transmission electron microscopy, X ray analysis and hardness measurements.

The mechanical alloying (MA) process detected consists of flake-forming, cold welding of the flaked powders, fracturing of the composite powders, formation of solid solution and amorphous phase. The amount of solute titanium in the composite powder after 493.2 ks MA was estimated to be about 17 mass% from the lattice parameter measurement and grain sizes of the matrix aluminum were in the range from about 20 to 60 nm. The amount of oxygen in mechanically alloyed powders increased with milling time, and dispersions of Al_2O_3 particles were observed by TEM. The spherorized composite powders with the average particle size of 0.6 μm after 2200 ks MA were amorphous. The amorphous particles showed halo patterns in electron diffraction and showed no grain boundary, no dislocation and few Al_2O_3 particles in TEM. A remarkable increase in hardness of the composite powders was explained in terms of solid solution hardening of titanium in aluminum, dispersion hardening of Al_2O_3 particles, work-hardening and hardening by grain refinement.

Nihon Kinzoku Gaku Kaishi
Vol.54, No.8, 1990
919-924

Carbothermic Reduction of Synthetic Complex Chromite $(Fe_xMg_{1-x})Cr_2O_4$ at High Temperatures

Toshio Shimoo*

The mechanism of reduction of synthetic complex chromite $(Fe_xMg_{1-x})Cr_2O_4$ with solid carbon was studied at high temperatures from 1673 to 1973 K under an argon atmosphere. The rate of reduction was measured by means of thermogravimetry, and the reduction behavior was investigated by microscopic observation and chemical analysis.

The reduction of the $FeCr_2O_4$ component preceded that of $MgCr_2O_4$, although both components was reduced simultaneously in the transient period. During the reduction of the $FeCr_2O_4$ component, FeO was preferentially reduced.

In the case of the reduction of the powdered chromite, the molten Fe-Cr-C alloy was finely dispersed except at 1673 K. The temperature dependence of the reduction rate at lower temperatures was significantly larger than that at higher temperatures. The reduction at 1973 K was slower than at 1873 K. These results showed the difference in the reaction mechanism or the rate determining step for the different temperature range.

The reduction of the coarse particles proceeded topochemically and was controlled by the gas diffusion through the porous product layer. The different reaction mechanism of the chromite with a lower ratio of Cr/Fe was due to the meltdown of the alloy layer from the oxide particles.

Keywords: *smelting reduction of chromite ore, carbothermic reduction, synthetic complex chromite,* $(Fe_xMg_{1-x})Cr_2O_4$*, reduction kinetics, reaction mechanism*

Nihon Kinzoku Gaku Kaishi
Vol.54, No.8, 1990
948-954

High Temperature Oxidation Behavior of TiAl-Base Alloys with Additions of Third Elements*

Kazuo Kasahara**, Kenki Hashimoto**,
Haruo Doi** and Tokuzou Tsujimoto**

The oxidation behavior of the intermetallic compound TiAl with additions of Cr, Y, Mn and Si as the third elements has been investigated in a temperature range between 1123 and 1223 K under the atmospheric environment. The oxidation products have been examined by X-ray diffraction, scanning electron microscopy, and electron probe microanalysis.

The mass gain by oxidation increased with small additions of Cr or Y and decreased with their additions above 1 at%. The oxidation rates of those alloys were always larger than those without the third elements. Thus, it was concluded that the addition of Cr or Y does not improve the oxidation resistance. The oxidation resistance of the alloy containing Mn was not good. The addition of Si decreased the mass gain with increasing Si content up to 0.5 mass%. However, no further increase in oxidation resistance was observed by adding more than 0.5 mass%Si.

The surface oxides were composed predominatly of three layers, i.e., TiO_2, Al_2O_3 and $TiO_2+Al_2O_3$ from the outer side. Only in the alloys containing Mn and Si, other oxides, i.e., $MnTiO_3$ and SiO_2, were detected. A continuous film of SiO_2 was formed at the alloy/oxide interface in the alloys containing more than 0.5 mass%Si. It was concluded that the formation of the continuous SiO_2 film assisted the protective ability of the Al_2O_3 layer against oxidation by decreasing the diffusion rates of the alloy elements and oxygen ions.

The weight of the oxide spalled on cooling decreased considerably in the alloys containing Y as compared with those of the other alloys. This result indicates that the addition of Y improves the adherence of the surface oxide.

Keywords: *intermetallic compound, titanium-aluminum-chromium alloy, titanium-aluminum-silicon alloy, titanium-aluminum-manganese alloy, titanium-aluminum-yttrium alloy, high temperature oxidation, oxide layers, oxide analysis*

Zairyo
Vol.39, No.443
Aug. 1990
1151-1156

An Experimental Study on Pressurized Thermal Shock (PTS) Problem by Using Photoelastic Technique

Masaaki MATSUBARA*, Tachio TAKANO** and Hiroyuki OKAMURA**

This paper describes an experimental study on pressurized thermal shock, PTS, problem by using a photoelastic technique for the purpose of confirming the validity of application of statically indeterminate fracture mechanics to the problem. The following points are made clear from the test results :

(1) Thermal stresses obtained from the photoelastic test results agree well with those given by nonstationary thermal conduction analysis.

(2) Bending moments obtained from observation of photoelastic fringes agree well with those given by nonstationary thermal conduction analysis. It was experimentally confirmed that bending moment occurred by constraint in such structure that bending deformation was restricted. The compliance of the end of specimen was quantitatively evaluated.

(3) The good agreement was observed between the stress intensity factor obtained from observation of photoelastic fringes near a crack tip and that given by application of statistically indeterminate fracture mechanics which was described in the previous paper. It was confirmed that statically indeterminate fracture mechanics which was valid for theoretical evaluation of the stress intensity factor under PTS. Also by this experimental results, It was made clear that bending moment by constraint influenced significantly the stress intensity factor under PTS.

Key words : Experimental mechanics, Photoelastic technique, Pressurized thermal shock, Stress intensity factor, Nonstationary thermal conduction analysis

---

Zairyo
Vol.39, No.443
Aug. 1990
1162-1166

Detection of Cracks in Semi-Translucent Ceramics by Slit Light

Akira ISHII*, Shigemi K. SASAKI*, Yasuo OCHI*
and Hiroyoshi HAYASHI**

An experimental visual inspection technique using the slit light for the detection of cracks in/on alumina ceramics circuit boards has been presented. Since the alumina ceramics has a well light-diffusible property over all of visible wavelength range, it is difficult to detect cracks in the material by an ordinary inspection with the human eye or optical microscope observation with coaxial illumination. In the present technique, the surface of the specimen placed on a X-Y stage is illuminated from a proper direction by the slit light, which is adjusted to a small width with several condensing lenses, and the line image of the surface is sensed by a CCD line sensor camera through an object lens and inputted into the image device as intensity signal. The X-Y stage, which is driven by pulse motors with high accuracy, is used for the mechanical scanning for obtaining the two dimensional image of the surface.

As for the results, under specific observing conditions, including the camera position relative to the slit light, the incident angle to the surface, and the width of the slit light, some characteristic intensity changes were found not only around the crack, but also on the edge of the board and of the installation holes for IC parts. The optimum condition for the detection of the crack was experimentally examined. In order to interpret these features, a simple model is proposed, and it is clarified that the light uniformly diffused into the specimen gives rise to the characteristic pattern due to the reflection at the crack surface. Finally, utilizing these characteristic patterns, one image processing algorithm, which detects only cracks in the ceramics board and has a possibility to process in high speed, is presented.

Key words : Crack detection, Slit light, Line sensor camera, Alumina ceramics, Image processing

---

Nihon Kinzoku Gaku Kaishi
Vol.54, No.8, 1990
853-860

Effects of β Grain Size and Morphology of α Precipitate on the Mechanical Properties of Ti-15V-3Cr-3Sn-3Al Alloy

Teruhiko Inaba**, Kei Ameyama*** and Masaharu Tokizane***

The effect of (1) β grain size and (2) α precipitate morphology on the mechanical properties (i.e., tensile strength, elongation) of a meta-stable β titanium alloy (Ti-15V-3Cr-3Sn-3Al) has been investigated. β single phase specimens of varying grain size (i.e.,~15 to 200 μm) were obtained by solution heat treatment above the β transus temperatures for various periods of time, followed by water quenching. The specimens were prepared for mechanical testing by (1) isothermal aging, and (2) two-stage aging, followed by water quenching. In the case of solution treated specimens, both the tensile strength and the elongation increase with decreasing β grain size. After aging in the $(\alpha+\beta)$ two-phase region, regardless of the aging method, the specimens having the same β grain size show increasing tensile strength and decreasing elongation with α precipitate refinement. However, when the morphology of α precipitates (i.e., shape, size and distribution) is approximately the same, the tensile strength is found to be independent of the β grain size, whereas the elongation increases with decreasing β grain size. Improvements in the ductility are likely due to suppression of brittle rupture at or near the grain boundaries through the refinement of β grain size.

Keywords: *Ti-15V-3Cr-3Sn-3Al Alloy, β titanium alloy, microstructure, mechanical properties, precipitation, morphology, grain size.*

DAILY RECORD

* Hayashi Denko has developed a ceramic platinum resistance thermometer bulb element by sputtering deposition. Compared with the conventional one, the production method for this element is capable of mass-producing more uniform and highly accurate elements.

* The Government Industrial Research Institute, Nagoya, of the Agency of Industrial Science and Technology has developed a new method for coating titanium artificial bones with calcium phosphate. By this method, the material solution is coated on the titanium surface followed by heating, so that calcium phosphate-coated titanium artificial bones can be made with ease.

* The Research Institute for Pollution and Resources of the Agency of Industrial Science and Technology in cooperation with Toho Oribin Kogyo, has succeeded in synthesizing spheroidal magnesium sulfate of 99.9% purity from serpentine.

* Murata Mfg. Co., Ltd. has developed a new isolator for portable telephones and car telephones, 6.3 × 6.8 × 4.0mm in external dimensions, the smallest in the world. The cubic volume was decreased to 1/3 of the conventional size by substituting highly dielectric barium-neodymium ceramics substrates for conventional alumina and using low-loss ferrite materials.

* The Japan Atomic Energy Research Institute, in cooperation with Mitsubishi Heavy Industries, Ltd., has developed a complete oil-free roughing vacuum pump. It is the first oil-free roughing pump, and uses a ceramic rotor and gas bearings.

* The Tokyo Metropolitan Industrial Technology Center has developed a low-cost artificial marble crystallized glass for building materials, suing waste fire resistant stone, a kind of volcanic rock. Because it consists chiefly of inexpensive fire resistant stone and lime, the cost of raw materials has been reduced by half.

* The Government Industrial Research Institute, Nagoya, of the Agency of Industrial Science and Technology has developed a new method of coating the surface of micrograins with other components. By the method making use of the hydrolysis of metal alkoxide, the surface of hydrophilic inert micrograins, such as α-alumina, are coated with metal oxides.

* Toray Precision Co., Ltd. has developed an electric discharge machine based on a new method of moving the electrode with a dielectric element. It has realized a super miniaturization of 1/65 the volume of the conventional machine.

* Murata Mfg. Co., Ltd. has developed two kinds of small LC filter for cordless telephones. They are 6.8mm high and 3.0mm thick, the smallest in the industry, resulting from high density electrode printing and ceramic derivative processing.

* The National Institute for Research in Metals of the Agency of Science and Technology has developed a new method to measure with high accuracy localized micro deformations of materials. This is called the electron beam Moire method, by which the dimension of material deformation is measured from a change in intervals of stripes formed by the secondary electrons coming from a substance irradiated with electron beam.

* Ishizuka Electron Co., Ltd. has developed a thermistor fitted with a lead line, realizing a 1/3 cost reduction from the past by establishing an automated mass production technique. For connecting the lead line to the ceramic thermistor, the lead frame method applied in semiconductor chips was used.

* Goheijima Chemical Industries Co., Ltd. has developed a new technology of breeding KDP (tetracalcium phosphate) monocrystal laser wavelength sensing elements at 3.5 times the previous rate. By this technique, seed crystals are put in a breeding bath to a desired base area, with crystals growing only lengthwise while the crosswise growing is suppressed by adding ions, such as those of chromium and aluminum, into the water solution.

* Ohbayashi Corp., Onoda Cement Co., Ltd., Sanwa Shutter Corp. and Naigai Mokuzai Kogyo Co. have developed a new fire door made of ceramic-artificial wood. Far the raw material of the man-made wood, calcium-silicate-system zoilite is used. The characteristics include an excellent fire resistance and fire protection capacity as well as a good thermal insulating capacity superior to fire doors made of metals, preventing a fire from spreading.

* Swiss Net Co. of Switzerland has developed a new composite material, "CORENET," chiefly aiming at using it as a material for car and airplane parts. For raw materials, chiefly glass fiber and phenol resin are used.

* Pilkington Electro Optics of the UK have developed a process of evaporating diamond thin films onto various materials at low pressure and low temperature. The technique combines high energy plasma with chemical evaporation, using methane as a basic material.

* Dowa Mining Co., Ltd., in cooperation with Murakami Screen and Murakami Techno has developed a desk top screen printing machine and the peripheral equipment for oxide superconductive thick film.

* Ushio Inc. has completed an auto magazine changer for a precision punching machine "MP–7150" used for ceramic substrate.

* Tenakku has completed a guide-pin "EX Coating Nut" for weld nuts.

The research group on "Strength and Fracture of Materials" led by Asst. Prof. T. Yokomitsu of Tohoku University has established a testing method capable of easily forecasting the growth of high-temperature creep cracks. They say that the method is applicable to the high temperature brittleness of materials such as structural ceramics.

* The department of Materials Properties Engineering of National Defense Academy and Titan Kogyo K.K. have developed a whisker-reinforced composite material (FRM) using titanium oxide powder for raw material. The method for FRM is different from the conventional method in that for the starting material intermetallic compound whisker grown by reaction is used instead of the existing whisker.